DISS. ETH NO. 23988

MULTICIRCULAR HOLOGRAPHIC SAR TOMOGRAPHY
OVER FORESTED AREAS

A thesis submitted to attain the degree of

DOCTOR OF SCIENCES

(Dr. sc. ETH Zurich)

presented by

OCTAVIO PONCE MADRIGAL

Ingeniero en Telemática, Instituto Tecnológico Autónomo de México

born on 15.02.1985

Mexican citizen

accepted on the recommendation of

Prof. Dr. Irena Hajnsek, examiner
Prof. Dr. Alberto Moreira, co-examiner
Prof. Dr. Lars M. H. Ulander, co-examiner
Prof. Dr. Laurent Ferro-Famil, co-examiner

2017

Acknowledgements

Contents

Abstract

The research of this PhD thesis is devoted to investigate the 3-D backscattering signature of vegetation, particularly forests, by using L- and P-band fully polarimetric data in the circular synthetic aperture radar (CSAR) and the holographic SAR tomography (HoloSAR) modes. The understanding of the radar backscattering of vegetation is of significant interest to retrieve physical parameters in the biosphere, such as height, ground topography and extinction factor, and consequently to estimate biomass. Several experiments have been performed to study the vertical structure of vegetation with conventional linear SAR modes, such as polarimetric SAR interferometry (PolinSAR) and SAR tomography (TomoSAR). However, an inherent limitation of these techniques is the narrow angular azimuth measurements. In order to increase the range of aspect angle measurements, a wide angular synthetic aperture, such as circular, should be formed. Sensing with CSAR and HoloSAR modes allows the measurement of the volumetric scattering over $360°$, thereby being able to fully characterise the objects of interest. In this context, the contribution of this thesis aims to investigate the full acquisition and processing chain of both modes, and consequently to obtain fully polarimetric 3-D images of forested areas. These goals can be summarised in five points. The first proposes a computational efficient implementation of the time-domain fast factorised back-projection (FFBP) algorithm for circular tracks. The second contribution of this research encompasses the first experimental CSAR airborne data collection at L-band, where the validation of volumetric reconstructions by coherent and incoherent imaging is accomplished. The third is the introduction and characterisation of the HoloSAR mode through the study of the 3-D impulse response function in time and frequency domains. The fourth is the development of a phase calibration algorithm based on the singular-value decomposition and a phase sensitivity study for mismatches in the navigation data. The last part of the thesis contains the first experimental demonstration of HoloSAR over forested areas with an airborne SAR platform at P- and L-band. Additionally, non-linear approaches such as compressive sensing (CS) and the generalised likelihood ratio test (GLRT) are investigated for distributed backscattering.

Kurzfassung

Die Forschung dieser Dissertation widmet sich der Untersuchung der dreidimensionalen Rückstreuung der Vegetation, insbesondere der Wälder, durch die Verwendung von L- und P-band polarimetrischen Daten im zirkularen synthetischen Aperturradar (circular synthetic aperture radar - CSAR) und der holographischen SAR-Tomographie (holographic SAR tomography - HoloSAR) Modi. Das Verständnis der Radarrückstreuung von Vegetation ist von erheblichem Interesse, um physikalische Parameter in der Biosphäre, wie Höhe, Boden-Topographie und Extinktionskoeffizient, zu erfassen und somit Biomasse abzuschätzen. Mehrere Experimente wurden durchgeführt, um die vertikale Struktur der Vegetation mit konventionellen linearen SAR-Modi, wie polarimetrische SAR-Interferometrie (PolinSAR) und SAR-Tomographie (TomoSAR), zu untersuchen. Eine inhärente Grenze dieser Techniken ist jedoch die schmalen Winkelazimutmessungen. Um den Bereich von Aspektwinkelmessungen zu erhöhen, sollte eine breite winkelförmige synthetische Apertur, wie z. B. kreisförmig gebildet werden. Die Datenerfassung mit CSAR- und HoloSAR-Modi ermöglicht die Messung der volumetrischen Streuung über $360°$, wodurch bestimmten Zielen vollständig charakterisiert werden können. In diesem Zusammenhang zielt der Beitrag dieser Arbeit darauf ab, die vollständige Aufnahme- und Verarbeitungskette beider Modi zu untersuchen und somit vollständig polarimetrische 3D-Bilder von bewaldeten Gebieten zu erhalten. Diese Ziele lassen sich in fünf Punkte zusammenfassen. Der Erste schlägt eine rechnereffiziente Implementierung des Zeitbereiches schnell-faktorisiertes Rückprojektion (fast factorised back-projection - FBP) -Algorithmus für zirkulare Flugstrecken vor. Der zweite Beitrag dieser Forschung umfasst die erste experimentelle CSAR-flugzeuggestützte Datenaufnahme im L-Band, bei der die Validierung volumetrischer Rekonstruktionen durch kohärente und inkohärente Abbildung erreicht wird. Die Dritte ist die Einführung und Charakterisierung des HoloSAR-Modus durch die Untersuchung der 3-D-Impulsantwortfunktion in Zeit- und Frequenzbereichen. Der Vierte ist die Entwicklung eines Phasenkalibrierungsalgorithmus auf der Grundlage der Singulärwertzerlegung und einer Phasenempfindlichkeitsstudie für Fehlanpassungen in den Navigationsdaten. Der letzte Teil der Arbeit enthält die erste experimentelle Demonstration von HoloSAR über bewaldeten Gebieten mit einem flugzeuggestützten SAR-System im P- und L-Band. Darüber hinaus werden nicht-lineares Verfahren, wie der komprimierte Abtasten (compressive sensing - CS) -Algorithmus und das Likelihood-Quotienten-Test (generalised likelihood ratio test - GLRT) -Verfahren für verteilte Rückstreuung untersucht.

List of Figures

List of Tables

List of Symbols and Acronyms

A	steering or sensing matrix
α_{pol}	rotation of the 2-D basis of the scattering mechanism
$\overline{\alpha}_{\mathrm{pol}}$	mean value of α_{pol}
α_{in}	terrain slope component in the zero-Doppler plane
α_{tilt}	tilt angle of the interferometric baseline
α_{w}	weighting factor
B	interferometric baseline
$B_\perp$	normal interferometric baseline
$B_{\perp,\mathrm{crit}}$	critical baseline
BW	system bandwidth
BW_{new}	effective bandwidth
c	speed of light
D_{a}	antenna length in azimuth
δ_{a}	real antenna resolution
δ_{az}	azimuth resolution of linear SAR modes
$\delta_{\mathrm{az,strip}}$	azimuth resolution of stripmap SAR
$\delta_{\mathrm{LOS}_\perp}$	resolution in elevation
$\delta_{\mathrm{LOS}_{\perp,\mathrm{amb}}}$	height of ambiguity in elevation
δ_{r}	range resolution
δ_{gr}	ground-range resolution
δ_x	resolution in the x direction
δ_y	resolution in the y direction
δ_z	resolution in the z direction
Δf_{r}	spectral shift
ΔB_{L}	separation between tracks
$\Delta B_{\mathrm{L},\perp}$	sampling in elevation
$\vec{e}$	eigenvector
$E(\cdot)$	expectation operator
$\vec{E}_{\mathrm{tot}}$	total electric field
$\vec{E}_{\mathrm{H}}$	complex horizontal wave
$\vec{E}_{\mathrm{V}}$	complex vertical wave
ϕ	azimuth angular variation that corresponds to t in linear SAR modes
ϕ_{chirp}	chirp phase
f_{chirp}	chirp instantaneous frequency
f_{c}	central frequency

K_az	chirp rate in azimuth
K_cr	chirp rate in range
f_D	Doppler frequency
γ_az	constant factor in the azimuth compressed data
γ_rg	constant factor in the range compressed data
γ_coh	interferometric coherence
g_ϕ	free space Green's function
G_ϕ	g_ϕ in the frequency domain
$G(x, r)$	stack of 2-D single-look complex images
h	height of the target of interest
H	entropy
$\vec{H}$	unitary vector in the horizontal direction
$J_n(\cdot)$	Bessel function of first kind n order
$\vec{k} = (k_x, k_y, k_z)$	wavenumber of f_c
$\vec{k}_\text{scat}$	3-D scattering vector
$\vec{k}_{[S],\text{L}}$	3-D scattering vector representing the lexicographic basis
$\vec{k}_{[S],\text{P}}$	3-D scattering vector representing the Pauli basis
k_r	ground projection of $\vec{k}$
λ_c	radar wavelength
λ_e	eigenvalues
L_sa	length of the synthetic aperture in azimuth
L_H	length of the synthetic aperture in elevation
$L_{\text{H},\perp}$	length of the normal synthetic aperture in elevation
$\text{LOS}_\perp$	elevation direction or direction perpendicular to the line of sight
$\mu(\cdot)$	mutual coherence
ω	range (fast-time) angular frequency
$\vec{p} = (p_x, p_y, p_z)$	corresponds to the target of interest
Ψ	basis with which X can be represented as sparse
r_0	range distance of closest approach
$\mid \vec{r} \mid = r$	range distances from the platform to the target
$\mid \vec{r}_\text{max} \mid$	largest range distance from the platform to the target
$\vec{r}_\text{grid} = (r_x, r_y, r_z)$	imaging grid
$\vec{R} = (R_x, R_y, R_z)$	platform track
σ	complex reflectivity
$s(\cdot)$	single-look complex image
$S(\cdot)$	Fourier representation of the complex reflectivity $s(\cdot)$
s_a	compressed signal in azimuth
$s_\text{az,filter}$	matched filter in azimuth
$s_\text{az,Rx}$	received signal in azimuth
s_chirp	chirp signal
s_ϕ	projection of the complex reflectivity $s(\cdot)$ at ϕ
S_r	range swath length
s_r	compressed signal in range
$s_\text{r,Rx}$	received signal in range
s_raw	collected data after quadrature demodulation

$s_{\text{chirp,Tx}}$	transmitted signal in range
$[S]$	scattering matrix
T_{chirp}	period of the transmitted chirp
T_{pulse}	period of the transmitted pulse
T_{obs}	observation time
$T_{[S],\text{L}}$	coherence matrix from the lexicographic basis
$T_{[S],\text{P}}$	coherence matrix from the Pauli basis
t	azimuth time or slow time
t_0	instant of closest approach
τ	range time or fast time
τ_0	delay time of the received echo
θ_{a}	3 dB angular resolution in azimuth
θ_{el}	elevation angle
θ_{rg}	3 dB angular resolution in range
θ_{obs}	angular observation interval
θ_{sq}	squint angle at the beam center
v_0	forward velocity
$\vec{V}$	unitary vector in the vertical direction
φ	interferometric phase
φ_{fe}	flat Earth phase
φ_{σ}	polarimetric phase
X	vector or matrix of unknown reflectivities
Y	vector or matrix of measurements
(x, r)	2-D slant-range plane
$(x, r, \theta_{\text{el}}$	3-D slant-range plane
(x, y)	2-D Cartesian grid or ground-range plane
(x, z)	2-D Cartesian grid perpendicular to y
(x, y, z)	3-D Cartesian grid
(α, r)	2-D polar grid
$(\alpha, r, \theta_{\text{el}})$	3-D polar grid
$\| (\cdot) \|$	indicates the magnitude of a vector
$\langle \cdots \rangle$	indicates the expected value
$^{*}(\cdot)$	stands for complex conjugate
$[\cdot]^{\text{T}}$	indicates the transpose of a vector or a matrix
$(\cdot)^{\dagger}$	denotes the adjoint matrix or complex conjugate transpose
$(\cdot)_{\perp}$	refers to the perpendicular direction
$\|(\cdot)\|_1$	l_1 norm
$\|(\cdot)\|_F$	Frobenius norm
$\|(\cdot)\|_{\text{TV}}$	Total-variation norm

ATI	Along-Track Interferometry
BF	Beamforming
BP	Back-Projection
CAT	Computed Axial Tomography
CS	Compressive Sensing
CSAR	Circular SAR
DEM	Digital Elevation Model (above mean sea level)
DGM	Digital Ground Model (above mean sea level)
DBP	Direct BP
E-SAR	Experimental SAR of DLR
FBP	Fast BP
FFBP	Fast Factorised BP
FFT	Fast Fourier Transform
IFFT	Inverse FFT
FM	Frequency Modulated
GLRT	Generalised Likelihood Ratio Test
GPS	Global Positioning System
GPU	Graphic Processing Unit
HoloSAR	Holographic SAR Tomography
HH	horizontally received, horizontally transmitted
HV	horizontally received, vertically transmitted
InSAR	SAR Interferometry
ISAR	Inverse SAR
IRF	Impulse Response Function
LFM	Linear FM
LOS	Line Of Sight
LSSR	Least-Squares Super Resolution
MUSIC	Multiple Signal Classification
MVM	Capon's Minimum Variance Method
PGA	Phase Gradient Autofocus
PolSAR	SAR Polarimetry
PRF	Pulse Repetition Frequency
PSLR	Peak-to-Sidelobe Ratio
RCM	Range Cell Migration
RCMC	Range Cell Migration Correction
RIP	Restricted Isometric Property
SAR	Synthetic Aperture Radar
TomoSAR	SAR Tomography
SCR	Signal-to-Clutter Ratio
SNR	Signal-to-Noise Ratio
SPECAN	Spectral Analysis algorithm
SVD	Singular Value Decomposition
UHF	Ultra-High Frequency
VH	vertically received, horizontally transmitted
VV	vertically received, vertically transmitted

| VHF | Very-High Frequency |
| XTI | Across-Track Interferometry |

1 Introduction

1.1 Radar remote sensing

Remote sensing is a technique that consists in the acquisition of information from a target of interest without establishing physical contact with it. Radio detection and ranging, better known as *radar*, was originally developed for military and surveillance purposes during the World War II in order to determine the position and velocity of aircrafts and ships through heavy weather and independent from the daylight. Interests on radars arose significantly and in fact after this period, they started to be also used for civil applications [Skol 00, Skol 01, Brow 99].

Sensors are mainly divided in passive and active. Passive sensors are constituted by a receiver only. They measure the energy radiated by objects acting as natural sources or the energy reflected by objects using an external illumination source. Among others, well-established passive sensors are film photography, infrared detectors and radiometers. On the other hand, active sensors, such as radars, are formed by a transmitter and a receiver. Their main task is to measure the reflected energy using their own illumination source. Commonly, radars are used as active sensors for remote sensing. They operate emitting radio waves and infer physical properties (e.g., roughness, spatial orientation and dielectric constant) by measuring the backscattered signal or echo. Usually, these sensors are employed for target detection, screening (estimation of position and velocity), and 2-D and 3-D imaging. If the transmit and receive antennas are in the same platform, then the radar will be called *monostatic*, otherwise, if they are in different platforms, then it will be called *bistatic* or *multistatic* depending on the number of transmitters and receivers.

The complex reflectivity of a target is the measurement quality of radars, and it is determined by the carrier frequency and the polarisation of the transmitted signal. Usually, radars operate in the microwave region of the electromagnetic spectrum with typical wavelengths between 0.001 m and 1 m, i.e., 300 GHz - 300 MHz. The selection of the wavelength allows one to control the penetration capabilities of the signal depending on the properties of the region of interest. Within this spectrum, the section of lower frequencies (usually below 1.25 GHz) is sensitive to semi-transparent media, such as tree canopies, ice sheets, and dry soil, whereas the section of higher frequencies is reflected, primarily, from surfaces. Moreover, microwaves are sensitive to the morphological structure, as well as to changes in conductivity of the targets, e.g., soil and forests [Brow 99]. All these features led radars to evolve, thus being preferred with respect to optical sensors for certain applications.

Synthetic aperture radar (SAR), a special kind of active sensors, has represented a significant advancement in the radar history [Wile 65]. Its principle is based on the side-looking (left or right) transmission of a pulse with a certain bandwidth, where the received echo is demodulated and stored to allow offline processing of the acquired data. The fundamental properties offered by SAR are frequency and spatial diversities, which allow the preservation of phase information over the whole processing. Frequency diversity is given by the system bandwidth, while spatial diversity is achieved by the relative motion between the platform and the targets. Furthermore, SAR systems own an active and controllable radiation source, which defines the frequency and polarisation of the transmitted wave [Curl 91].

Stripmap SAR and *spotlight SAR*, two of the most used monostatic *linear SAR imaging modes*, are characterised by forming a linear synthetic aperture during the acquisition. In stripmap SAR, the antenna beam is illuminating the scene in a fixed position perpendicular to the flight direction, whereas in spotlight SAR the antenna beam is steered to illuminate always the same spot. The coherent combination of the echoes, during the time interval that the targets are seen by the radar, allows one to achieve high resolution in the flight direction or azimuth. Particularly, spotlight SAR illuminates the targets for a longer period than stripmap SAR, thus achieving a finer resolution, while acquiring information from several aspect angles. On the other hand, the resolution in across-track or range coordinate, orthogonal to the azimuth, is basically defined by the transmitted bandwidth as in the case of standard pulsed radars.

Typically, SAR sensors can be mounted in airborne or spaceborne platforms. Airborne SAR systems are characterised by difficulties to maintain an ideal trajectory (commonly straight) due to turbulence, bad weather and strong winds. These deviations from the ideal path have to be taken into account during the processing to generate a well-focused image. Contrarily, spaceborne SAR sensors own the feature of having a stable platform motion [DErr 12, Sand 10]. However, processing of raw data must consider other aspects such as atmospheric (e.g., ionospheric and tropospheric) effects to achieve good quality in the final image. Contributions of the ionosphere have to be taken into account particularly for frequencies in the range of 1 GHz to 300 MHz, since they are caused by its dispersive nature. Tropospheric effects cause a delay in the signal due to the water vapour content.

One of the limitations of the linear SAR imaging modes is the retrieval of heights of targets of interest due to the cone-shaped symmetry of the acquisition geometry. To tackle this problem, researchers developed a new remote sensing technique called SAR interferometry (InSAR), which enables the highly accurate measurement of surface topography, ground deformation and subsidence, as well as glacier movements [Baml 99, Rose 00, Mass 98, Hans 01]. The basic concept of InSAR is the comparison of two or more complex images, which are taken from different positions or at different times. This comparison allows the detection and measurement of differences in the scene with a precision of centimetres or even millimetres.

If the second acquisition is performed by flying parallel to the first track and separated by a certain baseline, the technique is called across-track interferometry (XTI). XTI allows to extract the topographic information of the scene in a digital elevation model (DEM) or in a digital surface model (DSM). Usually, the two flights are identified as master and slave. The first demonstrations of InSAR were performed by L. C. Graham [Grah 74] using an airborne sensor and

in 1986 by [Zebk 86] and 1988 by [Gabr 88] using spaceborne platforms, respectively. Moreover, if the acquisitions are carried out along the same path but separated by a short temporal baseline, then it is possible to estimate fast changes in the scene. This technique is known as along-track interferometry (ATI), and it is used for applications in ocean currents and traffic monitoring. On the other hand, if the temporal baseline is large enough, then subtle changes in the observed scene can be estimated with a technique called differential SAR interferometry (DInSAR). Among others, the most common applications of DInSAR are measurements of ground subsidence, large-scale displacements after earthquakes, monitoring and detection of landslides or glacier flow [Rose 00, Ferr 01].

One of the main assumptions of InSAR is that the recovered three-dimensional information represents the terrain topography only for a plain surface with a single scatterer in the direction perpendicular to the line of sight ($LOS_\perp$). If there are many scatterers in one resolution cell, they will be superimposed and they will not be solved by InSAR. In this case, the retrieved height will correspond, generally, to an average between the minimum and the maximum height of the targets, thereby resulting in a value that does not match the actual terrain topography. *SAR tomography* (TomoSAR) determines the scattering distribution along the $LOS_\perp$ by means of the formation of a synthetic aperture in elevation[1] with conventional stripmap SAR acquisitions [Home 96]. Consequently, this mode opened a new branch as an extension of InSAR that has become a mature technique.

In TomoSAR, the maximum baseline between the first and the last track should be large enough to achieve the required resolution. Assuming that the Nyquist requirements are met, these two constraints imply a large number of acquisitions. The first experimental airborne demonstration of TomoSAR was carried out in 1998 with 13 tracks in [Reig 00], and later with 20 passes in [Nann 09b, Nann 12]. Due to its high potential, efforts have been done to make it feasible for spaceborne data with 40 tracks, and even to extend it to the 4-D case (i.e., space and time) in [Forn 03, Forn 05, She 02, Lomb 05b], and with 60 passes in [Forn 06, Forn 09, Sera 05]. The performance of experimental airborne or spaceborne acquisitions could become unfeasible, since it leads to complicated manoeuvres while flying, to temporal decorrelation (i.e., over forested areas), and to high costs. Therefore, in the past years, research has been pointed to reduce the number of acquisitions and to improve the resolution with non-linear methods such as Capon's minimum variance method (MVM), multiple signal classification (MUSIC) and compressive sensing (CS) [Lomb 03, Frey 11a, Nann 09b, Huan 12, Agui 13].

1.2 Circular and multicircular SAR acquisitions

One inherent limitation of linear SAR imaging modes is the narrow azimuth angular aperture. Since many scattering signatures depend directly on the observation angle, targets of interest cannot be fully characterised. Interestingly, these limitations can be tackled by forming wide-angular synthetic apertures, such as circular apertures. *Circular SAR* (CSAR) is characterised by flying a circular trajectory, while illuminating always the same spot in a monostatic

---

[1]Elevation indicates the direction perpendicular to the line of sight (i.e., $LOS_\perp$) or the direction perpendicular to the slant-range plane.

configuration. Its importance has risen in the last few years, due to the inherent powerful potentials caused by the acquisition of multi-angular measurements over $360°$ and dependent on the persistence of the scatterer: subwavelength resolution in the (x, y) plane independent from the system bandwidth, 3-D reconstruction with a single pass, shadow reduction and a better understanding of the coherent 3-D radar backscattering [Soum 99, Ishi 98]. A comparison between the stripmap SAR and CSAR imaging modes in the (x, y) plane is shown in Figure 1.1. Notably, one can see that a better characterisation of the backscattering can be retrieved with the CSAR imaging mode. The properties of CSAR have been analysed by using the impulse response function (IRF) and under the assumption of isotropic targets in [Soum 99, Soum 96, Ishi 98, Axel 04, Maju 07, Zhan 08, Vu 12, Moor 10]. In this context, it was shown that 2-D images focused in the (x, y) plane at the wrong height of the targets cause undesired sidelobes, such as ring or arcs that distort the image. These artefacts correspond to the cone-shaped sidelobes of the 3-D IRF, and occur due to the low resolution in the direction perpendicular to the line of sight ($\text{LOS}_\perp$). In fact, this effect is analogous to the depth of focus in confocal imaging, which helps to solve scatterers in the z direction [Ishi 98, Moor 07]. Similarly, individual object signatures are identical to those of the *Inverse SAR* (ISAR) imaging mode, where the synthetic aperture is formed by the platform rotation, while the radar remains stationary [Soum 99, Mens 91].

(a) Stripmap SAR. (b) CSAR. (c) Optics.
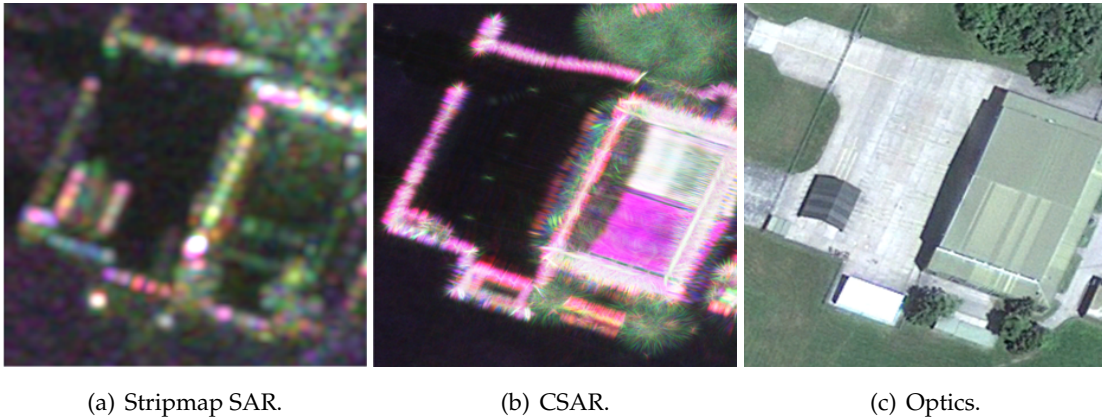
Figure 1.1: Comparison between (a) stripmap SAR (1 m x 1.8 m sampling), (b) circular SAR (CSAR) (0.06 m x 0.06 m sampling) and (c) optical images. The radar images were acquired with the E-SAR system of DLR at L-band. The scene size is 160 m x 160 m, and it shows a hangar with a gable roof (see also Figure 5.8).

The CSAR imaging mode has been object of study with real data at X-band for 2-D and 3-D reconstructions of man-made (highly directive) targets in [Soum 99, Coll 08a, Erti 07], and at a very-high frequency (VHF)-band, L-band and P-band for foliage penetration and concealed target detection [Froe 08, Coll 06, Froe 12, Hall 05]. Processing of 2-D and 3-D images was accomplished with algorithms in frequency domain with the wavefront reconstruction assuming an ideal circular trajectory, and in time-domain with the direct back-projection (DBP) using the real track. An important aspect that has to be considered while focusing is the integration time of the synthetic aperture. This means that processing can be performed either by the coherent addition of the full synthetic aperture, or by the coherent addition of small angular segments and subsequent combination of the information of all subaperture images in two different ways, i.e., by adding incoherently their intensities or by analysing them statistically,

e.g., with the generalised likelihood ratio test (GLRT) [Vocc 09]. Usually, the first approach is referred as *coherent imaging*, while the second and the third methods are called *incoherent imaging* and *GLRT imaging*, respectively. Coherent addition and incoherent addition have been compared before with simulated data of man-made targets at X-band and ultra-high frequency (UHF) data in [DeGr 05].

As aforementioned, CSAR images are corrupted by cone-shaped sidelobes due to the low resolution in the $LOS_\perp$ direction. As a matter of fact, these artefacts can be reduced by forming an additional synthetic aperture in elevation, similar to the TomoSAR mode. The synergy of CSAR and TomoSAR with multicircular acquisitions in elevation provides full 3-D reconstructions, i.e., resolution in the (x, y, z) space and in the $LOS_\perp$ direction over $360°$ [Soum 99, Ferr 09, Axel 04, Sego 10, Redd 03]. This extended CSAR imaging mode has been identified by different authors also as elevation CSAR, multipass CSAR and multicircular SAR. Figure 1.2 gives a better insight on the impact of having an additional synthetic aperture in elevation. It shows a comparison of the 3-D IRF corresponding to a single and multiple circular passes from the backscattering of a Luneburg lens. Note that cone-shaped sidelobes are mitigated with the vertical synthetic aperture.

(a) CSAR, 1 track.

(b) Multicircular SAR, 19 tracks.
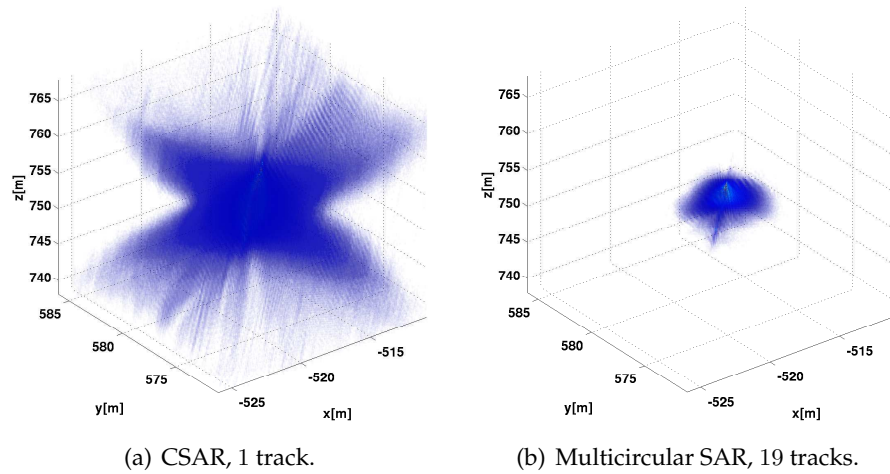
Figure 1.2: Total power of the 3-D impulse response function (IRF) of CSAR and multicircular SAR obtained with the real data of a Luneburg lens (see also Figure 6.29).

The multicircular SAR mode was studied with a simulated backhoe data in [DeGr 05, Aust 08, Mose 05] at X-band and at UHF, with a real airborne data collection at X-band called GOTCHA in [Aust 11, Erti 07, Ferr 09, Lee 11, Aust 09, Erti 10] using a total of eight circular-like tracks, and using a turntable acquisition in [Soum 99, Brya 03]. All these studies coincide with the analysis of man-made objects, i.e., highly directive targets, where basically object corners and surfaces are imaged. The most common processing algorithms for multicircular acquisitions are the DBP and the wavefront reconstruction, provided that the Nyquist requirements are met for both apertures, i.e., the circular one and the one in elevation. Similar to the TomoSAR imaging mode, attempts have been done to reduce the number of circular acquisitions by means of non-linear reconstructions. The most used non-linear methods have been the least-squares super resolution (LSSR), MVM, MUSIC and CS, while improving the image quality [DeGr 05, Aust 11].

In particular, CS has been object of study in signal processing in order to sense and reconstruct the signal of interest in a compressed form and at reduced data rate, i.e., falling short of the Nyquist criterion [Cand 08b, Cand 11]. This technique is driven by the fact that data are often compressed right after sensing, e.g., image compression in digital cameras. Sensing and reconstruction with CS are performed under certain a priori knowledge of the unknown. First, it should be possible to represent the desired signal as sparse (few elements different from zero) under certain basis. Second, sampling should be carried out as random (non-regular) as possible in order to reduce aliasing and to collect as much information as possible of the scene. Due to its adaptability, CS has been widely used for SAR processing in [Onho 12, Sama 11, Ceti 01, Zhu 12, Aust 11, Tell 10].

A further aspect related to the processing of the airborne SAR data is the accurate estimation and consideration of the platform trajectory, if defocusing wants to be avoided. Usually, the navigation data are affected by residual motion errors in the order of 1 - 10 cm because of the limited accuracy of the GPS system under high frequency movements, and by high bank angles during the circular flight that might cause loss of some satellites. Focusing wide-angular apertures requires a much more demanding precision in terms of trajectory knowledge, which in practice is hard to achieve, thus leading to the implementation of autofocus algorithms. As established in the literature, the most common ones are the Map-Drift [Manc 81, Samc 06] and the Phase Gradient Autofocus (PGA) [Carr 95a, Mace 08]. Specifically, the PGA is an iterative algorithm that estimates phase errors directly from the range-compressed data. Nevertheless, it requires the presence of point-like scatterers with enough signal-to-clutter ratio (SCR) during the whole synthetic aperture. In a real scenario, such targets are not easy to find in a CSAR image, since they must have an isotropic behaviour [Coll 08a]. In fact, the SCR is an important factor that makes the PGA converge either faster or slower. Efforts have been done to improve the SCR by filtering the range-compressed signal. In [Jako 93], the eigenvalue decomposition of neighbouring pixels in the azimuth direction was used to reduce the number of iterations in the PGA. However, at the cost of increasing sampling rate in the azimuth direction to preserve the same resolution. In addition, other approaches estimate these errors without point-like targets and based on other metrics, e.g., contrast optimisation or entropy [Ash 12, Krag 09, Cant 11], and via sparse representation in [Ende 12, Lee 08]. However, these algorithms do not usually achieve the same performance as those based on strong and know targets, since a much smaller angular persistence of the back-scattering is used. In [Torg 14, Torg 16], a solution based on a factorized geometrical autofocus for ultrawideband SAR was presented. This algorithm refocuses the image iteratively and in subapertures by tuning the platform track parameters until the intensity correlation is maximized, thereby resulting in a sharp image. Moreover, a frequency-domain autofocus algorithm was proposed for circular synthetic apertures to achieve subwavelength resolution [Ponc 14a]. This solution is based on the analysis of low SCR isotropic targets in the frequency domain, and it corrects errors in the measured track to achieve the highest possible resolution. However, it only works for areas close to the reference target [Mott 92].

1.3   Thesis contribution

This PhD thesis is the result of research that has been carried out at the Microwaves and Radar Institute (HR) of the German Aerospace Center (DLR), Germany.

1.3.1   Objectives, scope and justification

The main objectives of this research can be summarised as follows:

1. The development of a computational efficient time-domain fast factorised back-projection (FFBP) processor for circular trajectories.

2. Circular SAR acquisition analysis:

    (a) The first realisation of a fully polarimetric CSAR airborne experiment at L-band. This includes the demonstration of volumetric reconstructions and subwavelength resolutions in the presence of distributed (i.e., trees, semitransparent media), man-made (i.e., buildings), and ideal isotropic (i.e., Luneburg lens) scatterers. It also encompasses an analysis and an assessment of coherent and incoherent imaging.

3. Multicircular SAR acquisition analysis:

    (a) The introduction of *holographic SAR tomography (HoloSAR)* with multicircular acquisitions, and the analytical expression of its 3-D IRF for a target in and off the center. The IRF is analysed in terms of resolution, sidelobe power and geometric position as a function of the acquisition geometry and radar properties.

    (b) The development of a phase calibration algorithm based on the singular-value decomposition (SVD) and using strong ground returns for the improvement of focusing in the $\mathrm{LOS}_\perp$ direction.

    (c) A study of a PGA-based autofocus algorithm for circular synthetic apertures, which makes use of the phase sensitivity in the LOS direction to estimate mismatches in the navigation data.

    (d) The first experimental demonstrations of HoloSAR over forested areas with an airborne SAR platform at P- and L-band. This encompasses the analysis and assessment of HoloSAR focusing for distributed scatterers with different focusing methods, namely coherent, incoherent and GLRT imaging approaches.

Despite their great potential, CSAR and HoloSAR imaging modes lead to some challenges for processing. Perfect circular flights are a real challenge for the pilot when acquiring data in airborne SAR platforms. This results in deviations of the ideal track that have to be considered during processing to achieve high quality images. The accomplishment of high quality images in a reasonable time is a real challenge, since the amount of data and the sampling requirements of the imaging grids could be much larger than in the linear SAR imaging modes. A compromise between image quality and computational burden has been made just for linear SAR imaging modes by means of time-domain factorised back-projection techniques. In

this work, a multiple-stage time-domain FFBP algorithm for circular trajectories is presented. This algorithm takes into account the focusing accuracy, the topography accommodation and the computational efficiency, thus being suitable for circular airborne acquisitions. The implementation and the limitations of this algorithm are analysed and discussed. Furthermore, this method has been implemented in a graphics processing unit (GPU) in order to further accelerate the processing.

As aforementioned, CSAR has the potential to provide subwavelength resolution and to retrieve 3-D information. Previous CSAR experiments have been conducted with interests on the analysis and detection of man-made targets (i.e., highly directive), considering that all of them are anisotropic, thereby focusing in subapertures. For this reason, these approaches do not focus all targets at their maximum resolution since angular persistence for most of them is unknown. In this thesis, the investigations of previous work are extended by analysing the properties at L-band of both man-made and natural targets when processing with coherent and incoherent imaging approaches. In fact, this frequency band offers foliage penetration and, hence the potential of volume information retrieval. Moreover, this thesis shows the first demonstration of CSAR 3-D fully polarimetric imaging with real data at L-band using a single circular flight, as well as high-resolution imaging in the (x, y) plane close to the theoretical value of $\sim \lambda/4$. To that end, a CSAR data collection was run with the E-SAR sensor of DLR over a forested region close to Kaufbeuren, Germany in 2008.

The extension of CSAR to multiple circular acquisitions in elevation is the third main area of study in this thesis. In this respect, the concept of holographic SAR tomography (Holo-SAR) is introduced. This mode is defined by the strong similarities that exist in acquisition and processing between HoloSAR and two fundamental techniques, namely tomography (e.g., tomosynthesis and ectomography) and optics (e.g., holography with coherent light) [Gran 72, Knut 80, Dale 88, Alek 75, Ferr 11, Shan 09]. In fact, some attempts have been done to compare SAR with the two techniques, and consequently many concepts such as hologram radar, microwave holograms, quasi-holograms and more recently the TomoSAR mode have been defined [Knae 95, Muns 83, Reig 00, Brow 67, Brow 69, Cutr 66, Leit 71, Pasm 05a, Mens 80, Mens 82]. Interestingly, the holographic tomography technique in optics using a circular synthetic aperture was first demonstrated in [Groh 71]. However, it was not until the beginning of the 1990s that a similar concept, called holographic SAR, was introduced with circular acquisitions [Glaz 93, Schi 93]. In either case, the concept of HoloSAR was not clearly described, and consequently it was not adopted by the SAR community. In this thesis, the HoloSAR imaging mode is redefined as the synergy of holography, tomography and multicircular SAR acquisitions. In this way, describing this mode as a solution to fully characterise the 3-D backscattering of the scene of interest over $360°$.

Furthermore, the IRF of HoloSAR has been studied with an infinite horizontal synthetic aperture by using concentric circles and showing the 2-D IRF for an infinite synthetic aperture [Axel 04]. However, the IRF has not been analysed as a function of resolution, PSLR and acquisition geometry in elevation, and particularly for a target off the center. This thesis presents an analytical expression that describes the IRF of HoloSAR for a target in the center of the illuminated scene. The IRF is analysed as a function of the central frequency, the system bandwidth, thus evaluating the resolutions in x, y, z and $LOS_\perp$ directions as a function of the geometry

of the circular tracks in elevation. In this way, it is possible to optimise the flight geometry to achieve the best possible 3-D sidelobe suppression and resolution. To analyse the IRF for a target off the center, an assessment of the spectrum of the IRF for different acquisition geometries has been performed.

Similar to CSAR, the precision of the measured track in HoloSAR imaging mode is an important aspect that must be considered when processing. In fact, this mode is more demanding due to the additional synthetic aperture in elevation. In this thesis the two autofocus approaches are studied. On the one hand, a PGA based algorithm has been adapted for circular synthetic apertures to achieve theoretical resolutions. This encompasses the methodology of reference targets setup, and the sensitivity analysis of the phase containing motion and constant errors of the navigation data. On the other hand, most of the autofocus approaches use strong reference targets that are hard to find in a real scenario. In view of this fact, the second calibration proposed in this thesis offers a solution to estimate constant phase errors from strong ground signatures of multiple 2-D coregistered images, which are focused in the (α, r) plane, i.e., polar coordinates. This approach uses the SVD of ground returns that can be corrupted by noise (e.g., speckle and thermal). Consequently, it achieves an improved focusing in the $\text{LOS}_\perp$ direction.

Until now, all multicircular experiments have been run at high frequencies (X-band) with the objective to study highly-directive targets, i.e., man-made targets such as vehicles, to get information about the object's shape surfaces, and they have never been carried out with semi-transparent media for 3-D reconstruction at lower frequency bands, where their penetration capabilities allow the extraction of further information, e.g., the volume structure of forested areas. In view of this fact, this thesis gives an additional contribution, namely the first demonstration of fully polarimetric HoloSAR reconstructions at L- and P-band over forested areas. A further aspect investigated in this work is the use of CS for HoloSAR to retrieve the energy along the $\text{LOS}_\perp$ direction for distributed scatterers, i.e., natural targets. In addition, the impact of isotropy and anisotropy of forested areas with coherent, incoherent, and GLRT imaging approaches is analysed. The demonstrations are performed with two real data collections using the F-SAR airborne system of DLR. The first one was acquired in the area of Vordemwald, Switzerland in 2012 at P-band with seven circular passes irregularly distributed in elevation. Likewise, the second data collection was run over the area of Kaufbeuren, Germany in the same year in L-band with nineteen circular passes.

1.3.2 Outline

The structure of this thesis is delineated as follows. Chapter 2 is devoted basically to fundamental aspects of the linear SAR imaging modes, i.e., stripmap and spotlight, in terms of resolution and processing. Afterward the basic theory of polarimetric SAR systems as an important tool to acquire full scattering information of the targets of interest is presented. Next, SAR interferometry is introduced as the first alternative to retrieve 3-D information assuming a single phase center in elevation. Then, its extension to TomoSAR to solve the 3-D scattering profile for several phase centres is given. Finally, a comparison of SAR and medical tomography is given through the well-known projection-slice theorem and the Radon transform.

Chapter 3 gives the basic theory of CSAR. This includes an analysis of the IRF for a target in and off the center in terms of resolution and sidelobe power, and its topography dependency. Afterward the fundamental definition of the time-domain DBP algorithm is given as a starting point to understand the background of the FFBP method for circular trajectories, which is one of the main contributions of this thesis. Then, the non-linear compressive sensing method is introduced. In fact, this method is used to focus in elevation when the number of samples fall short of the Nyquist criterion. In the last part of this chapter, the different concepts of autofocusing algorithms, such as the PGA, its extension using eigenvalue decomposition, and a frequency-based autofocus method, are introduced. The three algorithms estimate mismatches in the navigation system, and allow a more accurate focusing for high resolution imaging.

Chapter 4 presents a brief but important introduction on the time-domain fast back-projection techniques for linear SAR imaging modes. This theory is further extended to circular trajectories, thus resulting in the first contribution of this thesis. The FFBP approach for circular trajectories accommodates accurately the real track, azimuth and topographic changes, while being efficient in terms of computational cost. In addition, an assessment of this algorithm compared to the DBP, and implemented in both, CPUs and a GPU is given.

Chapter 5 gives the contributions of this thesis regarding the potentials of single circular SAR apertures. This encompasses the first experimental analysis and assessment at L-band for 2-D and 3-D imaging for distributed and man-made targets. Moreover, the validation of the FFBP algorithm for circular trajectories with real data is presented. An analysis of coherent and incoherent imaging is given, and a comparison between stripmap SAR and CSAR imaging modes is performed. The airborne CSAR data, acquired by the DLR's E-SAR system, are used.

Chapter 6 presents the theory and the first demonstration of holographic SAR tomography (HoloSAR). The IRF of HoloSAR is analysed in terms of resolution and sidelobe power as a function of the acquisition geometry and radar configuration. In order to achieve an accurate focusing, inaccuracies of the navigation data are studied by means of a PGA for circular trajectories. Furthermore, the HoloSAR theory is validated and assessed with two multicircular acquisitions at P- and L-band for forested areas (i.e., distributed targets), thereby being the last contribution of this thesis. The two multicircular data collections, run with the DLR's F-SAR sensor, are introduced.

Lastly, in Chapter 7 the conclusions to all contributions of this thesis are given. A discussion on the potential Earth observation applications of the HoloSAR technique is presented, as well as key concepts for future work with airborne and spaceborne SAR.

2 Synthetic Aperture Radar

In this Chapter, the basic knowledge of SAR is provided. In the first place, the fundamental concepts of the linear SAR imaging modes are described in terms of resolution and acquisition geometry. Afterward, the aspects on SAR processing in range and azimuth directions are given. This theory is followed by two of the established SAR techniques, interferometry and polarimetry. Lastly, the analogy of SAR and CAT is discussed in order to introduce one of the emerging SAR techniques, called SAR tomography.

2.1 SAR resolution

Resolution is defined as the ability to distinguish or isolate two scattering centres represented by their complex reflectivity, σ. In radar systems, it is one of the most important features for characterisation. Interestingly, synthetic aperture radar (SAR) systems allow high resolution imaging by the motion of either the platform or the object of interest. This particular feature has made SAR one of the most used remote sensing techniques [Skol 01, Cumm 05, Carr 95b, Soum 99, Curl 91].

The SAR principle is based on the side-looking (left or right) transmission of pulses of electromagnetic energy with period of $1/PRF$ sec or frequency of PRF[1] Hz, which travel to the target to be scattered back to the platform as echoes. Figure 2.1 shows the acquisition geometry that corresponds to two of the most used monostatic linear SAR modes, namely stripmap and spotlight. Two possible resolutions in orthogonal directions are defined in these modes: *range* or *slant-range*, and *along-track* or *azimuth* [Cumm 05, Carr 95b]. The projection of the slant-range on the ground is known as *ground-range*, and the direction orthogonal to the slant-range and the azimuth directions is the elevation or the direction perpendicular to the line of sight, $\text{LOS}_\perp$.

2.1.1 Range resolution

The resolution in range direction is defined as the minimum distance between two contiguous targets that ensures non-overlapping of their echoes at the receiver, given by

$$\delta_{\text{r}} = \alpha_{\text{w}} \cdot \frac{c \cdot T_{\text{pulse}}}{2},$$

(2.1)

---

[1]Pulse repetition frequency (PRF).

11
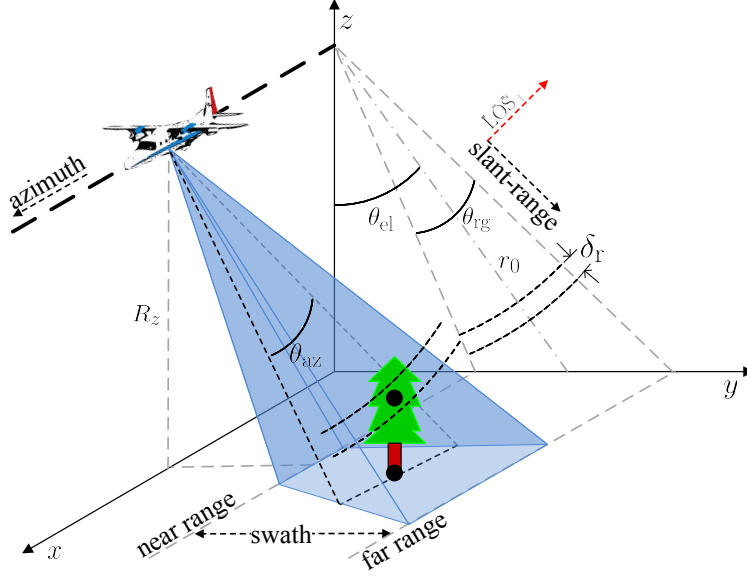
Figure 2.1: Geometry of monostatic linear SAR imaging modes.

where α_{w} is the factor that corresponds to the weighting during processing (see Table 2.1), T_{pulse} is the period of the transmitted pulse in seconds, c is the speed of light in meters per second, and the factor 2 accounts for the two-way path. Eq. (2.1) shows that to achieve a better resolution, a short pulse duration have to be used, thus yielding high peak transmitted power.

In order to reduce the high power demand and to achieve fine resolution, frequency modulated pulses are used instead of short pulses. The most common type of pulse in SAR systems is the linearly frequency modulated waveform (LFM), which is well known as *chirp* (Figure 2.2). The chirp is defined by the following expression

$$s_{\mathrm{chirp}}(\tau) = \mathrm{rect}\left(\frac{\tau - \tau_0}{T_{\mathrm{chirp}}}\right) \cdot e^{\mathrm{j}\pi K_{\mathrm{cr}} \cdot (\tau - \tau_0)^2} \tag{2.2}$$

where T_{chirp}, in the rect function[2], is the chirp length in seconds, $\tau \,\epsilon\, [-T_{\mathrm{chirp}}/2, T_{\mathrm{chirp}}/2]$, τ_0 is the delay time of the received echo, and K_{cr} is the *chirp rate* in Hertz per second. Figure 2.2(a) shows the real (black line) and the imaginary (red dotted line) parts of (2.2).

One can see that the phase of $s_{\mathrm{chirp}}(\tau)$ is quadratic

$$\phi_{\mathrm{chirp}}(\tau) = \pi K_{\mathrm{cr}} \cdot (\tau - \tau_0)^2, \tag{2.3}$$

and the instantaneous frequency is linear

$$f_{\mathrm{chirp}}(\tau) = \frac{1}{2\pi}\frac{\partial \phi_{\mathrm{chirp}}}{\partial \tau} = K_{\mathrm{cr}} \cdot (\tau - \tau_0), \tag{2.4}$$

(see Figure 2.2(b)). Subsequently, the transmitted bandwidth can be defined from (2.4) as $BW = |K_{\mathrm{cr}}| \cdot T_{\mathrm{chirp}}$. Due to the properties of the chirp signal, the range resolution differs from (2.1) after processing, in the following form

$$\delta_{\mathrm{r}} = \alpha_{\mathrm{w}} \cdot \frac{c}{2 \cdot BW}, \tag{2.5}$$

where the system bandwidth depends not only on the chirp duration, but also on the chirp rate. Notably, a wide chirp bandwidth is needed to enhance the resolution, δ_{r}.

---

[2] $\mathrm{rect}(x) = 1$, if $|x| \leq 0.5$, or $\mathrm{rect}(x) = 0$ otherwise.
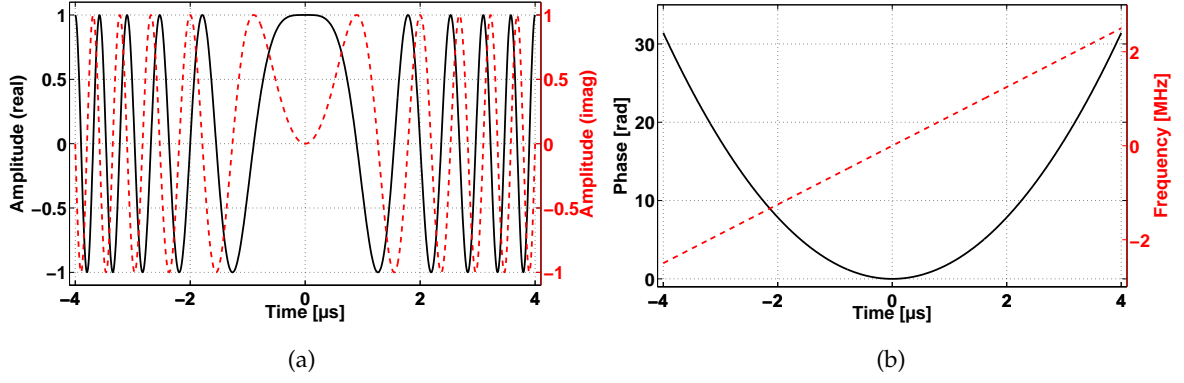
Figure 2.2: Amplitude and phase of a baseband linear frequency modulated (FM) pulse (chirp). (a) Chirp amplitude, real (black line) and imaginary (red dotted line) parts. (b) Signal phase (black line) and instantaneous frequency (red dotted line) of the chirp.

2.1.2 Azimuth resolution for Stripmap and Spotlight SAR

The geometric resolution achieved by a planar antenna, i.e., real aperture radar, in the azimuth direction is given by

$$\delta_{\mathrm{a}} = \sin(\theta_{\mathrm{a}}) \cdot r_0 \approx \theta_{\mathrm{a}} \cdot r_0 \approx \frac{\lambda_{\mathrm{c}}}{D_{\mathrm{a}}} \cdot r_0, \tag{2.6}$$

where θ_{a} is the 3 dB angular resolution defined by the radiation pattern of the antenna, r_0 is the range distance of closest approach to the target of interest, λ_c is the wavelength that corresponds to the central frequency, f_{c}, and D_{a} is the antenna length in the azimuth direction. In this case, δ_{a} depends directly on the range distance to the target, r_0, and the angular resolution, θ_{a}. This fact leads to the need of a very long physical antenna in order to achieve a fine resolution, which is practically infeasible. Interestingly, this limitation can be overcome by the formation of a synthetic aperture as shown next.

Stripmap SAR and spotlight SAR are characterised by a linear synthetic aperture. The acquisition geometry in stripmap SAR mode points the radar antenna beam to a fixed direction during the acquisition, i.e., perpendicular to the azimuth axis (or x direction). The covered area is a strip that is limited only in the range direction by the elevation angle, θ_{el}, and the range antenna beamwidth, θ_{rg}. Unlike stripmap SAR, in spotlight SAR mode the antenna beam is pointed to a specific region during the flight, thus increasing the geometric resolution, since the region of interest is observed for a longer acquisition time, i.e., a greater observation angle, θ_{obs} [Cumm 05, Carr 95b]. However, this improvement occurs at the cost of imaging a smaller area in the along-track direction. Figure 2.3 shows a comparison between these two modes. Practically, the imaged area in stripmap SAR is unlimited, but it is shown as the $\overline{AB}$ strip for the same flight length.

In order to achieve an azimuth resolution, δ_{az}, comparable to the one in range, all echoes corresponding to a certain scatterer, p, are coherently combined. In this way, the resolution can be estimated from the Doppler frequency, which is the derivative of the phase $\frac{4\pi}{\lambda_{\mathrm{c}}} \cdot |\vec{r}(t; r_0)|$ (see
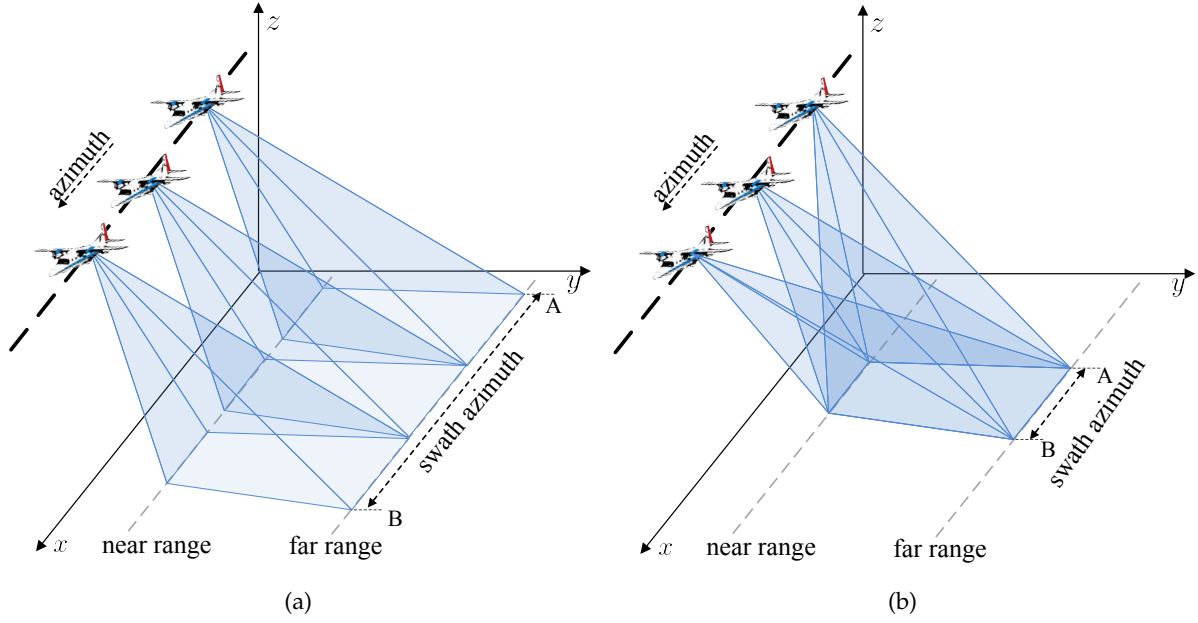
Figure 2.3: Comparison of the imaged area between stripmap and spotlight SAR modes. Note that the antenna beam is steered to a fixed position in spotlight SAR mode, thus the swath in azimuth direction, $\overline{AB}$, is smaller than in the stripmap SAR case for the same flight length. (a) Stripmap SAR. (b) Spotlight SAR.

2.14), as follows

$$f_{\mathrm{D}} = \frac{\partial(\frac{4\pi}{\lambda_{\mathrm{c}}} \cdot |\vec{r}(t;r_0)|)}{\partial t} \cdot \frac{1}{2\pi} = \frac{\partial(\frac{4\pi}{\lambda_{\mathrm{c}}} \cdot \sqrt{r_0^2 + (v_0 \cdot t)^2})}{\partial t} \cdot \frac{1}{2\pi} = \frac{2v_0}{\lambda_{\mathrm{c}}} \cdot \frac{v_0 \cdot t}{|\vec{r}(t;r_0)|}, \tag{2.7}$$

where $|\vec{r}(t;r_0)|$ describes de relative movement between the target of interest and the sensor, v_0 is the forward velocity, and t is the slow-time. Subsequently, the maximum Doppler frequency is obtained when $t = t_{\max}$ and $|\vec{r}(t;r_0)| = |\vec{r}_{\max}(t;r_0)|$

$$f_{\mathrm{D,max}} = \frac{2\,v_0}{\lambda_{\mathrm{c}}} \cdot \frac{v_0 \cdot t_{\max}}{|\vec{r}_{\max}(t;r_0)|} = \frac{2\,v_0}{\lambda_{\mathrm{c}}} \cdot \sin\left(\theta_{\mathrm{sq}} + \frac{\theta_{\mathrm{obs}}}{2}\right), \tag{2.8}$$

where $|\vec{r}_{\max}(t;r_0)|$ is the magnitude of the largest distance vector between the target and the sensor, L_{sa} is the length of the synthetic aperture, θ_{sq} is the squint angle at the beam center (the off-boresight angle), and θ_{obs} is the angular observation interval that is the range of aspect angles in which a certain scatterer is seen by the sensor during the acquisition (see Figure 2.4).

The general expression of the resolution in the azimuth direction for both modes can be estimated from (2.7) as

$$\delta_{\mathrm{az}} \approx \alpha_{\mathrm{w}} \cdot \frac{\lambda_{\mathrm{c}}}{2 \cdot L_{\mathrm{sa}}} \cdot |\vec{r}_{\max}(t;r_0)|. \tag{2.9}$$

Particularly, (2.9) can be simplified for the stripmap SAR mode with the following expression

$$\delta_{\mathrm{az}} \approx \alpha_{\mathrm{w}} \cdot \frac{\lambda_{\mathrm{c}}}{2 \cdot \theta_{\mathrm{obs}} \cdot r_0} \cdot r_0 = \alpha_{\mathrm{w}} \cdot \frac{\lambda_{\mathrm{c}}}{2 \cdot \theta_{\mathrm{obs}}}, \tag{2.10}$$

where an angular observation interval θ_{obs} and a large $|\vec{r}_{\max}|$ are considered. In addition, θ_{obs} is considered to be equal to the angular resolution of the physical antenna, thus yielding

$$\delta_{\mathrm{az,strip}} = \alpha_{\mathrm{w}} \cdot \frac{\lambda_{\mathrm{c}}}{2 \cdot \theta_{\mathrm{a}} \cdot r_0} \cdot r_o = \alpha_{\mathrm{w}} \cdot \frac{\lambda_{\mathrm{c}}}{2 \cdot (\frac{\lambda_{\mathrm{c}}}{D_{\mathrm{a}}} \cdot r_0)} \cdot r_0 = \alpha_{\mathrm{w}} \cdot \frac{D_{\mathrm{a}}}{2}, \tag{2.11}$$

where the resolution only depends on the physical antenna size, D_a, and more importantly, it is independent of r_0 and λ_c. This advantage is a great benefit for spaceborne SAR, since the closest distances are in the order of hundreds of kilometres.
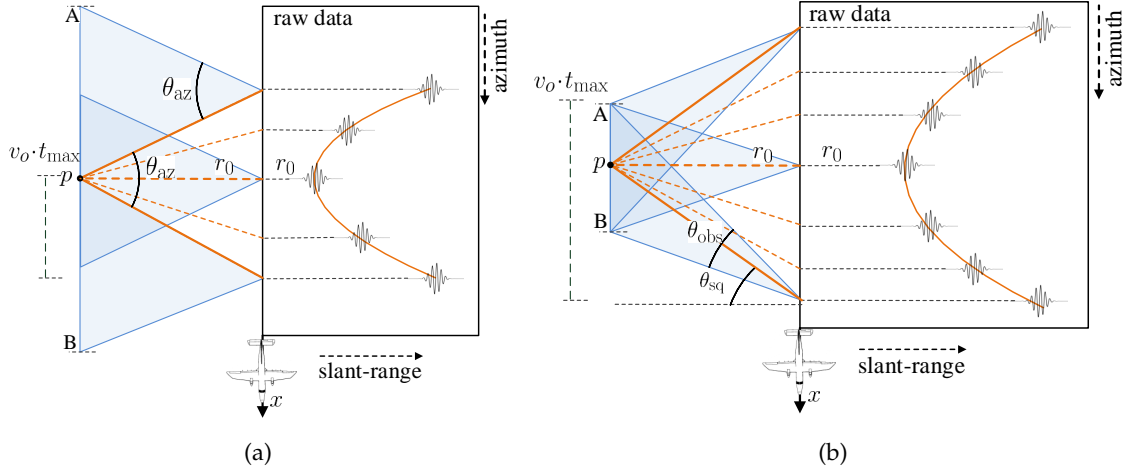
Figure 2.4: Stripmap and Spotlight SAR azimuth geometry and range cell migration (RCM). The segment $\overline{AB}$ indicates the imaged area, v_0 is the platform velocity, $t_{\max}$ is half of the total illumination time, p is the target of interest, r_0 is the closest approach, θ_{sq} is the squint angle, and θ_{obs} is the angular observation interval. (a) Stripmap SAR. (b) Spotlight SAR.

Furthermore, the PRF should be greater or equal to the greater or equal to the Doppler bandwidth in order to meet the Nyquist requirements, but lower than the two-way travel time of the range swath to avoid range ambiguities [Cumm 05]

$$\frac{4\,v_0}{\lambda_c} \cdot \sin\left(\theta_{sq} + \frac{\theta_{obs}}{2}\right) \leq PRF \leq \frac{c \cdot S_r}{2}, \tag{2.12}$$

where $S_r = \frac{\theta_{rg} \cdot r_0}{\cos(\theta_{el})}$ is the range swath length in meters, which is defined by the near- and far-range corresponding to the 3 dB width of the antenna pattern in elevation.

2.2 SAR processing

All backscattered echoes that reach the receiver are sampled according to the system bandwidth, BW, and stored in a matrix. This matrix is better known as *raw data*, and it is processed in the range and azimuth directions in order to get the focused or final image in the slant-range plane, i.e., (x, r). These two orthogonal dimensions are expressed as a function of *fast time* (range) and *slow time* (azimuth). The fast-time is indicated by τ and it is the time delay of the received echo, which is proportional to the range distance. Similarly, the slow-time is indicated by t and it is proportional to the flight track. SAR processors are divided in two groups: frequency-domain and time-domain based processors. The former is well known due to its efficiency in computational burden, however at the cost of loosing accuracy due to several approximations when very high resolution images are desired (see Section 2.2.2). The latter requires more computational burden but achieves a more precise focusing. Among others the most common frequency-domain processors are the *chirp scaling*, the *range Doppler*, the *ω-k*,

and the *SPECAN* (spectral analysis) algorithms [Cumm 05, Carr 95b]. On the other hand, the most common time-domain processors are the *direct back-projection (DBP)* and the *fast factorised back-projection (FFBP)* algorithms [Soum 99, Yegu 99, Ulan 03]. The next subsections present the basic principles of nominal SAR processors, based on signal correlations, which are better known as matched filters [Cumm 05]. The time-domain processors are explained in Section 3.5, since one of the main contributions of this thesis is based on time-domain processing.

2.2.1 Nominal range imaging

Imaging in the range direction by means of a matched filter is a signal processing technique that convolves the received echo with the transmitted pulse, (2.2). The purpose of this compression is to maximise the signal-to-noise ratio (SNR), maximise the peak power, and achieve a fine range resolution, δ_r. This process is also known as pulse compression and is expressed by the following convolution

$$s_\mathrm{r}(\tau) = s_\mathrm{r,Rx}(\tau - \tau_0) \otimes s^*_\mathrm{chirp,Tx}(-\tau) \approx \gamma_\mathrm{rg} \cdot \mathrm{sinc}(|K_\mathrm{cr}| \cdot T_\mathrm{chirp} \cdot (\tau - \tau_0)), \qquad (2.13)$$

where $s_\mathrm{r}(\tau)$ is the compressed signal in range, described by a $\mathrm{sinc}(\cdot)$ function [3], $s_\mathrm{r,Rx}(\tau - \tau_0)$ and $s_\mathrm{chirp,Tx}(-\tau)$ are the received and transmitted signals, respectively, $^*(\cdot)$ stands for complex conjugate, τ_0 is the time of the received echo, and γ_rg is a constant factor. The resolution of (2.13) is the distance that corresponds to the -3 dB width of the normalised main lobe, which is 0.707 times below the peak magnitude. For this reason, the resolution in range given by (2.5) is multiplied by a factor of $\alpha_\mathrm{w} = 0.886$. This factor is a function of the applied spectral weighting, as described in the next subsection.

2.2.2 Nominal azimuth imaging

Azimuth imaging is the feature that differentiates SAR from other radars. The acquired echoes in the along-track direction are added up coherently in order to achieve fine resolution for a certain scatterer, p. Usually, processing in linear SAR modes assumes that scatterers are isotropic, i.e., remain coherent during the integration time. The azimuth reference function, $s_\mathrm{az,Rx}(t; r_0)$, considered for the nominal azimuth imaging is described as

$$s_\mathrm{az,Rx}(t; r_0) = \mathrm{rect}\left(\frac{t - t_0}{T_\mathrm{obs}}\right) \cdot e^{-\mathrm{j}2k_\mathrm{az} \cdot |\vec{r}(t; r_0)|} = \mathrm{rect}\left(\frac{t - t_0}{T_\mathrm{obs}}\right) \cdot e^{-\mathrm{j}2k_\mathrm{az} \cdot \sqrt{x(t)^2 + r_0^2}}, \qquad (2.14)$$

where t_0 is the instant of closest approach, $T_\mathrm{obs} = \frac{\theta_\mathrm{obs} \cdot r_0}{v_0}$ is the observation time, k_az is the wavenumber in the azimuth direction, $|\vec{r}(t; r_0)|$ is the magnitude of the distance vector from the platform to the scatterer, r_0 is the distance of closest approach, and $x(t) = v_0 \cdot (t - t_0)$.

The range history, given by $\vec{r}(t; r_0)$, describes an hyperbola in which the energy of a certain target is spread in both azimuth and range directions, i.e., it indicates a two-dimensional space-variant dependency in the azimuth imaging (see Figure 2.4). This effect, called range cell migration (RCM), is a geometric property of the acquired data caused by changes in the relative

---

[3]The $\mathrm{sinc}(\cdot)$ function is defined as $\gamma_{(\cdot)} \cdot \mathrm{sinc}(|K_{(\cdot)}| \cdot T_{(\cdot)} \cdot (x - \hat{x})) \approx (s_\mathrm{Rx}(x - \hat{x}) \otimes s^*_\mathrm{Tx}(-x))$.

distance between the platform and a fixed point on the ground [Cumm 05]. To avoid defocusing, the RCM should be corrected because the energy of the target of interest does not only occupy a single range bin, but several, i.e., a non-stationary two-dimensional reference function should be correlated with the collected data. As discussed in the SAR literature, this is the most challenging processing aspect regarding frequency-based processors to achieve high resolution images, since many approximations have to be done.

In particular, one of the approximations to estimate the RCM is based on the Taylor expansion of second order. In this way, (2.14) can be expressed as

$$s_{\mathrm{az,Rx}}(t; r_0) \approx \mathrm{rect}\left(\frac{t - t_0}{T_{\mathrm{obs}}}\right) \cdot e^{-\mathrm{j}2k_{\mathrm{az}} \cdot r_0} \cdot e^{-\mathrm{j}2k_{\mathrm{az}} \cdot \frac{x(t)^2}{2r_0}}, \tag{2.15}$$

where the first exponential term is kept for applications of 3-D SAR with a synthetic aperture in elevation, such as SAR interferometry (InSAR) and SAR tomography (TomoSAR) [Baml 99, Reig 00]. Subsequently, the second term corresponds to a LFM signal or chirp, which has a quadratic phase. In this respect, the azimuth chirp rate, K_{az}, of the second term is dictated by

$$K_{\mathrm{az}} \approx -\frac{2v_0^2}{\lambda_{\mathrm{c}} \cdot r_0}. \tag{2.16}$$

To perform the nominal azimuth imaging, it is assumed that the RCM has already been corrected [Cumm 05]. Similar to the range compression, a matched filter in the azimuth direction is considered to compress the energy. In this way, the azimuth compressed signal is defined as:

$$s_{\mathrm{az}}(t) = s_{\mathrm{az,Rx}}(t - t_0) \otimes s_{\mathrm{az,filter}}^*(-t) \approx \gamma_{\mathrm{az}} \cdot e^{-\mathrm{j}2k_{\mathrm{az}} \cdot r_0} \cdot \mathrm{sinc}(|K_{\mathrm{az}}| \cdot T_{\mathrm{obs}} \cdot (t - t_0)), \tag{2.17}$$

where the resolution of the compressed signal matches (2.10). Figure 2.5 depicts the processing steps of the nominal SAR processing by means of matched filters. This includes the raw data as input, the range compression, RCMC and the azimuth compression with simulated data.

Figure 2.6 shows the 2-D IRF of a stripmap SAR in the (x, r) plane. Note that the peak-to-sidelobe ratio (PSLR) is about -13 dB with respect to the main lobe in both dimensions. This value is one of the main features of a rectangular function and can be reduced using a weighting function at the cost of geometric resolution [Cumm 05]. The most common weighting functions are listed in Table 2.1.

Table 2.1: List of weighting functions for linear SAR modes. α_{w} is the factor that multiplies the resolution, a represents the maximum frequency, and PSLR stands for peak-to-sidelobe ratio.

Weighting function	α_{w} (3 dB)	PSLR (dB)	Analytical expression, $|f| \leq a$
Rect	0.89	-13	$w(f) = \Pi(\frac{f}{2a})$
Hanning	1.44	-32	$w(f) = 0.5 + 0.5 \cdot \cos(\frac{\pi f}{a})$
Hamming	1.30	-43	$w(f) = 0.54 + 0.46 \cdot \cos(\frac{\pi f}{a})$
Gaussian 3.5	1.79	-69	$w(f) = e^{-\frac{1}{2}\left(3.5\frac{f}{a}\right)^2}$

(a)

(b)

(c)

(d)
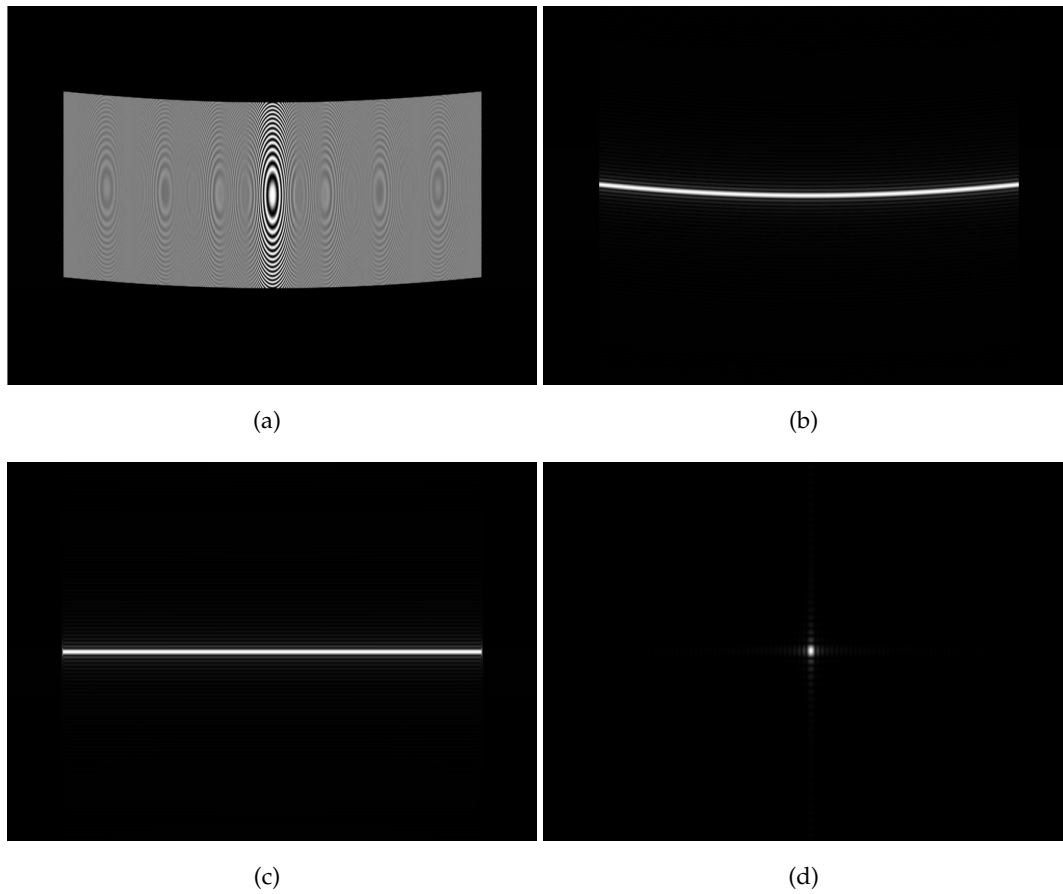
Figure 2.5: Nominal SAR processing using matched filters. (a) Raw data. (b) Range compression. (c) Range cell migration (RCM) correction. (d) Azimuth compression to get the focused data.

(a)

(b)
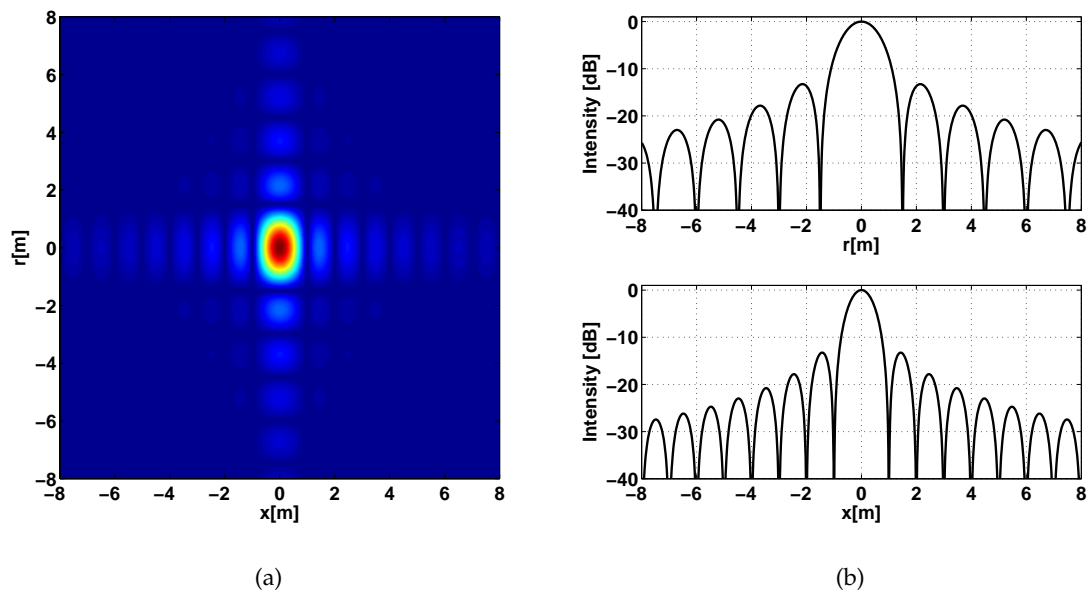
Figure 2.6: Impulse response function (IRF) of the linear SAR modes. (a) Amplitude of the 2-D IRF. (b) Intensity of the 1-D IRF.

2.3   SAR interferometry

A focused SAR image using a single pass in stripmap or spotlight modes is the projection of a 3-D scene onto a 2-D plane (slant-range and azimuth), where the contribution of point targets at the same slant-range falls in one resolution cell, thus causing uncertainty concerning their height. This problem can be overcome by having two passes at different positions in elevation and exploiting the phase differences between the images, a concept known as SAR interferometry (InSAR) [Grah 74, Zebk 86, Gabr 88, Baml 99, Rose 00, Mass 98, Hans 01].

The key idea of InSAR is to compute, for a given scene, the phase difference of two complex radar images that have been acquired with a certain baseline in space or time. To that end, it has to be ensured that the phase of closest approach is preserved after focusing, as mentioned before in Section 2.2.2. Notably, this phase contains the range difference information with an accuracy of a fraction of the radar wavelength, λ_c, in this way being able to detect and measure differences within centimetres or millimetres. This phase is normally used for surfaces, i.e., assuming a single scatterer in the $LOS_\perp$ direction, however in case of having several scatterers, their energy will be superimposed and will not be solved. In this case the retrieved phase will correspond, generally, to an average between the phases.

InSAR acquisitions are categorised into two geometries: *along-track interferometer (ATI)* and *across-track interferometry (XTI)*. In the former, the acquisition is run with a 0 m across-track baseline, thus being able to estimate temporal changes between the two images, e.g., soil deformation or the velocity of moving targets. In XTI, the survey is performed with an across-track baseline different from 0 m, in this way retrieving information concerning the topography, i.e., the height to form digital elevation models (DEM). In addition, these modes can also be defined by a single-pass or repeat-pass acquisitions. *Single-pass interferometry* is carried out within a single survey, whereas the *repeat-pass* case is performed using different acquisitions separated in time. Particularly, repeat-pass interferograms contain information about the change of the scene, i.e., temporal decorrelation.

The main contribution of this thesis deals with repeat-pass acquisitions in across-track geometry. Therefore, the following analysis is centred in this mode.

2.3.1   Across-track interferometry (XTI)

The basic geometry of XTI is shown in Figure 2.7, where both antennas are separated by a baseline B with a tilt angle α_{tilt}. The target p_1 is observed by the master track with a range distance of r_1, at an unknown elevation angle of $\theta_{\text{el},1}$ and at an unknown height h_1. Note that the distance to the second target p_2 is the same, therefore neither the height h_1 nor h_2 can be estimated with a single pass. Certainly, $\theta_{\text{el},1}$ can be estimated with an additional track, since the range distances, r_2 and r_3, to the first and the second targets are different. Using the law of cosines, the difference between the range distances r_1 and r_2 of the master and slave tracks, respectively, is dictated by

$$\Delta r_{12} = r_2 - r_1 = \sqrt{r_1^2 + B^2 - 2r_1 B \cdot \sin(\theta_{\text{el},1} - \alpha_{\text{tilt}})} - r_1. \tag{2.18}$$

The angle $\theta_{\text{el},1}$ can be derived from (2.18), as follows

$$\theta_{\text{el},1} = \sin^{-1}\left(\frac{r_1^2 + B^2 - (\Delta r_{12} + r_1)^2}{2r_1 B}\right) + \alpha_{\text{tilt}}. \tag{2.19}$$

In this way the height h_1 is defined as

$$h_1 = R_z - r_1 \cdot \cos(\theta_{\text{el},1}), \tag{2.20}$$

where R_z is the height of the platform. The estimation of Δr_{12} from image correlation is known as *radar stereogrammetry*, and its main drawback is the limited accuracy, which directly depends on the precision of the position of the target, i.e., usually with a resolution in range direction in the order of meters [Lebe 91, Lebe 76]. Specifically, the accuracy of h_1 can be expressed by

$$\zeta_h = \frac{\partial h_1}{\partial \Delta r_{12}} \cdot \zeta_{\Delta r_{12}} = -\frac{r_1 \cdot \sin(\theta_{\text{el},1})}{B_\perp} \cdot \zeta_{\Delta r_{12}}, \tag{2.21}$$

where $B_\perp = B \cdot \cos(\theta_{\text{el},1} - \alpha_{\text{tilt}})$ is the normal baseline and $\zeta_{\Delta r_{12}}$ is the precision of the measured range distances that is in the order of $\delta r/16$. As a numerical example, if the following parameters are considered: $r_1 = 4000$ m, $B = 15$ m, $\theta_{\text{el},1} = 45\,°$, $\alpha_{\text{tilt}} = 20\,°$, and $\delta r = 1.5$ m ($BW = 100$ MHz), then the height accuracy would be $\zeta_h \approx 20$ m. Although ζ_h is much greater than the azimuth and range resolutions, it can be improved by increasing B, but upon a certain limit called the *critical baseline* [Baml 99]. In fact, this problem can be tackled by means of the interferometric phase of both acquisitions, where much higher accuracy in the order of a fraction of λ_c can be achieved.

Figure 2.7: Geometry of across-track interferometry to solve the height of p_1 and p_2. Note that p_1 has the same range distance to the master track, which is not the case for the slave track.

The height estimation, h_1, can be then retrieved by multiplying the first image with the complex conjugate of the second, in the following manner. The phase of both observations φ_1 and φ_2 from the master and slave tracks, respectively, are defined as

$$\varphi_1 = -\frac{4\pi}{\lambda_c} \cdot r_1 + \varphi_{\sigma,1}, \tag{2.22}$$

$$\varphi_2 = -\frac{4\pi}{\lambda_c} \cdot r_2 + \varphi_{\sigma,2}, \tag{2.23}$$

where $\varphi_{\sigma,(.)}$ is the phase of the target's reflectivity or the polarimetric phase of the given scene. Subsequently, the phase difference retrieved from the interferogram is given by

$$\varphi = \varphi_2 - \varphi_1 = \frac{4\pi}{\lambda_c} \cdot (r_2 - r_1) = \frac{4\pi}{\lambda_c} \cdot \Delta r_{12}, \tag{2.24}$$

where $\varphi_{\sigma,1}$ is assumed to be equal to $\varphi_{\sigma,2}$. As a result $\zeta_{\Delta r_{12}}$ is directly proportional to the accuracy of the measured phase, in the following manner

$$\zeta_{\Delta r_{12}} = \frac{\lambda_c}{4\pi} \cdot \zeta_\varphi. \tag{2.25}$$

If now it is considered a $\zeta_\varphi = 30°$ with the same parameters as the previous example, then $\zeta_h \approx 2$ m, which shows a huge improvement with respect to radar stereogrammetry. However, one of the problematics by using this method is that φ is wrapped within $(-\pi, \pi]$, since the wavelength is much smaller than the range distance. This fact led to develop *phase unwrapping* methods, which are used to estimate a continuous phase and compute the topographic component [Reig 97, Xu 99, Spag 95].

A further aspect that has to be considered in (2.27) is the *flat-Earth* component. This component is a residual phase relative to the range distance that should be taken into account to directly associate the interferometric phase to the topography of the scene. Having (2.19) in a different form as

$$B \cdot \sin(\theta_{el,1} - \alpha_{tilt}) = \frac{B^2}{2r_1} - \frac{\Delta r_{12}^2}{2r_1} + \Delta r_{12}, \tag{2.26}$$

and supposing that $r_1 \gg B$, then the first two terms of the right side can be ignored, thus (2.24) can be approximated as

$$\varphi = \frac{4\pi}{\lambda_c} \cdot \Delta r_{12} \approx \frac{4\pi}{\lambda_c} \cdot B \cdot \sin(\theta_{el,1} - \alpha_{tilt}). \tag{2.27}$$

Since it is known that $\theta_{el,1}$ depends on R_z and r_1, then φ can be approximated using the Taylor expansion of first order

$$\varphi = \frac{\partial \varphi}{\partial r_1} \cdot \delta r + \frac{\partial \varphi}{\partial R_z} \cdot \delta R_z. \tag{2.28}$$

Consequently, the mean elevation angle and mean range distance should be used to get a more accurate estimation

$$\theta_{el} = \frac{\theta_{el,1} + \theta_{el,2}}{2} \qquad \text{or} \qquad \theta_{el} = \frac{\theta_{el,1} + \theta_{el,3}}{2}, \tag{2.29}$$

$$r = \frac{r_1 + r_2}{2} \qquad \text{or} \qquad r = \frac{r_1 + r_3}{2}. \tag{2.30}$$

Supposing that a third target, p_3, lies at the same height as p_1 but at different range distance, then the range change rate that describes the flat-Earth term is

$$\frac{\partial \varphi}{\partial r} = -\frac{4\pi}{\lambda_c} \cdot \frac{B \cdot \cos(\theta_{el} - \alpha_{tilt})}{r \cdot \tan(\theta_{el})}, \tag{2.31}$$

(see Figure 2.7). Likewise, if the target p_2 lies at a different height but at the same range distance, r_1, as p_1 with respect to the master track, then the phase increment corresponds to

$$\frac{\partial\varphi}{\partial R_z} = -\frac{4\pi}{\lambda_{\rm c}} \cdot \frac{B \cdot \cos(\theta_{\rm el} - \alpha_{\rm tilt})}{r \cdot \sin(\theta_{\rm el})}, \tag{2.32}$$

which corresponds to the *height sensitivity*. This important factor quantifies the resolution of the interferogram, and represents the fringe rate with respect to the topography.

From (2.31) and (2.32) the total phase increment between two pixels, corresponding to the master and slave, is given by

$$\varphi = \varphi_{\rm fe} + \varphi_{\rm h} = -\frac{4\pi}{\lambda_{\rm c}} \cdot \frac{B \cdot \cos(\theta_{\rm el} - \alpha_{\rm tilt})}{r \cdot \tan(\theta_{\rm el})} \cdot \delta r - \frac{4\pi}{\lambda_{\rm c}} \cdot \frac{B \cdot \cos(\theta_{\rm el} - \alpha_{\rm tilt})}{r \cdot \sin(\theta_{\rm el})} \cdot \delta h, \tag{2.33}$$

with δh as the height increment between the two pixels.

As seen in (2.32) and in the right term of (2.33), in order to gain resolution in the interferogram, the fringe rate should be large for a small change in height, and this can be achieved with large baselines. Nevertheless, the use of large baselines degrades the quality of the interferometric measurements by decorrelation, which can be quantified by the *interferometric coherence*. In fact, the effect of decorrelation can be reduced for surfaces by filtering the non-overlapping part of the spectra, but at the cost of resolution (see (2.36)).

The interferometric coherence gives information about the quality of the measured phase, and it is defined as the normalised complex cross-correlation between two observations

$$\gamma_{\rm coh} \cdot e^{{\rm j}\varphi} = \frac{|E(s_1(x,r) \cdot s_2(x,r)^*)|}{\sqrt{E(s_1(x,r) \cdot s_1(x,r)^*) \cdot E(s_2(x,r) \cdot s_2(x,r)^*)}}, \tag{2.34}$$

where the magnitude $\gamma_{\rm coh}$ is usually called *coherence*, $E(\cdot)$ is the expectation operator that is normally approximated by spatial averaging or multi-looking, and $s_{(\cdot)}(x,r)$ is the single-look[4] complex image.

There are different sources that cause decorrelation and degrade the coherence. The most important are the following [Zebk 92, Baml 99]:

- Thermal noise decorrelation is caused by the hardware design of the radar.

- Temporal decorrelation occurs due to changes in the scene of interest between acquisitions (e.g., movement of vehicles, ground, glaciers, ocean waves, tree canopies due to strong wind).

- Volume decorrelation is caused when the phase center between both acquisitions changes due to small changes in the elevation and looking angles. This can be seen in natural targets (e.g., forested areas, snow, soil).

- Geometric decorrelation is originated by the difference in the elevation angles of both acquisitions. This can be seen as non-overlapped range spectra.

- Doppler Centroid decorrelation is caused by the non-overlapped azimuth spectra.

---

[4]Single-look image is a complex image without spatial averaging.

- Processing decorrelation arise upon the accuracy of the SAR processors (e.g., processing kernels).

In fact, the contribution of these sources can be modelled as a product

$$\gamma_{\text{coh,tot}} = \gamma_{\text{thermal}} \cdot \gamma_{\text{temporal}} \cdot \gamma_{\text{volume}} \cdot \gamma_{\text{doppler}} \cdot \gamma_{\text{processing}} \cdot \gamma_{\text{geometric}}. \tag{2.35}$$

Particularly, the geometric decorrelation is linked to the largest possible baseline, called the *critical baseline* ($B_{\perp,\text{crit}}$), which is directly associated with the spectral shift, Δf_{r}, as follows

$$\Delta f_{\text{r}} = \frac{c}{4\pi} \cdot \frac{\partial \varphi_{\text{fe}}}{\partial \delta r} = -\frac{c \cdot B_{\perp}}{\lambda_c \cdot r \cdot \tan(\theta_{\text{el}} - \alpha_{\text{in}})}, \tag{2.36}$$

where α_{in} is the terrain slope component in the zero-Doppler plane. The spectral shift indicates the movement of the ground reflectivity spectrum between the spectra of both observations, which is caused by the slight difference in the elevation angle. The critical baseline indicates the distance where the spectra do not have overlap, and this occurs when the spectral shift is equal to the system bandwidth, i.e., $\Delta f_{\text{r}} = BW$,

$$B_{\perp,\text{crit}} = \frac{\lambda_c}{c} \cdot BW \cdot r \cdot \tan(\theta_{\text{el}} - \alpha_{\text{in}}). \tag{2.37}$$

A baseline beyond $B_{\perp,\text{crit}}$ results in two images totally decorrelated, i.e., $\gamma_{\text{coh}} = 0$, whereas two totally correlated images correspond to a coherence of $\gamma_{\text{coh}} = 1$, however no interferometric information related to height is given. Therefore, there should be a compromise between correlation and height sensitivity. In fact, the contribution of both $\gamma_{\text{geometric}}$ and γ_{doppler} can be improved by discarding the non-overlapped spectra projected on ground. To that end, the common part can be estimated from (2.36).

Another aspect that must be considered before computing interferograms is the *coregistration*. It has been assumed until now that both imaging grids of $s_1(x, r)$ and $s_2(x, r)$ coincide, however, this is not the case because the data were acquired from different positions. Coregistration ensures that both images match each other, and it should be performed in sub-pixel precision (i.e., at least 10% of the resolution cell), since it has a strong impact in the reliability and accuracy of the results. Among others, coregistration techniques are based on coherence maximisation, spectral diversity, or using the known acquisition geometry [Baml 99, Forn 95, Sche 00, Prat 04]. Throughout this thesis, coregistration is achieved by using the geometry (DEM and tracks), i.e., projecting the slave image onto the grid of the master, thus getting the best possible match.

Figure 2.8(c) depicts the interferogram of two complex images, $s_1(x, r)$ and $s_2(x, r)$, that were acquired in 2012 by the F-SAR sensor in the region of Kaufbeuren, Germany. The survey was run at X-band ($\lambda_c = 0.03$ m) in repeat-pass across-track configuration with a baseline of $B = 10$ m. In this image, the flat-Earth component was removed and the phase was unwrapped. Figure 2.8(b) represents the coherence of the same pair of images. Clearly, surfaces and persistent scatterers indicate high coherence, whereas vegetation presents low coherence since the phase center is displaced between both acquisitions. Finally, the retrieved DEM is depicted in Figure 2.8(d).

(a)

(b)

(c)

(d)
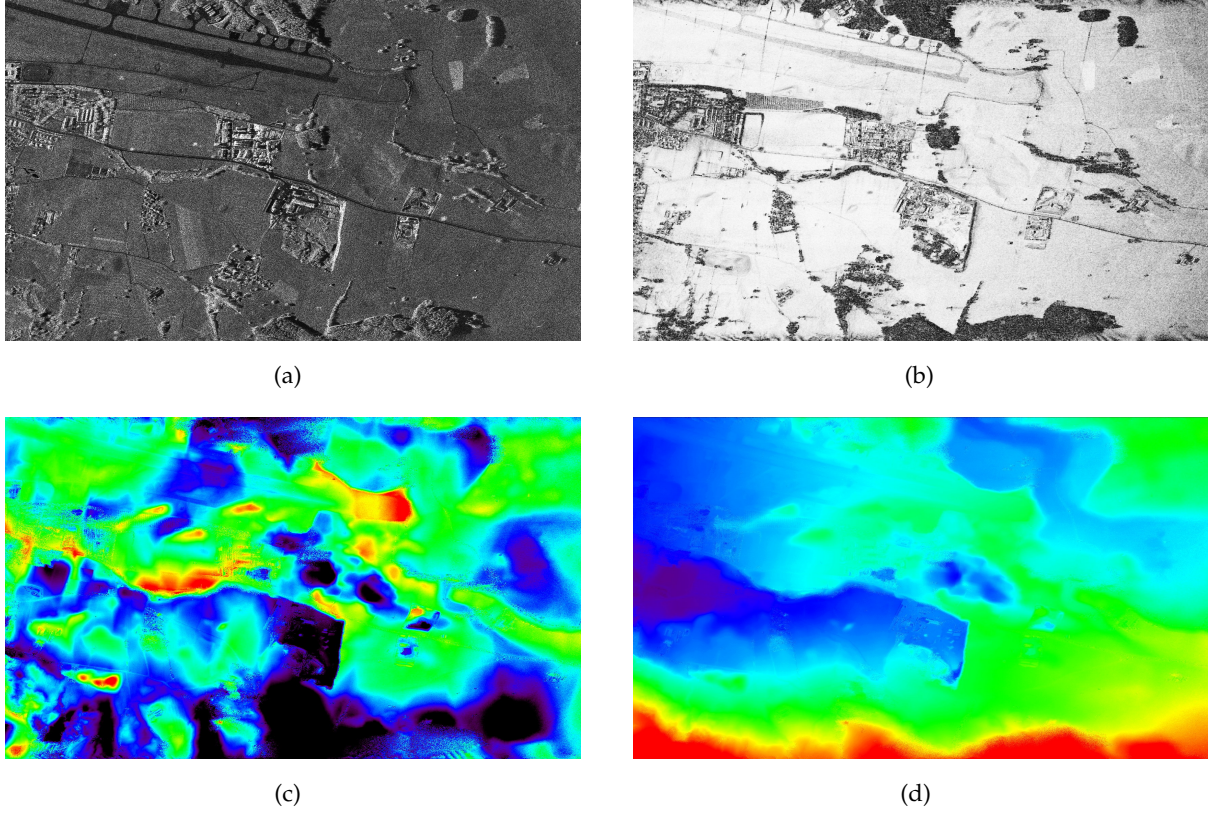
Figure 2.8: Repeat-pass across-track data acquired by DLR F-SAR system over the region of Kaufbeuren, Germany. (a) Amplitude of the master track. (b) Coherence. The colormap goes from 0 (black) to 1 (white). (c) Interferogram without the flat-Earth component and with unwrapped phase. The colormap goes from 0 to 2π. (d) Digital elevation model (DEM) retrieved from the interferogram.

2.4 SAR polarimetry

Another feature characterising a radar system is the polarisation [Lee 09]. This means that a SAR system can transmit polarised waves to measure the backscattered electric field that interacts with the scene. This interaction occurs according to the polarisation that is transmitted. Unlike single-channel SAR, polarimetric SAR systems can be used to identify different scattering mechanisms within the same resolution cell.

The time-varying behaviour of the total electric field is defined by the polarisation of the electromagnetic wave. The total electric field, $\vec{E}_{\text{tot}}$, should satisfy the superposition principle, which is the sum of one or more electric fields orthogonal to the propagation direction that forms the reference basis [Chen 93, Mott 92], as follows

$$\vec{E}_{\text{tot}}(r) = \vec{H} \cdot E_{\text{H}}(r) + \vec{V} \cdot E_{\text{V}}(r), \tag{2.38}$$

where $E_{\text{H}}(r)$ and $E_{\text{V}}(r)$ are complex numbers of the two polarised waves with direction described by the unitary vectors $\vec{H}$ and $\vec{V}$. If $\vec{E}_{\text{tot}}(r)$ is fixed in one direction, then the wave is said to be characterised by a linear polarisation, i.e., $|E_{\text{H}}(r)| = 0$ for vertically polarised or $|E_{\text{V}}(r)| = 0$ for horizontally polarised waves and phase difference of zero. On the other hand, if the phase difference changes as a function of time, then the wave can be identified by an

ellipsoidal polarisation. Particularly, if $|E_V(r)| = |E_H(r)|$ and the phase difference varies between $\pm\pi$ rad, then the wave is left- or right-hand circularly polarised. Throughout this thesis, a linearly polarised SAR system is used to carry out airborne experiments (see Appendix A.1).

Moreover, the transition of the incidence electric field when it interacts with the scatterers on the illuminated scene can be described by the scattering matrix, which can be deduced from the following expression

$$\vec{E}_{\mathrm{Rx}} = [S]\vec{E}_{\mathrm{Tx}} = \begin{bmatrix} s_{\mathrm{HH}}(x,r) & s_{\mathrm{HV}}(x,r) \\ s_{\mathrm{VH}}(x,r) & s_{\mathrm{VV}}(x,r) \end{bmatrix} \vec{E}_{\mathrm{Tx}}, \tag{2.39}$$

where $s(x,r)$ are the measured complex images with a transmitted electrical field, $\vec{E}_{\mathrm{Tx}}$, and a received electrical field, $\vec{E}_{\mathrm{Rx}}$, in horizontal and vertical polarisations. In order to extract different properties of the polarimetric signature, σ, the scattering matrix can be decomposed coherently or incoherently [Lee 09].

Coherent decompositions consist in projecting $[S]$ onto suitable orthonormal basis, which form a 3-D scattering vector, $\vec{k}_{\mathrm{scat}}$ [Clou 96]. Depending on how the channels are combined, one can extract different scattering properties from the scattering matrix. The most common basis are called lexicographic and Pauli. The former results in the following expression

$$\vec{k}_{[S],\mathrm{L}} = [s_{\mathrm{HH}}(x,r), \sqrt{2} \cdot s_{\mathrm{HV}}(x,r), s_{\mathrm{VV}}(x,r)]^{\mathrm{T}}, \tag{2.40}$$

while the latter corresponds to

$$\vec{k}_{[S],\mathrm{P}} = \frac{1}{\sqrt{2}} \cdot [s_{\mathrm{HH}}(x,r) + s_{\mathrm{VV}}(x,r), s_{\mathrm{HH}}(x,r) - s_{\mathrm{VV}}(x,r), 2 \cdot s_{\mathrm{HV}}(x,r)]^{\mathrm{T}}. \tag{2.41}$$

The Pauli decomposition is directly related to the physical properties of the scatterers. The first component of (2.41) indicates odd-bounce wave interaction, such as the one from Luneburg lenses (isotropic), trihedral corner reflectors (highly-directive), flat surfaces (isotropic) or edges of man-made targets (highly-directive). The second component is related to an even-bounce number of reflections, for instance top hats (highly-directive), walls of buildings (highly-directive), light poles (isotropic-like), fences (highly-directive) or tree-trunks (isotropic-like). Finally, the third component corresponds to even-bounce scattering with a rotation of $\frac{\pi}{4}$ rad of the incidence electric field. This interaction is caused by targets like dihedral corner reflectors, and random volumetric structures.

In order to identify targets by their persistence, it is important to introduce at this point the following definitions:

1. **Isotropic or isotropic-like**, when they remain coherent, i.e., they keep an identical polarimetric signature during the full synthetic aperture.

2. **Anisotropic**

   - *Highly-directive*, when they are seen just for a short segment of the synthetic aperture.
   - *Distributed or random*, when their polarimetric signature or phase center changes for slight differences in elevation and/or looking angles, i.e., they own a non-deterministic signature.

On the other hand, incoherent decompositions allow the understanding of scattering mechanisms that are not deterministic, e.g., distributed [Clou 95, Clou 96]. The phase center of these targets is a result of the *speckle noise,* which is the random superposition of several coherent contributions within a resolution cell. To handle non-deterministic targets second-order statistics of the scattering matrix are used. Specifically, the *covariance matrix* is a solution that allows the definition of polarimetric statistical processes. The covariance matrix can be computed directly from the scattering vectors in lexicographic or Pauli decompositions, as follows

$$T_{[S],\mathrm{L}} = \langle \vec{k}_{[S],\mathrm{L}} \, \vec{k}^{\dagger}_{[S],\mathrm{L}} \rangle, \tag{2.42}$$

and

$$T_{[S],\mathrm{P}} = \langle \vec{k}_{[S],\mathrm{P}} \, \vec{k}^{\dagger}_{[S],\mathrm{P}} \rangle, \tag{2.43}$$

where $\langle \cdots \rangle$ is the expected value using neighbouring pixels from the range and/or azimuth direction, and † denotes the adjoint matrix or complex conjugate transpose. Although the covariance matrix allows the retrieval of stable signatures, the geometric resolution is degraded by coherent averaging depending on the number of neighbouring pixels. Both matrices (2.42) and (2.43) contain information about the correlation and variance of the elements of $[S]$ in the corresponding basis (lexicographic or Pauli). Interestingly, the covariance matrix is Hermitian[5], positive semi-definite[6], and full rank due to the spatial averaging. Consequently, $T_{[S],(\cdot)}$ can be diagonalised in the following manner

$$T_{[S],(\cdot)} = \sum_i \lambda_{\mathrm{e},i} \cdot (\vec{e}_i \, \vec{e}^{\dagger}_i), \tag{2.44}$$

where $i \, \epsilon \, [1, 2, 3]$, $\lambda_{\mathrm{e},i}$ are the corresponding eigenvalues and $\vec{e}_i$ the eigenvectors (unitary three-dimensional vectors). The interpretation of this diagonalisation starts with the eigenvalues that can be directly related to the amplitude of the scatterers. This information helps to compute the polarimetric scattering entropy, that corresponds to

$$H = \sum_i - P_i \cdot \log_3(P_i), \quad P_i = \frac{\lambda_{\mathrm{e},i}}{\sum_l \lambda_{\mathrm{e},l}}. \tag{2.45}$$

where the logarithmic basis corresponds to the polarimetric dimension (3 for monostatic mode and 4 for bistatic mode) [Lee 09].The entropy, $0 \leq H \leq 1$, is related to the complexity of the scattering process, i.e., the deterministic nature of the scatterers. An entropy $H = 0$ means that only one significant scattering mechanism is presented, whereas an entropy of $H = 1$ indicates equally dominant contributions.

Until now, the eigenvectors (orthogonal components) have not been related with the physics of certain scattering process. To that end, the eigenvectors $\vec{e}_i$ can be expressed as a function of five angles

$$\vec{e}_i = \left[\cos(\alpha_{\mathrm{pol},i}) \, e^{\mathrm{j} \cdot \varphi_{\sigma,i}} \quad \sin(\alpha_{\mathrm{pol},i}) \cos(\beta_{\mathrm{pol},i}) \, e^{\mathrm{j} \cdot (\varphi_{\sigma,i} + \delta_{\mathrm{pol},i})} \quad \sin(\alpha_{\mathrm{pol},i}) \sin(\beta_{\mathrm{pol},i}) \, e^{\mathrm{j} \cdot (\varphi_{\sigma,i} + \gamma_{\mathrm{pol},i})} \right],$$
$$\tag{2.46}$$

---

[5] $T_{[S],(\cdot)} = T^{\dagger}_{[S],(\cdot)}$.
[6] Every eigenvalue is non-negative and real.

where $\varphi_{\sigma,i}$ corresponds to the target absolute phase, $\beta_{\mathrm{pol},i}$, $\delta_{\mathrm{pol},i}$ and $\gamma_{\mathrm{pol},i}$ are usually used to identify the target orientation angle with respect to the radar, and $\alpha_{\mathrm{pol},i}$ defines the rotation of the two-dimensional basis of the scattering mechanism. Despite the information about the physical properties of targets that $\alpha_{\mathrm{pol},i}$ gives, the mean value, $\overline{\alpha}_{\mathrm{pol}} \, \epsilon \, [0, \frac{\pi}{2}]$, should be computed to get a better estimation of the dominant scattering mechanism

$$\overline{\alpha}_{\mathrm{pol}} = \sum_i P_i \cdot \alpha_{\mathrm{pol},i}. \tag{2.47}$$

In addition, the following information about the type of scatterer can be retrieved: $\overline{\alpha}_{\mathrm{pol}} = 0$ represents isotropic flat surfaces, $\overline{\alpha}_{\mathrm{pol}} = \frac{\pi}{2}$ corresponds to isotropic dihedral or helix scattering, $\overline{\alpha}_{\mathrm{pol}} = \frac{\pi}{4}$ agrees the behaviour of dipole scattering, and all other values correspond to anisotropic scattering mechanisms.

Notably, SAR polarimetry (PolSAR) allows the retrieval of scattering mechanisms occurring in the same resolution cell by their physical properties (e.g., orientation and shape) and dielectric constants. Although this technique cannot be used to retrieve the energy in the third dimension, it can be used for 3-D images to identify different phase centres contained inside the same voxel (3-D pixel), as described in Section 2.5.2.

2.5 Tomography

In the beginning of the 20th century the concept of tomography (in Greek *tomo* means slice) and later a technique called computed axial tomography (CAT) that works in the X-ray wavelength range (0.01 nm to 10 nm) provided a huge technological improvement in medical imaging [Scud 78, Herm 02]. The basic principle of this technique is to reconstruct the *internal structure* of an object by rays that propagate straight through the object, usually acquired over multiple observations by the rotation of the sensor in a plane to form a 2-D cross-sectional image. The reconstruction of the signal, i.e., tomogram, is performed using the Radon transform, which is based on the Fourier projection-slice theorem [Poul 10]. Subsequently, the third dimension is formed by stacking several 2-D images acquired at different positions along the perpendicular axis to the rotation plane.

2.5.1 Analogy with spotlight SAR

Driven by the concept of tomographic imaging, Munson in 1983 compared tomography with the spotlight SAR mode by using the 2-D projection-slice theorem [Muns 83]. This comparison was performed under the following assumptions: first, every observation is the 1-D projection of a 2-D plane, and second, the system model accepts plane wavefronts under the Born approximation. In CAT, every projection is acquired with multiple highly directive sensors on the opposite side of the transmitters, whereas in SAR the transmitted signal is backscattered and collected in a monostatic mode in different range bins, that correspond to an echo. Figure 2.9(a) and Figure 2.9(b) show this analogy for an acquired observation. Similar to the rotation of the CAT sensors, the motion of the SAR sensor allows the acquisition of information of the illuminated object from different aspect angles. Particularly, the projection of the volume

$s(x, y)$ can be described as an integral at a certain angle ϕ over the v axis. In this way, the 1-D projection can be written as

$$S(u, \phi) = \int_{-\infty}^{\infty} s_\phi(u, v) \, \mathrm{d}v, \tag{2.48}$$

where $u = x \cdot \cos(\phi) + y \cdot \sin(\phi)$ and $v = -x \cdot \sin(\phi) + y \cdot \cos(\phi)$, which represent the rotation of the reference plane (x, y). According to the projection-slice theorem, the forward Fourier transform of $S(u, \phi)$ with respect to u represents a part of the 2-D Fourier transform $S(k_x, k_y)$ at ϕ degrees as follows

$$
\begin{aligned}
\mathcal{F}_u(S(u, \phi)) &= \iint_{-\infty}^{\infty} s_\phi(u, v) \cdot e^{-\mathrm{j}k_u\, u} \, \mathrm{d}v \, \mathrm{d}u \\
&= \iint_{-\infty}^{\infty} s_\phi(u, v) \cdot e^{-\mathrm{j}k_u(x \cdot \cos(\phi) + y \cdot \sin(\phi))} \, \mathrm{d}v \, \mathrm{d}u.
\end{aligned}
\tag{2.49}
$$

If $k_x = k_u \cdot \cos(\phi)$ and $k_y = k_u \cdot \sin(\phi)$ with $k_u = 2k \cdot \sin(\theta_{\mathrm{el}})$, and $k = \frac{2\pi}{\lambda}$, then (2.49) is described as a function of spatial frequencies

$$S(k_x, k_y) = \iint_{-\infty}^{\infty} s(x, y) \cdot e^{-\mathrm{j}(xk_x + yk_y)} \, \mathrm{d}x \, \mathrm{d}y, \tag{2.50}$$

and due to the Fourier properties of a circularly symmetric function [Poul 10]

$$s(x, y) = \iint_{-\infty}^{\infty} S(k_x, k_y) \cdot e^{\mathrm{j}(xk_x + yk_y)} \, \mathrm{d}k_x \, \mathrm{d}k_y. \tag{2.51}$$

Lastly, making a change of the variables (x, y), which represent the scene of interest, to polar coordinates $x = r \cdot \cos(\vartheta)$ and $y = r \cdot \sin(\vartheta)$, then $s(x, y)$ is described as the 2-D back-projection

$$s(x, y) = \int_\phi \int_k k \cdot S(k, \phi) \cdot e^{\mathrm{j}2k \cdot r \cdot \cos(\phi - \vartheta)} \, \mathrm{d}k \, \mathrm{d}\phi, \tag{2.52}$$

where the limits with respect to k and ϕ depend on the system bandwidth and the synthetic aperture in the flight direction, respectively. The solution of (2.52) can be approximated as the 2-D sinc function described by the equations (2.13) and (2.17).

2.5.2   SAR tomography

As mentioned in Section 2.3, linear SAR modes cannot solve the complex reflectivity in the third dimension, i.e., along the direction perpendicular to the line of sight, $\mathrm{LOS}_\perp$. Moreover, it was shown that using the InSAR mode it is possible to retrieve topographic information from the interferometric phase of a pair of complex SAR images. However, this mode does not provide information about the complex scattering distribution neither for two nor for several targets. Certainly, this problem can be overcome by extending the InSAR mode with more than two passes in elevation. This technique is better known as SAR tomography (TomoSAR),

(a) CAT.   (b) Spotlight SAR.   (c) TomoSAR.
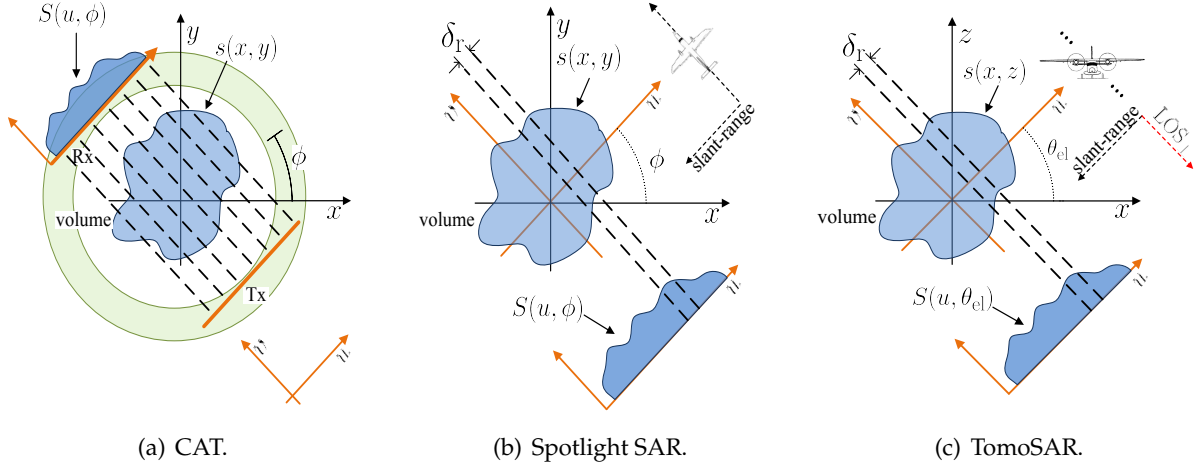
Figure 2.9: Analogy of computed axial tomography (CAT) with spotlight SAR and SAR tomography (TomoSAR) modes using the projection-slice theorem. $s(x,y)$ and $s(x,z)$ are the unknown complex reflectivities of the imaged volumes, $S(u, \phi)$ and $S(u, \theta_{\mathrm{el}})$ are the projections of $s(x,y)$ and $s(x,z)$, respectively, onto the axis u, which rotates as a function of the angle ϕ and θ_{el}, and δ_{r} is the resolution in the slant-range direction.

and unlike InSAR, it combines coherently all acquisitions to have real geometric resolution in the LOS$_\perp$ direction, thus being able to reconstruct volumetric targets within the imaged scene [Home 96].

TomoSAR was compared before to CAT in [Reig 00]. It was pointed out that one of the main differences is that the third dimension in CAT is performed by repeating the same 2-D reconstruction along the normal axis, whereas TomoSAR retrieves the energy by using tomographic techniques. Therefore, TomoSAR processing was modelled through the projection-slice theorem in a similar way as spotlight SAR (see Figure 2.9(c)). In this way, the complex reflectivity, $s(x,z)$, is defined as follows

$$s(x,z) = \int\limits_{\theta_{\mathrm{el}}} \int\limits_{k} k \cdot S(k, \theta_{\mathrm{el}}) \cdot e^{\mathrm{j}2k \cdot r \cdot \cos(\theta_{\mathrm{el}} - \vartheta)} \, \mathrm{d}k \, \mathrm{d}\theta_{\mathrm{el}}, \tag{2.53}$$

where the dimension that differs from (2.52) is the elevation angle, θ_{el}, which is defined by the synthetic aperture in elevation.

In order to cover the spectrum in the LOS$_\perp$ direction, the geometry of the synthetic aperture in elevation can be performed either horizontally (normal to the flight track and z direction), vertically (z direction) or diagonally (normal to the slant-range direction). Figure 2.10 depicts the geometry of the TomoSAR acquisition in vertical configuration, where L_{H} is the total length of the synthetic aperture, and the separation between tracks is ΔB_{L}. Throughout this thesis, the vertical configuration will be used, since it is more practical to perform multicircular airborne experiments (see Chapter 6).

The first experimental TomoSAR demonstration was presented in [Reig 00]. It was shown that compression in elevation can be decoupled from the range and the azimuth imaging by exploiting the phase corresponding to the range of closest approach, described in (2.53). In this way, the input of the tomographic approach consists in a stack of M_{t} 2-D complex images acquired
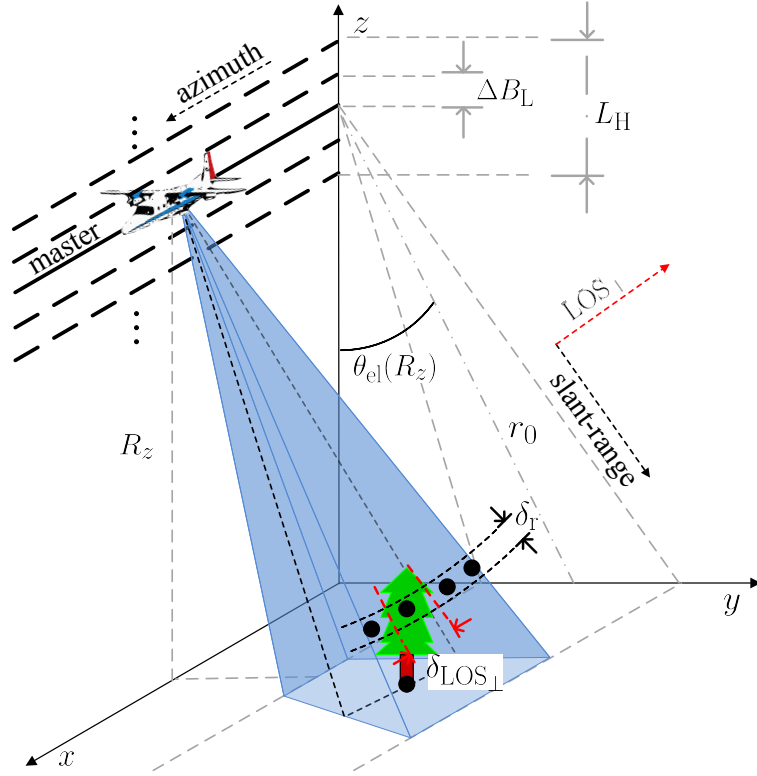
Figure 2.10: Geometry of TomoSAR mode as an extension of Figure 2.7. L_H is the total length of the synthetic aperture, the separation between tracks is ΔB_L, the retrieved resolution is $\delta_{\mathrm{LOS}_\perp}$.

at different elevation angles and focused in the (x, r) plane.

Nominal reconstruction - beamforming (BF)

Figure 2.11 depicts the flow chart of the nominal TomoSAR reconstruction, which is described as follows. Let us denote the stack of 2-D images by

$$G(x, r) = [s_1(x, r), \cdots, s_l(x, r), \cdots, s_{M_t}(x, r)], \tag{2.54}$$

where the track number is indicated by $l = [1, .., l_m, .., M_t]$, with l_m being the master track used as reference to define the imaging geometry. As described in Section 2.3, all M_t images should be first coregistered with respect to the master image, $s_{l_m}(x, r)$. In fact coregistration is performed in this thesis by the projection of every image l to a common grid (x, r) defined with respect to the master track. Furthermore, the 3-D final imaging grid is defined as (x, r, θ_{el}), where the third coordinate depends directly on the elevation angle.

The compression in elevation in the following analysis is performed for a given position (x_o, r_o), i.e., 1-D tomographic signals will be retrieved. In this way, the system can be modelled as $Y = A \cdot X$, where $Y \epsilon \mathbb{C}^{M_t}$ is a complex vector with input measurements $G(x_o, r_o)$ of M_t samples, $X \epsilon \mathbb{C}^{N_{el}}$ is the desired complex reflectivity with N_{el} elements and coordinates
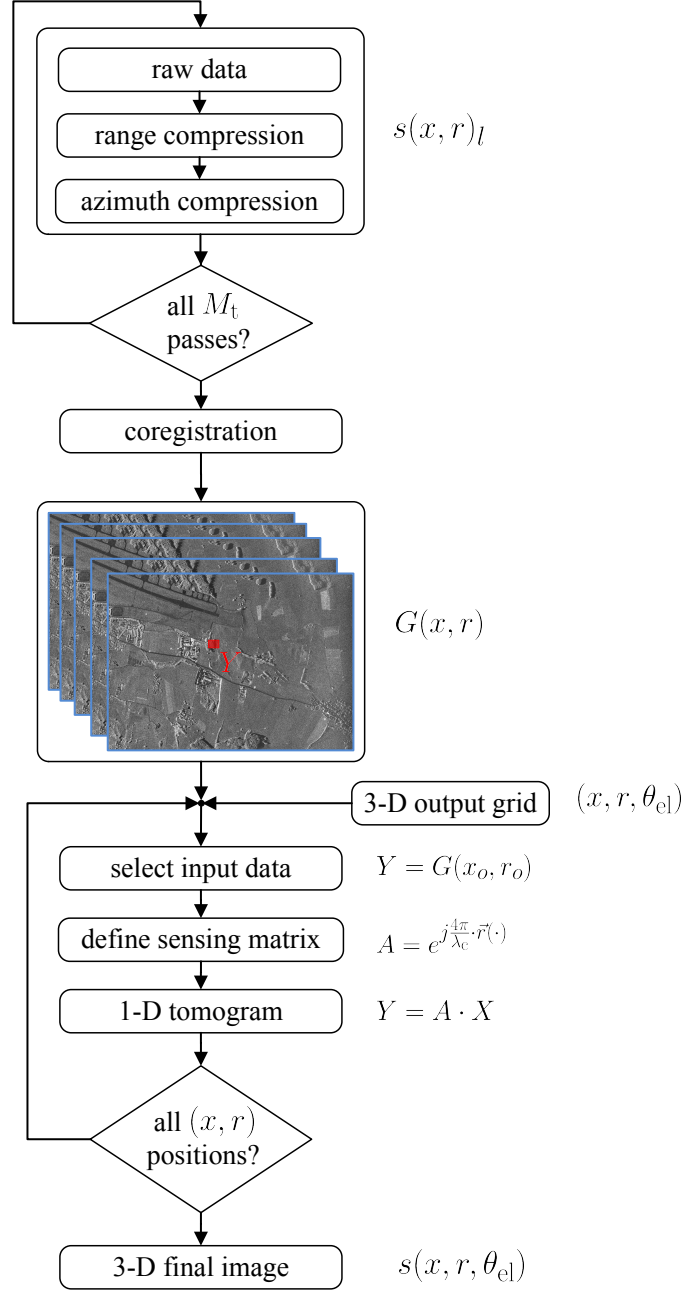
Figure 2.11: Flow chart of the TomoSAR reconstruction. Note that the third dimension is compressed iteratively after range and azimuth compression.

$(x_o, r_o, \theta_{\mathrm{el}})$, and

$$
A = \begin{bmatrix}
e^{\mathrm{j}\frac{4\pi}{\lambda_{\mathrm{c}}}\cdot|\vec{r}(\cdot)_{1,1}|} & \cdots & e^{\mathrm{j}\frac{4\pi}{\lambda_{\mathrm{c}}}\cdot|\vec{r}(\cdot)_{1,n}|} & \cdots & e^{\mathrm{j}\frac{4\pi}{\lambda_{\mathrm{c}}}\cdot|\vec{r}(\cdot)_{1,N_{\mathrm{el}}}|} \\
\cdots & \cdots & \cdots & & \\
e^{\mathrm{j}\frac{4\pi}{\lambda_{\mathrm{c}}}\cdot|\vec{r}(\cdot)_{l,1}|} & \cdots & e^{\mathrm{j}\frac{4\pi}{\lambda_{\mathrm{c}}}\cdot|\vec{r}(\cdot)_{l,n}|} & \cdots & e^{\mathrm{j}\frac{4\pi}{\lambda_{\mathrm{c}}}\cdot|\vec{r}(\cdot)_{l,N_{\mathrm{el}}}|} \\
\cdots & \cdots & \cdots & & \\
e^{\mathrm{j}\frac{4\pi}{\lambda_{\mathrm{c}}}\cdot|\vec{r}(\cdot)_{M_{\mathrm{t}},1}|} & \cdots & e^{\mathrm{j}\frac{4\pi}{\lambda_{\mathrm{c}}}\cdot|\vec{r}(\cdot)_{M_{\mathrm{t}},n}|} & \cdots & e^{\mathrm{j}\frac{4\pi}{\lambda_{\mathrm{c}}}\cdot|\vec{r}(\cdot)_{M_{\mathrm{t}},N_{\mathrm{el}}}|}
\end{bmatrix} \tag{2.55}
$$

is the sensing matrix that is defined by the acquisition geometry and the desired imaging grid. Particularly, the magnitude of the distance vector, $|\vec{r}(\cdot)|$, is given by

$$
|\vec{r}(\theta_{\mathrm{el}}, R_{z,\perp})| = \sqrt{(R_{z,\perp} - z(\theta_{\mathrm{el}}))^2 + r_0^2} \approx r_0 + \frac{(R_{z,\perp} - z(\theta_{\mathrm{el}}))^2}{2r_0}, \tag{2.56}
$$

where $R_{z,\perp}$ and $z(\theta_{el})$ are the platform height and the height positions of the imaging grid in the LOS$_\perp$ direction, respectively. One can observe that the curve described by (2.56) is approximated by a quadratic term and, hence, corresponds to the phase of a chirp function.

In [Reig 00], the SPECAN algorithm was used to efficiently perform the tomographic imaging. This is carried out by multiplying the sensing matrix, A, by a factor that has the form $e^{-j\frac{4\pi}{\lambda_c}\cdot R_{z,\perp}^2}$, which corrects the quadratic term [Cumm 05]. This operation is better known as *phase deramping* and allows the compression of the signal by means of a Fourier transform, i.e., A can be replaced by the coefficients of the Fourier transform. Interestingly, after this operation every row of A describes a sine with a frequency relative to $-2R_{z,\perp}z(\theta_{el}) + z(\theta_{el})^2$, from the platform to the imaging grid. The compressed signal can be afterwards expressed as

$$s(x_o, r_o, \theta_{el}) \approx \gamma \cdot \text{sinc}\left(\frac{2 \cdot L_{H,\perp}}{\lambda_c \cdot r_0} \cdot (z(\theta_{el}) - z_0)\right), \tag{2.57}$$

where $L_{H,\perp}$ is the length of the normal synthetic aperture in elevation, and z_0 is the actual position of the target in the LOS$_\perp$ direction (see Figure 2.12). Clearly, the IRF of TomoSAR is a 3-D sinc function, where the resolution cell of the tomogram is better known as *voxel*.

Similar to the spotlight SAR mode, the resolution in the LOS$_\perp$ direction depends on the length of the synthetic aperture. This resolution can be written as

$$\delta_{\text{LOS}_\perp} = \frac{\lambda_c \cdot r_0}{2 \cdot L_{H,\perp}}, \tag{2.58}$$

where r_0 is the distance of closest approach from the master track to the desired scatterer. Due to discretisation of the tomographic aperture, one has to consider the Nyquist criterion, thus avoiding aliasing and high sidelobes. Subsequently, the height of ambiguity is given by the minimum distance between contiguous tracks, as follows

$$\delta_{\text{LOS}_\perp,\text{amb}} = \frac{\lambda_c \cdot r_0}{2 \cdot \Delta B_{L,\perp}}, \tag{2.59}$$

where $\Delta B_{L,\perp}$ is the normal baseline between contiguous tracks. As an example, if it is considered an acquisition geometry with the following parameters: $\lambda_c = 0.24$ m, $L_{H,\perp} = 250$ m, $r_0 = 4000$ m, and $\Delta B_{L,\perp} = 12$ m, then the resolution would be $\delta_{\text{LOS}_\perp} = 1.92$ m and the height of ambiguity $\delta_{\text{LOS}_\perp,\text{amb}} = 40$ m. In addition, to get a finer resolution, the length of the synthetic aperture in elevation must be greater than 250 m, but at the cost of having more passes to keep the same height of ambiguity. Likewise, a smaller spacing between tracks is needed to image structures whose height is longer than 40 m.

Polarimetric TomoSAR

As discussed in Section 2.4, the complex reflectivity, σ, is characterised by its polarisation, i.e., HH, VV, VH and HV. In polarimetric TomoSAR, scatterers in the LOS$_\perp$ direction can be separated by their geometric resolution, and also classified by their polarimetric signature. Hence, the scattering matrix, $[S_{\text{tom}}]$, can be described as a function of polarisations in the following manner

$$[S_{\text{tom}}] = \begin{bmatrix} s_{HH}(x, r, \theta_{el}) & s_{HV}(x, r, \theta_{el}) \\ s_{VH}(x, r, \theta_{el}) & s_{VV}(x, r, \theta_{el}) \end{bmatrix}, \tag{2.60}$$
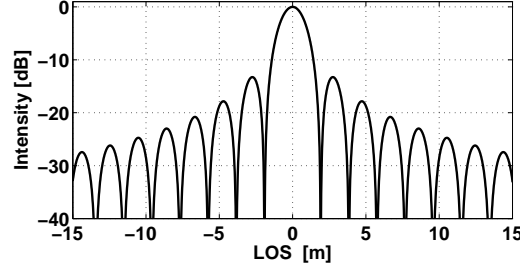
Figure 2.12: Impulse response function (IRF) of TomoSAR at L-band ($\lambda_{\mathrm{c}} = 0.24$ m)with $L_{\mathrm{H},\perp} = 250$ m, $r_0 = 4000$ m and $\delta_{\mathrm{LOS}_\perp} = 1.92$ m.

where $[S_{\mathrm{tom}}]$ differs from (2.39) in the third dimension. In this case the images are three-dimensional tomograms in different polarisations. As described in Section 2.4, coherent and incoherent decompositions can be carried out in order to extract different target properties. In this thesis the Lexicographic and Pauli coherent decompositions are used in the analysis of results. Both expressions correspond to

$$\vec{k}_{[S_{\mathrm{tom}}],\mathrm{L}} = [s_{\mathrm{HH}}(x, r, \theta_{\mathrm{el}}), \sqrt{2} \cdot s_{\mathrm{HV}}(x, r, \theta_{\mathrm{el}}), s_{\mathrm{VV}}(x, r, \theta_{\mathrm{el}})]^{\mathrm{T}}, \tag{2.61}$$

and

$$\vec{k}_{[S_{\mathrm{tom}}],\mathrm{P}} = \frac{1}{\sqrt{2}} \cdot [s_{\mathrm{HH}}(x, r, \theta_{\mathrm{el}}) + s_{\mathrm{VV}}(x, r, \theta_{\mathrm{el}}), s_{\mathrm{HH}}(x, r, \theta_{\mathrm{el}}) - s_{\mathrm{VV}}(x, r, \theta_{\mathrm{el}}), 2 \cdot s_{\mathrm{HV}}(x, r, \theta_{\mathrm{el}})]^{\mathrm{T}}. \tag{2.62}$$

Subsequently, the covariance matrices are defined as

$$T_{[S_{\mathrm{tom}},\mathrm{L}]} = \langle \vec{k}_{[S_{\mathrm{tom}}],\mathrm{L}} \, \vec{k}^{\dagger}_{[S_{\mathrm{tom}}],\mathrm{L}} \rangle, \tag{2.63}$$

and

$$T_{[S_{\mathrm{tom}},\mathrm{P}]} = \langle \vec{k}_{[S_{\mathrm{tom}}],\mathrm{P}} \, \vec{k}^{\dagger}_{[S_{\mathrm{tom}}],\mathrm{P}} \rangle, \tag{2.64}$$

where the expected value or spatial averaging is taken usually from the neighbouring pixels in range and azimuth directions, rather than in elevation because in a real scenario there are far more independent resolution cells, i.e., the resolution is better, in the (x, r) plane than in the $\mathrm{LOS}_\perp$. Moreover, the interpretation of the entropy given in (2.45) in forested areas and for a value close to 0 indicates the presence of deterministic or persistent scatterers, such as tree-trunks, whereas the values close to 1 result in the presence of canopy reflections.

As mentioned before, to fulfil the Nyquist requirements and to obtain a high geometric resolution, a large synthetic aperture should be formed with relatively small uniform distances between contiguous acquisitions. In the case of airborne SAR, this results in very expensive experiments because many passes have to be flown at regular baselines. In the case of spaceborne sensors, the baseline distribution is irregular, since they are restricted to orbital tubes. Consequently, this limitation leads to an increment in the sidelobe level, when conventional BF algorithms are used for processing. In the past few years, non-linear approaches have been developed to improve the geometric resolution (2.58) and the sidelobe level for a reduced number of samples in elevation. Among others, the most used methods are the least-squares super-resolution (LSSR), Capon's minimum variance method (MVM), multiple signal classification

(MUSIC) and compressive sensing (CS) [DeGr 05, Mose 05, Aust 08, Erti 07, Minh 15, Ferr 09, Lomb 03, Frey 11a, Nann 09b, Nann 09a, Zhu 12, Agui 13, Huan 12, Ferr 14].

Certainly, TomoSAR is a promising technique that has been developed in the last decades, however, one of its limitations is that the scene is illuminated only from a narrow angular range in the along-track direction. In fact, 3-D reconstruction can also be performed by changing the geometry of the synthetic aperture to a single circular flight. This mode, called CSAR, and its extension to multicircular passes allow the acquisition of measurements over a wide angular range, thus, being able to achieve subwavelength resolution, 3-D reconstruction, and shadow reduction. These topics are the focus of this thesis and will be analysed in Chapter 6.

3 Circular Synthetic Aperture Radar

This chapter introduces the theory of the circular synthetic aperture (CSAR) imaging mode. First, the basic concepts of CSAR in terms of resolution and peak-to-sidelobe ratio (PSLR) are presented by analysing the 3-D impulse response function (IRF). Then, state-of-the-art focusing methods for 2-D and 3-D imaging are described, in particular, the time-domain direct back-projection (DBP), the frequency-domain wavefront reconstruction, the generalised likelihood ratio test (GLRT), and the non-linear compressive sensing (CS). Finally, autofocus algorithms to estimate and compensate residual errors in the navigation data and to improve the imaging quality are introduced. This includes the phase gradient autofocus (PGA) algorithm, the maximum-likelihood estimation for PGA, and a frequency-based solution.

Parts of this chapter have been published in [Ponc 14a] and [Ponc 16b].

3.1 Impulse response function (IRF)

The following system model is considered to analyse the IRF under the assumption of start-stop (hop-and-go) approximation[1] in the context of SAR based on a moving platform [Soum 99, Ishi 98, Axel 04, Zhan 08, Vu 12, Moor 10]. The radar platform moves along a circular trajectory over a spotlighted region with coordinates $\vec{R}(\phi) = (R_{xy} \cdot \cos(\phi), R_{xy} \cdot \sin(\phi), R_z)$, where R_{xy} is the radius of the track and $\phi \, \epsilon \, [0, 2\pi]$ is the azimuth angular variation that corresponds to the slow time in stripmap SAR mode (see Fig. 3.1). In order to optimise the CSAR capabilities, the area of interest, marked with an orange circle, should be included within the 3 dB footprint of the antenna pattern during the whole flight. As described in Section 2.1, the antenna 3 dB width is defined by θ_{az} and θ_{rg}, in the azimuth and range directions, respectively.

For the given acquisition geometry, the collected data after quadrature demodulation are described as

$$s_{\text{raw}}(\tau, \phi) = \int s(\vec{r}_{\text{grid}}) \cdot s_{\text{T}_x} (\tau - \tau_0(\phi)) \, d\vec{r}_{\text{grid}}, \tag{3.1}$$

where $s(\vec{r}_{\text{grid}})$ is the complex reflectivity of the imaging grid defined by $\vec{r}_{\text{grid}} = (r_x, r_y, r_z)$, $s_{\text{T}_x}(\tau - \tau_0(\phi))$ is the time-delayed transmitted signal with τ as the fast-time and $\tau_0(\phi) = 2 \cdot |\vec{r}_{\text{grid}} - \vec{R}(\phi)|/c$ as the time delay that depends on the two-way path. Note that for simplicity, the amplitude scaling factors have been omitted.

---

[1] The start-stop approximation is valid when the difference between fast- and slow-time is large. Thus assuming that the platform does not move while the radar sends a pulse and receives an echo.
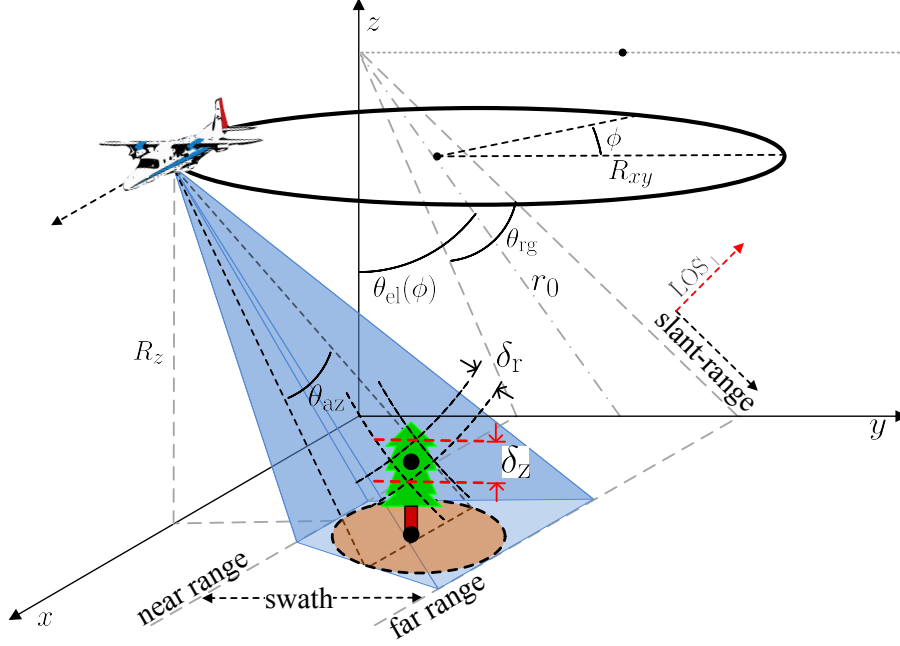
Figure 3.1: Geometry of circular SAR.

Eq. (3.1) in the spatial-frequency domain and after range compression can be written as

$$s_{\text{raw}}(\vec{k}) = \int s(\vec{r}_{\text{grid}}) \cdot e^{-\text{j}2k \cdot |\vec{r}_{\text{grid}} - \vec{R}(\phi)|} \, \text{d}\vec{r}_{\text{grid}}, \tag{3.2}$$

where the exponential term indicates the delay due to the two-way traveled distance, and the wavenumber is $\vec{k}(\omega, \phi, \theta_{\text{el}}) = (k_x, k_y, k_z)$, where the three orthogonal components corresponding to a point target in the center $\vec{p} = (0, 0, 0)$ are

$$
\begin{aligned}
k_x &= k_r \cdot \cos(\phi), \\
k_y &= k_r \cdot \sin(\phi), \\
k_z &= 2k \cdot \cos(\theta_{\text{el}}),
\end{aligned} \tag{3.3}
$$

respectively, with a magnitude $k = |\vec{k}| = 2\pi/\lambda_{\text{c}}(\omega)$ and ω as the range (fast-time) angular frequency. Subsequently, the ground projection of $\vec{k}$ can be defined as

$$k_r = 2k \cdot \sin(\theta_{\text{el}}) = \sqrt{k_x^2 + k_y^2}. \tag{3.4}$$

In addition, the complex reflectivity of the targets or scene $s(\vec{p})$ with coordinates $\vec{p} = (p_x, p_y, p_z)$ is considered as a 3-D Dirac delta function for simplification, thereby $s(\vec{r}_{\text{grid}}) = 1$ for $\vec{r}_{\text{grid}} = \vec{p}$ and 0 otherwise. Thus, the unknown $s(\vec{r}_{\text{grid}})$ can be defined as

$$s(\vec{r}_{\text{grid}}) = \int s_{\text{raw}}(\vec{k}) \cdot e^{\text{j}2k |\vec{r}_{\text{grid}} - \vec{R}(\phi)|} \, \text{d}\vec{k} \tag{3.5}$$

with $s_{\text{raw}}(\vec{k}) = e^{-\text{j}2k |\vec{p} - \vec{R}(\phi)|}$.

Subsequently, knowing that the frequency components of the Ewald sphere[2] are filled as the radar follows a circular geometry, then [Will 99]

$$s(\vec{r}_{\text{grid}}) = \iiint_{\theta_{\text{el}} \; k \; \phi} k^2 \cdot \sin(\theta_{\text{el}}) \cdot e^{-\text{j}2k \cdot |\vec{p} - \vec{R}(\phi)|} \cdot e^{\text{j}2k \cdot |\vec{r}_{\text{grid}} - \vec{R}(\phi)|} \, \text{d}\phi \, \text{d}k \, \text{d}\theta_{\text{el}}, \tag{3.6}$$

---

[2]The Ewald sphere is a geometric construction in the far field radiation, which demonstrates the connection between the wave vector of the incident and diffracted radar beams [Will 99].

where θ_{el} is the elevation angle given by the flight altitude, i.e., constant for a single circular flight (see Figure 3.1), and $g_\phi = e^{\pm j2k\cdot|(\cdot)-\vec{R}(\phi)|}$ is known as the free-space Green's function.

In order to get a closed arithmetical solution of the expression given by (3.6), it has to be assumed that the height of the target and the height of the platform are much smaller than the actual distance from the center of the scene to the circular track, i.e., $p_z \ll |\vec{R}(\phi)|$, $r_z \ll |\vec{R}(\phi)|$, as follows [Soum 99]

$$s(\vec{r}_{grid}) = \int_k \int_\phi k^2 \cdot \sin(\theta_{el}) \cdot e^{-jk_z\cdot(p_z-r_z)} \cdot e^{-jk_r\cdot(|\vec{p}_{xy}-\vec{R}_{xy}(\phi)|)} \cdot e^{jk_r\cdot(|\vec{r}_{xy}-\vec{R}_{xy}(\phi)|)} \, d\phi \, dk, \quad (3.7)$$

where θ_{el} is not considered as an integral because it is constant, $\vec{R}_{xy}(\phi) = (R_x, R_y)$, $\vec{r}_{xy} = (r_x, r_y, r_z = 0)$ and $\vec{p}_{xy} = (p_x, p_y, p_z = 0)$. In the following part of this subsection, the IRF is analysed for the case of a target in and off the center of the scene.

3.1.1 Target in the center

(a)

(b)

(c)

(d)
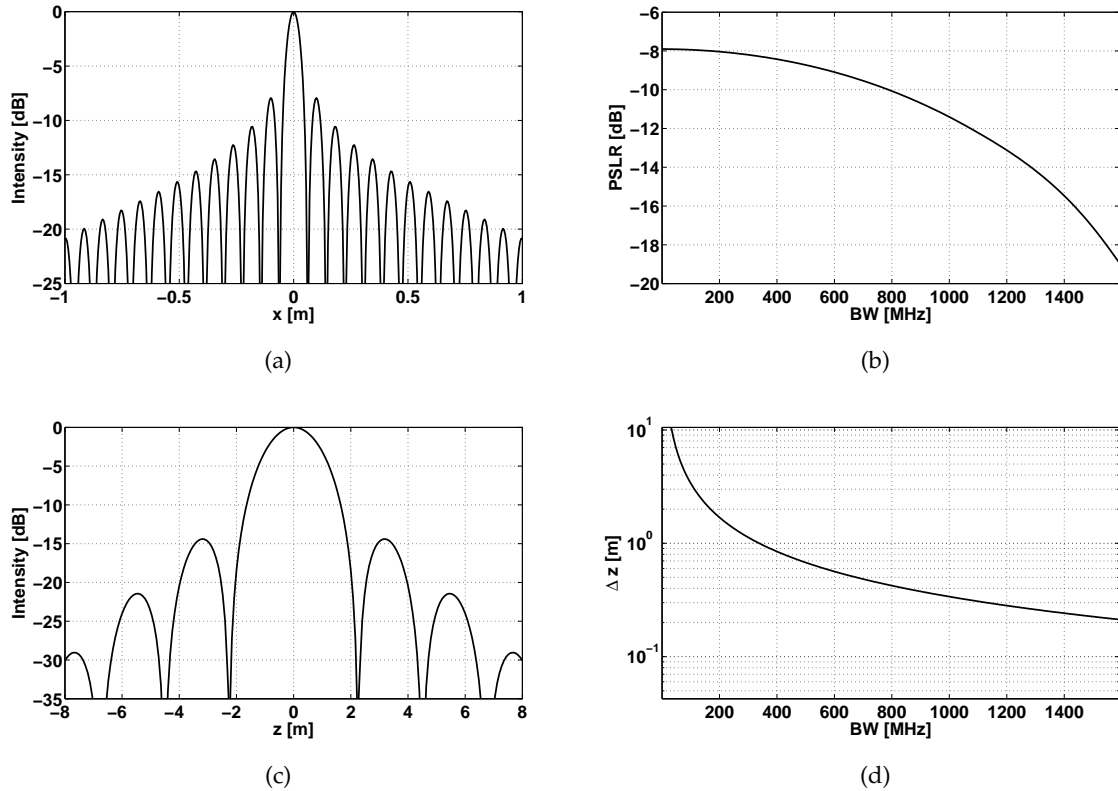
Figure 3.2: Simulated IRF of CSAR for a target located at $\vec{p} = (0,0,0)$. (a) Difference of two Bessel functions in the x direction, as described in (3.12). (b) PSLR as a function of the bandwidth of the system. Note that the power of the sidelobes decreases when the bandwidth increases. (c) Sinc function in the z direction given by (3.14). (d) Resolution as a function of the bandwidth of the system, BW, as mentioned in section 3.2.

If the target is in the center $\vec{p} = (0,0,0)$, then (3.7) becomes

$$s(\vec{r}_{grid}) = \int_k \int_\phi k^2 \cdot \sin(\theta_{el}) \cdot e^{jk_z\cdot r_z} \cdot e^{-jk_r(|\vec{R}_{xy}(\phi)|-|\vec{r}_{xy}-\vec{R}_{xy}(\phi)|)} \, d\phi \, dk. \quad (3.8)$$

Moreover, by solving the integral with respect to ϕ, making a change of variables from (k, θ_{el}) to k_r and knowing that $k_z = k_r \cdot \cot(\theta_{\text{el}})$ then

$$s(\vec{r}_{\text{grid}}) = 2\pi \int_{k_r} k_r \cdot e^{jk_r \cdot \cot(\theta_{\text{el}}) \cdot r_z} \cdot J_0(k_r \cdot |\vec{r}_{xy}|) \, dk_r, \tag{3.9}$$

where $J_n(.)$ is the Bessel function of first kind n order, and the exponential term corresponds to a phase modulation in the k_r wavenumber domain that results in arc- or ring-shaped artefacts in the (x, y) plane or cone-shaped sidelobes in the (x, y, z) space. Notably, (3.9) has the form of a Hankel transform, which is used to solve partial differential equations and in most of the cases the solution is an integral [Poul 10, Lebe 65] (see Appendix A.3).

If now the target is focused at height $r_z = 0$, then the 2-D IRF is given by

$$s(\vec{r}_{xy}) = 2\pi \int_{k_{r_1}}^{k_{r_2}} k_r \cdot J_0(k_r \cdot |\vec{r}_{xy}|) \, dk_r \tag{3.10}$$

where $k_{r_1} = 2k_{\min} \cdot \sin(\theta_{\text{el}})$ and $k_{r_2} = 2k_{\max} \cdot \sin(\theta_{\text{el}})$. For a narrow bandwidth, i.e., $k_{r_2} \approx k_{r_1}$, the solution of the integral of (3.10) has the following form

$$s(\vec{r}_{xy}) = 2\pi \cdot k_r \cdot J_0(k_r \cdot |\vec{r}_{xy}|), \tag{3.11}$$

and for a wide bandwidth, i.e., $k_{r_2} > k_{r_1}$, the solution is

$$s(\vec{r}_{xy}) = \frac{2\pi}{|\vec{r}_{xy}|} \left[k_{r_2} \cdot J_1(k_{r_2} \cdot |\vec{r}_{xy}|) - k_{r_1} \cdot J_1(k_{r_1} \cdot |\vec{r}_{xy}|) \right]. \tag{3.12}$$

Fig. 3.2(a) shows the profile of the IRF of CSAR from (3.12), with an elevation angle of $\theta_{\text{el}} = 45\,°$, a wavelength of $\lambda_c = 0.24$ m and a bandwidth $BW = 100$ MHz. It is interesting to note, that the PSLR depends on the bandwidth and the wavelength [Mens 91, Zhan 08, Vu 12]. Fig. 3.2(b) shows the PSLR for different transmitted bandwidths as derived from (3.12). Note that large bandwidth values lead to a lower PSLR, given by the non-linear factor $k_{r,(.)}/|\vec{r}_{xy}|$ that multiplies the Bessel functions in (3.12). Particularly, for the 100 MHz bandwidth the PSLR is -8 dB. As a first solution, one can think on the use of weighting functions to suppress sidelobes (see Section 2.2.2). However, previous research has indicated that weighting methods do not decrease the sidelobe power of Bessel functions, as they do with sinc functions, but rather they increase it [Mens 91].

On the other hand, if the IRF is analysed in the z direction, then (3.8) becomes

$$s(\vec{r}_z) = \int_k k^2 \cdot \sin(\theta_{\text{el}}) \cdot e^{jk_z \cdot r_z} \cdot J_0(0) \, dk, \tag{3.13}$$

with $J_0(0) = 1$. In order to approximate the solution of this integral, a transformation from (k, θ_{el}) to (k_r, k_z) should be performed

$$s(\vec{r}_z) = \int_{k_{z_1}}^{k_{z_2}} \int_{k_{r_1}}^{k_{r_2}} k_r \cdot e^{jk_z \cdot r_z} \, dk_r \, dk_z \approx (k_{r_2}^2 - k_{r_1}^2) \cdot (k_{z_2} - k_{z_1}) \cdot \text{sinc}((k_{z_2} - k_{z_1}) \cdot |\vec{r}_z|), \tag{3.14}$$
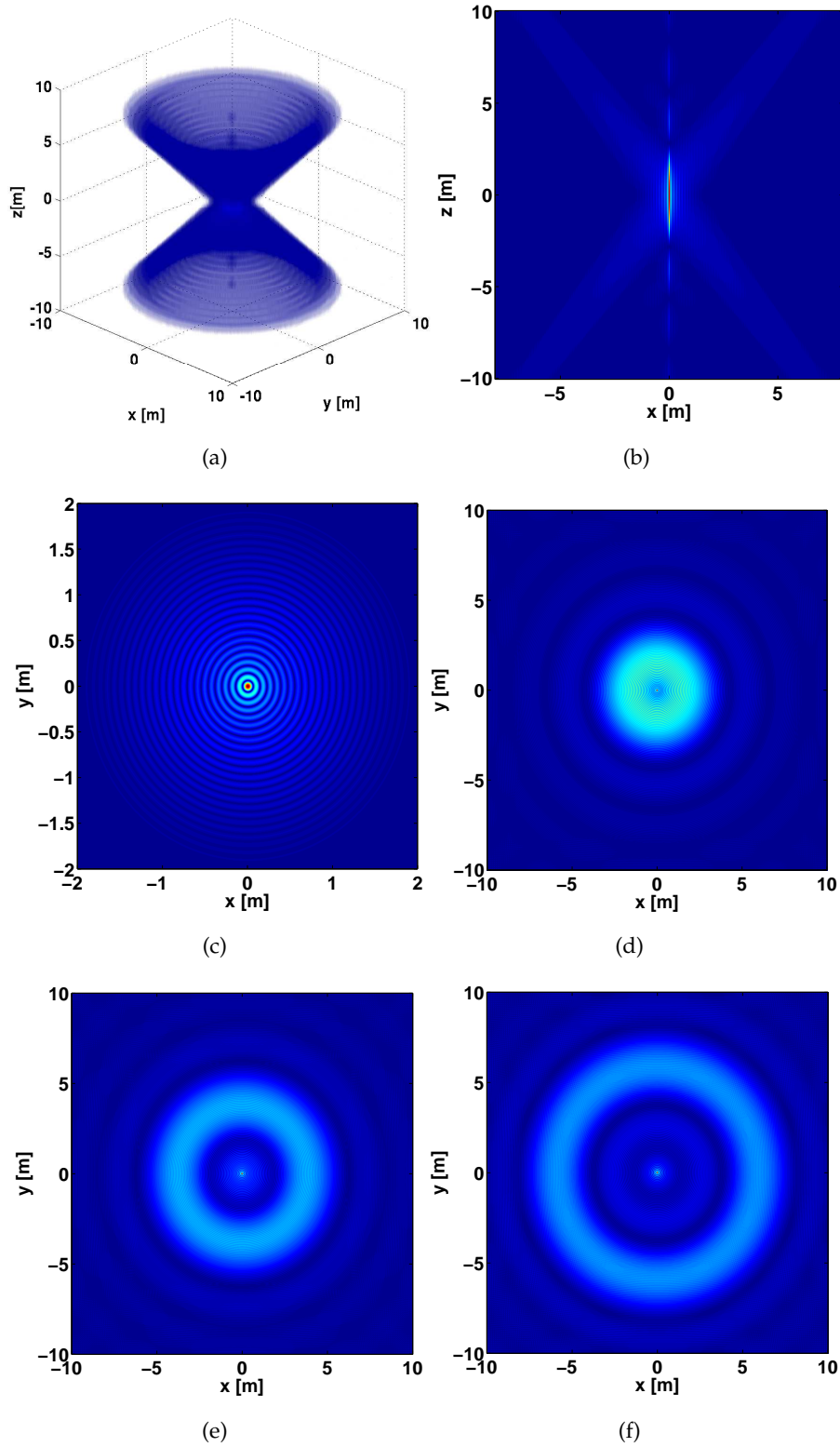
Figure 3.3: (a) 3-D representation of the CSAR IRF in the center, $\vec{p} = (0, 0, 0)$. (b) (x, z) slice at the position of the maximum intensity along the y direction. Note the cone-shaped sidelobes formed by the low resolution in the LOS$_\perp$ direction. (c) (x, y) slice at the true height of the target given by (3.12). (d-f) (x, y) slices with a certain offset in height. (d) 2 m, (e) 4 m, and (f) 6 m. Note that the width of the ring corresponds to the ground range resolution, i.e., the projection of δ_r on the ground.

where $k_{z_1} = 2k_{\min} \cdot \cos(\theta_{\text{el}})$ and $k_{z_2} = 2k_{\max} \cdot \cos(\theta_{\text{el}})$, and the k_r components remain the same as in (3.10). Figure 3.2(c) shows the sinc function along the z direction using the same geometry and radar parameters. Interestingly, the resolution of this expression depends directly on the bandwidth of the system, i.e., $BW = k_{\max} - k_{\min}$, as depicted in Figure 3.2(d). As a matter of fact, the resolutions in the (x, y, z) space will be later discussed in Section 3.2.

In order to generate the 3-D IRF, the expression given in (3.9) has to be solved for a range of r_z values. Figure 3.3 depicts the three-dimensional IRF, as well as two-dimensional slices for different planes. The size of the focused region is $x = 20$ m by $y = 20$ m by $z = 20$ m. Figures 3.3(a) and 3.3(b) show the cone-shaped artefacts that occur due to the low resolution in the $\text{LOS}_\perp$ direction. Note the sinc function in the (x, z) plane at $x = 0$. In addition, the (x, y) slices illustrate the 2-D Bessel function, and the ring sidelobes that are formed when the target is out of focus. In fact, the true height can be retrieved by analysing the geometry of the IRF, as later described in section 3.3, but only for an image with few and sparse point targets.

3.1.2 Target off the center

For a target in the center of the scene, the IRF of CSAR has been a factor of intensive study. As aforementioned, this case allows the computation of closed analytical expressions. In the (x, y) plane, the approximation is given by a Bessel function, while in the z direction the IRF can be described with a sinc function. For a target that is off the center, the integral given in (3.6) should be solved assuming $\vec{p} \neq (0, 0, 0)$, thereby, leading to the following expression

$$s(\vec{r}_{\text{grid}}) = \int_k \int_\phi k^2 \cdot \sin(\theta_{\text{el}}) \cdot e^{\text{j}k \cdot h} \cdot e^{\text{j}k \cdot g \cos(\phi)} \, \mathrm{d}\phi \, \mathrm{d}k, \tag{3.15}$$

where $g = \frac{b}{\sqrt{a}} - \frac{d}{\sqrt{c}}$, $h = 2\left(\sqrt{a} - \sqrt{c}\right)$ with

$$a = |\vec{R}(\phi)|^2 + |\vec{r}_{\text{grid}}|^2 - 2 \cdot |\vec{R}(\phi)| \cdot |\vec{r}_z| \cdot \cos(\theta_{\text{el}}),$$
$$b = -2 \cdot |\vec{R}(\phi)| \cdot |\vec{r}_{xy}| \cdot \sin(\theta_{\text{el}}),$$
$$c = |\vec{R}(\phi)|^2 + |\vec{p}|^2 - 2 \cdot |\vec{R}(\phi)| \cdot |\vec{p}_z| \cdot \cos(\theta_{\text{el}}), \tag{3.16}$$
$$d = -2 \cdot |\vec{R}(\phi)| \cdot |\vec{p}_{xy}| \cdot \sin(\theta_{\text{el}}),$$

and the integral with respect to θ_{el} is also neglected because it is constant during the whole circular aperture (see Appendix A.3).

Subsequently, Eq. (3.15) can be reduced to an integral with respect to a Bessel function of zero order, similar to (3.9), as follows

$$s(\vec{r}_{\text{grid}}) = 2\pi \int_k k^2 \cdot \sin(\theta_{\text{el}}) \cdot e^{\text{j}kh} \cdot J_0(k \cdot g) \, \mathrm{d}k, \tag{3.17}$$

Figure 3.4 illustrates the 3-D IRF of CSAR for a target at $\vec{p} = (1500, 1500, 50)$ for the following configuration: an elevation angle of $\theta_{\text{el}} = 45\,°$, a wavelength of $\lambda_{\text{c}} = 0.24$ m and a bandwidth $BW = 100$ MHz. The position of the target was chosen faraway from the center in order to emphasize the effects in the signature, which otherwise might be very similar for a target closer
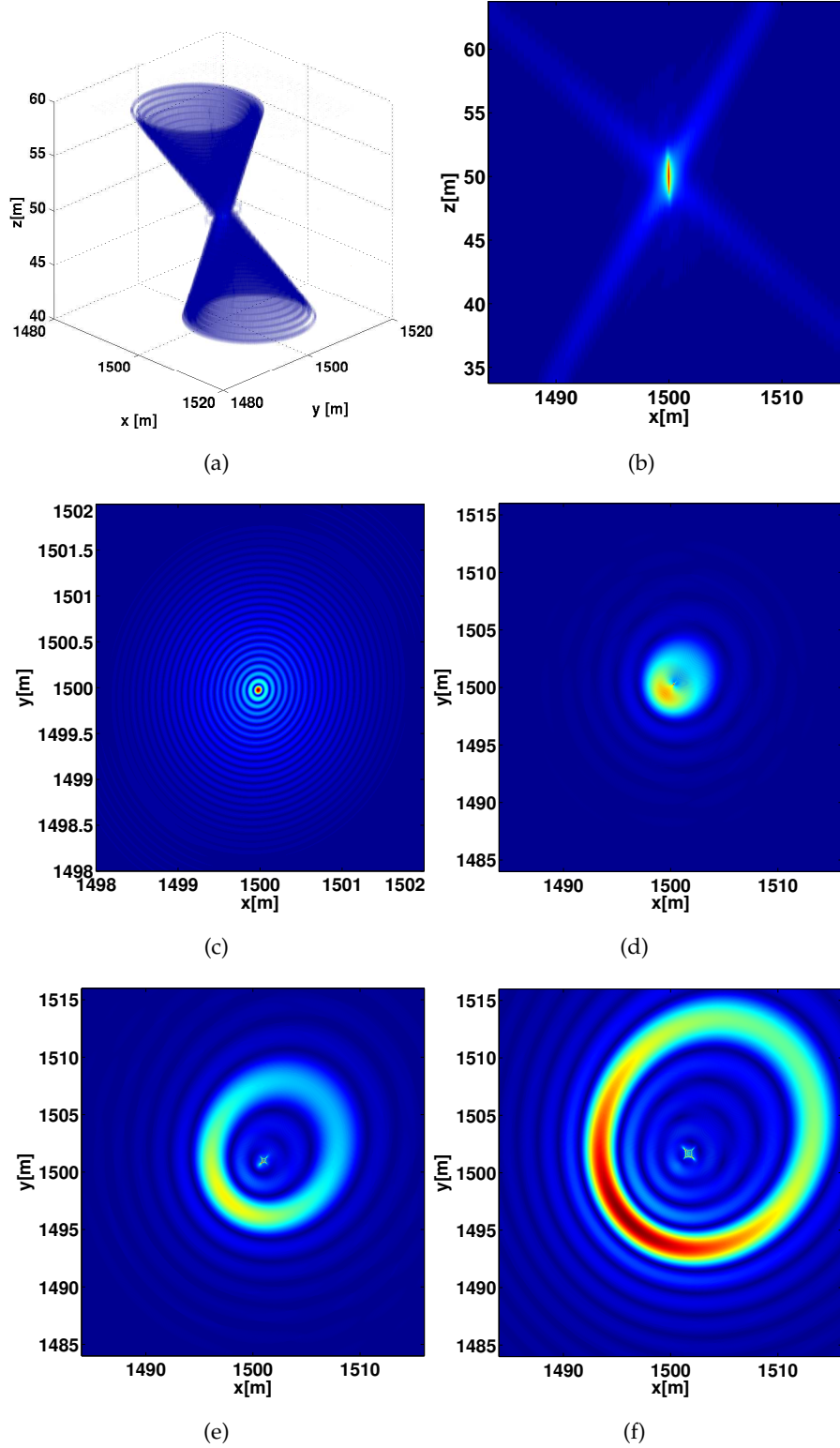
Figure 3.4: (a) 3-D representation of the CSAR IRF off the center, $\vec{p} = (1500, 1500, 50)$. (b) (x, z) slice at the position of the maximum intensity along the y direction. Note the rotated cone-shaped sidelobes formed by the low resolution in the $\text{LOS}_\perp$ direction and the actual position of the target. (c) (x, y) slice at the true height of the target. (d-f) (x, y) slices with a certain offset in height. (d) -2 m, (e) -6 m, and (f) -10 m. Note that the width of the ring changes with respect to the rotation angle ϕ.

to the center, e.g., only 100 m away. Although the 3-D IRF off the center can be approximated as a translated and rotated version of the IRF in the center, it is more complex to be understood due to its spatial variation. If the distance of the target from the center is large, then it will show more changes in the relative distance platform-target with respect to ϕ, i.e., $|\vec{p} - \vec{R}(\phi)|$. Consequently, the curved patterns in the (x, y) plane are no more circles but ellipses, which are described by a variation in the ring widths in comparison to a target in the center, as depicted in the (x, y) slices.

In [Moor 10], an analytical approximation of (3.17) was evaluated with *Mathematica*. As a result, the following expression was given

$$s(\vec{r}_{\text{grid}}) = 2\sqrt{\frac{2\pi}{g}} \cdot [\vartheta_1(k_2, g, h, -1) + \vartheta_1(k_2, g, h, 1) - \vartheta_1(k_1, g, h, -1) - \vartheta_1(k_1, g, h, 1)] , \quad (3.18)$$

where

$$\vartheta_1(k_r, g, h, \varepsilon) = k^{5/2} \cdot \left(-\frac{(\frac{\sqrt{2}}{4} + \varepsilon \frac{j\sqrt{2}}{4}) \cdot \Gamma(\varepsilon \cdot jgk - jhk, \frac{5}{2})}{(\varepsilon \cdot jgk - jhk)^{5/2}} \right), \quad (3.19)$$

and $\Gamma(.)$ is the upper-incomplete Gamma function, which is also represented by integrals (see also Appendix A.3).

3.1.3 Pulse repetition frequency

The range history of a target $\vec{p}$ in CSAR mode is described by the phase of the free-space Green's function (g_ϕ), i.e., $|\vec{p} - \vec{R}(\phi(t))|$, as given by (3.6). This expression describes sine-like range curves of different amplitude and phase that depend directly on the relative position of the targets with respect to the circular trajectory. Correspondingly, the derivative of g_ϕ with respect to time t is defines the Doppler frequency, whose maximum delineates the sampling requirements in the along-track direction, i.e., pulse repetition frequency (PRF), as follows

$$\begin{aligned}
f_D &= \frac{\partial(-2k \cdot |\vec{p} - \vec{R}(t)|)}{\partial t} \cdot \frac{1}{2\pi} \\
&= -\frac{2v_0 \cdot r_0 \cdot r_p}{\lambda_c \cdot R_{xy} \cdot r(t)} \cdot \sin(\theta_{\text{el}}) \cdot \sin(\phi - \alpha_p) \\
&= -\frac{2v_0 \cdot (R_{xy}^2 + R_z^2)}{\lambda_c \cdot R_{xy} \cdot r(t)} \cdot \tan\left(\frac{\theta_{\text{az}}}{2}\right) \cdot \sin(\theta_{\text{el}}) \cdot \sin(\phi - \alpha_p),
\end{aligned} \quad (3.20)$$

where $r_p = \sqrt{p_x^2 + p_y^2} = r_0 \cdot \tan\left(\frac{\theta_{\text{az}}}{2}\right)$ and $\alpha_p = \operatorname{atan}(p_y/p_x)$ are the polar coordinates of the spotlighted region with θ_{az} as the angular aperture of the antenna in the along-track direction, $\phi(t) = \frac{v_0 \cdot t}{R_{xy}}$ describes the angular synthetic aperture as a function of the platform velocity v_0 and the radius of the circular track R_{xy}. One can see that to maximise (3.20), it is necessary to take the outer most target of interest, which defines the maximum spotlighted radius, r_p, and the necessary angular aperture in azimuth, θ_{az}, and range, θ_{rg} directions.

In view of this fact, the PRF should be chosen under the following constraints to avoid range and azimuth ambiguities

$$\begin{aligned}
-\frac{4v_0 \cdot (R_{xy}^2 + R_z^2)}{\lambda_c \cdot R_{xy} \cdot |r_{\max}(t)|} \cdot \tan\left(\frac{\theta_{\text{az}}}{2}\right) \cdot \sin(\theta_{\text{el}}) \cdot \\
\sin(\phi - \alpha_p) \le \text{PRF} \le \frac{c}{2 \cdot S_r},
\end{aligned} \quad (3.21)$$

where again the swath in the range direction is defined as $S_r = \frac{\theta_{rg} \cdot r_0}{\cos(\theta_{el})}$. Certainly, to maximise the effective observed area, the antenna aperture in both directions should be of the same order, i.e., $\theta_{az} \approx \theta_{rg}$. Eq. (3.21) indicates that the PRF is directly proportional to the platform speed v_0 and the imaged area r_p, which does not mean a finer resolution in the (x, y) plane. This can be seen for a target in the center, whose Doppler frequency is zero. In contrast, the PRF in linear SAR modes is directly related to the azimuth resolution and the platform velocity, i.e., the sampling frequency has to be increased for a higher velocity or for a finer resolution.

Table 3.1: Position of the targets of interest for the range history analysis.

Target	Position	Target	Position
$\vec{p}_1$	$(0, 0, 0)$	$\vec{p}_5$	$(-500, 0.200)$
$\vec{p}_2$	$(500, 0, 30)$	$\vec{p}_6$	$(-500, -500, 20)$
$\vec{p}_3$	$(500, 500, 10)$	$\vec{p}_7$	$(500, -500, 0)$
$\vec{p}_4$	$(-500, 500, 100)$	$\vec{p}_8$	$(0, 0, 500)$

In order to better understand the bounds of the PRF, the range history of eight targets at different positions is analysed (see Table 3.1). The main parameters of the simulation are defined as $R_{xy} = 4$ km, $R_z = 4$ km, $v_0 = 90$ m/s, $\lambda_c = 0.24$ m, while the radius of the spotlighted area is 1.5 km. Figure 3.5 depicts the simulation geometry, as well as the range histories and Doppler frequencies for the different target positions.

Note that the position the target p_4 defines the maximum Doppler frequency because is the target with the largest distance from the center of the scene. That is to say that the spotlighted area is $r_p = 1.5$ km, and therefore for a single-polarised SAR system, the minimum and maximum PRF are 190 Hz and 75 kHz, respectively. Contrarily, targets close to the center, such as $\vec{p}_2$ and $\vec{p}_5$, show lower PRF requirements, as previously discussed.

3.2 Geometric resolutions

Besides the PSLR, another metric to measure the system performance is the resolution. Unlike the stripmap SAR mode, the maximum resolution of the focused CSAR image in the horizontal plane (x, y) depends directly on the central frequency f_c. The theoretical resolutions δ_x, δ_y, and δ_z can be calculated by analysing the spectrum of the compressed data in the scatterer orientation ϕ_n and its perpendicular axis, in the following manner [Soum 99] (see Fig. 3.6)

$$\delta_x = \frac{\pi}{\sin(\theta_{el}) \cdot (k_{max} - k_{min} \cos(\phi_0))}, \tag{3.22}$$

with $\phi_0 \in [0, \pi]$ for an angular persistence of $[\phi_n - \phi_0, \phi_n + \phi_0]$ with ϕ_n defining the scatterer orientation. For simplicity, it is assumed that the target is at $\phi_n = 0$, $k_{max} = (2\pi \cdot (f_c + BW/2)/c_0)$, and $k_{min} = (2\pi \cdot (f_c + \nu_{\delta_x} \cdot BW/2)/c_0)$, f_c is the central frequency, BW is the transmitted
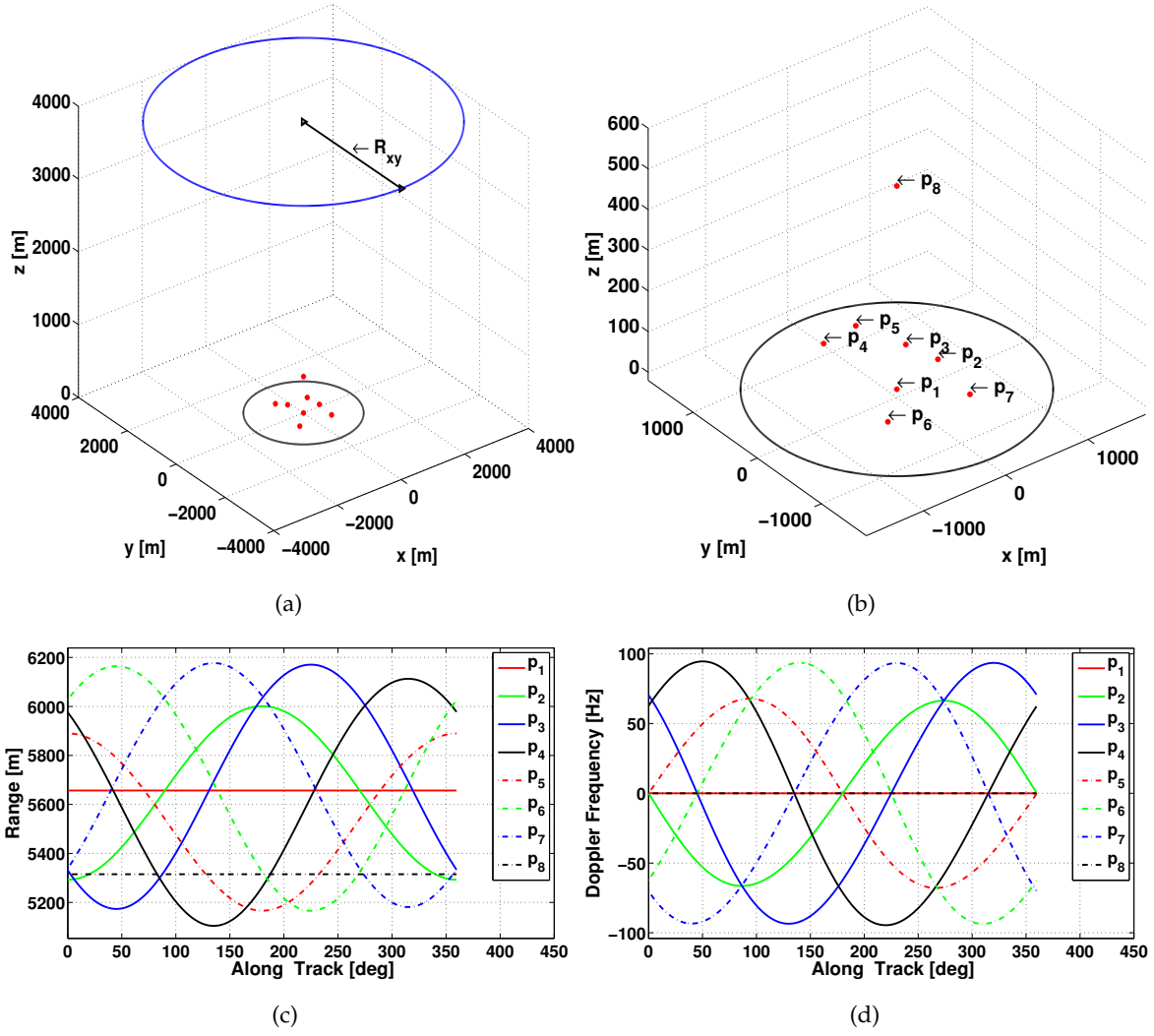
Figure 3.5: CSAR geometry, range histories and Doppler frequencies of eight point targets at different positions, see also Table 3.1. (a) Full view of the geometry, where the CSAR track is indicated in blue, the spotlighted area in black, and the targets of interest in red. (b) Zoom of the spotlighted area. Note that the targets are at different heights and distances from the center of the scene. (c) Range histories of the targets of interest. (d) Doppler frequencies.

bandwidth, c_0 is the speed of the light, and

$$\nu_{\delta_x} = \begin{cases} -1 & 0 < \phi_0 \leq \frac{\pi}{2} \\ 1 & \frac{\pi}{2} < \phi_0 \leq \pi \end{cases}.$$

The resolution in y is determined by [Soum 99]

$$\delta_y = \frac{\pi}{2 \cdot k_{\max} \cdot \gamma_{\delta_y} \cdot \sin(\theta_{\mathrm{el}})}, \tag{3.23}$$

where

$$\gamma_{\delta y} = \begin{cases} \sin(\phi_0) & 0 < \phi_0 \leq \frac{\pi}{2} \\ 1 & \phi_0 > \frac{\pi}{2} \end{cases}.$$

Note that both (3.22) and (3.23) depend on the aperture angle ϕ_0. In fact, only scatterers holding an angular persistence ϕ_0 greater than $\pi/8$ radians in the plane (x, y) have a resolution in the z

(a)   (b)
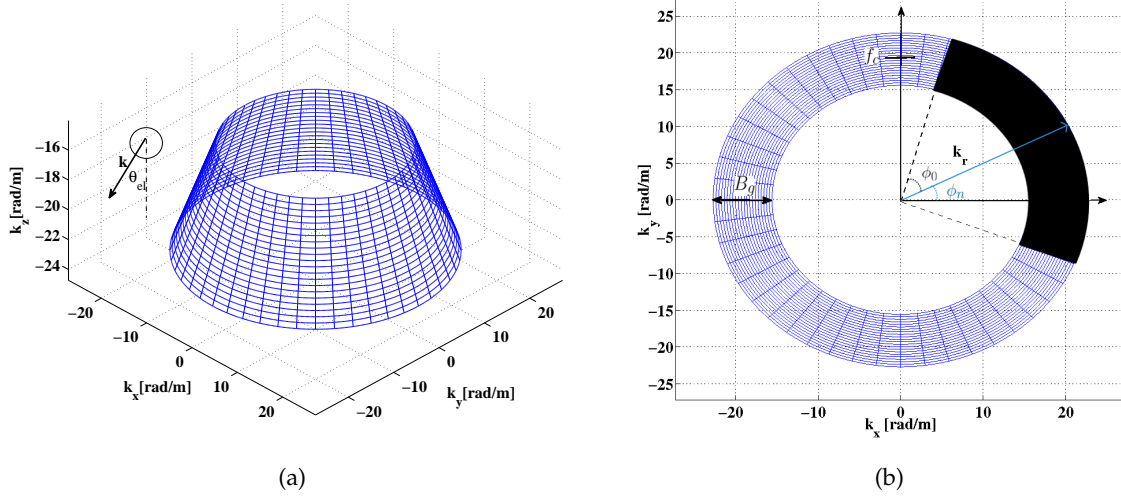
Figure 3.6: Circular SAR spectrum analysis of a target located at $\vec{p} = (0,0,0)$ to estimate resolutions in x, y and z directions. (a) Three-dimensional CSAR spectrum in slant range. (b) Two-dimensional spectrum in ground range, which is the projection of the 3-D spectrum onto the (k_x, k_y) plane.

direction comparable to the range resolution [Moor 07, Ishi 98], i.e.,

$$\delta_z = \frac{2}{\sqrt{2\pi} \cdot \cos(\theta_{\text{el}})} \cdot \frac{c_0}{BW}. \tag{3.24}$$

Moreover, isotropic targets seen over $\phi_0 = 180\,^\circ$ own the maximum resolution in the plane (x,y) resulting in $\delta_x = \delta_y = \frac{\lambda_c}{4 \cdot \sin(\theta_{\text{el}})}$ with $\phi_0 = \pi$ and assuming that the bandwidth of the system can be neglected because $fc \gg \frac{BW}{2}$. For instance, given $\lambda_c = 0.24$ m (L-band) and $\theta_{\text{el}} = 45\,^\circ$, the resolution would result in 0.08485 m (see Fig. 3.2(a)).

3.3 Topography dependency

As already shown in Figure 3.3, if targets are focused at the wrong height, then circular patterns appear due to the sidelobes in the direction perpendicular to the line of sight (LOS$_\perp$). This implies a degradation in the image when the topography is not precisely known. The height mismatch Δh can be estimated by knowing the diameter D of the sidelobes and the elevation angle $\theta_{\text{el}}(\phi)$ at a given azimuth angular moment ϕ [Coll 08b, Coll 08a, Moor 07]

$$\Delta h = \frac{D}{2 \cdot \cot(\theta_{\text{el}}(\phi))}. \tag{3.25}$$

Nevertheless, this is only possible for point-like targets with a long angular integration time ϕ_0 and high signal-to-clutter ratio (SCR).

Another approach to estimate the 3-D structure of the observed objects is through the layover effect [Dung 11]. Assuming two scatterers at the same (x,y) coordinate but different heights, when focusing at the height of the first one, the second will be separated a distance l that can be

measured. From this distance and the elevation angle θ_{el}, its real altitude can be derived with

$$h = \frac{l}{\cot(\theta_{el})}. \tag{3.26}$$

This solution has been exploited with directive point-like scatterers, e.g., the different elements forming a vehicle as shown in [Dung 11].

3.4 Multicircular acquisitions

As mentioned before, imaging with CSAR mode causes arc- and ring-shaped artefacts in the case of 2-D imaging, and cone-shaped sidelobes for 3-D imaging due to the low resolution in the $LOS_{\perp}$ direction (see Figure 3.3). Interestingly, by forming an additional synthetic aperture in elevation with several multicircular acquisitions, it is possible to reduce the cone-shaped artefacts, thus having a full 3-D reconstruction over $360°$, i.e., resolution in the (x, y, z) space and the $LOS_{\perp}$ direction [Soum 99, Ferr 09, Axel 04, Sego 10]. This extended mode has been identified by different authors as elevation CSAR, multipass CSAR, and multicircular SAR.

The collected data of this mode can be modelled by (3.6), but always considering the integral with respect to θ_{el} since it describes the synthetic aperture in elevation. Due to the complexity of getting a closed analytical solution to analyse de IRF, research on this topic has not been deeply carried out. In fact, all the current studies restrict the analysis to man-made objects, i.e., highly directive targets, where surfaces are imaged. For instance, multicircular SAR acquisitions have been object of study in [DeGr 05, Aust 08, Mose 05] at X-band and at UHF with simulated backhoe data, in [Aust 11, Erti 07, Ferr 09, Lee 11, Aust 09, Erti 10] using a collection called the GOTCHA data set at X-band and using a total of eight circular-like tracks, and in [Soum 99, Brya 03] using a turntable acquisition at X-band. In these studies, processing has been carried out with the direct back-projection (DBP) and the wavefront reconstruction provided that the Nyquist criterion is met, and with non-linear acquisitions, such as least-squares super resolution (LSSR), Capon's minimum variance method (MVM), multiple signal classification (MUSIC) and compressive sensing (CS) for a limited number of tracks in elevation.

In the following section, state-of-the-art processing aspects of the DBP, the wavefront reconstruction and CS for circular synthetic apertures are discussed. CSAR with multicircular acquisitions is one of the main contributions of this thesis, and will be analysed in Chapter 6, in particular over forested areas, i.e., distributed scatterers and semi-transparent media.

3.5 Focusing algorithms

As described in section 2.2, SAR processors are divided mainly in time- and frequency-domain. Both types of processing differ in regard to the trade-off between computational burden and image quality [Jako 06, Soum 99]. In the case of circular synthetic apertures, the most common method in time domain is the DBP, while in frequency domain is the wavefront reconstruction [Soum 99]. Particularly, frequency-domain approaches are developed under the assumption of

an ideal-shaped synthetic aperture, which make them improper for airborne SAR because of turbulence or deviations due to strong winds. Despite the efforts to compensate this motions, time-domain algorithms have been more appropriate to get very high resolution images since they use the real track of the acquisitions. On the other hand, time- and frequency-domain algorithms assume that the Nyquist requirements are met, however this is not always achievable in real scenarios (e.g., when sampling in elevation with multicircular SAR acquisitions). There are a variety of non-linear solution that allow the retrieval of the unknown complex reflectivity when the sampling falls short of the Nyquist criterion. Particularly, CS is a non-linear algorithm that has been developed in the last few years for SAR imaging under the assumption that the signal can be represented as sparse, i.e., with few scatterers different from zero.

Furthermore, one of the main paradigms of focusing wide-angular apertures is whether the backscattering should be treated as isotropic or anisotropic. In the first case, the image is the result of adding coherently all the projected energy of the echoes on a grid that should fulfil the Nyquist requirements of the highest resolutions, i.e., $\sim \lambda_c/4$. Theoretically, the focused objects should achieve their maximum resolution, however at the cost of increasing the computational burden. In the second case, imaging under the supposition of only anisotropic targets is first carried out coherently in subapertures, but mixing the information of all subimages in two different ways: adding incoherently the intensities or using the generalised likelihood ratio test (GLRT), which can be approximated as taking the maximum non-coherent intensity over all subaperture images for a given voxel [Vocc 09]. The subaperture-based approaches require lower resolution grids, thus decreasing the number of operations. However, they do not focus the targets at their maximum resolution since their directivity and persistence are not known. Throughout this thesis, the three methods will be identified as *coherent imaging*, *incoherent imaging* and *GLRT imaging*, respectively.

3.5.1 Wavefront reconstruction

The wavefront reconstruction algorithm was originally developed for the ISAR mode with a turntable acquisition, thereby assuming an ideal circular track [Soum 99, Brya 03]. The system model considered by this method assumes the start-stop (hop-and-go) approximation and takes into account the expression of the collected data given by (3.2), where the exponential term describes the free space Green's function $g_\phi(\vec{k}, \vec{r}_{\text{grid}}) = e^{\text{j}2k \cdot |\vec{r}_{\text{grid}} - \vec{R}(\phi)|}$

$$s_{\text{raw}}(\omega, \phi) = \int s(\vec{r}_{\text{grid}}) \cdot g_\phi^*(\omega, \vec{r}_{\text{grid}}) \, d\vec{r}_{\text{grid}}. \tag{3.27}$$

To retrieve the unknown complex reflectivity $s(\vec{r}_{\text{grid}})$, the first step is to define the Green's function in the polar spatial frequency domain $(k_x, k_y) \Rightarrow (k_r, \phi_k)$ as

$$G_{\phi,\text{p}}(\omega, k_r, \phi_k) = G_\phi(\omega, k_x, k_y) = e^{-\text{j}\sqrt{4k^2 - k_r^2} \cdot R_z - jk_r R_{xy} \cdot \cos(\phi - \phi_k)}, \tag{3.28}$$

where $k_r = \sqrt{k_x^2 + k_y^2}$, $\phi_k = \tan^{-1}(k_y/k_x)$. In order to simplify the problem, the unknown reflectivity will be retrieved in the ground plane $(r_x, r_y, r_z = 0)$ as $s_{xy}(\vec{r}_{xy})$. If the Fourier transform of the unknown reflectivity in polar coordinates is $S_{\text{p}}(k_r, \phi_k) = \mathcal{F}[s(\vec{r}_{xy})] = S(k_x, k_y)$, then the collected data can be rewritten as follows

$$s_{\text{raw}}(\omega, \phi) = \iint\limits_{\phi_p k_r} k_r \cdot S_{\text{p}}(k_r, \phi_k) \cdot G_{\phi,\text{p}}(\omega, k_r, \phi_k) \, dk_r \, d\phi_{\text{p}}. \tag{3.29}$$

Subsequently, to retrieve the complex reflectivity in the ground plane from (3.29), the collected data should be rewritten as

$$s_{\text{raw}}(\omega, \phi) = \int_{k_r} \Lambda(\omega, k_r) \cdot S_{\text{xy}}(k_r, \phi) \, \mathrm{d}k_r, \tag{3.30}$$

where $r_z = 0$,

$$\Lambda(\omega, k_r) = e^{-\mathrm{j}\sqrt{4k^2 - k_r^2} \cdot R_z} \tag{3.31}$$

is known as a 2-D windowed phase modulated signal in the k_r space, and

$$S_{xy}(k_r, \phi) = k_r \int_{\phi_k} S_{\text{p}}(k_r, \phi_k) \cdot e^{-jk_r R_{xy} \cdot \cos(\phi - \phi_k)} \mathrm{d}\phi_k \tag{3.32}$$

is directly related to the system model of CSAR for a point target in the (x, y) plane. In view of this fact, the following step to find the desired complex reflectivity from (3.30) is to invert the linear shift-varying system $\Lambda(\omega, k_r)$ as follows

$$S_{xy}(k_r, \phi) = \int \Lambda^{-1}(\omega, k_r) \cdot s_{\text{raw}}(\omega, \phi) \, \mathrm{d}\omega. \tag{3.33}$$

This inversion will allow to proceed with the solution of (3.32). To that end, let us denote (3.32) as a convolution with respect to ϕ

$$S_{xy}(k_r, \phi) = S_{\text{p}}(k_r, \phi) \otimes S_{xy,0}(k_r, \phi), \tag{3.34}$$

where $S_{xy,0}(k_r, \phi) = e^{-jk_r R_{xy} \cdot \cos(\phi)}$. Notably, this expression indicates that the unknown can be retrieved through a match filter, as follows

$$S_{\text{p}}(k_r, \xi) = S_{xy}(k_r, \xi) \cdot S_{xy,0}^*(k_r, \xi), \tag{3.35}$$

where ξ represents the spatial frequency domain with respect to ϕ. In fact, the Fourier transform of $S_{xy,0}(k_r, \phi)$ with respect to ϕ is given by

$$S_{xy,0}(k_r, \xi) = \mathcal{H}_\xi^2(k_r R_{xy}) \cdot e^{-\mathrm{j}\pi \cdot \frac{\xi}{2}}, \tag{3.36}$$

where $\mathcal{H}_\xi^2$ is the Hankel transform of the second kind and order ξ (see Appendix A.3). Afterward, $S(k_x, k_y)$ is obtained by the inverse Fourier transform of (3.35) with respect to ϕ, and an interpolation from the (k_r, ϕ) space to the (k_x, k_y) space. Lastly, the desired reflectivity $s_{xy}(\vec{r}_{xy})$ is computed by a 2-D FFT with respect to k_x and k_y.

On the other hand, the extension of this inversion to multicircular acquisitions takes also as a model (3.2), but the main difference is that the components R_z and r_z are taken into account. If the following expression is considered $r_z \ll |\vec{R}(\phi)|$, then the free space Green's function in the frequency domain with respect to θ_{el} can be rewritten as

$$g_{xyz}(\omega, \phi, k_{\theta_{\text{el}}}) = e^{-\mathrm{j}k_r \cdot (|\vec{r}_{xy} - \vec{R}_{xy}(\phi)|)} \cdot e^{-\mathrm{j}k_{\theta_{\text{el}}} \cdot (r_z - R_{z,0})}, \tag{3.37}$$

where $R_{z,0}$ is the height that corresponds to the middle circular track, and $k_z = k_{\theta_{\text{el}}}$. Subsequently, the model described by (3.2) is modified as

$$s_{\text{raw}}(\omega, \phi, k_{\theta_{\text{el}}}) = \iiint\limits_{x\ y\ z} s(\vec{r}_{\text{grid}}) \cdot e^{-\mathrm{j}k_r \cdot (|\vec{r}_{xy} - \vec{R}_{xy}(\phi)|)} \cdot e^{-\mathrm{j}k_{\theta_{\text{el}}} \cdot (r_z - R_{z,0})} \, \mathrm{d}x \, \mathrm{d}y \, \mathrm{d}z =$$

$$e^{\mathrm{j}k_{\theta_{\text{el}}} \cdot R_{z,0}} \cdot \iint\limits_{x\ y} \mathcal{F}_{k_{\theta_{\text{el}}}}[s(\vec{r}_{\text{grid}})] \cdot e^{-\mathrm{j}k_r \cdot (|\vec{r}_{xy} - \vec{R}_{xy}(\phi)|)} \, \mathrm{d}x \, \mathrm{d}y, \tag{3.38}$$

where the second term is identical to the expression described by (3.32), and contains the two integrals with respect to x and y. Therefore, the inversion of the system can be performed in a similar way as

$$S(k_x, k_y, k_z) = e^{-\mathrm{j}k_{\theta_{\mathrm{el}}} \cdot R_{z,0}} \cdot \mathcal{F}_\xi^{-1} \left[\frac{S_{\mathrm{raw}}(\omega, \xi, k_{\theta_{\mathrm{el}}})}{\mathcal{H}_\xi^2(k_r R_{xy}) \cdot e^{-\mathrm{j}\pi \cdot \frac{\xi}{2}}} \right]. \tag{3.39}$$

It can be observed that (3.39) is expressed in the spatial frequency domain as $S(k_x, k_y, k_z) = \mathcal{F}[s(\vec{r}_{\mathrm{grid}})]$, and assumes that the interpolation from $(k_r, \phi, k_{\theta_{\mathrm{el}}})$ to (k_x, k_y, k_z) has already been performed. Finally, the unknown complex reflectivity $s(\vec{r}_{\mathrm{grid}})$ is obtained by a 3-D FFT.

3.5.2 Time-domain direct back-projection (DBP)

The back-projection (BP) algorithm was first conceived in computed axial tomography (CAT) to achieve highly accurate two-dimensional imaging [Soum 99, Poul 10]. However, it was until the beginning of the 1990's when scientists found the mathematical similarities between SAR image reconstruction and CAT, thus developing the *direct back-projection (DBP)* for SAR [Desa 92]. As a matter of fact, two variations of this algorithm were defined: the back-projection filtering, and the convolution back-projection [Zeng 94]. In the former, every echo is back-projected on the image grid, then filtered. In the latter, the data is first convolved with a kernel function, then the back-projection of each echo is accomplished. In fact, the most accurate and suitable method is the convolution back-projection, since it offers higher accuracy and lower PSLR.

As mentioned before frequency-domain approaches rely on ideal synthetic apertures in order to get high-resolution images, thereby decreasing its feasibility for real scenarios and for wide-angular apertures, especially with airborne SAR. In fact, this limitation can be overcome with the DBP due to the following advantages

1. The DBP does not need to assume ideal trajectories, since it uses the real position of the platform, i.e., it offers the exact inversion of the synthetic aperture.

2. It does not need polar-to-cartesian interpolations in the Fourier domain, because it works directly with the k-space data.

As discussed in section 2.5, the Radon transform is the underlying fundamental concept for CAT and for the back-projection algorithm [Poul 10]. This transform maps the spatial-time domain (x, y) to the (u, ϕ) domain, where every point of $S(u, \phi)$ corresponds to a line of $s(x, y)$. This mapping is analytically expressed by (2.52) for SAR under the assumption of planar wavefronts.

The general expression of the DBP, which considers the curvature of the wavefront, is given by (3.6). This expression can be further reduced to

$$s(\vec{r}_{\mathrm{grid}}) = \gamma_{DBP} \cdot \iint\limits_{\theta_{\mathrm{el}} \, \phi} \mathrm{sinc}\left(|K_{\mathrm{cr}}| \cdot \left(\tau - \frac{2 \cdot |\vec{r}_{\mathrm{grid}} - \vec{R}(\phi)|}{c} \right) \right) \cdot e^{\mathrm{j}2k \cdot |\vec{r}_{\mathrm{grid}} - \vec{R}(\phi)|} \, \mathrm{d}\phi \, \mathrm{d}\theta_{\mathrm{el}}, \tag{3.40}$$

where γ_{DBP} is a constant factor, the sinc function is the filtered echo in the range direction corresponding to the range-compressed data, and the exponential term is the complex conjugate azimuth modulation term, aimed to add all the energy constructively, i.e., coherent imaging. Moreover, the limits of the integral are given by $\phi \, \epsilon \, [-\pi, \pi]$ in the case of a circular synthetic aperture, and θ_{el} for an additional synthetic aperture in elevation, as discussed in Chapter 6.

Similarly, the incoherent imaging approach is derivable from (3.40) as

$$s(\vec{r}_{\mathrm{grid}}) = \gamma_{DBP} \cdot \sum_i^{N_{\mathrm{sub}}} I_i \left[\int_{\theta_{\mathrm{el}}} \int_{\phi_i \pm \frac{\Delta\phi}{2}} \mathrm{sinc}(\cdot) \cdot e^{\mathrm{j}2k \cdot |\vec{r}_{\mathrm{grid}} - \vec{R}(\phi_i)|} \cdot e^{-\mathrm{j}2k \cdot r_0} \, \mathrm{d}\phi_i \right] \mathrm{d}\theta_{\mathrm{el}}, \qquad (3.41)$$

with N_{sub} as the total number of subapertures, I_i as the intensity of the subaperture image i, $\Delta\phi$ as the interval of integration at the angle ϕ_i, and the second exponential term as the factor that should be kept to perform 3-D SAR imaging in elevation. If $\Delta\phi$ is small enough, then 3-D reconstruction can be performed in a similar way as in the TomoSAR mode (see Section 2.5.2).

Eq. (3.40) and Eq. (3.41) describe the compression in azimuth direction as a convolution in the temporal domain, which means that for every position in the imaging grid $\vec{r}_{\mathrm{grid}} = (r_x, r_y, r_z)$, the energy of every range-compressed echo is projected at the correspondent range distance to the platform position $|\vec{r}_{\mathrm{grid}} - \vec{R}(\phi)|$. Note that the information contained in each pulse is spread over $\vec{r}_{\mathrm{grid}}$ with constant values along concentric spheres with origin at the antenna phase center. In view of this fact, two aspects have to be taken into account during this process: the interpolation of the range-compressed signal at the desired range position, and the sampling requirements of the imaging grid.
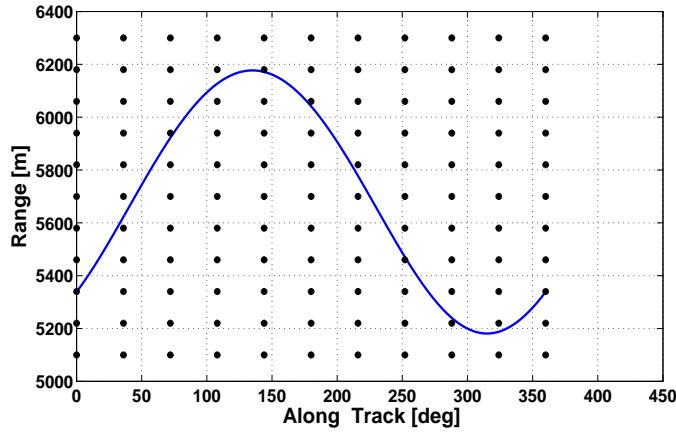
Figure 3.7: Raw data samples (black dots) that show the necessity of interpolation since the samples do not always meet the positions (blue line) of one particular target. In fact, the blue line represents the range history of a given pixel in CSAR mode.

The sampling rate of the raw data is defined by the bandwidth of the system and the integration time, respectively, in range and azimuth directions. For that reason, it does not follow the target information that is spread over several sinus with different amplitude and phase in the raw data. This fact makes necessary the use of interpolations for the DBP (see Fig. 3.7). That is to say that the range-compressed echoes are discrete time signals that were sampled according to the Nyquist criteria, therefore, they can be interpolated to an arbitrarily accuracy using an

appropriate interpolator kernel, e.g. linear, zero padding with a cubic kernel, truncated sinc or truncated sinc with a Knab pulse (see Chapter 4).

On the other hand, the sampling requirements of the imaging grid depend on (3.22), (3.23), and (3.24). In the worst case, the sampling criteria is defined by the maximum resolutions, which are $\sim \lambda_c/4$ in the (x, y) plane and in the order of the system bandwidth, BW, along the z direction. Notably, this brings a very high computational burden to the processing chain, particularly for circular synthetic apertures since they provide a much finer resolution than linear SAR modes. The number of operations is in the order of $O(L_{\text{full}} \cdot M_{\text{cart}}^3)$ for a total number of pulses of L_{full} and a total number of pixels in the three-dimensional cartesian grid $\vec{r}_{\text{grid}}$ of M_{cart}^3.

As a solution, the long processing time can be tackled either by parallel computing (e.g., many CPUs or GPUs) or by using fast back-projection techniques at an acceptably cost in the image quality by adapting the DBP to more suitable grids with less pixels. Both methodologies are part of the contributions of this thesis and will be analysed in detail in Chapter 4 and 5.

3.5.3 Generalised likelihood ratio test (GLRT)

The *generalized likelihood ratio test (GLRT)* is a method based on detection and estimation theory, and it is mainly used to detect specific targets based on a priori knowledge [Vocc 09]. Particularly, for wide-angular SAR applications, it is used to identify the presence and location of objects by analysing the angular variation of their reflectivity. The GLRT is divided into two main steps: 1) the likelihood ratio test to determine whether the target is present; 2) the maximum likelihood estimation to retrieve the unknown parameter, which is the location of the reflectivity of a certain target in the scene.

In order to perform the likelihood ratio test, the model defined by (3.2) is considered. This equation describes the collected data $s_{\text{raw}}(\omega, \phi)$ after range compression, and contains the unknown variable $s(\vec{r}_{\text{grid}})$. In this way, to determine the presence of the target, a test statistic $\Lambda(s(\vec{r}_{\text{grid}}))$ for each possible unknown within the (x, y, z) space has to be performed

$$\Lambda(s(\vec{r}_{\text{grid}})) = \frac{f_\Lambda(H_{s(\cdot)}[s_{\text{raw}} + \eta(\omega, \phi)])}{f_\Lambda(H_0[\eta(\omega, \phi)])}, \tag{3.42}$$

where the probability density functions $f_\Lambda(\cdot)$ are defined under the following hypothesis

$$\begin{aligned} H_0 &: \eta(\omega, \phi), \\ H_1 &: s_{\text{raw}}(\omega, \phi) + \eta(\omega, \phi), \end{aligned} \tag{3.43}$$

with $\eta(\omega, \phi)$ described as additive white Gaussian noise (AWGN). Interestingly, in [Vocc 09], it was demonstrated that the solution to the test statistic $\Lambda(s(\vec{r}_{\text{grid}}))$ is equivalent to the DBP algorithm, and thus the first step of the GLRT is accomplished by focusing the image using (3.40).

Subsequently, the maximum likelihood estimation is performed by maximising the test statistic $\Lambda(s(\vec{r}_{\text{grid}}))$ over the imaging grid $\vec{r}_{\text{grid}} \epsilon (x, y, z)$

$$\widehat{s}(\vec{r}_{\text{grid}}) = \arg \max_{\vec{r}_{\text{grid}}} \left\| \gamma_{DBP} \cdot \int\limits_{\theta_{\text{el}}} \int\limits_{\phi} \text{sinc}(\cdot) \cdot e^{\text{j}2k \cdot |\vec{r}_{\text{grid}} - \vec{R}(\phi)|} \cdot e^{-\text{j}2k \cdot r_0} \, \mathrm{d}\phi \, \mathrm{d}\theta_{\text{el}} \right\|, \tag{3.44}$$

where $\widehat{s}(\vec{r}_{\text{grid}})$ is the estimated complex reflectivity of the target or unknown.

Particularly, the GLRT has been used for wide-angular SAR imaging, i.e., random paths, circular and multicircular acquisitions [Erti 07, Mose 05, Mose 04, Aust 08, Aust 11, Erti 10, Ferr 09, Aust 09]. Imaging in 2-D and 3-D was accomplished under the assumption of limited-persistence targets, i.e., man-made targets with highly-directive responses, by integrating segments of few degrees (e.g., $\Delta\phi = 2°$) of the full synthetic aperture. Therefore, instead of using the isotropic model given by (3.44), the GLRT imaging was performed in subapertures, as follows

$$I_G[\widehat{s}(\vec{r}_{\text{grid}})] = \arg\max_{\phi_i,\Delta\phi,pol} \|I_i\left[s(\vec{r}_{\text{grid}};\phi_i,\Delta\phi,pol)\right]\|, \qquad (3.45)$$

where $I_i(\cdot)$ is the intensity of the subaperture image i, centred at the angle ϕ_i with an integration angle of $\Delta\phi$, and polarisation pol. In fact, the subaperture images can be obtained either by using the DBP or CS, as described by (3.41) and by (3.51), respectively, but instead of adding the energy incoherently, the maximum likelihood estimation is performed. Certainly, the GLRT imaging described by (3.45) can be approximated as taking the maximum non-coherent value of all subaperture images and polarisations for a given pixel or voxel [Vocc 09].

Lastly, another aspect that has to be considered to further understand the retrieved information with this approach, is the visualisation. Visualisation can be performed as a single image of intensities, or it can be performed as a function of the aspect angle, i.e., denoting every subaperture index with a different colour. Throughout this thesis, the GLRT is used to image fully polarimetric 3-D volumes with the DBP and CS in Chapter 6.

3.5.4 Compressive sensing (CS) reconstruction

Focusing algorithms based on linear inversions, such as the DBP or the wavefront reconstruction, assume that the Nyquist requirements are fulfilled. Although it is possible to achieve a focused image, these approaches suffer of shortcomings, like limited geometric resolution and sidelobe artefacts that degrade the image. Recently, extended research has been carried out to overcome these limitations by exploiting a priori knowledge of the scene based on sparsity. An unknown signal is said to be S sparse, when it contains S non-zero elements. If S is much smaller than the number of total pixels in the image, then super-resolution and feature enhancement can be achieved. In fact, sparsity has mostly being exploited to address real-valued problems [Pott 10, Onho 12].

On the other hand, recording as many samples as defined by the Nyquist theorem can become unfeasible for practical realisations, particularly when it is desired to sample a tomographic aperture in elevation, e.g., multibaseline and multicircular acquisitions, or forming a random synthetic aperture in the (x, y, z) space. Therefore, reconstruction of the unknown signal with linear methods to achieve fine geometric resolution and low PSLR becomes almost impossible. Consequently, a solution based on non-linear methods, such as *compressive sensing (CS)*, has to be found. CS has been object of study in the last few years for signal processing in various fields (e.g., medical imaging, communications, astronomy, optics, digital holography, and radar) in order to sense in a compressed form and at a reduced data rate. The basic theory behind this

technique is to exploit the sparse representation or compression of the unknown signal in a certain basis to solve undetermined linear problems, where the Nyquist criterion is not fulfilled [Cand 06, Dono 06, Cand 08a, Cand 08b, Cand 11].

According to CS, the unknown signal $X \in \mathbb{C}^N$ can be reconstructed as follows

$$Y = AX + n_0, \tag{3.46}$$

where $Y \in \mathbb{C}^M$ are the measurements, $A \in \mathbb{C}^{M \times N}$ is the forward operator or sensing matrix, and n_0 is the system noise (e.g., thermal noise). If $M \ll N$, then (3.46) becomes an undetermined problem, which can be regularised with CS with high probability by making the following statements: 1) the unknown X can be represented as S sparse in a certain basis Ψ (e.g., identity matrix, Fourier, wavelet, curvelets, gradient operator, and adapted dictionaries); 2) it is known that the noise power is bounded by $\|n_0\|_2 < \varepsilon$, where ε is the maximum expected noise power in the signal.

In addition, the sensing matrix A should fulfil the restricted isometric property (RIP), which is defined by the smallest $\delta_S \in (0, 1)$ that satisfies the following inequality

$$(1 - \delta_S) \|X\|_2^2 \le \|AX\|_2^2 \le (1 + \delta_S) \|X\|_2^2, \tag{3.47}$$

under the assumption of X having at most S non-zero elements [Cand 08a, Pott 10]. Consequently, the CS theory states that the solution to (3.46) can be found through the l_1 norm

$$\arg \min_X \|\Psi \cdot X\|_1 \quad \text{subject to} \quad \|Y - AX\|_2^2 \le \varepsilon^2, \tag{3.48}$$

which results in an optimisation problem. In fact, the RIP is still fulfilled for the cases where the sensing matrix is not precise, e.g., when the SAR data is not well calibrated, however the disturbances should be close to zero [Pott 10].

On the other hand, the mutual coherence[3] $\mu(A)$ is a measurement that sets a conservative bound on the RIP by $\delta_S \le (S - 1)\mu(A)$, and it is defined as

$$\mu(A) = \max_{i \ne j} \frac{|a_i' a_j|}{\|a_i\| \, \|a_j\|}, \tag{3.49}$$

where the mutual coherence of the columns of the sensing matrix defines the optimal sparsity constraint. As a matter of fact, low coherence values will assure a more stable inversion of (3.48) than high coherence values. Likewise, the basis Ψ, in which X is sparse, as well as the pair (A, Ψ) should show low coherence. If the coherence has a value of zero, then it is said that the matrix or matrices are orthonormal. In order to be as close as possible to the ideal reconstruction with a low RIP and a low mutual coherence, the sensing matrix should be defined as a random matrix, i.e., the sampling shall be random. In fact, randomisation applied to SAR imaging with linear reconstructions has shown a considerable reduction of aliasing, thus having chances to recover the complex reflectivity of the unknown, however at the cost of an increased clutter power [Axel 04].

Furthermore, in [Cand 08b], it was shown that X can be exactly recovered when the number of samples satisfies the following expression

$$M \ge C_{\text{cs}} \cdot \mu^2(A, \Psi) \cdot S \cdot \log(N), \tag{3.50}$$

---

[3]The expression coherence in this context is not related to coherence in the SAR interferometry field.

with the appropriate constant C_{cs}.

As documented in the literature, there are three different approaches to solve the optimisation problem given by (3.48): the l_p-norm regularisation, fast greedy heuristics, and the l_2-norm minimisation to approximate the l_1-norm minimisation iteratively [Pott 10]. Particularly, the basis pursuit denoising (BPDN) is a l_p-norm regularisation method, which is defined as

$$\widehat{X} = \arg \min_X \|Y - AX\|_F^2 + \lambda_1 \|\Psi \cdot X\|_p , \qquad (3.51)$$

where $0 < p \le 1$, $\| \cdot \|_F$ denotes the Frobenius norm, and λ_1 is a positive value that controls the trade-off between sparsity in Ψ and the model mismatch.

Compressive sensing in the SAR field has been widely used for 2-D and 3-D imaging and for different type of targets, applications and sensor configurations. In fact, most of the current research has been carried out for highly-directive targets and assuming plane wavefronts since the model can be easily adapted to the theory of CS.

The model that has been used for CS is based on the projection slice theorem, and it is given by (2.50) in 2-D, and

$$S(k_x, k_y, k_z) = \int\!\!\!\int\limits_{-\infty}^{\infty}\!\!\!\int s(x, y, z) \cdot e^{-\mathrm{j}(xk_x + yk_y + zk_z)} \, \mathrm{d}x \, \mathrm{d}y \, \mathrm{d}z, \qquad (3.52)$$

in 3-D [Ceti 01]. Generally, the unknown signal, the sensing matrix and the measurements in 2-D and 3-D can be expressed in a vectorised form in order to fit them to the expression given in (3.51). That is to say that in the case of 2-D imaging, $X = s(x, y) \, \epsilon \, \mathbb{C}^{N^2 \times 1}$ is the unknown signal, $A \, \epsilon \, \mathbb{C}^{M^2 \times N^2}$ is the observation kernel, and $Y \, \epsilon \, \mathbb{C}^{M^2}$ are the measurements, and in a similar way for 3-D imaging. The limits of the integral are defined by the radius of the spotlighted area, and the number of pixels of the focused image is assumed to be N by N, whereas the number of collected pulses is M with M range bins.

The variable that has not been yet defined is the sparsity basis Ψ, which is a square matrix of N^2 by N^2 elements, for the given unknown X. One of the proposed solutions to this variable has been the gradient operator, which is multiplied by the magnitude of the measurements instead of the complex reflectivity [Ceti 01]

$$\widehat{X} = \arg \min_X \|Y - AX\|_F^2 + \lambda_1 \|\Psi \cdot |X|\|_1 . \qquad (3.53)$$

Particularly, this method assumes sparsity on the spatial derivatives of the magnitude, which leads to find for a smooth solution that suppresses the presence of speckle noise. In fact, this solution was chosen under the assumption that the phase of the complex reflectivity is usually highly random and uncorrelated. In [Sama 11], the sparsity basis Ψ was defined by the wavelet dictionary for 2-D SAR imaging to sparsely represent and solve the magnitude of the complex reflectivity. Particularly, the Haar wavelet, the Daubechies, and the spike-wavelet overcomplete dictionaries were used, since they can often sparsely represent natural imagery and man-made targets with high SCR.

Certainly, a straight forward definition of Ψ is to assume that the unknown is sparse in space, where Ψ is the identity matrix. In [Mose 05, Aust 08], this solution has been exploited for wide-angle acquisitions with the simulated data of a backhoe at X-band and UHF. In [Mose 05], a

spotlight SAR simulation with an azimuthal aperture of $110°$ was carried out for 2-D imaging. The reconstruction was based on 2-D FFTs and the BPDN assuming sparsity in space. Moreover, imaging was carried out in subapertures by using the GLTR with both the DBP and CS, and assuming the presence of just highly-directive targets. As a result, images focused with CS showed an improved resolution and sidelobe reduction in comparison with the conventional Fourier approach, i.e., the DBP. Likewise, in [Aust 08], this methodology was extended for 3-D imaging with a non-linear sparse-path acquisition of the backhoe. Correspondingly, it was demonstrated that the same model was also suitable to reconstruct 3-D images with arbitrary tracks and also considering only a few highly-directive targets.

In [Aust 11, Ferr 09, Aust 09, Erti 10], an airborne multicircular SAR data acquisition was run with eight circular-like passes at X-band for highly-directive targets, e.g., vehicles. In the same way as the last methods, limited-persistence targets and planar wavefronts were assumed, and processing was performed by integrating coherently segments of few degrees (e.g., $\Delta\phi = 2°$) using the DBP and CS. In addition, the reconstruction was also based on 3-D FFTs and on two sparsity-based techniques: BPDN, and CoSaMP (i.e., fast greedy heuristic method) supposing that the number of significant scatterers is known. The 3-D images of all subapertures were combined with both incoherent imaging and GLRT imaging. Results of CS showed that cone-shaped sidelobes were considerably reduced when compared to DBP images, the effect of layover was solved and only prominent scatterers were recovered.

Until now, it has been assumed that imaging is performed in 2-D and 3-D for highly-directive scatterers. Another approach that has been recently researched is the use of the TomoSAR model to retrieve the energy in the $\text{LOS}_\perp$ direction, i.e., a reduced model to a 1-D problem in stripmap mode at a limited look angles. Particularly, this model has been used with distributed scatterers, i.e., forested areas in [Agui 13]. As described in Section 2.5.2 the input of the system is given by 2-D coregistered images, focused in the (r, x) plane. In order to deal with this kind of targets, including speckle noise, second-order statistics, i.e., the covariance matrix, were adopted

$$\widehat{X} = \arg\min_{p} \left\| YY^\dagger - A\operatorname{diag}(P) A^\dagger \right\|_F^2 + \lambda_1 \left\| \Psi \cdot P \right\|_1 + \lambda_2 \left\| P \right\|_{\text{TV}}, \tag{3.54}$$

where $Y \in \mathbb{C}^{M\times L}$ with L neighbouring pixels in the (r, x) space, and A is the steering matrix defined by the acquisition geometry and $P = \operatorname{diag}(XX^\dagger) = \operatorname{d}(XX^\dagger)$ as the desired reflectivity that contains the intensity of X, however, at the cost of loosing resolution in both r and x directions. The definition of the sparsity basis Ψ was the Daubechies symmlet wavelet dictionary, whereas the total-variation (TV) norm regularisation was added to reduce noise or random signatures, analogous to the gradient operator [Rudi 92]. Imaging was performed with a data set that was acquired in stripmap mode at L-band with 20 tracks in elevation, i.e., horizontal baseline, over a forested area, i.e., semi-transparent media. Tests with several baseline distributions up to a minimum of 5 tracks were carried out.

3.6 Autofocus algorithms

Besides the need of high-precision focusing algorithms to retrieve high-quality images, another aspect related to the processing of airborne SAR data of wide-angle synthetic apertures is the accurate estimation of the antenna phase center, i.e., the platform trajectory. Particularly, the navigation data of airborne SAR are susceptible to errors in the GPS measurements of around 1 - 10 cm due to turbulence and high bank angles during circular flights. Due to the larger integrated aperture when compared to stripmap SAR, the requirements in terms of trajectory knowledge are more demanding. Similarly, techniques that use multiple passes in elevation, such as multibaseline and multicircular SAR acquisitions, also require an estimation of the phase center with very high precision. These errors can be estimated and corrected by using autofocus algorithms.

The most common approaches are the map-drift and the phase gradient autofocus (PGA) algorithms[Manc 81, Samc 06, Carr 95a, Mace 08]. Specifically, the PGA is an iterative method that can estimate phase errors using the range-compressed data by evaluating persistent scatterers with sufficient SCR. In addition, in [Jako 93], the eigenvector decomposition of contiguous samples in the azimuth direction of the range-compressed data was used within the PGA to enhance the signature of the persistent targets, thus making the algorithm converge in less iterations. Recently, an iterative frequency-domain autofocus algorithm was proposed [Ponc 14a]. This solution tackles the problem of requiring high-SCR returns by analysing the IRF of isotropic-like targets in the frequency domain. Thereby, achieving the highest possible resolution, e.g., $\sim \lambda_c/4$ with CSAR. In this section, the aforementioned autofocusing solutions are introduced, since they establish the basic principle of the contributions in this thesis regarding phase error estimation.

On the other hand, different autofocus approaches based on other metrics have been developed in the last few years. In [Cant 11], an autofocus method based on multilateration was developed by measuring the relative displacement between small images of ground reflectivity obtained from adjacent subapertures. In [Ash 12], contrast optimisation or entropy maximisation was used to improve focusing. However, this technique do not usually achieve the same performance as those based on strong deterministic targets. Likewise, in [Krag 09], autofocus was performed by optimising the 3-D SAR image entropy from multiple coherently aligned 2-D SAR images at different look angles. In [Ende 12, Lee 08], sparse representation solutions were used in order to find phase corrections that make the image reflectivity become sparse, i.e., focused.

3.6.1 Phase gradient autofocusing (PGA)

The basic principle of the PGA is to use the derivative in the along-track direction of the range-compressed data of a persistent scatterer, in order to retrieve phase histories and directly estimate phase errors. The main advantage of the PGA is that the recovered phase is unwrapped, thereby avoiding the use of complex unwrapping methods. The retrieved phase of a single reference target gives information that corresponds to the line-of-sight (LOS) direction. This

allows one to estimate errors in the LOS for a region close to the reference target, but not for the whole image. In fact, this is a particularity of airborne acquisitions, since the difference between near and far ranges is comparable to the height of the flight. Therefore, the phase error estimation becomes range dependent, thus requiring at least two persistent reference targets with high SCR for the whole synthetic aperture and at different range bins, in order to perform the correction for the whole scene. However, this might be difficult to achieve for CSAR acquisitions since targets at different ranges for a certain position ϕ_1 can be at the same range distance for another position ϕ_2, and usually they are not available for the $360°$.

In order to start implementing the PGA, the area that remains illuminated during the whole acquisition and within the 3 dB antenna pattern has to be identified. Afterward, the reference targets at different range distances are selected. Indeed, these targets are usually corner reflectors or Luneburg lenses to ensure the existence of strong point-like backscattering.

The range-compressed data of a reference target n can be expressed as

$$s_{\mathrm{r},n}(t) = |s_{\mathrm{r},n}(t)| \cdot e^{-j\frac{4\pi}{\lambda_c} \cdot r_{\mathrm{real},n}(t)} \cdot e^{j\frac{4\pi}{\lambda_c} \cdot r_{o,n}(t)} = |s_{\mathrm{r},n}(t)| \cdot e^{j\frac{4\pi}{\lambda_c} \cdot r_{\mathrm{err},n}(t)}, \qquad (3.55)$$

where $|s_{\mathrm{r},n}(t)|$ is the amplitude of the range compressed data, $r_{\mathrm{real},n}$ corresponds to the real distance to the target, the second exponential is the modulation term with $r_{o,n}$ as the distance computed from the platform to the reference point, and $r_{\mathrm{err},n}$ is the remaining error in the LOS.

In view of this fact, the error $r_{\mathrm{err},n}$ can be estimated by computing the derivative of $s_{\mathrm{r},n}(t)$, as follows

$$r_{\mathrm{err},n} = \frac{\lambda}{4\pi \cdot |s_{\mathrm{r},n}(t)|^2} \cdot \Im\left(\frac{\partial s_{\mathrm{r},n}(t)}{\partial t} \cdot s_{\mathrm{r},n}^*(t)\right), \qquad (3.56)$$

where $\Im(\cdot)$ indicates the imaginary part and $s^*(\cdot)$ the conjugate of $s.(\cdot)$. As previously mentioned, this expression gives information about the error in LOS, which is range dependent. Therefore, the derivative should be computed for at least two reference targets. Subsequently, to compute the components in the (x, y, z) space, a linear inversion is needed. This inversion allows the retrieval of two unknowns, namely horizontal and vertical error components, Υ_h and Υ_v, respectively. If more than two reference targets are given, then the system becomes overdetermined. Consequently, the solution is obtained by means of the least squares minimisation [Reig 06]

$$\Upsilon_{hv} = (A^{\mathrm{T}}A)^{-1}A^{\mathrm{T}}R_{\mathrm{err}}, \qquad (3.57)$$

where

$$\Upsilon_{hv} = \begin{bmatrix} \frac{\partial \Upsilon_h}{\partial t} \\ \frac{\partial \Upsilon_v}{\partial t} \end{bmatrix}, \quad A = \begin{bmatrix} \pm\sin(\theta_{\mathrm{el},1}) & \cos(\theta_{\mathrm{el},1}) \\ \pm\sin(\theta_{\mathrm{el},2}) & \cos(\theta_{\mathrm{el},2}) \\ \cdots & \cdots \\ \pm\sin(\theta_{\mathrm{el},n}) & \cos(\theta_{\mathrm{el},n}) \end{bmatrix}, \quad R_{\mathrm{err}} = \begin{bmatrix} r_{\mathrm{err},1} \\ r_{\mathrm{err},2} \\ \cdots \\ r_{\mathrm{err},n} \end{bmatrix}, \qquad (3.58)$$

where $\theta_{\mathrm{el},n}$ corresponds to the elevation angle of the reference target n for a given position in azimuth, R_{err} is the vector with the estimated errors in the LOS direction, and Υ_{hv} is the vector containing the derivative of the unknowns, which have to be integrated with respect to t. Figure 3.8 depicts the geometry to perform the linear inversion for a given position in azimuth. Clearly, it can be seen that the real track differs from the assumed track by Υ_h and Υ_v.
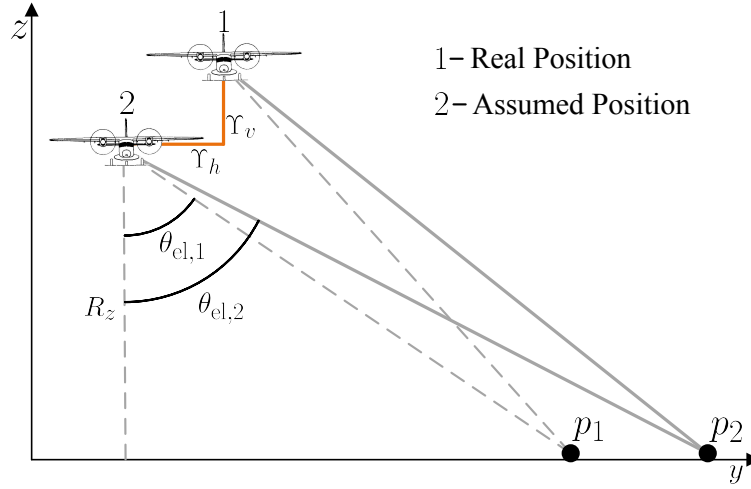
Figure 3.8: Geometry to perform the PGA algorithm, where $\theta_{\text{el},n}$ is the elevation angle to the target n, Υ_h and Υ_v are the estimated horizontal and vertical error components. p_1 and p_2 are the reference targets at different range bins.

In addition, a change of coordinates might be necessary to use Υ_{hv} for error correction depending on the reference system of the given track. Particularly, in CSAR the errors have to be expressed in the (x, y, z) space, which is the coordinate system of the circular track throughout this thesis. In order to represent the estimated errors in the proper coordinate system, the following transformation has to be carried out

$$\begin{bmatrix} \Upsilon_x \\ \Upsilon_y \end{bmatrix} = \begin{bmatrix} \Upsilon_h \cdot \cos(\phi(t)) \\ \Upsilon_h \cdot \sin(\phi(t)) \end{bmatrix}, \tag{3.59}$$

where ϕ represents the position of the antenna along the circular trajectory. The component in the vertical direction, z, is given by Υ_v. After this conversion, the track should be corrected to run iteratively the PGA until the error R_{err} reaches a certain threshold depending on the required precision, e.g., $\pi/4$.

In linear SAR modes, constant errors in the LOS are reflected as constant phase offsets in the scene, i.e., as shifted targets with respect to their real position (see Figure 3.9). Contrarily, in CSAR acquisitions, constant errors in the LOS result in smeared targets in the focused images. These errors cause ring-shaped sidelobes with radius directly proportional to the error in the LOS. In fact, this effect is similar to the one caused by displacements in height, as shown in Figure 3.3.

3.6.2 Maximum-likelihood estimation for PGA

One of the main requirements of the PGA is the need of high SCR reference targets, which are hard to find in many real scenarios, especially if no reference targets are deployed. If the SCR is low, then the algorithm may only converge after many iterations, i.e., usually five or six, or it may not converge at all. Interestingly, this problem can be addressed with a variant of the PGA, a method called maximum-likelihood (ML) estimation for PGA [Jako 93]. This algorithm filters the range-compressed signal by using the eigenvector decomposition of the covariance matrix, which is formed with neighbouring samples in range and azimuth.
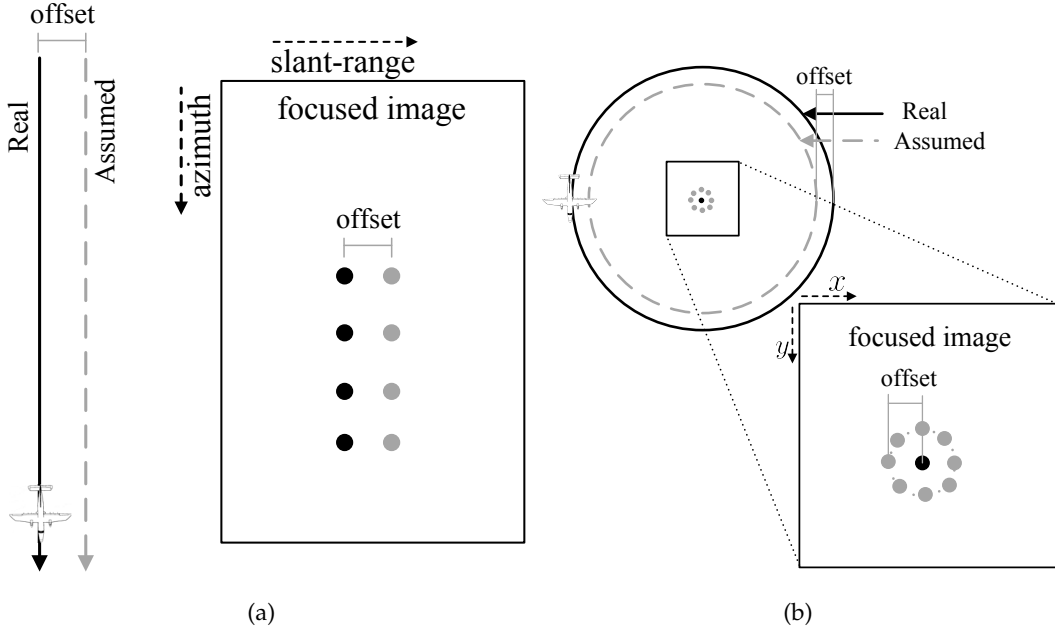
Figure 3.9: (a) Linear SAR imaging modes: constant error in the LOS direction reflected in the focused image as a constant shift with respect to the actual position of the target. (b) Circular SAR mode: constant error in the LOS result in ring- or arc-shaped sidelobes.

Let us consider the range-compressed data as a matrix of L_r range bins by L_a pulses, where clutter is treated as white Gaussian noise, and the samples of the reference target n are assumed as statistically independent among them. In order to estimate the contribution of the given target n, the input measurements have to be defined by matrix $B_n \in \mathbb{C}^{M_r \mathrm{x} M_a}$ with $M_r \leq L_r$ by $M_a \leq L_a$ neighbouring pixels in range and azimuth directions, respectively, as follows

$$
B_n = \begin{bmatrix} s_{\mathrm{r},1,1}(t) + \eta_{1,1}(t) & \cdots & s_{\mathrm{r},1,k}(t) + \eta_{1,k}(t) & \cdots & s_{\mathrm{r},1,M_a}(t) + \eta_{1,M_a}(t) \\ \cdots & \cdots & \cdots & \cdots & \cdots \\ s_{\mathrm{r},l,1}(t) + \eta_{l,1}(t) & \cdots & s_{\mathrm{r},l,k}(t) + \eta_{l,k}(t) & \cdots & s_{\mathrm{r},l,M_a}(t) + \eta_{l,M_a}(t) \\ \cdots & \cdots & \cdots & \cdots & \cdots \\ s_{\mathrm{r},M_r,1}(t) + \eta_{M_r,1}(t) & \cdots & s_{\mathrm{r},M_r,k}(t) + \eta_{M_r,k}(t) & \cdots & s_{\mathrm{r},M_r,M_a}(t) + \eta_{M_r,M_a}(t) \end{bmatrix}, \quad (3.60)
$$

where every $s_{\mathrm{r},l,k}(t)$ term contains the distance error $r_{\mathrm{err},l,k}(t)$, as shown in (3.55), and every $\eta_{l,k}(t)$ is the contribution of the clutter. Unlike the PGA, this model considers M_r by M_a neighbouring pixels as input to the system, and as a result it allows the estimation of the non-corrupted phase-error vector $\widehat{B}_n \in \mathbb{C}^{M_a}$, i.e., without the contribution of the clutter $\eta_{(.)}(t)$. This is done through the ML estimation by finding the specific value of $\Phi_{\mathrm{err},n}$ that maximises the logarithm of the conditional probability density function of B_n

$$
\ln p(B_n | \Phi_{\mathrm{err},n}) = -M_r \cdot \ln(\pi^{M_a} \cdot |C_n|) - \sum_{l=1}^{M_r} B_{n,l}^{\dagger} C_{n,l}^{-1} B_{n,l}, \quad (3.61)
$$

where $C_{n,l}$ is the covariance matrix corresponding to a certain range line l as follows

$$
C_{n,l} = \mathrm{Var}(\eta_l)^2 I + \mathrm{Var}(s_{\mathrm{r},l}(t))^2 \widehat{B}_{n,l} \widehat{B}_{n,l}^{\dagger}, \quad (3.62)
$$

with $\mathrm{Var}(\cdot)$ indicating the variance, and $\widehat{B}_{n,l}$ as the non-corrupted version of $B_{n,l}$. Subsequently, Eq. (3.61) can be reduced by discarding the left term of the right side, since it does not depend

on $R_{\mathrm{err},n}$. In view of this fact, the solution of the maximisation can be denoted by

$$Q_n = \sum_{l=1}^{M_{\mathrm{r}}} B_{n,l}^\dagger \, \widehat{B}_{n,l} \, \widehat{B}_{n,l}^\dagger \, B_{n,l} = \sum_{l=1}^{M_{\mathrm{r}}} \widehat{B}_{n,l}^\dagger \, B_{n,l} \, B_{n,l}^\dagger \, \widehat{B}_{n,l} =$$

$$\widehat{B}_n^\dagger \left(\sum_{l=1}^{M_{\mathrm{r}}} B_{n,l} \, B_{n,l}^\dagger \right) \widehat{B}_n = \widehat{B}_n^\dagger \, \widehat{C}_n \, \widehat{B}_n,$$

(3.63)

which is subject to $||\widehat{B}_n||^2 = \widehat{B}_n^\dagger \, \widehat{B}_n = M_{\mathrm{a}}$, and where

$$\widehat{C}_n = \frac{1}{M_{\mathrm{r}}} \cdot \sum_{l=1}^{M_{\mathrm{r}}} B_{n,l} \, B_{n,l}^\dagger,$$

(3.64)

is the sample covariance matrix, which is also an Hermitian matrix. $\widehat{B}_n$ is the eigenvector that corresponds to the largest eigenvalue of $\widehat{C}_n$ for sufficient neighbouring pixels. For this reason, $\widehat{B}_n$ contains the most dominant contribution of the scene, i.e., the non-corrupted phase given by the reference target n. In this way, a better estimation of the errors is achieved in much less iterations compared to the common PGA.

A special case of this method is when $M_{\mathrm{a}} = 2$, since the result of the ML estimator is

$$r_{\mathrm{err},n} = \frac{\partial s_{\mathrm{r},n(t)}}{\partial t},$$

(3.65)

which corresponds to the phase gradient computed in (3.56). Clearly, the ML estimator with $M_{\mathrm{a}} = 2$ allows a better estimation of the phase differences of adjacent pulses in comparison to the common PGA. However, an improved estimation is achieved when $M_{\mathrm{a}} \gg 2$.

After the signal $\widehat{B}_n$ is estimated, its derivative can be performed to compute the vertical and horizontal components, as in the common PGA. Figure 3.10 depicts a comparison of the three presented common PGA and the eigenvector PGA through block diagrams.

3.6.3   Frequency-domain autofocus

The frequency-domain autofocus exploits the well-known angle-frequency relation in SAR. In other words, the relation between the circular trajectory of the platform as a function of the aspect angle ϕ and the elevation angle θ_{el}, and the 2-D spectrum of the focused image of an isotropic-like target in the (k_x, k_y) space at a given range (fast-time) angular frequency ω, as follows

$$\phi = \tan^{-1}\left(\frac{y}{x}\right) = \tan^{-1}\left(\frac{k_y}{k_x}\right),$$

(3.66)

and

$$k_r(\omega) = \frac{4\pi}{\lambda(\omega)} \cdot \sin(\theta_{\mathrm{el}}) = \sqrt{k_x^2 + k_y^2}.$$

(3.67)

For a given target n at a certain ϕ, (3.67) and (3.66) allow the retrieval of residual errors from the phase of the 2-D spectrum

$$r_n(\phi, \theta_{\mathrm{el}}, \omega) = \frac{k_r(\omega)}{\sin(\theta_{\mathrm{el}})} \cdot r_{\mathrm{err},n},$$

(3.68)
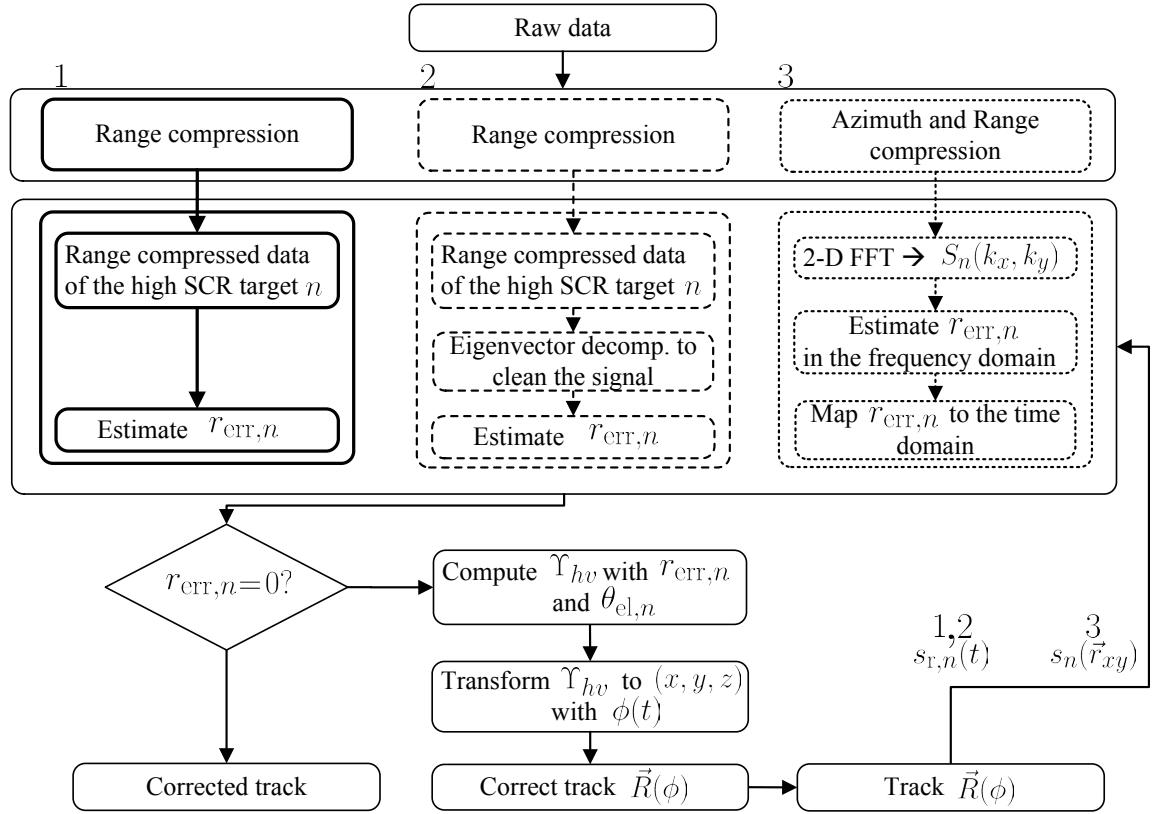
Figure 3.10: Flow chart of 1) the common PGA, 2) the maximum-likelihood estimation for PGA, and 3) the frequency-domain autofocus. Note that the first two approaches differ in the eigenvector decomposition step, which can be seen as a filter to reduce noise in the signal and make the PGA converge in less iterations.

(see Figure 3.6). Certainly, (3.68) shows how the error at a given angular instant ϕ, is mapped onto a certain spectral component (k_x, k_y). After the mapping from frequency to time domain is performed, the retrieved components in the LOS direction can be used to compute Υ_{hv}, i.e., the horizontal and vertical components for a given ϕ, and subsequently transformed to the track coordinates $\vec{R}(\phi)$ in the (x, y, z) space through the linear inversion previously defined in Section 3.6.1, but only if the information of at least two reference targets at different ranges is provided.

In light of that, this autofocus solution can be summarised by the following steps. First, a high-resolution CSAR image of an isotropic target is focused at its true height in the (x, y) plane. Then, its 2-D spectrum is computed after shifting the target to the origin in order to remove undesired phase ramps. Afterward, the LOS phase error is estimated in the frequency domain and mapped (interpolated) to time-domain as described in the previous equations. Note that usually a certain bandwidth is available, so that the information of several bins located at the same angular frequency can be averaged to reduce phase noise. Finally, the error is mapped to cartesian coordinates in order to correct the navigation data. Figure 3.10 depicts the methodology of this algorithm, as well as a comparison with the PGA and the eigenvector PGA.

In Chapter 5, this method will be used with the real data of a Luneburg lens [Mott 92]. This kind of reflector owns the features of an isotropic-like target for circular or wide-angular apertures, and due to its limited size of about 60 cm of diameter, the power of the range-compressed

signal is well below the clutter level. Therefore, the frequency-domain autofocus approach is used to estimate errors of the navigation system, thus making possible the achievement of subwavelength resolution in the (x, y) plane, as well as 3-D reconstruction [Ponc 14a].

Summarising, this chapter has presented the basic theory of CSAR imaging mode through the analysis of the IRF in time and frequency domains. Unlike the linear SAR modes, CSAR owns special properties, such as wavelength resolution and 3-D reconstruction due to the simultaneous acquisition of multi-angular measurements. Furthermore, this mode also provides shadow reduction and the advantage to better understand the coherent 3-D radar backscattering. Nevertheless, both potentials are linked to the backscattering persistence of the targets for long illumination angles, hence limiting the performance in real-world scenarios, where the targets tend to be anisotropic. In the second part of this chapter, the most used focusing algorithms for CSAR were described, and correspondingly, pros and cons were addressed. In the third part, autofocusing approaches for error estimation in the navigation data were described and analysed. It was shown that besides the use of an accurate focusing kernel, a precise estimation of the antenna phase center is required for high-resolution imaging.

4 Fast Factorised Back-Projection for CSAR

In this chapter, an efficient implementation of the fast factorised back-projection (FFBP) algorithm for circular synthetic apertures is described. In the first part, the fundamental theory of fast back-projection techniques for linear SAR modes is introduced. In the second part, this theory is extended to non-linear trajectories, and differences in terms of geometry, sampling requirements, and computational burden are discussed. The proposed method can accommodate non-ideal circular trajectories and topographic information, while reducing considerably the number of operations with respect to the direct back-projection (DBP).

Parts of this chapter have been published in [Ponc 14a].

4.1 FFBP for linear SAR imaging modes

In this section, the basic concepts of the fast back-projection methods for linear SAR imaging modes are introduced. The fast BP (FBP) is explained as the first solution proposed to reduce the number of operations in comparison with the DBP. The second solution is the extension of the FBP, called the FFBP, which is an improved version based on a recursive factorisation of the synthetic aperture.

4.1.1 Fast back-projection

Despite the high accuracy of the DBP, its main drawback is the high computational burden. After the development of this algorithm, researchers started to look for more efficient solutions. In the last decade, the FBP algorithm was proposed as a solution to reduce the number of operations, however at an acceptable cost of focusing accuracy [Yegu 99]. This approach was originally implemented for linear SAR modes, and will be introduced by considering the spotlight SAR mode for simplicity. The FBP's basic principle is to divide the full synthetic aperture L_{full} into subapertures of dimension L_{sub}. In this way, $N_{\text{sub}} = L_{\text{full}}/L_{\text{sub}}$ low-resolution images can be obtained by performing the polar BP, i.e., by back-projecting the energy of every pulse and every subaperture n into local polar grids identified by $\vec{r}_{\text{grid},n}(\alpha, r)$, where α and r indicate the polar coordinates. Afterward, all images are interpolated to a global imaging grid $\vec{r}_{\text{grid}}(x, r)$, where the final high-resolution image is formed by coherent addition (see Figure

4.1(a)).
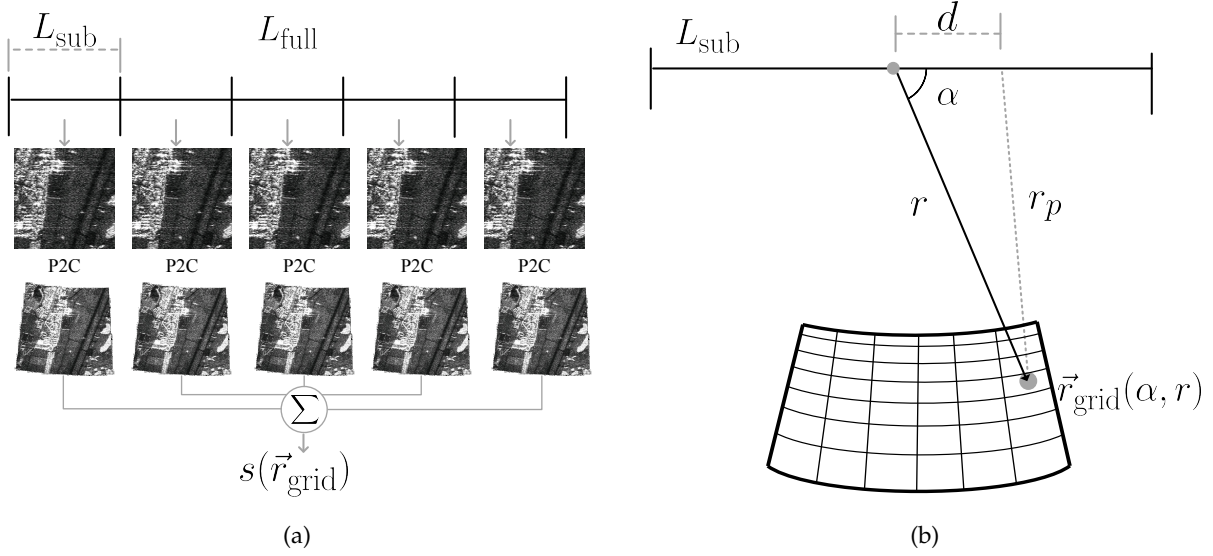
Figure 4.1: Fast back-projection (FBP) algorithm. (a) Methodology: first, the full synthetic aperture is divided in subapertures of L_{sub} pulses; then, for every subaperture a coarse-resolution image is focused to a local polar grid, $\vec{r}_{grid}(\alpha, r)$; afterward, every image is interpolated to a global cartesian grid, $\vec{r}_{grid}(x, r)$ through polar to cartesian interpolations (P2C); finally, they are coherently added to form the final high-resolution image, $s(\vec{r}_{grid})$. (b) Representation of the back-projection in polar coordinates $\vec{r}_{grid}(\alpha, r)$ of the subaperture n of dimension L_{sub}.

The main aspect that has to be taken into account when back-projecting the energy of every subaperture is the imaging grid, $\vec{r}_{grid,n}$, which instead of being in cartesian coordinates (x, r), it is defined in polar coordinates (α, r). Interestingly, the advantage of using a polar geometry is that the number of pixels in the azimuth direction is considerably reduced, thus decreasing the number of operations. This can be better visualised in the frequency domain, as depicted in Figure 4.2 with the two-dimensional spectrum focused in both cartesian (a) and polar (b) grids. Certainly, the FBP takes the advantage of the low bandwidth in the angular direction, in this way relaxing the sampling requirements. This topic will be further discussed in the second part of Section 4.1.2.

The two components of every local polar coordinate system, (α, r), are defined with respect to the center of each subaperture, where α is the angle formed between the track or velocity vector, and the range component r, as shown in Figure 4.1(b). As a result, the analytical expression of the FBP in polar coordinates can be denoted from the DBP, (3.41), as

$$s(\vec{r}_{grid}) = \sum_{n=1}^{N_{sub}} \left[\int_{(n-1)\cdot L_{sub}+1}^{n\cdot L_{sub}} \gamma_{FBP} \cdot \text{sinc}(\cdot) \cdot e^{j2k\cdot|\vec{r}_{grid,n}(\alpha,r)-\vec{R}(\phi)|} \cdot e^{-j2k\cdot r_0} \right], \tag{4.1}$$

where γ_{FBP} is a constant factor, and the distance from the platform to the polar grid, $|\vec{r}_{grid}(\alpha, r) - \vec{R}(\phi)|$, is given by the law of cosines, as follows

$$r_p = |\vec{r}_{grid}(\alpha, r) - \vec{R}(\phi)| = \sqrt{r^2 + d^2 - 2rd \cdot \cos(\alpha)}, \tag{4.2}$$

with d defined as the distance from the center of the subaperture n to the position of the considered pulse (see Figure 4.1(b)). After the low-resolution images are focused in polar grids, they

(a) (b)
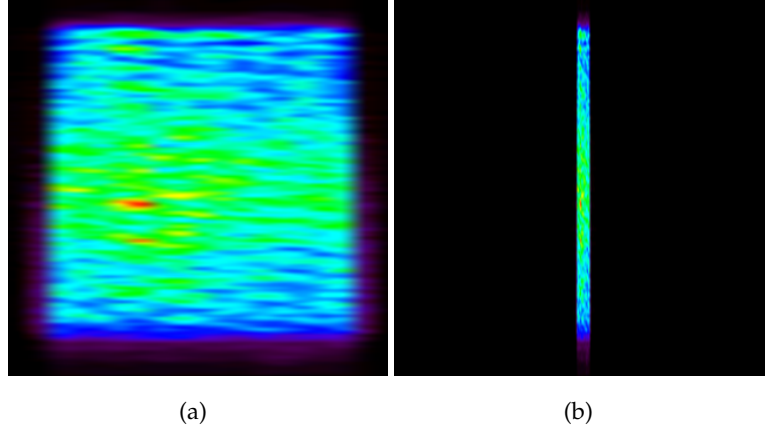
Figure 4.2: 2-D spectrum of a subaperture image focused in (a) cartesian coordinates (k_x, k_r), and (b) polar coordinates (k_α, k_r). Note that the bandwidth in the angular direction is reduced, thus relaxing the sampling requirements.

are interpolated to a global cartesian grid $\vec{r}_{\text{grid}}(x, r)$, where all images are added coherently to form the full-resolution image.

4.1.2 Fast factorised back-projection

Despite the decreased computational burden of the FBP with respect to the DBP algorithm, researchers tried to further improve the number of operations to focus SAR images in the time domain. To that end, the fast FBP (FFBP) algorithm was proposed. The FFBP differs from the FBP in the following aspects [Ulan 03]:

1. It requires interpolations from low-resolution polar grids to polar grids of finer resolution. These interpolations are referred in this thesis as P2P.

2. It can be implemented in a recursive way.

3. Interpolations from polar to cartesian grids (P2C) are performed as the last step and only for the full synthetic aperture to obtain the final high-resolution image.

The FFBP method speeds up the processing time by dividing the full synthetic aperture of dimension L_{full}, k times by a factor n in a recursive way until the minimum subaperture size L_{min} is reached. Figure 4.3 depicts the FFBP flow when the synthetic aperture is divided every stage i by a factor $n = 2$, which will be used throughout this thesis. The number of pulses of each subaperture at the stage $i \in [1, 2, ...k]$ are indicated by L_i. In fact, the FFBP of one stage, i.e., $i = k = 1$, corresponds to the aforementioned FBP, where $L_{\text{sub}} = L_{i=1} = L_{\text{min}}$.

After L_{min} is reached, the polar BP is carried out, thus focusing a total of 2^k coarse-resolution images of $N/2^k$ by M pixels in the angular and radial directions, respectively, where N and M are the total number of pixels of the final image. Afterward the angular resolution is enhanced by merging the information of two by two contiguous images by P2P interpolations.
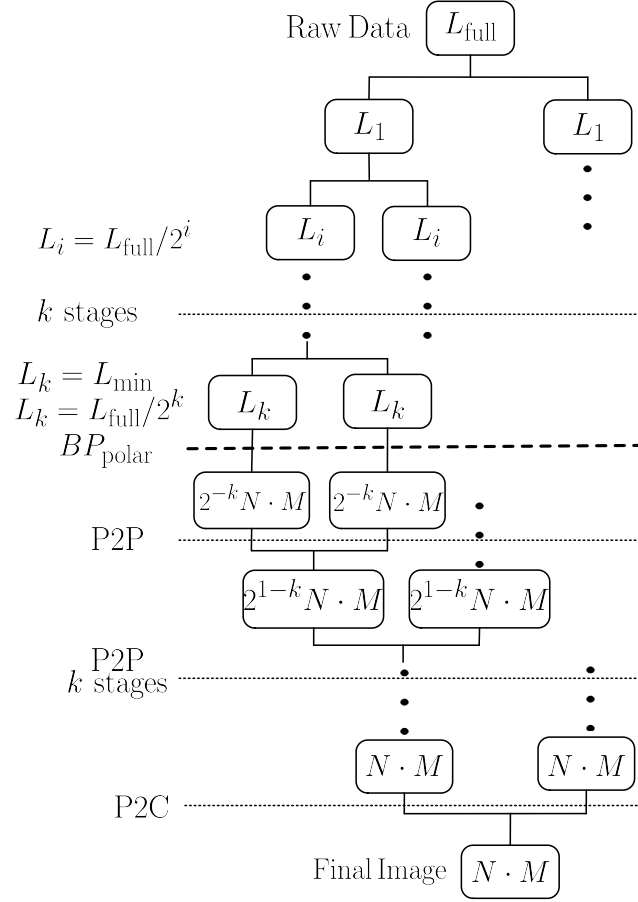
Figure 4.3: Block diagram of the fast factorised back-projection (FFBP) algorithm for linear SAR modes. Given the raw data, the full synthetic aperture L_{full} is divided recursively k stages by a factor of $n = 2$ until $L_i = L_{\text{min}}$. The polar back-projection (BP) is accomplished for the smallest subapertures, and afterward polar-to-polar (P2P) interpolations are used to merge the information of every two-by-two contiguous images. Lastly, images are interpolated from polar to a global cartesian (P2C) grid of N by M pixels, to be afterward coherently added.

To that end, let us denote the centres of two contiguous subapertures at the stage k as $\vec{q}_k$, and the center of the corresponding subaperture at stage $k-1$ as $\vec{q}_{k-1}$ (see Figure 4.4(a)). Subsequently, the polar grid $\vec{r}_{\text{grid},k-1}(\alpha, r)$ of $N/2^{k-1}$ by M pixels is defined with respect to $\vec{q}_k$. In order to interpolate the information of both left and right images from the stage k to the stage $k-1$, the distances r_k and angles α_k from every center $\vec{q}_k$ to $\vec{r}_{\text{grid},k-1}(\alpha, r)$ should be computed, thus defining a new grid $\vec{r}_{\text{grid},k-1}(\alpha_k, r_k)$.

As depicted in Figure 4.4(a), the distances r_k and angles α_k can be computed with the law of cosines, as follows

$$r_k = \sqrt{r_{k-1}^2 + d^2 - 2 \cdot r_{k-1} \cdot d \cdot \cos(\pi - \alpha_{k-1})}, \tag{4.3}$$

and

$$\alpha_k = \cos^{-1}\left(\frac{r_k^2 + d^2 - r_{k-1}^2}{2 \cdot r_k \cdot d}\right), \tag{4.4}$$

where d is the distance from $\vec{q}_k$ to $\vec{q}_{k-1}$. This interpolation is described for a single stage and a single subaperture, nevertheless it should be accomplished in a similar way for all k stages.
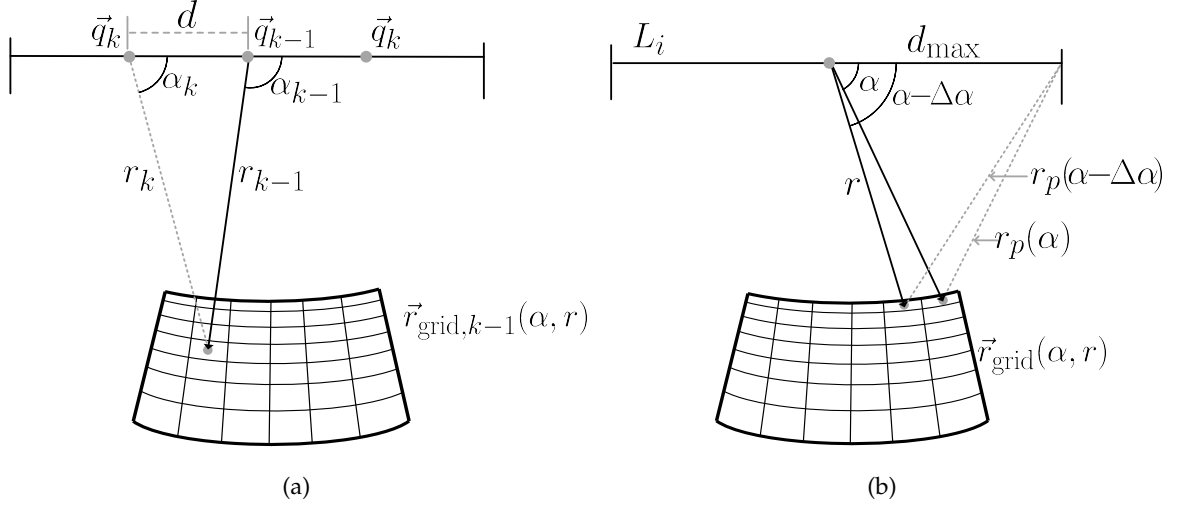
Figure 4.4: (a) Polar-to-polar interpolation (P2P) from the small subaperture k with center $\vec{q}_k$ to the bigger subaperture $k-1$ with center $\vec{q}_{k-1}$. (b) Geometry considered to estimate the sampling requirements. This is based on the range difference between two neighbouring pixels, namely (α, r) and $(\alpha - \Delta\alpha, r)$, in the angular direction. L_i indicates the number of pulses of a given subaperture at the stage i, d_{max} is the distance from the center of the subaperture to one of its ends.

The last step is the definition of a global cartesian grid $\vec{r}_{grid}(x, r)$, where the information of the images in polar grids will be merged through a P2C interpolation to form the final image. Provided $k - 1$ as the last stage of the FFBP for exemplification, the P2C can be performed as

$$r_{k-1} = \sqrt{x^2 + r^2}, \tag{4.5}$$

and

$$\alpha_{k-1} = \pi - \tan^{-1}\left(\frac{r}{x}\right). \tag{4.6}$$

Moreover, the sampling requirements in the radial and angular dimensions are defined according to the Nyquist criterion [Ulan 03, Rodr 11]. In the radial direction, the sampling Δr should be equal or lower than the range resolution given by (2.5)

$$\Delta r \leq \frac{c}{2 \cdot BW} = \delta r. \tag{4.7}$$

On the other hand, the sampling factor in the angular direction is computed through the distance between two contiguous samples, $\Delta r_p = r_p(\alpha + \triangle\alpha) - r_p(\alpha)$. This distance has to be taken from the minimum range, r_{min}, and the minimum angle, α_{min}, of the polar grid $\vec{r}_{grid}(\alpha, r)$, since it is considered the worst case to avoid aliasing in the angular dimension. To that end, the expression of Δr_p is given by

$$\Delta r_p = r_p(\alpha_{min} + \triangle\alpha) - r_p(\alpha_{min}) \approx \frac{r_p^2(\alpha_{min} + \triangle\alpha) - r_p^2(\alpha_{min})}{2 \cdot r_p(\alpha_{min})} \leq \Delta r. \tag{4.8}$$

Subsequently, the requirement for the angular sampling in terms of cosines is defined as follows

$$\Delta\cos(\alpha) \leq \Delta r \cdot \left[\frac{r_p(\alpha_{min})}{r_{min} \cdot d_{max}}\right], \tag{4.9}$$
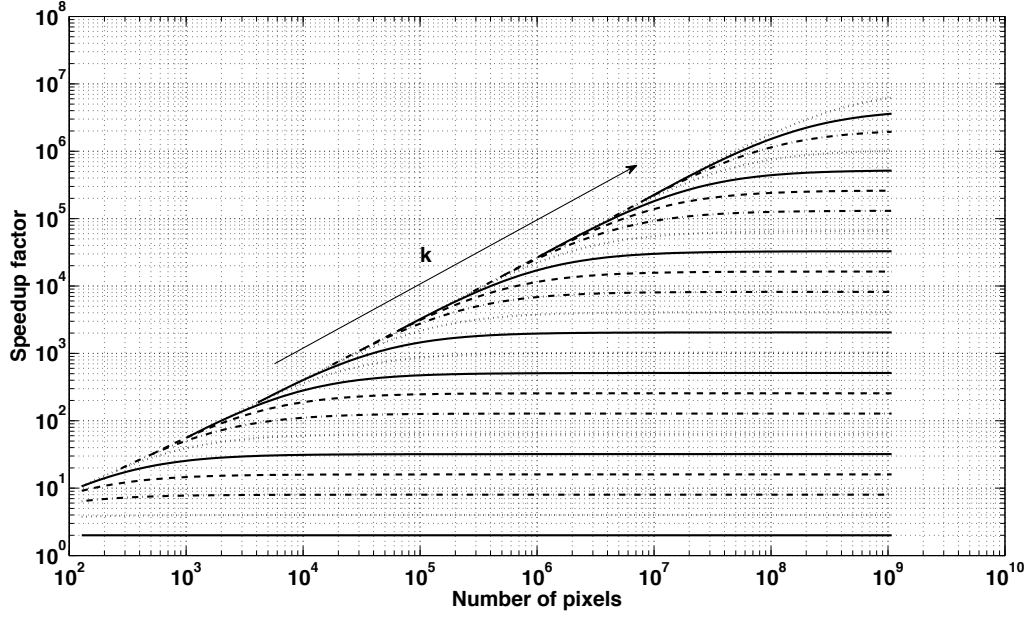
Figure 4.5: Performance of the FFBP for linear SAR modes given by (4.10), which takes the DBP as reference. The number of pixels considers different sizes of the imaging grid, and k is the number of stages of the FFBP. Note that the speedup factor improves as the number of stages and the number of pixels increase.

where $r_p(\alpha_{\min}) = \sqrt{r_{\min}^2 + d_{\max}^2 - 2 \cdot r_{\min} \cdot d_{\max} \cdot \cos(\alpha_{\min})}$ with $d_{\max}$ as the distance from the center of the subaperture to one of its ends (see Figure 4.4(b)). Correspondingly, it can be seen that (4.9) depends directly on the size of the subaperture, thereby improving the savings in number of operations with respect to the DBP, $O(DBP)/O(FFBP)$, significantly for small-sized subapertures. In fact, the speedup factor is given by

$$\frac{O(DBP)}{O(FFBP)} = \frac{L_{\text{full}} \cdot N \cdot M}{\left(\frac{L_{\text{full}}}{2^k} + 2k - 2\right) \cdot N \cdot M} = \frac{L_{\text{full}}}{2 \cdot \log_2(L_{\text{full}}/2)}, \tag{4.10}$$

assuming a minimum subaperture size of $L_{\min} = 2$ and $L_{\text{full}} = M = N$ [Ulan 03]. Figure 4.5 shows the performance of the FFBP for different pixel sizes and for several number of stages. It can be seen that the speedup factor improves as the number of stages increase. Conversely, the computational burden tend to a limit for an increasing number of pixels and a constant number of stages.

4.2 FFBP for circular trajectories

In order to adapt the basic theory of the FFBP algorithm for linear SAR modes to circular trajectories, two main issues have to be considered. First, a linear-like flight track in the cross-range direction can no longer be assumed. Second, the high spatial resolution in CSAR increases the computational burden of DBP with respect to the FFBP in comparison to stripmap. As depicted in Figure 4.6, the DBP back-projects each echo to the output Cartesian grids $\vec{r}_{\text{grid,s}}(x, r)$ and $\vec{r}_{\text{grid,c}}(x, y, z)$ for stripmap and CSAR, respectively (see Section 3.5.2). Interestingly, $\vec{r}_{\text{grid,s}}(x, r)$ has a much coarser resolution than the CSAR grid, and as aforementioned, the computational burden of the DBP increases exponentially with the number of output samples, while FFBP

only in a logarithmic fashion. Consequently, the FFBP will be more efficient when applied to CSAR data than with stripmap data.
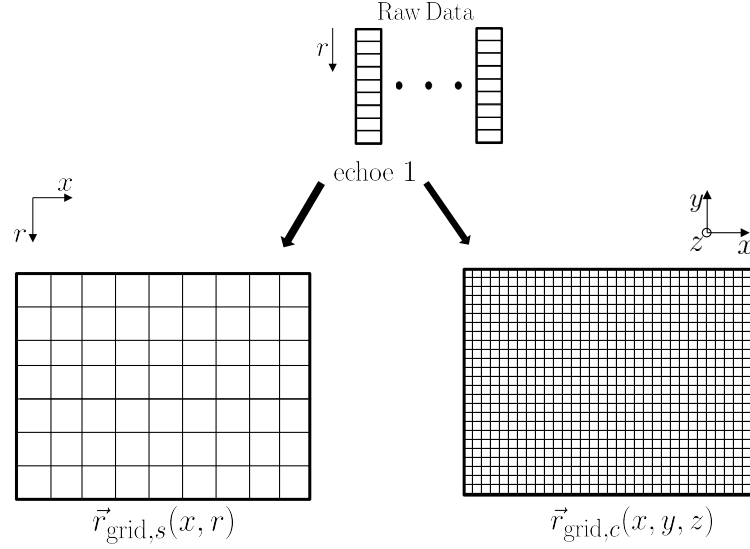
Figure 4.6: Back-projected energy from an echo to the output Cartesian grids $\vec{r}_{\text{grid,s}}(x, r)$ and $\vec{r}_{\text{grid,c}}(x, y, z)$ for stripmap and CSAR, respectively. Note that the CSAR grid has far more samples, which makes the speedup factor higher than with stripmap SAR when compared to the FFBP.

4.2.1 Geometry

The geometry of CSAR for the FFBP algorithm is able to consider a non-ideal circular trajectory illuminating the same spot region over $360°$ and taking also into account the topographic information of the individual targets. Let us define a global Cartesian coordinate system $\vec{r}_{\text{grid,c}}(x, y, z)$ with origin at $(0, 0, 0)$ that will be used as reference to obtain the final image. In the CSAR mode, for each subaperture a polar coordinate system $\vec{r}_{\text{grid}}(\alpha, r)$, tangent to the circumference, is translated to the center of each subaperture and rotated $\beta = tan^{-1}(x/(-y))$ degrees with respect to $\vec{r}_{\text{grid,c}}(x, y, z)$. Consequently, the circumference can be seen as a polygon of $L_{\text{full}}/L_{\text{max}}$ equal sides, with L_{max} as the length of the biggest subaperture where the polar grids are defined (see Figure 4.7(a)).

4.2.2 Methodology

Similar to the FFBP algorithm for linear SAR modes, this process is divided in four parts: factorisation of the full synthetic aperture, performance of the BP in polar coordinates, P2P and P2C interpolations. However, there are some differences that will be pointed out in the remaining part of this subsection. Figure 4.8 summarises the algorithm in a block diagram.

The difference in the factorisation is that L_{full} is partitioned in equal segments of $L_i = L_{\text{max}}$ pulses. Subsequently, L_i is partitioned recursively k times or stages by a factor $n = 2$, until n^k sub-apertures of $L_k = L_{\text{min}}$ size are reached.
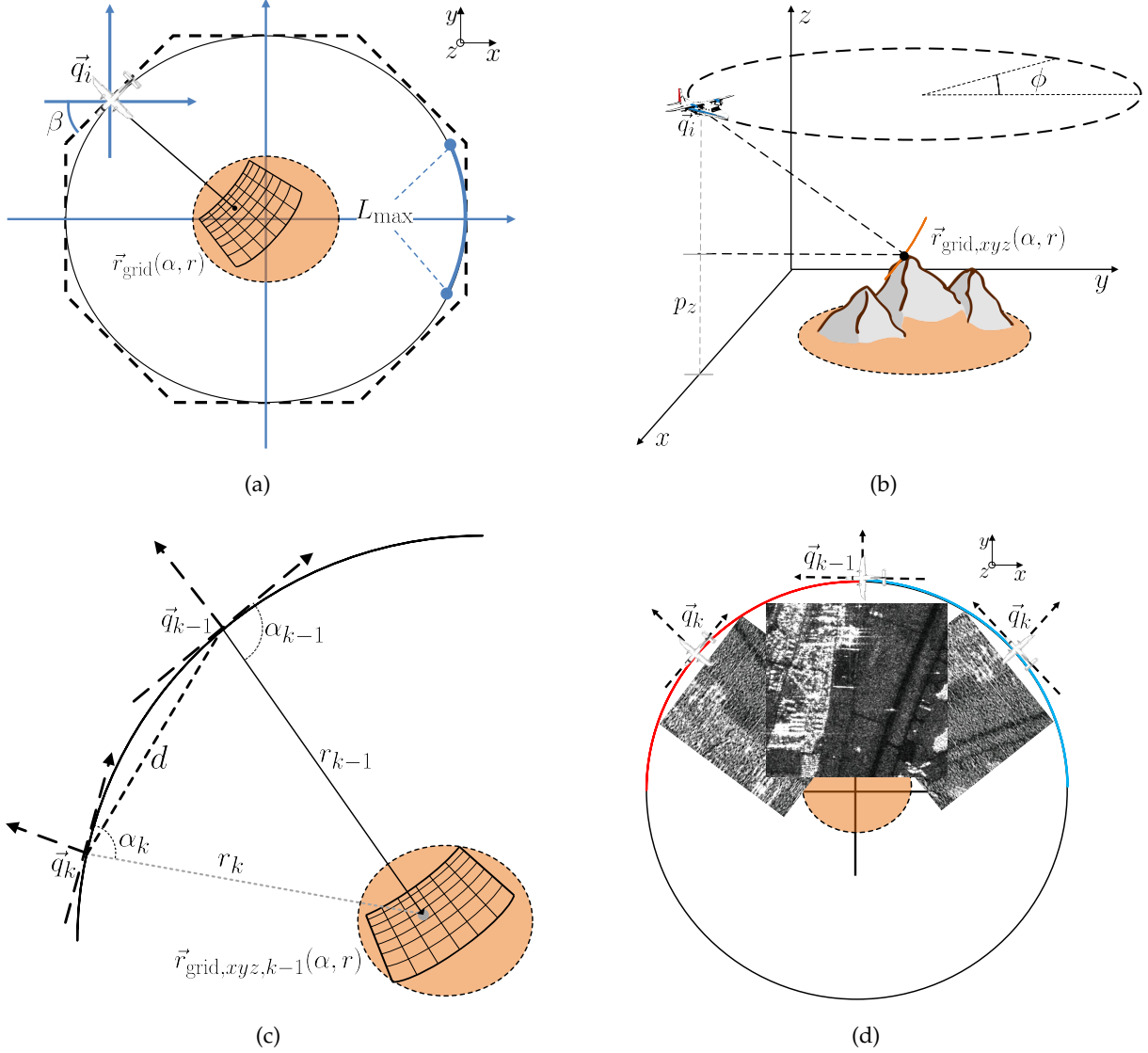
Figure 4.7: FFBP geometry for circular acquisitions. (a) Top view: polar coordinate systems $\vec{r}_{\text{grid}}(\alpha, r)$ have to be defined with respect to the tangent of every subaperture, i.e., they are translated to the subaperture center $\vec{q}_i$ and rotated β degrees with respect to the global Cartesian system. Δarc is the half of the size of the biggest subaperture L_{max} in meters. (b) 3-D view: the FFBP considers the real trajectory of the platform, $\vec{R}(\phi)$, and the topography of the scene, where p_z the height of the scatterer $\vec{p}$. (c) Zoom-in image of the top view: considered geometry to perform P2P interpolations, in this case from a small subaperture to a bigger subaperture at the k and $k-1$ stages. (d) Transition of two contiguous images through P2P interpolations. The information of both subapertures at the processing stage k are merged to form the image of the subaperture at the $k-1$ stage.

In the case of the polar BP, the local polar grids $\vec{r}_{\text{grid},k}(\alpha, r)$ have to be projected on ground and converted to a cartesian grid in order to take into account the topographic information. To that end, a linear translation and a rotation are needed

$$\vec{r}_{\text{grid},xyz}(\alpha, r) = \begin{bmatrix} \cos(\beta) & -\sin(\beta) \\ \sin(\beta) & \cos(\beta) \end{bmatrix} \vec{r}_{\text{grid}}(\alpha, r) + \vec{q}, \tag{4.11}$$

as depicted in Figure 4.7(b). That is to say that a polar grid $\vec{r}_{\text{grid},xyz}(\alpha, r)$ has to be computed

for every $L_i k$ subaperture with center $\vec{q}_i$, and at every stage. In this way, $\vec{r}_{\text{grid},xyz}(\alpha, r)$ (regular in (α, r)) can be now used to back-project the energy of every single echo. At this stage, the 2-D antenna pattern is projected into this grid to perform the radiometric calibration. As a result, 2^k coarse images of $(N/2^k) \cdot M$ pixels are focused, with N and M as the number of pixels in angular and range direction, respectively.

Afterward, every two contiguous coarse images of every stage i are used to form higher resolution images recursively through P2P interpolations. At this point, it must be mentioned that the law of cosines cannot be used as described in Section 4.1 as a result of the curved track. In fact, this can be better seen in Figure 4.7(c), since the polar grid $\vec{r}_{\text{grid},xyz,k-1}(\alpha, r)$ of $(N/2^{k-1})$ by M pixels is not defined with respect to the segment d, but with respect to the tangent of the center $\vec{q}_{k-1}$. In view of this fact, the distances r_k and angles α_k have to be computed by knowing $\vec{r}_{\text{grid},xyz,k-1}(\alpha, r)$ and $\vec{q}_k$ through the dot product $(\vec{A} \cdot \vec{B} = |AB| \cdot \cos(\alpha))$. This method is shown for one sub-aperture for simplicity, but it has to be implemented for every second subaperture in the same way.

Let us denote $\vec{s}_k = (\cos(\beta), \sin(\beta))$ as the unitary vector respective to the center $\vec{q}_k$, and $(\vec{r}_{\text{grid},xyz,k-1}(\alpha, r) - \vec{q}_k)$ as the second vector. With these two inputs, it is possible to get r_k and α_k, as follows

$$r_k = | \vec{r}_{\text{grid},xyz,k-1}(\alpha, r) - \vec{q}_k |, \tag{4.12}$$

and

$$\alpha_k = \cos^{-1}\left(\frac{(\vec{r}_{\text{grid},xyz,k-1}(\alpha, r) - \vec{q}_k) \cdot \vec{s}_k}{r_k} \right). \tag{4.13}$$

In this way, having the coordinates $\vec{r}_{\text{grid},xyz,k-1}(\alpha_k, r_k)$ to interpolate an image of $(N/2^{k-1}) \cdot M$. Afterward, the retrieved images have to be added coherently to enhance the resolution in the angular direction and proceed with the next stage. Figure 4.7(d) depicts the P2P interpolation from two contiguous coarse images of the stage k to a finer resolution image in the stage $k - 1$.

Finally, P2C interpolations are implemented in the same way as P2P, but instead of using $\vec{r}_{\text{grid},xyz,k-1}(\alpha, r)$, the final grid $\vec{r}_{\text{grid},c}(x, y, z)$ of P by P pixels and regular in cartesian coordinates is used.

4.2.3 Sampling requirements

The derivation of the sampling rates is done in a similar way as in Section 4.1, but taking into account the curvature of the synthetic aperture. To that end, let us denote the range difference of two consecutive samples of the image in the angular direction as given by (4.8). In addition, it is known that the resolution in the radial direction δr depends only on the system bandwidth, thus resulting in a wrapped spectrum as the subaperture size increases. In order to account for this folding and avoid any aliasing during P2P and P2C interpolations, one solution could be to leave δr as it is and unwrap the spectrum by multiplying the image by an exponential factor in the time-domain. Contrarily, the second solution could be to redefined δr as follows

$$\delta r = \frac{\pi}{k_{\max} - k_{\min} \cdot \cos\left(\frac{\Delta arc}{|\vec{R}_{xy}|}\right)}, \tag{4.14}$$
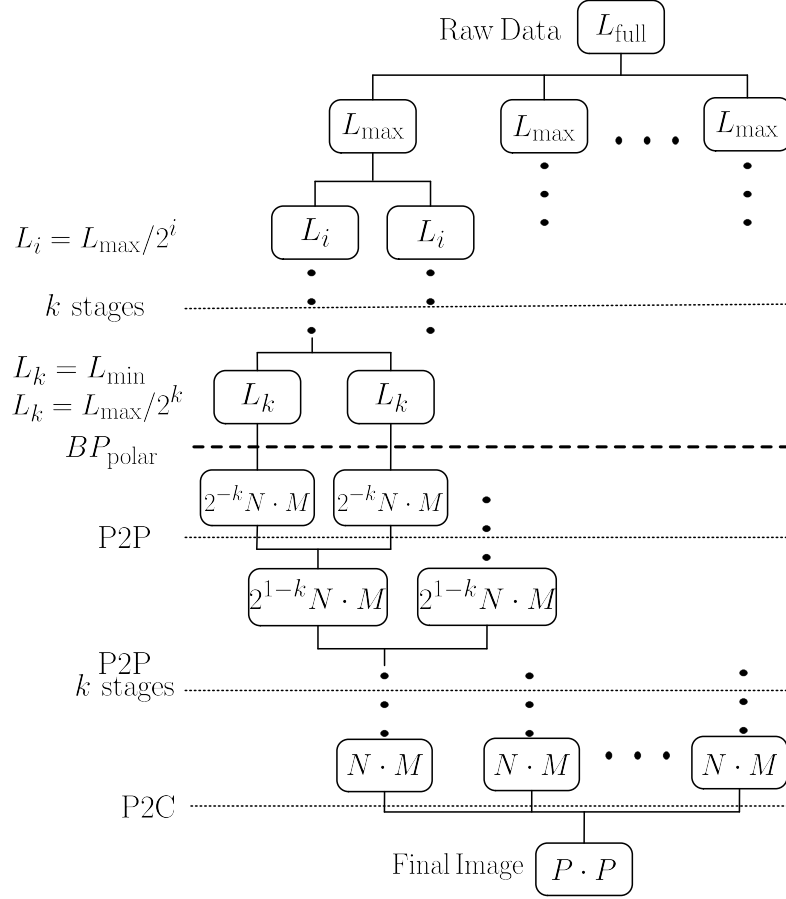
Figure 4.8: Block diagram of the FFBP algorithm for circular SAR (CSAR) for $n = 2$. It starts with the raw data as the input of the system, which is divided in sub-apertures by recursively k stages until $L_i = L_{\min}$. Then the BP in polar coordinates is performed for the smallest sub-apertures. It is followed by the mergence of every two-by-two contiguous images through a P2P interpolation k stages. The last step is the coherent addition of interpolated images from polar to a global Cartesian grid, i.e., P2C interpolations. N and M are the number of pixels in angular and range directions.

with $| \vec{R}_{xy} |$ as the radius of the circular track and Δarc as the size of the arc in meters from the center of the subaperture to one of its ends, since it is considered the worst case. Subsequently, the angular sampling in terms of $\cos(\alpha)$, and deduced from (4.8) is defined as

$$\Delta \cos(\alpha) \leq \Delta r \cdot \left[\frac{r_p(\alpha_{\min})}{r_{\min} \cdot \Delta\text{arc}} \right], \tag{4.15}$$

where $r_p(\alpha_{\min}) = \sqrt{r_{\min}^2 + \Delta\text{arc}^2 - 2 \cdot r_{\min} \cdot \Delta\text{arc} \cdot \cos(\alpha_{\min})}$. This approximation considers the length and the curvature of the subaperture, which indicates a resolution improvement not only in the angular direction, but also in the radial direction, δr, as the spectrum starts to curve (see Section 5.2).

Notably, this enhancement in resolution causes an increment in the sampling requirements in both directions. Therefore, it is not worth to keep interpolating polar grids until L_{full} is reached, and the step to Cartesian coordinates should be performed at $L_{\max}$. In other words, the total number of pixels in the polar grid $\vec{r}_{\text{grid}}(\alpha, r)$ will be in the same order of magnitude as the final Cartesian grid $\vec{r}_{\text{grid,c}}(x, y, z)$. This fact only implies a linear decrease of the computational

efficiency because images of large dimensions (in meters) can be processed.

The selection of L_{max} depends on the configuration of each experiment, i.e., the number of total pulses L_{full}, on the range (4.14) and angular (4.15) resolutions, oversampling factors and interpolation kernels, so that a numerical evaluation of the number of operations should give the most appropriate value. In Chapter 5, this will be analysed with simulated and real data. In fact, a L_{max} value corresponding to an aperture of $45\,°$ was selected as a good compromise.

4.2.4 Computational burden

The estimation of the computational burden in CSAR, unlike the FFBP for linear SAR modes, takes into account the cartesian output grid of P by P samples at the maximum resolution given by $\frac{\lambda_{\mathrm{c}}}{4\cdot\sin(\theta_{\mathrm{el}})}$, as well as the interpolation kernels used to compute polar grids assuming either a constant height or given a digital elevation model (DEM). The number of required operations to focus a CSAR image at full resolution can be defined as

$$O(DBP) \approx L_{\mathrm{full}} \cdot P^2 \tag{4.16}$$

and

$$O(FFBP) \approx O(BP) + O(P2P) + O(P2C) + O(grid) \tag{4.17}$$

for the DBP and the FFBP, respectively, where

$$O(BP) \approx \frac{L_{\mathrm{max}}}{2^k} \cdot \frac{N}{2^k} \cdot M \cdot 2^k \cdot \frac{L_{\mathrm{full}}}{L_{\mathrm{max}}}, \tag{4.18}$$

$$O(P2P) \approx \left(2 \cdot \frac{N}{2^{k-1}} \cdot M \cdot 2^{k-1} \right) \cdot (k-1) \cdot \frac{L_{\mathrm{full}}}{L_{\mathrm{max}}}, \tag{4.19}$$

$$O(P2C) \approx P^2 \cdot \frac{L_{\mathrm{full}}}{L_{\mathrm{max}}}, \tag{4.20}$$

$$O(grid) \approx \left(\frac{N}{2^k} \cdot M \cdot 2^k \right) \cdot k \cdot \frac{L_{\mathrm{full}}}{L_{\mathrm{max}}}, \tag{4.21}$$

N and M are the number of pixels in angular and range directions, and $k = \log_2(\frac{L_{\mathrm{max}}}{L_{\mathrm{min}}})$. Simplifying (4.16) and (4.17), the speedup factor can be described as

$$\frac{O(DBP)}{O(FFBP)} \approx \frac{L_{\mathrm{full}} \cdot P^2}{N \cdot M \cdot (\frac{L_{\mathrm{max}}}{2^k} - 2 + 3k) \cdot \frac{L_{\mathrm{full}}}{L_{\mathrm{max}}} + P^2 \cdot \frac{L_{\mathrm{full}}}{L_{\mathrm{max}}}}. \tag{4.22}$$

Thus, since the denominator is split into two additions, i.e., $P^2 > (N \cdot M \cdot (\cdot))$, and $L_{\mathrm{full}} > \frac{L_{\mathrm{full}}}{L_{\mathrm{max}}}$, the performance of the FFBP for CSAR increases much more than using the FFBP for linear SAR modes. In fact, nearest neighbour interpolations were considered in this analysis for simplicity.

Figure 4.9 shows the speedup factor of (4.22) in a logarithmic scale. It considers the ratio $\frac{P}{M} = \frac{\delta r}{\delta y}$ and $N = L_{\mathrm{max}}$, with δy defined for the maximum theoretical resolution of $\vec{r}_{\mathrm{grid,c}}(x,y,z)$. Correspondingly, it can be inferred that as the number of stages increases, a logarithmic curve is formed, showing the improvement of the speedup factor as the matrix size increases. In fact, there is a trade-off for a better speedup factor between the number of stages k and the size of the grid $\vec{r}_{\mathrm{grid,c}}(x,y,z)$ of P^2 pixels, since not always it is worth to increase the size of L_{max}.
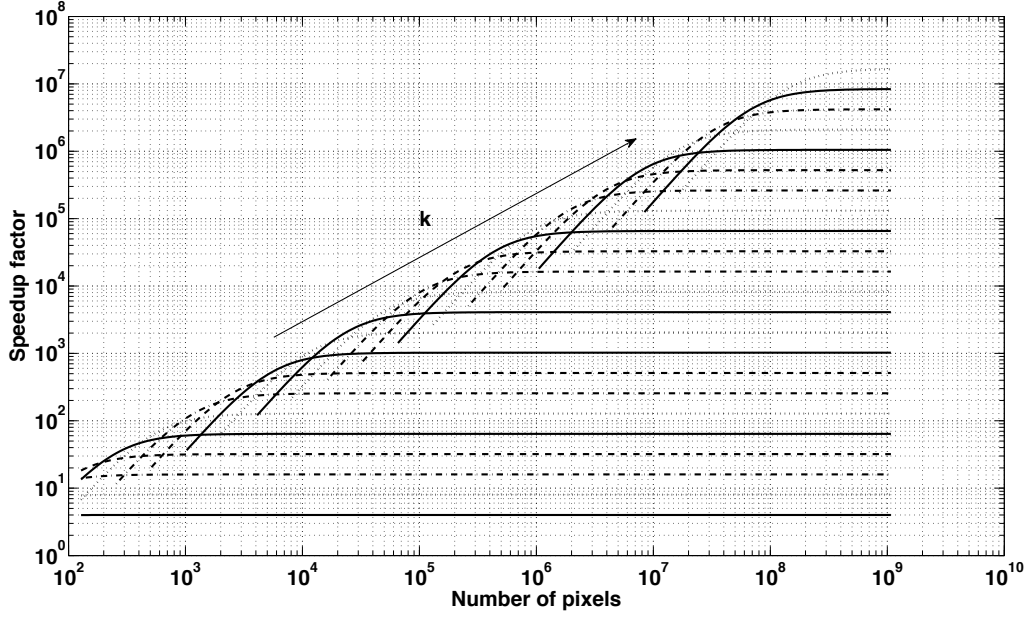
Figure 4.9: Performance of the FFBP algorithm adapted to circular flights compared to the DBP. The number of pixels considers different sizes of the imaging grid $\vec{r}_{\text{grid,c}}(x, y, z)$. k is the number of stages of the FFBP.

4.2.5 Assessment with simulated data

In order give a better insight about the performance of the FFBP for circular trajectories, a data acquisition was simulated with a non-ideal circular pass of ~ 4400 m radius at ~ 4200 m height, $\lambda_c = 0.24$ m and a flat terrain of 700 m. These parameters are also summarised in Table A.2. The DBP was taken as a reference to assess the accuracy and speed of the FFBP. Figure 4.10(a) depicts the comparison between the IRF of CSAR focused with DBP (black-solid) and FFBP (red-dotted), and Figure 4.10(b) its 2-D representation. Note that the focused IRF has a resolution of ~ 0.084 m and a PSLR in the order of -8 dB, which is in accordance with the theoretical investigations shown in Section 3.1. Certainly, the FFBP achieved the expected performance both in terms of resolution and PSLR.

The FFBP will be further assessed in Chapter 5 with the first experimental CSAR collection at L-band, and its implementation with parallel computing on a graphics processing unit (GPU). In fact, the FFBP for circular acquisitions, as one of the main contributions, was indispensable for the accomplishment of this thesis.

4.2.6 Practical implementation

Another important aspect that should be discussed, is the practical implementation of the FFBP. As aforementioned, the most convenient solution is to program the FFBP recursively (Figure 4.11). As a result, the range-compressed data is partitioned several times until L_{sub} reaches the minimum subaperture size. In every stage, the output is either an image in polar coordinates or an image in cartesian coordinates. Note that the full-resolution grid in cartesian coordinates is only computed once, whereas the coarse polar grids have to be computed every time the
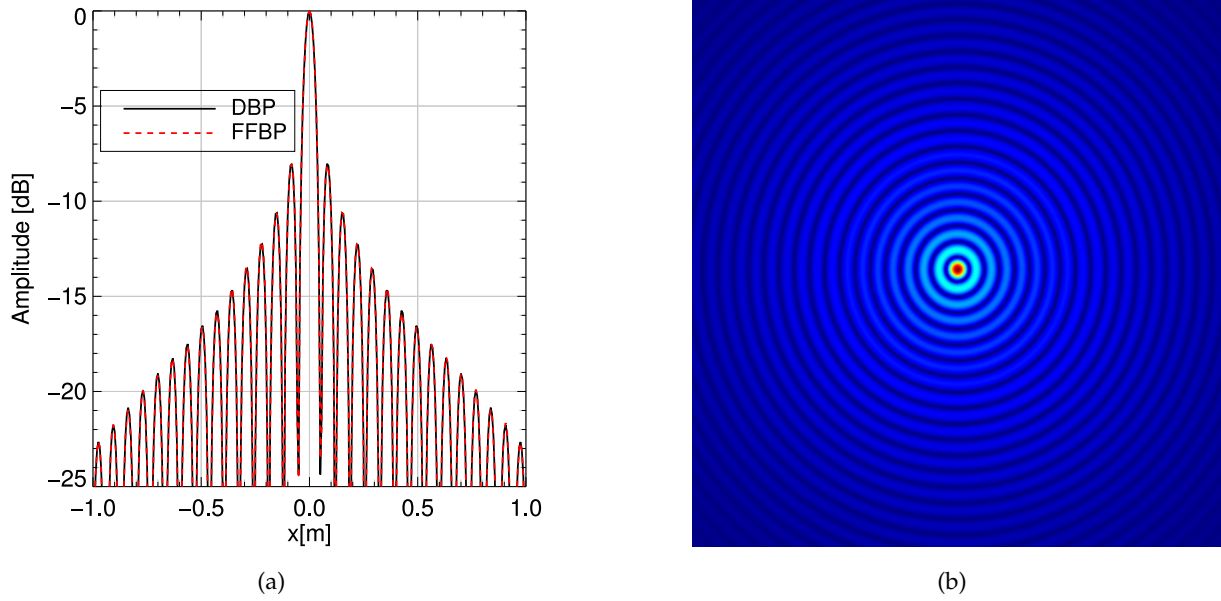
Figure 4.10: Impulse response function (IRF) focused with DBP and FFBP algorithms. (a) 1-D profile, DBP vs FFBP. (b) 2-D IRF, 2 m x 2 m image size, 0.06 m x 0.06 m sampling.

module *Recursivity* is called.

In order to speed up the processing, the main bottle necks should be parallelised. These are mainly the interpolations in the polar BP, as well as in the P2P and P2C steps. In this regard, there is a trade-off between accuracy and processing time depending on the selected interpolation kernel. Usually, cubic or linear interpolations are fast but they do not achieve a good accuracy. As an alternative, the data can be zero padded before using them, but at the cost of high computational burden. Another solution would be to use the sinc kernel or the base-band adaptive sinc kernel, indicated in this work as the Knab pulse. Both kernels offer high accuracy for base-band signals and they do not need zero-padded data [Knab 79]. In addition, the computation of the imaging grids in polar coordinates can also be parallelised to improve the speedup factor, since they are computed for every subaperture.

To sum up, in this Chapter differences of the FFBP for circular and linear tracks, as well as the performance and limitations of the new FFBP, were discussed. Particularly, the following aspects have to be taken into account when focusing circular trajectories:

- The theoretical resolution and the sampling criteria to define the final grid $\vec{r}_{\mathrm{grid,c}}(x, y, z)$ in global Cartesian coordinates at the highest resolution, makes the speedup factor higher than in the stripmap SAR case.

- L_{full} and L_{max} have to be defined and considered for the processing since P2P interpolations are not performed for the full circle.

- In order to perform the interpolations of the polar BP, P2P and P2C, the curvature of the circular track has to be taken into account as described in Section 4.2.2.

- The curvature of the circular track has to be also considered in the definition of the sampling criteria, as described in Section 4.2.3. In addition, oversampling, interpolator ker-
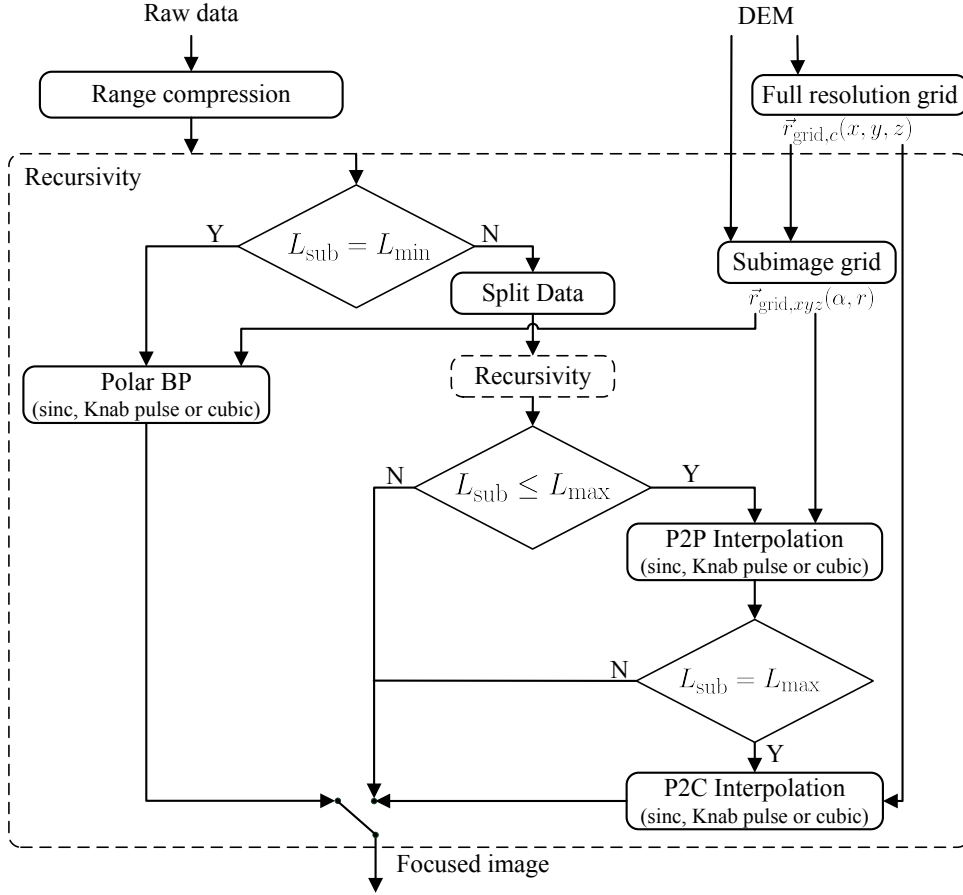
Figure 4.11: Practical implementation of the FFBP algorithm for circular trajectories. Note that the digital elevation model (DEM) is considered for the definition of every polar grid, $\vec{r}_{\text{grid},xyz}(\alpha,r)$. Similarly, interpolation kernels (e.g., sinc, Knab pulse or cubic) are used from the smallest subaperture image in the Polar BP, as well as in the P2P and P2C stages.

nels and the used hardware are key factors for the performance (accuracy and speedup factor) of the FFBP.

5 Fully Polarimetric High-Resolution 3-D Imaging with Circular SAR

This chapter is devoted to the analysis and understanding of the first fully polarimetric circular SAR (CSAR) acquisition at L-band over a scene with highly-directive, isotropic-like and particularly distributed targets. This data collection is dedicated to demonstrate the first fully polarimetric high-resolution images, particularly, of man-made targets (i.e., buildings, light poles, hangars, shelters and fences), of isotropic-like targets (i.e., Luneburg lens), and more importantly of natural scatterers (i.e., trees, forest, fields and ground). Additionally, this dataset allowed the first demonstration of 3-D imaging with CSAR of isotropic-like targets, and semi-transparent media[1]. Another aspect of high interest is the comparison of coherent and incoherent imaging approaches of the full synthetic aperture for distributed, highly-directive and isotropic-like targets, thus assessing advantages and disadvantages of each of both approaches. Furthermore, this campaign is also used to validate the time-domain FFBP algorithm for circular trajectories for small-sized and large-sized images. The FFBP for circular tracks offers computational-efficient and accurate processing for non-ideal tracks. Finally, the signature of a Luneburg lens was used to estimate residual motion errors with a frequency-based autofocus approach for CSAR configurations based on low SCR isotropic scatterers.

Parts of this chapter have been published in [Ponc 14a].

5.1 Circular L-band campaign

The data collection was performed in 2008 by the DLR's E-SAR airborne system at L-band (1.3 GHz) over the airport of Kaufbeuren, Germany (see Section A.1) [Pinh 09, Ponc 14a]. The resolution in the range direction was about $\delta_\mathrm{r} = 1.5$ m, considering a system bandwidth of 94 MHz. Moreover, the profile of the circular flight is shown in Figure 5.1(a), and an overview of the aircraft attitude parameters is given in Figures 5.1(b)-5.1(d).

The flight configuration was chosen according to the antenna patterns, the constraints of the flight manoeuvres, and the size of the desired test area. Regarding the antenna patterns, the main limitations were given by the fixed beam with depression angle of $30\,^\circ$ and the 3 dB angular aperture in both directions, azimuth and elevation (see Figure 5.2). As a consequence,

---

[1]Semi-transparent media refers to objects that can be penetrated by microwaves, e.g., forested areas, ice and dry soils. Throughout this thesis forested areas are studied.

(a)

(b)

(c)

(d)
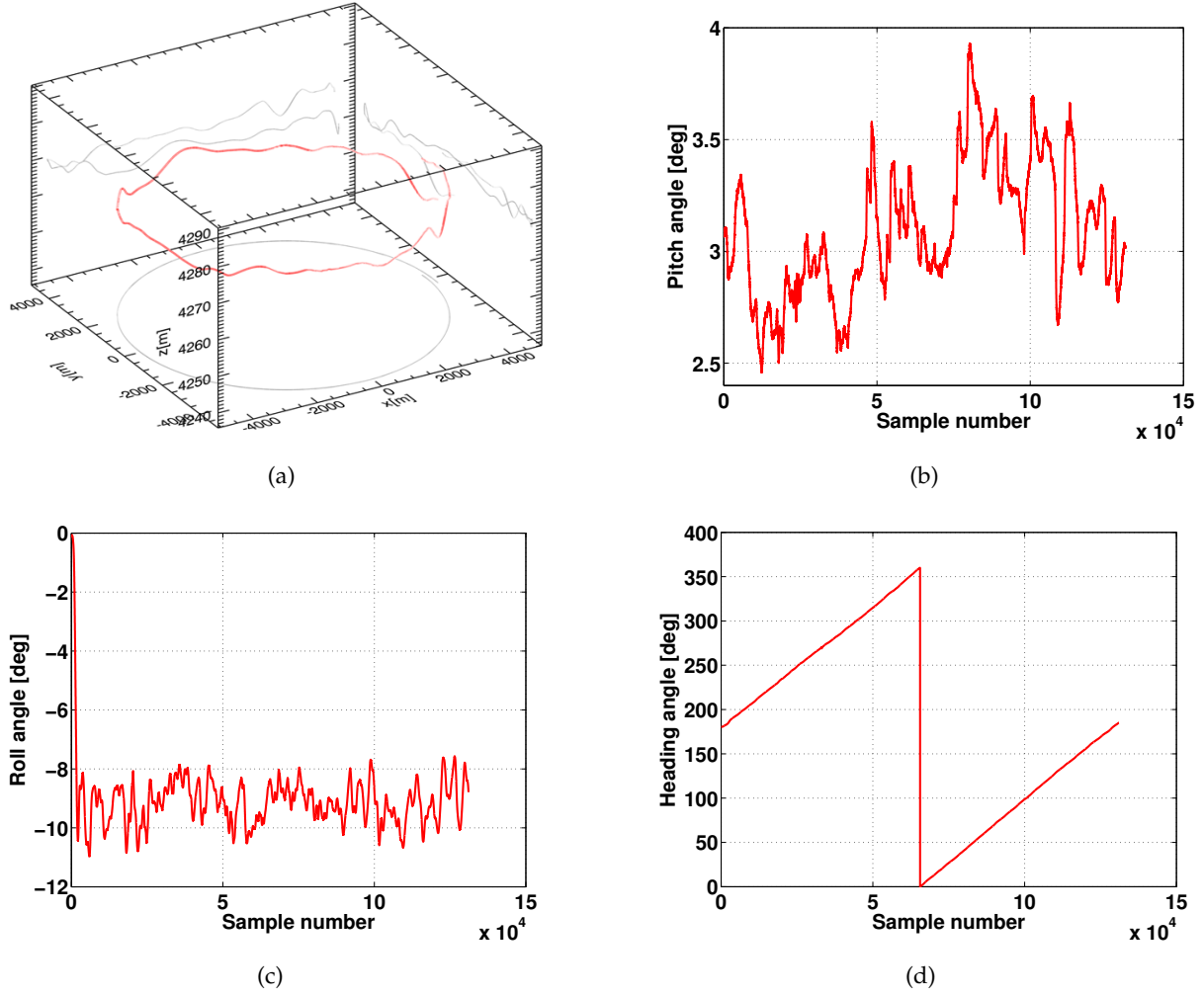
Figure 5.1: (a) 3-D track profile: campaign performed with the DLR's E-SAR sensor at L-band over the airport of Kaufbeuren, Germany in 2008. Mean altitude: 4200 m, mean radius: 4400 m. (b)-(d) Aircraft attitude for the experimental acquisition with a single circular pass. (b) Pitch angle: mean of $3°$. (c) Roll angle: mean of $-9°$. Note that this angle is close to zero for linear SAR acquisitions. (d) Heading angle: oscillates from $0°$ to $360°$ due to the rotation of the platform.

the flight was performed with a radius of 4400 m, a height of 4200 m with a roll angle, i.e., aircraft bank, of $-9°$, thus covering a spotlighted region of around 1.5 km by 1.5 km in the three polarisations, i.e., HH, HV and VV. In order to have a general overview of the experimental realisations used in throughout this thesis, the main parameters of the campaigns are also listed in Table A.2.

5.2 FFBP assessment with real data

It is important to remark that the obtained results, regarding accuracy and processing time, depend directly on the interpolation methods (linear, zero padding + cubic, truncated sinc or Knab pulse), up-sampling factor (in azimuth and range), as well as the used hardware (CPU and/or GPU) [Frol 06].
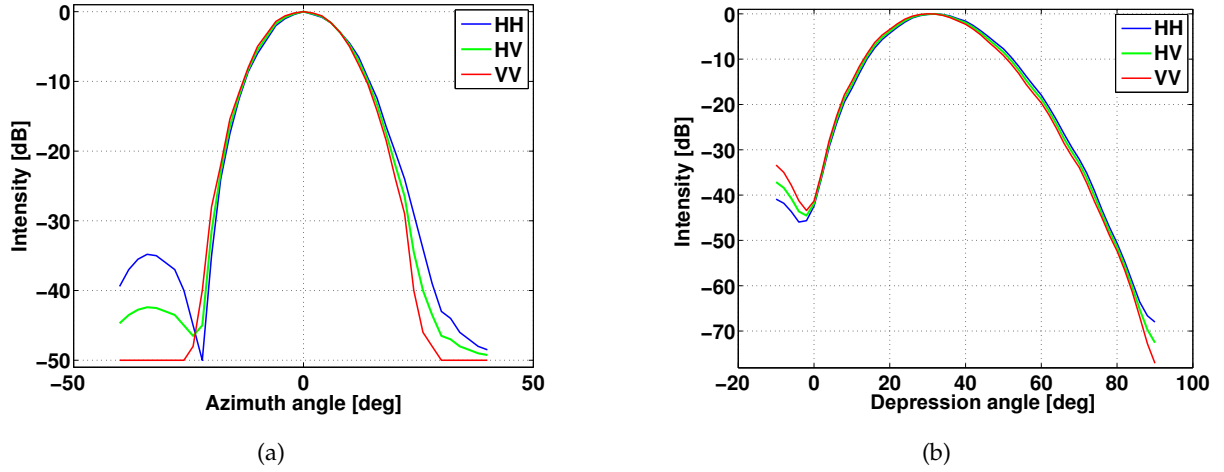
Figure 5.2: 1-D antenna patterns for the circular campaign at L-band. (a) Azimuth pattern with 3 dB width, i.e., angular resolution, of $20°$. (b) Depression pattern with an angular resolution of $28°$. Note that the antenna depression angle is about $30°$.

For this data collection the following interpolation methods were used:

- The polar back-projection (BP) at the stage $i = k$ of the FFBP processing was implemented with 1-D complex interpolations using 1-D FFTs + zero padding (factor 8) + cubic (4 points).

- The polar-to-polar (P2P) and polar-to-cartesian (P2C) interpolations for the following stages were performed with a 2-D truncated Knab pulse of 21 points since it provides high accuracy, it is efficient in terms of computational costs, and it can be adapted to band-limited signals [Knab 79].

- The imaging grids in polar coordinates were computed by 2-D double precision quadratic polynomial interpolation.

An eight-core Intel(R) Xeon(R) CPU of 2.4 GHz with 24 GB RAM, and OS Linux was used, and parallelisation was done using a GPU Tesla C2070 of 1.15 GHz, 2.0 compute capability, 6 GB global memory, and 448 cores [Fabe 09] [Gall 10]. Moreover, real and simulated data were focused with the FFBP using the next parameters: $L_{min} = 256 = 2^8$, $L_{max} = 16384 = 2^{14}$, and $L_{full} = 131072 = 2^{17}$. As described in Section 4.2, the full circular aperture was taken as input, and several output regions of size P by P pixels were processed at the maximum resolution with a sampling of 0.06 m: $P = 400, 800, 1.2K, 1.6K, 2K, 4K, 6K, 12K$ and $25K$.

Figure 5.3 shows the computational performance of the FFBP compared to the direct DBP in a logarithmic scale. Clearly, the speedup factor of the circular FFBP (CPU) improves as the output matrix size increases, obtaining up to ~ 500 times faster than the DBP. Additionally, this algorithm and the DBP were parallelised on the GPU, remaining the same theoretical speedup factor BP/FFBP but further accelerating the process and considering also the constraint of the 6 GB global memory. The computational time of the FFBP (GPU) was improved up to ~ 1800 times, while the DBP (GPU) improved only ~ 100 times. The performance of the GPU was limited by its available RAM memory and by the data throughput because images with large
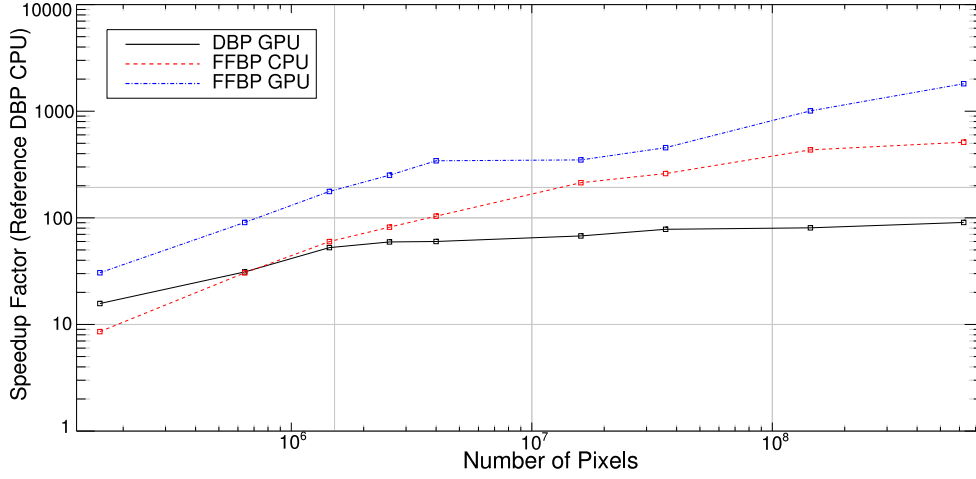
Figure 5.3: Experimentally evaluated speedup performance of fast factorised back-projection (FFBP) adapted to circular flights and compared with the direct back-projection (DBP) using both, CPU's and a graphics processing unit (GPU).

number of pixels have to be divided and processed in smaller blocks. Certainly, the enhancement of the speedup factor is more noticeable in the BP using polar coordinates, as well as in the 2-D interpolation stages. Both represent the main bottle-necks of the FFBP.

Furthermore, the coherence between the focused images with the FFBP and the DBP indicated a good focusing quality with a mean coherence of 0.99991, a standard deviation of the coherence of 0.0004521 and a phase standard deviation of $4.7\,°$. Given the maximum P value, the processing times for each polarimetric channel (HH-VV-HV) with the FFBP on CPU and GPU were ~ 11.2 hours (~ 0.5 days) and ~ 3.1 hours (~ 0.1 days), respectively, while with the DBP on CPU and GPU would have been ~ 5734 hours (~ 238 days) and ~ 63 hours (~ 3 days), respectively. Clearly, the FFBP results in a much more suitable algorithm than the common DBP.

To gain more insight, Figure 5.4 shows the results of the FFBP for circular trajectories for different aperture sizes, i.e., from $1.4\,°$ to $180\,°$ angular integration. Interestingly, the effect of the curvature in the spectrum can be seen as the angular aperture increases. As discussed in Section 4.2, this curvature has to be taken into account during focusing by increasing the sampling requirements in the radial direction, otherwise folding in the spectrum will be presented, thus causing aliasing. Certainly, this requirement becomes more demanding for bigger apertures. In fact, the maximum aperture size, with which P2P interpolations were performed, was $L_{\max} = 2^{14}$ or $45\,°$ for this realisation, as it was found to be a good compromise between the number of operations and the required accuracy.

5.3   Incoherent versus coherent imaging

As aforementioned, one of the main paradigms of focusing images in CSAR mode is whether the acquired data should be focused coherently or incoherently. This section analyses and compares both approaches for different type of targets, particularly distributed scatterers. Figure

| Spectrum. | Amplitude. | Spectrum. | Amplitude. |
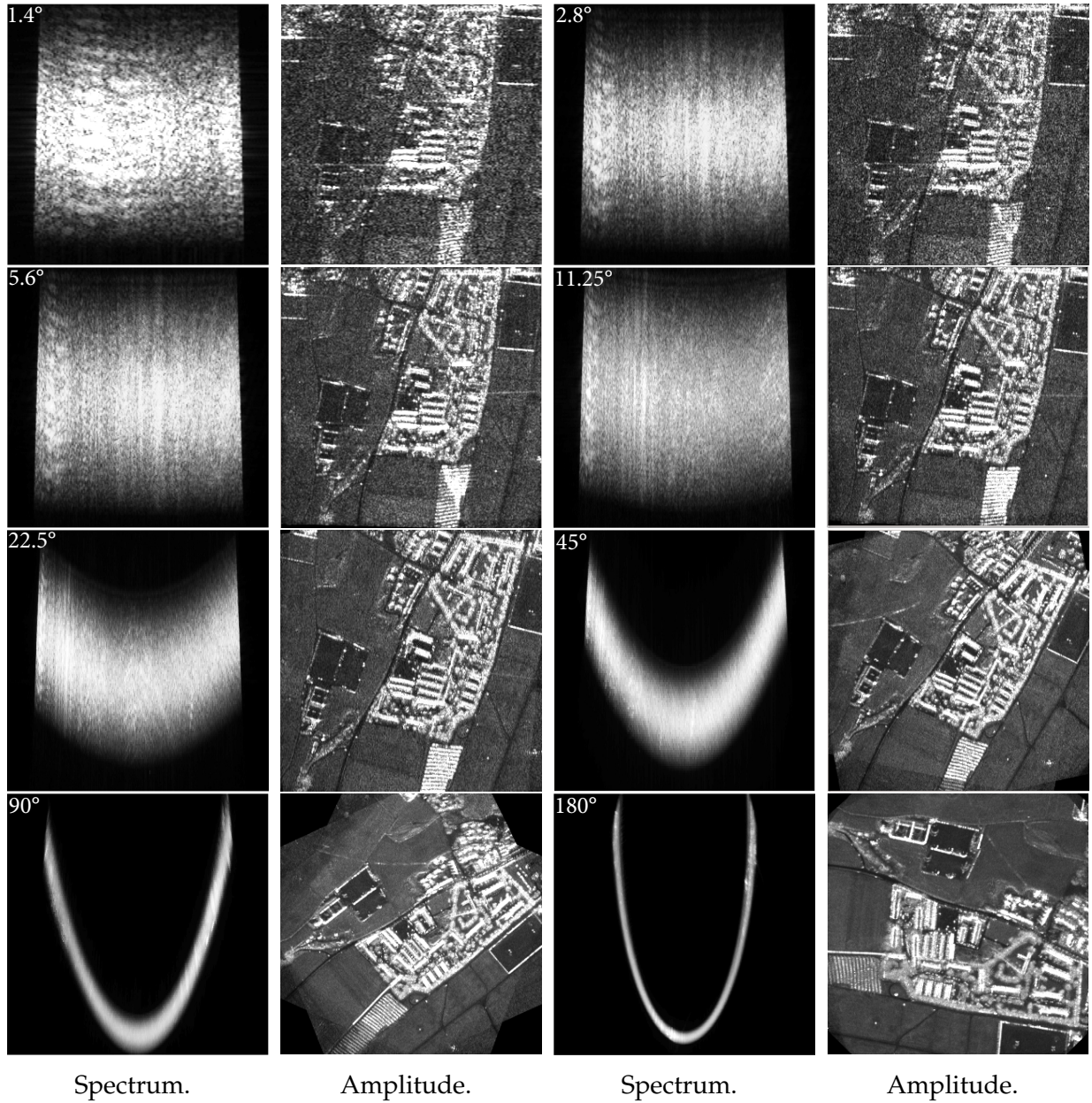
Figure 5.4: Analysis of the spectrum and its corresponding focused images in polar coordinates for the FFBP of circular trajectories with real data. The angular aperture is indicated in the upper-left corner of the spectrum images. The radial and angular dimensions correspond to the vertical and horizontal directions, respectively.

5.5 depicts the first comparison of both solutions with fully-polarimetric images in a global scale covering an area of 1500 m by 1500 m. Both images were focused on the $(x, y, z = h(x, y))$ grid using a DEM and decomposed in the Pauli basis.

Figure 5.5(a) shows a fully-polarimetric image processed by incoherent addition with sampling of 0.5 m by 0.5 m, i.e., first by adding coherently subapertures of $\Delta\phi = 10\,°$ and then merging the intensity of the 36 images incoherently. On the other hand, Figure 5.5(b) shows the solution of processing the CSAR data by coherent imaging over $360\,°$. The sampling criteria was 0.06 m by 0.06 m (25K x 25K pixels) in order to accommodate the theoretical resolution of $\delta_x = \delta_y = 0.084$ m given by (3.23). The basic scattering mechanisms can be clearly observed: double-

(a) Incoherent imaging.   (b) Coherent imaging.

Figure 5.5: Images in the Pauli basis (blue: HH+VV, red: HH-VV, green: 2HV) focused with the fast factorised back-projection (FFBP), 1500 m x 1500 m image size, airport of Kaufbeuren, Germany. (a) Subaperture segments of $\Delta\phi = 10\,°$, 0.5 m x 0.5 m sampling. Red circle indicates the position of the Luneburg lens. (b) 0.06 m x 0.06 m sampling.

bounces (red), such as fences and walls of buildings; single-bounces (blue) like the ground; and volume or distributed scatterers (green) particularly trees, forests and bushes. It is important to mention at this point that the persistence of the strongest signatures in the focused images is assumed.

Generally, the multiple-aspect measurements provide a better physical interpretation of the objects when compared to stripmap SAR. This is a result of the anisotropic behaviour of most of the targets in nature. In fact, this has been object of study in [Ferr 03]. Despite of this fact, incoherent imaging shows that most of the scatterers are not focused at their maximum resolution since their directivity and persistence are unknown. For this reason, the coherent imaging depicts improved resolution for most of the targets, however at the cost of an acceptable increment in the computational burden, since the FFBP is being used. This can be better seen in Figure 5.6, which illustrates close-ups around the middle of Figure 5.5. The upper row shows images focused with the incoherent approach, whereas the lower row with the coherent approach. In the first two columns, it is possible to see that some objects are lost in the resulting incoherent images, whereas in the coherent images they are kept and the SCR is improved. In addition, the ground in the third column looks similar in both images, however the signature of the figure processed coherently is sharper. Lastly, the last column shows a building, where the improvement is evident for the coherent case, since building signatures like walls, roofs and fences can be better observed, i.e., they are focused at their maximum resolution. Furthermore, some of the targets are out of focus since not all of them are located at the height given by the DEM, particularly for those that provide volumetric information, i.e., semi-transparent media. In fact, this will be deeply discussed in the following subsections.
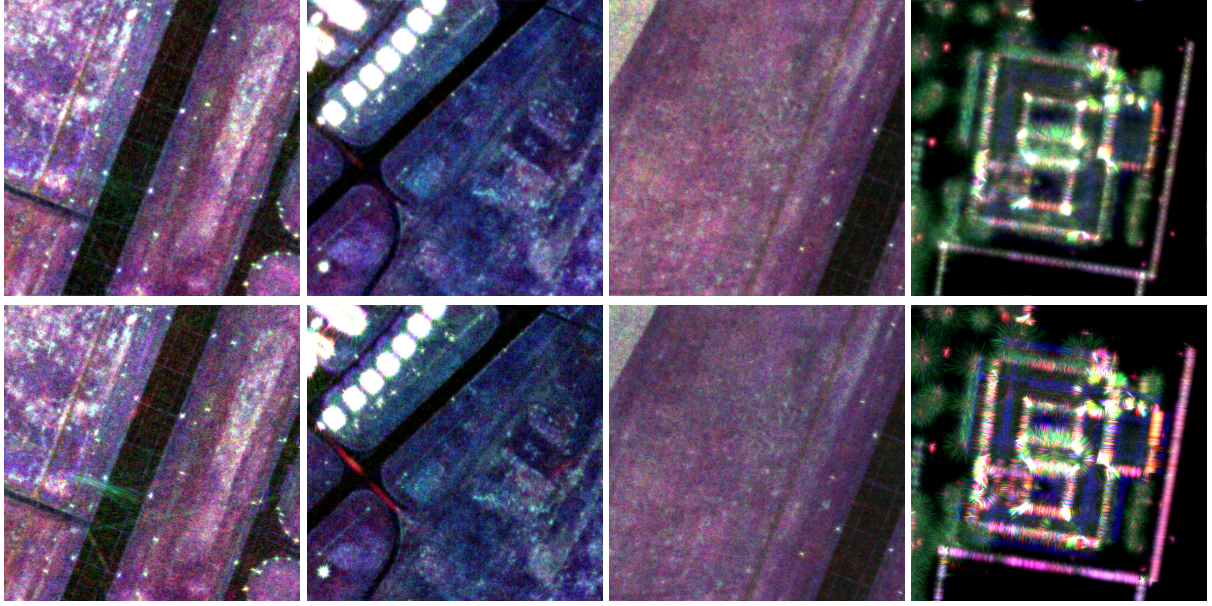
Figure 5.6: Comparison between images in the Pauli basis (blue: HH+VV, red: HH-VV, green: 2HV) processed by both coherent and incoherent imaging (subapertures of $\Delta\phi = 10°$) of the full synthetic aperture of an area with distributed and point-like targets, first two columns: 250 m x 250 m image size, third column: 200 m x 200 m image size, fourth column: 140 m x 140 m image size. Upper row: 0.06 m x 0.06 m sampling. Lower row: 0.5 m x 0.5 m sampling. The images correspond to close-ups of Figure 5.5.

5.4 Stripmap versus CSAR

Two of the limitations of linear SAR modes are the limited range of observation angles and the geometric resolution that can be achieved. A comparison between circular and stripmap SAR modes is depicted in Figure 5.7. In fact, all stripmap SAR images shown throughout this thesis have an integration interval of $10°$. The region was selected around the middle of Figure 5.5 to discuss and analyse the main differences and advantages of using a circular trajectory when focusing isotropic-like targets coherently. In this regard, due to the very high spatial resolution, the so called speckle *noise* is considerably mitigated or even absent in the CSAR image. This is a result of the small number of scattering elements within a resolution cell [Lomb 05a, Esch 10]. Note in any case that speckle is also reduced through the incoherent addition of the subapertures, since it is indeed multi-looking (see Figure 5.6).

As a matter of fact, speckle has been a real challenge for scientists working with PolSAR and PolInSAR because it leads to bias in statistical analysis [Lee 09, Hajn 09]. However, the statistical analysis of this kind of images will be subject of future research activities. Contrarily to stripmap SAR, a few objects with a size smaller than the wavelength ($\lambda_c = 0.24$ m) and an isotropic behaviour can be identified. For example, the lights along the runway indicated with red circles with a size of just 0.16 m x 0.2 m can be clearly seen (see Figure 5.7(c)). In fact, due to the vertical orientation of these lights, HH polarisation receives more power than VV. Furthermore, the improvement in the resolution of the ground can be explained by what could be an almost isotropic-like behaviour. Lastly, due to the multi-angular diversity, many more features and details of anisotropic structures can be identified, e.g., in the runway or objects on

(a) CSAR. (b) Stripmap SAR. (c) Runway lights.
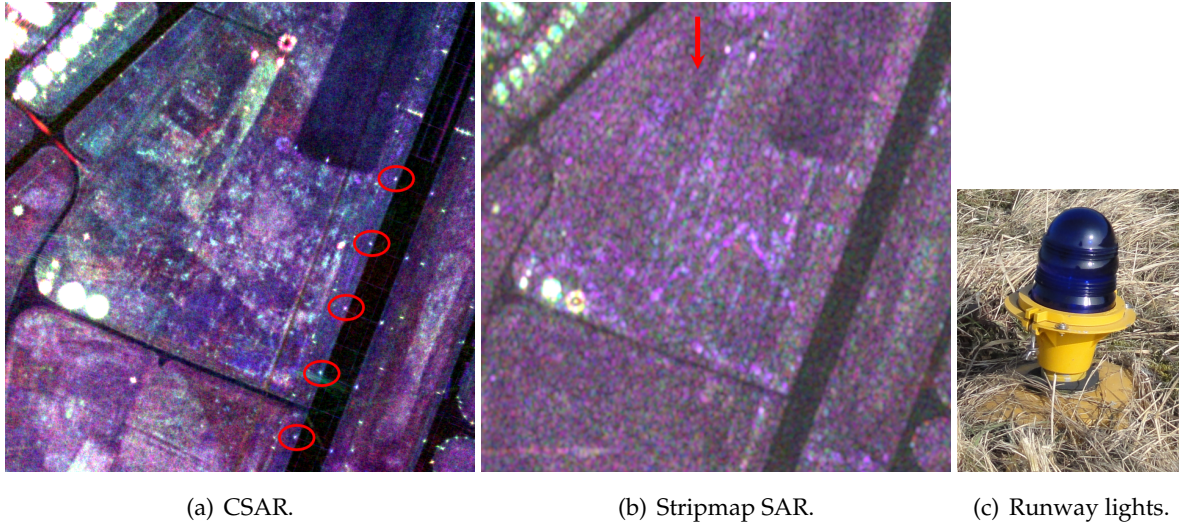
Figure 5.7: Comparison between circular and stripmap SAR modes using the same E-SAR system of DLR at L-band, 500 m x 500 m image size. (a) coherent imaging, 0.06 m x 0.06 m sampling, red circles indicate focused lights of 0.16 m by 0.2 m size and smaller than λ_c. Note a much larger amount of information available of the CSAR image when compared to stripmap. (b) 1 m x 1.8 m sampling, the red arrow indicates the direction of the radar illumination for stripmap. (c) Runway lights seen in (a).

the ground.

In addition, Figure 5.8 depicts close-ups of small regions of Figure 5.5(b) including again the comparison with stripmap, as well as an optical image to be used as reference. Firstly, man-made structures such as buildings, hangars, shelters and fences (highly directive) cannot be well identified from the stripmap SAR images. This kind of targets have a high directivity and can only be recognised under certain aspect angles. Clearly, the coherent processing of the full circular aperture allows a better distinction of the real shape of these targets and their polarimetric signatures [DeGr 05]. Moreover, in the last row of this set a group of trees are shown. Tree trunks are identified as double-bounces and isotropic-like targets, having a similar response as the light-poles at the lower-left corner. Since a DEM was used, canopies owning a volumetric response are slightly defocused. Although their response is similar to isotropic-like scatterers due to the ring-shaped sidelobes or circles of confusion, they have an anisotropic-like behaviour, as seen in the next subsection. A fence in V-form surrounding the building is seen as double-bounces in the middle of the trees, demonstrating a clear foliage penetration as expected at L-band.

5.5   3-D CSAR reconstruction

As mentioned in Chapter 3, an estimation of the 3-D reconstruction of man-made targets can be performed by means of layover in 2-D images [Dung 11]. In fact, this phenomenon is shown in Figure 5.9 with a building close to the center of the scene. The image is focused at the highest resolution and using a DEM. Upper corners of the building are seen as single-bounces (blue)

| (a) CSAR. | (b) Stripmap SAR. | (c) Optics. |
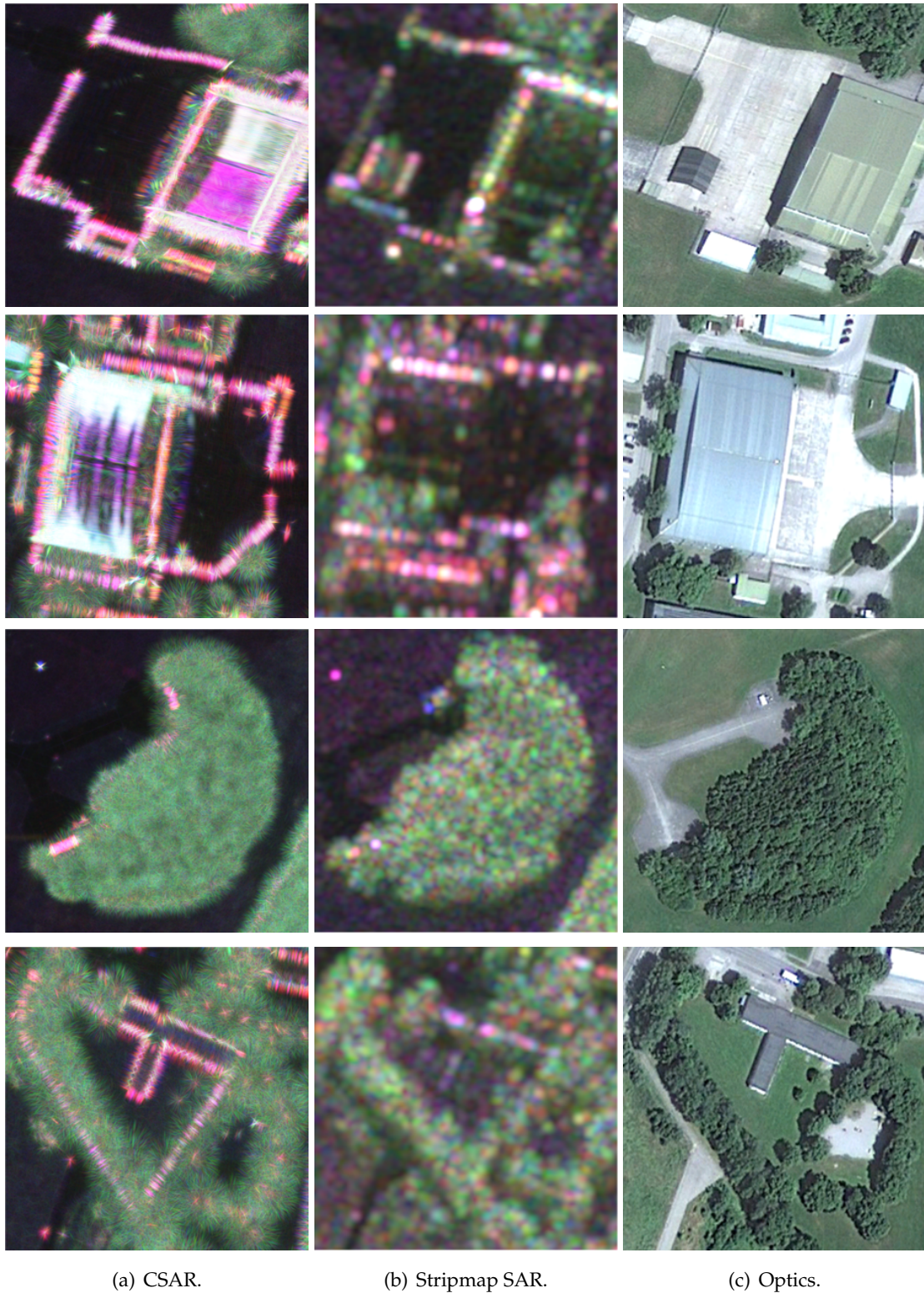
Figure 5.8: Comparison between stripmap SAR (1 m x 1.8 m sampling) and circular SAR (CSAR) (0.06 m x 0.06 m sampling) images using the same E-SAR system of DLR at L-band, and their optical representation with a size of 160 m x 160 m. First row: hangar with gable roof. Second row: hangar with arched roof. Third row: shelter covered with bushes. Fourth row: trees and man-made targets.

in layover, and walls as double-bounces (red) at their correct location. In order to estimate the height of the building and to form a 3-D representation, the distance between these two
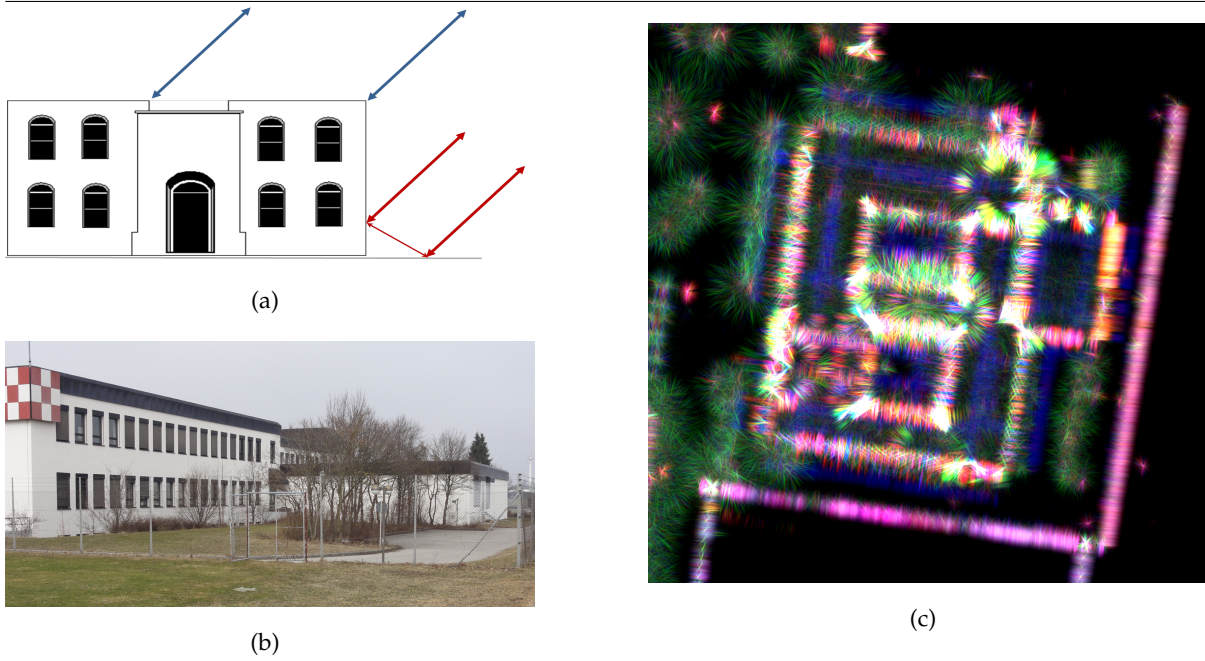
Figure 5.9: Phenomenon of layover for 3-D reconstruction of man-made targets (building). (a) Ray Tracing, red: double-bounces, blue: single-bounces. (b) Optical image. (c) 2-D amplitude image in the Pauli basis (blue: HH+VV, red: HH-VV, green: 2HV), 140 m x 140 m image size, 0.06 m x 0.06 m sampling.

mechanisms has to be measured provided the elevation angle θ_{el} to the edge at the roof of the building.

On the other hand, 3-D CSAR capabilities have been compared with confocal imaging in [Ishi 98]. Surely, 3-D imaging can be performed with a single circular pass because the collected data is the 2-D mapping of the three-dimensional scene from all over $360°$, and it contains information of the targets as a whole, similar to holographic data collection techniques [Pasm 05b]. However, low resolution in the direction perpendicular of the LOS, i.e., $\text{LOS}_{\perp}$, results in cone-shaped sidelobes when a single circular track is used.

Point-like targets: Luneburg lens

During this campaign, a Luneburg lens was placed in the spotlighted area aiming the achievement of the highest theoretical resolution in the (x, y) plane, as well as the energy retrieval in the vertical direction with real data. To that end, the Luneburg lens was focused in the (x, y, z) space covering a total area of 20 m by 20 m by 20 m with a sampling of 0.06 m by 0.06 m by 1.0 m in the three dimensions. The position of this reflector is indicated in Figure 5.5(a) with a red circle, and it has a diameter of 0.6 m.

The first challenge to achieve the aforementioned potentials of CSAR was the estimation and compensation of inaccuracies of the differential GPS (used in this campaign), which are in the order of ± 0.1 m in the (x, y, z) space. For this purpose, the frequency-domain autofocus approach was used (refer to Section 3.6.3). In fact, this algorithm is suitable for this kind of reflectors because of its low SCR, which is a result of the small dimensions of the lens with respect to the wavelength [Mott 92]. Due to the range-dependent geometry to estimate these
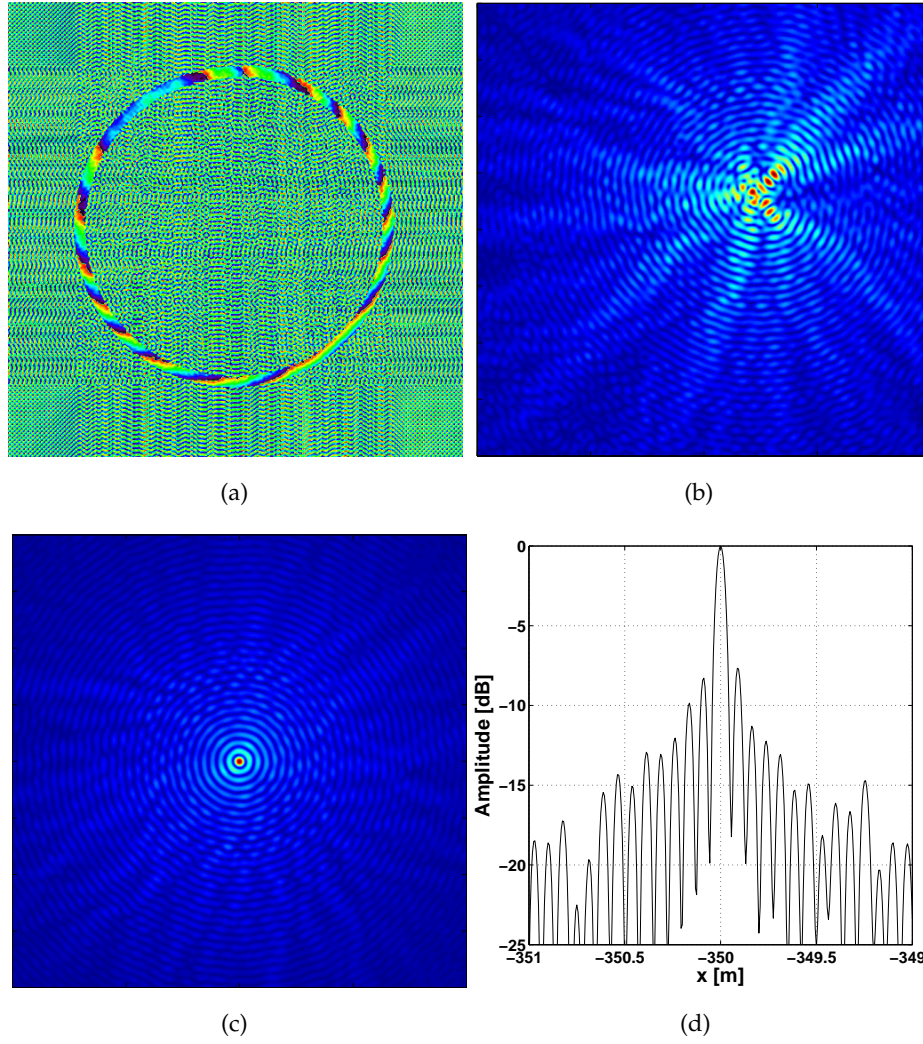
Figure 5.10: Experimental results of the frequency-based autofocusing approach using the impulse response function (IRF) of an isotropic target: Luneburg lens. The results indicate high accuracy for the estimation of residual motion errors, thus having the potential to achieve the theoretical resolutions. The image size corresponds to 2 m by 2 m. (a) 2-D IRF phase spectrum before autofocusing. (b), (c) 2-D IRF amplitude images before and after autofocusing. In addition to motion errors, constant errors (due to possible mismatch in the lever arm) are also corrected. (d) Normalised amplitude of the one-dimensional IRF, note that the PSLR is around -8 dB and the resolution is 0.085 m.

errors, the correction can only be applied to a region close to this target. Nevertheless, the lens was used to analyse the response of an ideal isotropic target with real data.

Results using the frequency-based autofocus approach are depicted as 2-D images before and after motion corrections in Figure 5.10. Interestingly, high-frequency inaccuracies in the navigation data defocus the IRF, whereas errors in the lever arm (also estimated) are reflected as constant shifts in x and y directions. These errors are depicted as fringes in the 2-D phase spectrum shown in Figure 5.10(a). The measured resolution in the (x, y) plane after the second iteration of the process was about 0.085 m similar to the expected theoretical one, and the PSLR was -8 dB as expected from the theoretical IRF (see Section 3.1). Finally, Figure 5.11 depicts the volumetric reconstruction of the Luneburg lens, thus showing the 3-D IRF of the CSAR
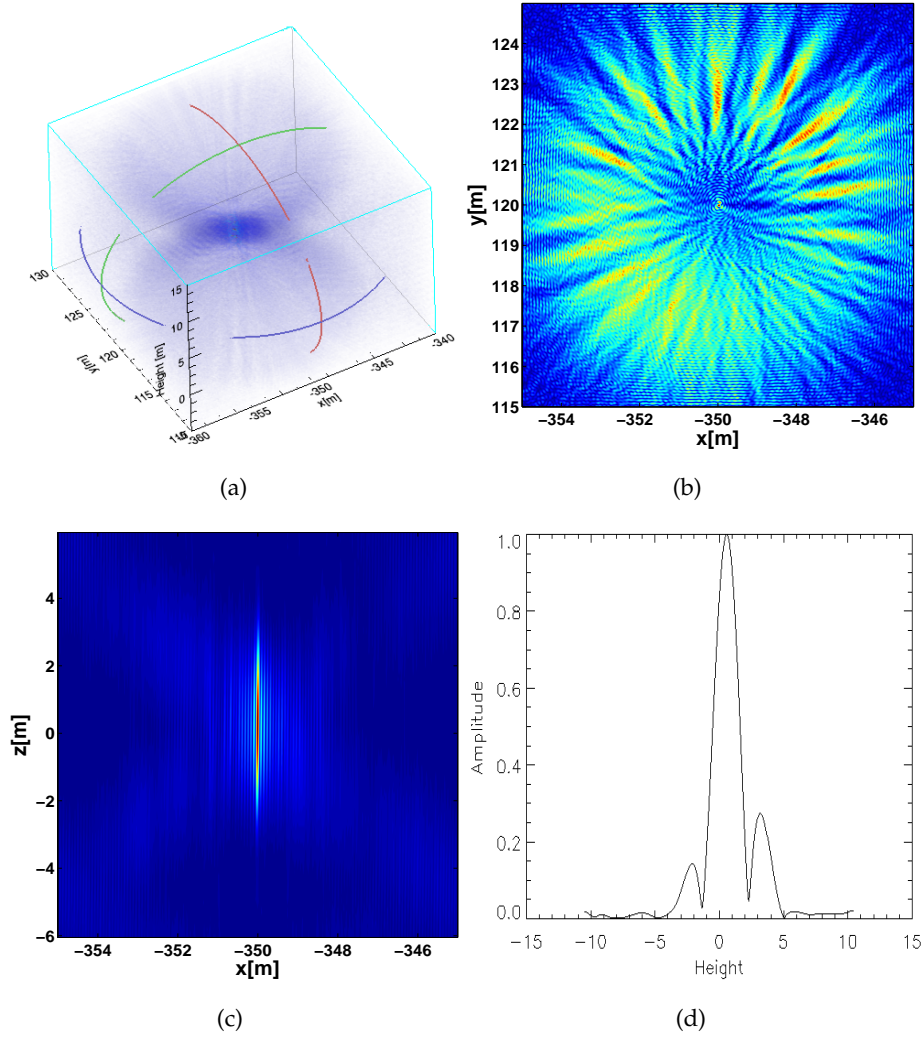
Figure 5.11: (a) First experimental reconstruction of the 3-D impulse response function (IRF) of an isotropic target: Luneburg lens. (b) (x, y) slice at 4 m erroneous height, note the ring-shaped sidelobes. (c) (x, z) slice, in this plane, the correct height of the Luneburg lens can be determined with a resolution similar to the bandwidth of the system $\delta_z = 1.6$ m at -3 dB, as defined in (3.24) and shown in (d). Cone-shaped sidelobes can be seen. (d) Height profile of the IRF along the z direction.

mode for a target close to the center. Note that cone-shaped sidelobes in the image are caused by the low resolution in the LOS$_\perp$ direction. The 2-D image in the (x, z) plane and the 1-D profile show the impulse response in elevation, where again the expected resolution of 1.6 m is achieved.

Natural targets: Trees

Similarly, a cube of dimensions 20 m by 20 m by 15 m in (x, y, z) around a tree was processed, as shown in Figure 5.12. 2-D polarimetric slices in the (x, y) plane of the tomogram were focused by coherent imaging (see Figure 5.12(c)). In the same image, the tree trunk shows an isotropic-like behaviour, whereas the tree canopy is mainly composed of anisotropic scatterers.
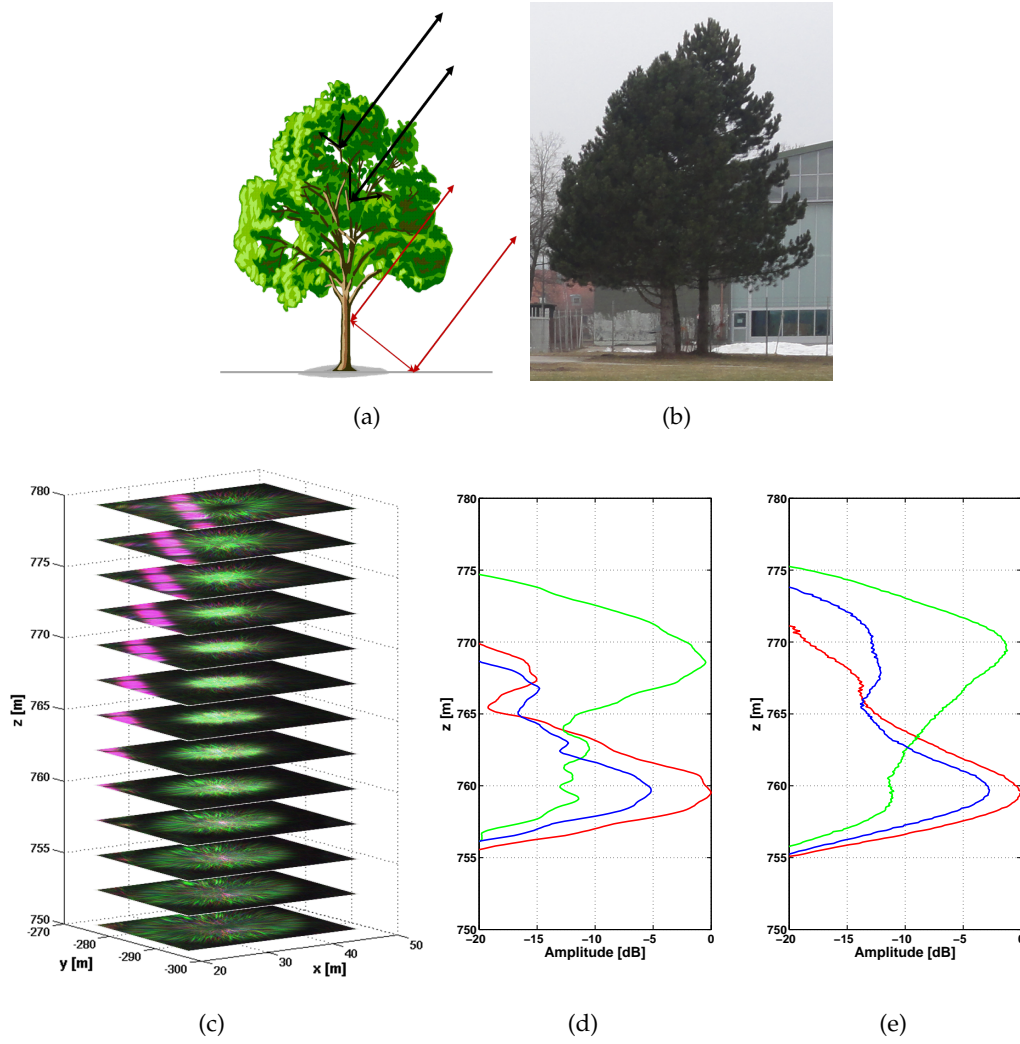
Figure 5.12: First 3-D reconstruction of a tree using a single circular pass at L-band, Pauli basis (blue: HH+VV, red: HH-VV, green: 2HV) with an image size of 20 m x 20 m, and sampling of 0.06 m x 0.06 m. (a) Ray Tracing. Red: double bounces. Black: volume. (b) Optical image. (c) Slices of the tomogram. (d) Height profile, coherent imaging, 5 x 5 x 1 multi-look. (e) Height profile, incoherent imaging with 36 subapertures of $\Delta\phi = 10°$.

Despite their complex signature, if both tree components are treated as isotropic, then similar scattering mechanisms in 3-D as PolInSAR and as TomoSAR can be retrieved [Neum 10, Frey 11b]. Figure 5.12(d) depicts the vertical scattering profiles of the tree shown in Figure 5.12(c) for the three Pauli components, i.e., surface (single-bounces blue), canopy (volume in green) and tree-trunk (double-bounces in red). This profile was obtained by averaging the intensity around the tree center at every height with a fixed window size of 5 by 5 pixels. On the other hand, the same region was processed incoherently, resulting in a smoother 3-D profile with worse SCR and resolution (see Figure 5.12(e)).

The approach to estimate the backscattering profile of the tree canopy is based on the imaging process as follows. When a given target is focused at its right height, its (x, y) coordinates are then also right, thus having the maximum energy at the height were most of the scatterers are located close to each other. Commonly, anisotropic targets at a slightly different height do not defocus, but instead are slightly shifted from their correct (x, y) coordinate. This is the

(a)   (b)   (c)   (d)
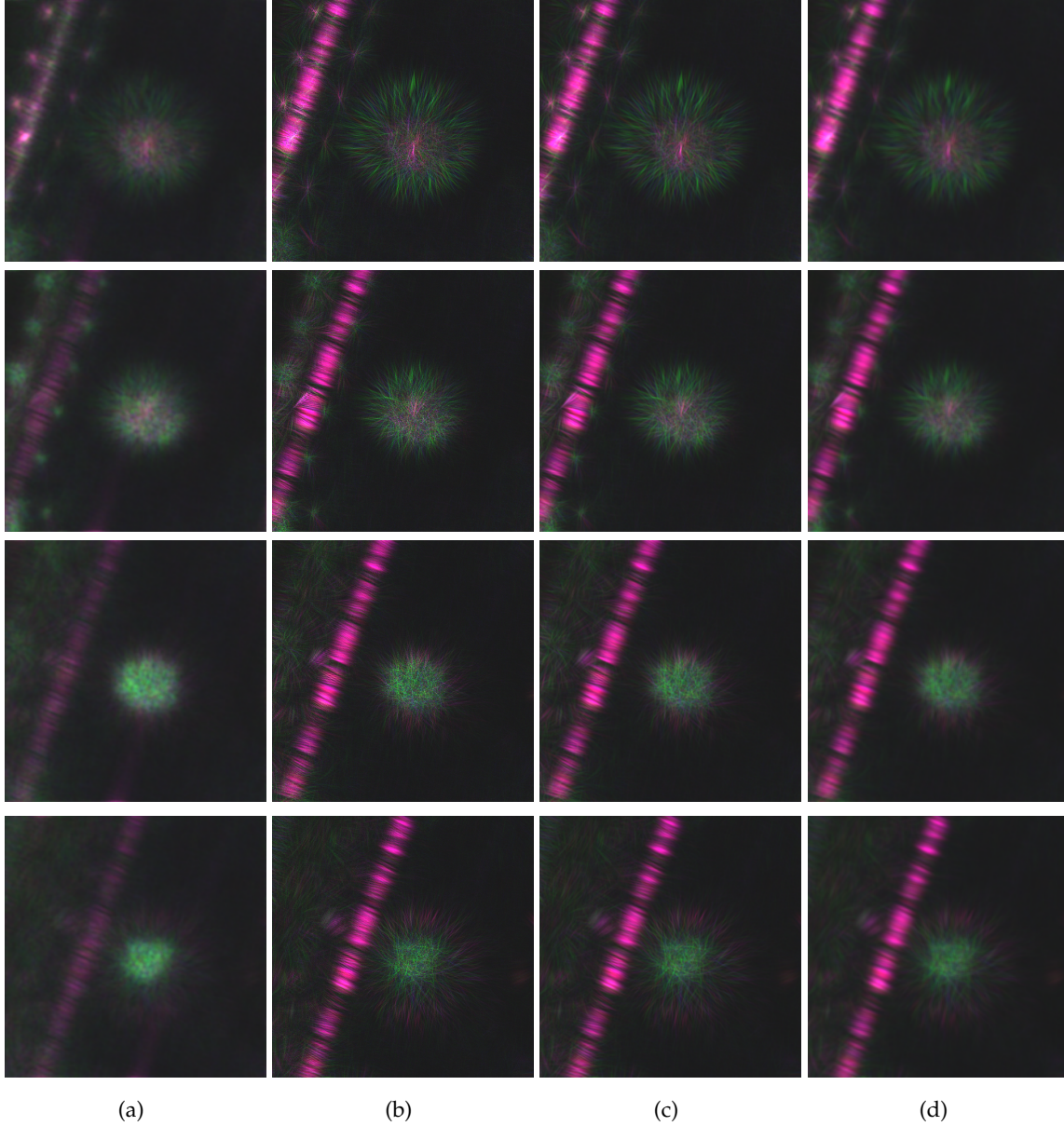
Figure 5.13: Comparison of 2-D (x, y) slices of a fully-polarimetric CSAR tomogram in the Pauli basis (blue: HH+VV, red: HH-VV, green: 2HV) of a tree by incoherent (subapertures of $\Delta\phi = 10\,°$) and coherent imaging with an image size of 20 m x 20 m. (a) Incoherent imaging, 0.5 m x 0.5 m sampling, (b)-(d) Coherent imaging, 0.06 m x 0.06 m sampling. (b) No multi-look. (c) 3 x 3 multi-look. (d) 11 x 11 multi-look. From the first to the fourth row: $z_1 = 757.5, z_2 = 762, z_3 = 766.6, z_4 = 771.1$ m. Note that the tree canopy shows an anisotropic behavior; nevertheless, if it is added coherently during the full synthetic aperture, it is focused with much higher resolution. The red line crossing the image results from the double bounce of a metal grid fence located nearby.

reason why the circles-of-confusion are present, even if the tree-canopy is mainly composed of anisotropic scatterers. Such effect slightly influences the energy computation for the height under consideration. In this sense, this effect introduces correlation in the estimated energy between closely located heights, e.g., acts as a low-pass filter. The role and influence of the estimation window, as well as further approaches to estimate the backscattering profile using CSAR data are subject of future research work.

Furthermore, Figure 5.13 shows 2-D slices of the same tree focused coherently and incoherently. Although the signature of tree canopies at the wrong height depicts arc sidelobes, phase centres change randomly even with a very small movement in the angular direction (e.g., aperture smaller than stripmap SAR), again this shows its anisotropic behavior. However, the coherent addition of this energy results in both the possibility of every scatterer to reach its maximum resolution in the (x, y) plane and the retrieval of the volumetric information, as already commented above in terms of the imaging process. On the other hand, Figure 5.12(c) and 5.13 also show the signature of a highly anisotropic target shown as a diagonal at the top of the tomogram that corresponds to a fence, i.e., double-bounce signature. This response smears very slowly in elevation, since it corresponds to a highly-directive signature.

(a) DEM + 0 m.   (b) DEM + 2 m.   (c) DEM + 3 m.   (d) DEM + 4 m.
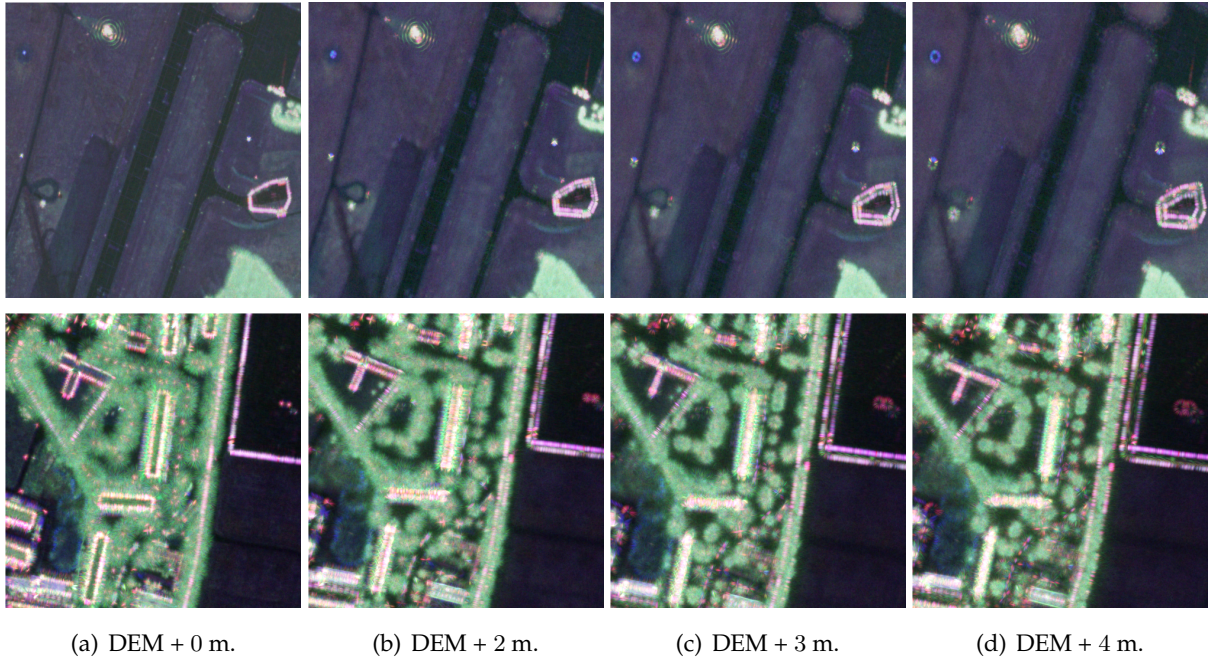
Figure 5.14: Fully-polarimetric CSAR tomography in the Pauli basis (blue: HH+VV, red: HH-VV, green: 2HV) using a single pass, 400 m x 400 m image size, 0.06 m x 0.06 m sampling, using as a reference (a) and with different height offsets (b) - (d). Upper row: man-made targets such as metal grid fences, a Luneburg lens or runway lights, and natural targets such as ground and a part of a forest. Lower row: man-made targets such as buildings, light-poles and metal grid fences, and distributed targets such as individual trees.

To conclude, Figure 5.14 shows 2-D images focused coherently at different heights ($h = $ DEM+1, DEM+2, DEM+3, DEM+4 m). It is intended to show the tomographic capabilities of CSAR in a wider area with any kind of signatures. In the first row, the ground can be approximated as several point-like scatterers close to each other, where the energy at the true height is added constructively and at the wrong height destructively, i.e., out of focus. This fact proves the isotropic-like behavior of the ground. Indeed, tree canopies and other targets are focused as h increases, while other targets get defocused, hence, starting to show circular and arc patterns. This fact shows undoubtedly the potential to retrieve 2-D and 3-D profiles of point-like and distributed areas.

In summary, this chapter has presented the first demonstration of fully-polarimetric high-resolution 3-D imaging with a single circular acquisition for man-made and natural targets.

The analysis of the acquired data of a Luneburg lens led to the demonstration of the main capabilities of CSAR with real data: subwavelength resolution and 3-D reconstruction. Likewise, the FFBP for circular trajectories was validated with real data and different configurations. The advantages and limitations of this algorithm were also discussed. Moreover, imaging by incoherent and coherent additions were compared with man-made and distributed targets. The coherent approach showed mostly better performance in terms of resolution and SCR, at an acceptable cost in computational burden since images are focused with the FFBP for CSAR. Finally, 3-D imaging at L-band with one circular pass was demonstrated for the first time for a point-like target, i.e., Luneburg lens, and semi-transparent media, i.e., trees. Interestingly, if the signature of the two components of a tree, i.e., canopy and trunk, are treated as isotropic, then a 3-D profile can be retrieved.

6 Fully Polarimetric Holographic SAR Tomography with Multicircular Acquisitions

This chapter is devoted to present and to investigate the holographic SAR tomography (Holo-SAR) imaging mode with fully polarimetric systems, and particularly for distributed scatterers. This encompasses a deep analysis of the 3-D IRF in time and frequency domains, the description and comparison of three imaging methods, namely coherent, incoherent and GLRT with coherent averaging, and the introduction of a phase calibration algorithm based on the singular value decomposition (SVD) of strong ground returns. The last part is dedicated to study two experimental realisations at P- and L-band over forested regions. In this respect, theory is discussed and validated for small and large regions, and different constellation configurations.

Parts of this chapter have been published in [Ponc 14b] and [Ponc 16b].

6.1 Holographic SAR tomography (HoloSAR)

In order to introduce the concept of HoloSAR, similarities between SAR, tomography and holography are discussed. The three techniques emerged in parallel timelines, and agree in several aspects regarding processing and data acquisition. The term of holographic tomography has been used in optics and it will be defined in the SAR context with a geometry described by a circular and a linear synthetic apertures. The intention of this analysis is not to give a detailed summary of holography and tomography, but rather to consider holographic and tomographic processes in the context of SAR, and in this way, to define the concept of HoloSAR.

6.1.1 HoloSAR with mutlicircular acquisitions

In the beginning of SAR sensors development, the range-Doppler approach was used to improve imaging resolution. However, the most accurate methods were based on coherent optical processors, formed by different lenses, since various processes were described as analogous to SAR, as first demonstrated by Cutrona in [Brow 67, Brow 69, Cutr 66, Leit 71]. The acquired information was encoded onto a film to be afterward optically processed in range and azimuth directions. The progress of this type of SAR processor formed the basis of a tech-

nique called *holography* (Greek *holos*: whole, *grafe*: drawing), which was based on recording and reconstructing the diffracted wavefront in amplitude and phase with the help of photographic plates [Pasm 05a]. A particular feature of holography is that every observation contains an integral Fourier transform of the 3-D backscattering, i.e., it has information about the object of interest as a whole, similar to SAR. In this respect, extended investigations were carried out to analyse the similarities between both techniques. In [Leit 71, Farh 75], the concept of *hologram radar* was referred as a direct microwave counterpart of optical holography, and holograms in the microwave range were called *microwave holograms*. In [Mens 91, Pasm 05a], radar imaging was based on a combination of holographic and tomographic approaches. It was shown that the resolution of coherent radar and coherent optical systems is dependent on the Doppler frequency shift, however limited by the linear geometry of the most common synthetic apertures, i.e., linear SAR imaging modes.

Until now, most of the comparisons between SAR and tomography have been done through CAT in a 2-D plane (see Section 2.5). However, other tomographic techniques were developed at the same time, and they were not compared to SAR despite their similarities. That is the case of *ectomography*, before known as tomosynthesis, which is a 3-D radiographic technique that was developed in order to decrease the patient dosage, but at the cost of resolution [Gran 72, Knut 80, Dale 88]. This technique consists in a slanted sensor that rotates around the object of interest to acquire a one-dimensional representation of a 3-D object, instead of a 2-D object as CAT does (see Figure 6.1(a)). As a result, the 3-D reflectivity of the given volume can be retrieved with a single circular data collection, rather than several. Nevertheless, the depth of focus occurs in the (x, y) plane as a consequence of the missing spatial frequencies, i.e., the Ewald sphere has the shape of a toroid, and therefore no plane contains fully unique information. Notably, this technique coincide with the CSAR imaging mode in the following aspects: acquisition geometry, effect of depth and more importantly the inversion of the problem by means of the 3-D projection-slice theorem, as depicted in Figure 6.1 [Knut 80, Knae 95].

In addition, in 1975, it was demonstrated that the Doppler frequency shift of coherent light reflected or scattered from the rotation of a monostatic source or rotating objects allows a much finer resolution than the classical limit of linear aperture imaging of holographic systems [Alek 75]. In the 1980s, the same idea was exploited to form a synthetic aperture in the microwave spectrum in order to produce high resolution images [Mens 80, Mens 82]. This imaging mode was referred as ISAR or CSAR depending on the configuration of the sensor and the region of interest.

In a similar way, but a few decades later, coherent light and the effect of backscattering were applied for 3-D imaging enhancement in biological microscopy by means of either rotating the illuminator or the object [Ferr 11, Shan 09]. This concept is based on a technique called diffraction tomography, and it is used in both optics and acoustics. *Holographic tomography*, a way of performing diffraction tomography with *semi-transparent media*, records separately the backscattering for different illumination directions to be, afterward, coherently combined in a digital form. This concept is analogous to the digitalised SAR sensing, instead of using films. In [Wu 87], diffraction tomography and multisource holography were described and compared in the frame of seismic imaging. Multisource holography was defined as a non-exact inversion algorithm, since it causes distortions in the reconstructed images. Alternatively, diffraction
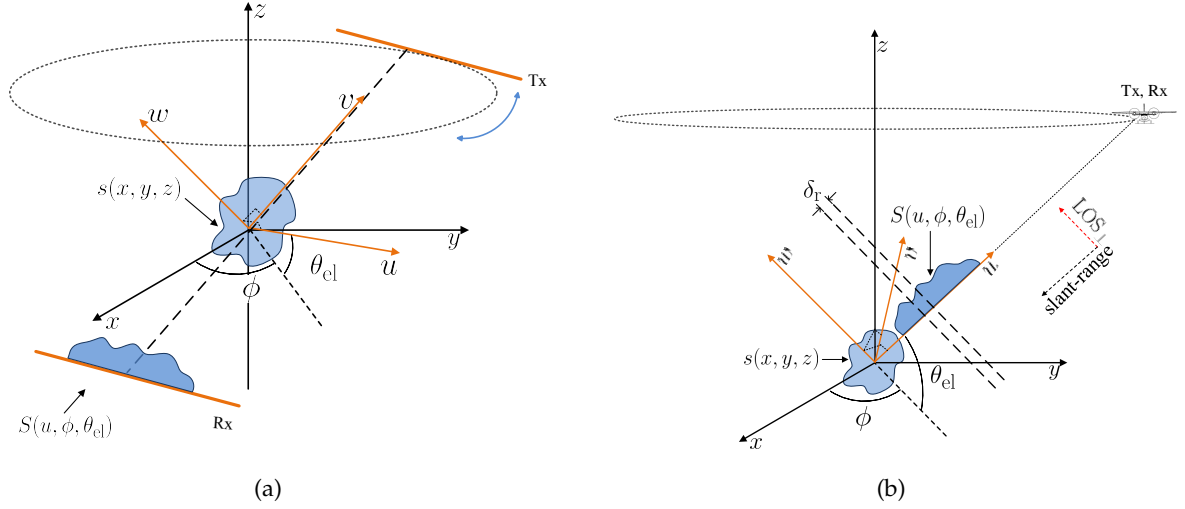
Figure 6.1: Analogy between ectomography (a) and circular SAR (b) using the three-dimensional projection-slice theorem. $s(x, y, z)$ is the unknown complex reflectivity of the object of interest, $S(u, \phi, \theta_{\text{el}})$ is the projection of $s(x, y, z)$ onto the axis u, which rotates as a function of the angle ϕ, and δ_{r} is the resolution in the slant-range direction. Note that it is possible to reconstruct in 3-D with a single circular pass, as a consequence of the slanted acquisition geometry.

tomography was introduced as a solution to mitigate distortions by using filtered data, i.e., it considers the Jacobian of the 3-D back-projection algorithm, as described by (6.4). Moreover, the concept of *holographic tomography* using a circular synthetic aperture and optical processing was first demonstrated in [Groh 71]. The basic idea was to move the sensor, in this case in the X-ray wavelength range, around the object of interest and record photographs for each angular position. Afterward, every photograph was illuminated using coherent light and synthesised to form the holographic tomogram. Similar to ectomography and CSAR, if the illumination source is rotated around a single axis, then the depth of focus occurs in the focused image, as a consequence of the missing spatial frequencies in the LOS$_\perp$ direction [Vert 09]. In addition, to perform a full 3-D reconstruction the illumination source has to be rotated not only over one axis, but it has to be moved along a second axis, analogous to the transition of CSAR to HoloSAR with multicircular acquisitions.

Again, the term of TomoSAR was defined using multibaseline linear SAR acquisitions primarily because processing can be formulated with tomographic techniques. In a similar way, the concept of holographic SAR tomography (HoloSAR) is recalled from previous definitions in optics and SAR to describe the reconstruction of full 3-D backscattering by means of multicircular acquisitions [Glaz 93, Schi 93]. That is to say that HoloSAR is defined by the following analogies with holography and tomography:

1. The acquisition geometry is formed by two synthetic apertures, namely circular and in elevation.

2. Potential three-dimensional reconstruction with a single rotational acquisition, and full 3-D reconstruction with an additional synthetic aperture in elevation. These imaging capabilities are primarily associated to the variation of the aspect and elevation angles,
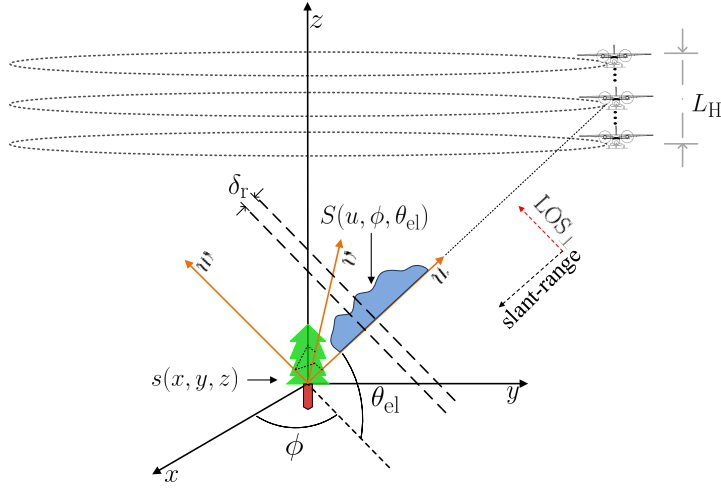
Figure 6.2: System model of holographic SAR tomography (HoloSAR) with multicircular acquisitions using the 3-D project-slice theorem. $s(x, y, z)$ is the unknown 3-D complex reflectivity and $S(u, \phi, \theta_{el})$ is the projection of the unknown along u and as function of the rotation angle ϕ, i.e., circular synthetic aperture, and the elevation angle θ_{el}, i.e. vertical synthetic aperture. Note that this acquisition geometry allows the retrieval of the 3-D full backscattering.

i.e., ϕ and θ_{el}.

3. Every observation contains an integral Fourier transform of the 3-D backscattering that gives information in amplitude and phase, i.e., it has information about the object as a whole. In addition, every measurement corresponds to what is referred as *microwave hologram* in the microwave range.

4. Processing can be formulated by using the 3-D projection-slice theorem.

5. The spectrum of the processed circular aperture in the horizontal plane (x, y) is directly associated to the shape of the track, which is not the case of linear synthetic apertures.

6. The goal of imaging is to get information about the internal structure of the scene over $360°$, which is achieved at low frequencies such as L- and P-band. Alternatively, the effect of layover is corrected at higher frequencies (e.g., X-band, Ka-band), in cases where the wave does not penetrate objects.

6.1.2 The 3-D projection-slice theorem

The previous tomographic analogies for 2-D imaging with linear SAR modes are extended to 3-D imaging for HoloSAR, as holographic tomography does [Knae 95, Shan 09, Ferr 11]. The considered geometry and main parameters are illustrated in Figure 6.2. By using this model, every observation at any range is described as the integral of the radar cross section density of the volume $s(x, y, z)$ over the (v, w) plane, which is perpendicular to u, and can be written as

$$S(u, \phi, \theta_{el}) = \iint\limits_{-\infty}^{\infty} s_\phi(u, v, w) \, dv \, dw, \tag{6.1}$$

where u direction is defined by the rotation and elevation angles ϕ and θ_{el}, respectively. The forward Fourier transform of $S(u, \phi, \theta_{el})$ with respect to u represents a part of the 3-D Fourier transform $S(x, y, z)$ and is defined as follows

$$\mathcal{F}_u(S(u, \phi, \theta_{el})) = \iiint\limits_{-\infty}^{\infty} S_\phi(u, v, w) \cdot e^{-j2ku} \, dv \, dw \, du, \tag{6.2}$$

where the relation between (u, v, w) and (x, y, z) is given by

$$
\begin{aligned}
u &= x\cos(\phi)\sin(\theta_{el}) + y\sin(\phi)\sin(\theta_{el}) + z\cos(\theta_{el}) \\
v &= -x\sin(\phi)\sin(\theta_{el}) + y\cos(\phi)\sin(\theta_{el}) \\
w &= x\cos(\phi)\cos(\theta_{el}) + y\sin(\phi)\cos(\theta_{el}) - z\sin(\theta_{el}).
\end{aligned}
\tag{6.3}
$$

After a space transformation and variable substitutions, (6.2) can be defined by the 3-D back-projection as [Knae 95]

$$s(x, y, z) = \iiint\limits_{\theta_{el} \; \phi \; k} k^2 \cdot \sin(\theta_{el}) \cdot S(k, \phi, \theta_{el}) \cdot e^{j2ku} \, dk \, d\phi \, d\theta_{el}, \tag{6.4}$$

where the new limits of the third integral, compared to (2.52), depend on the synthetic aperture in elevation. If θ_{el} is constant, then a synthetic aperture in elevation is not considered, and consequently the depth of focus occurs, which is seen as 3-D cone-shaped sidelobes in the (x, y, z) space. Contrarily, the depth of focus is decreased by having θ_{el} variable, i.e., by forming a synthetic aperture in elevation. Eq. (6.4) will be used in the following section to describe the 3-D IRF of HoloSAR.

6.1.3 Impulse response function (IRF)

Knowing that the trajectory of the radar follows a cylindrical geometry, the complex reflectivity (3-D delta function for simplification) of the scene can be described as [Moor 10]

$$s(\vec{r}_{grid}) = \iiint\limits_{\theta_{el} \; k \; \phi} k^2 \cdot \sin(\theta_{el}) \cdot e^{-j2k|\vec{p} - \vec{R}(\phi, \theta_{el})|} e^{j2k|\vec{r}_{grid} - \vec{R}(\phi, \theta_{el})|} \, d\phi \, dk \, d\theta_{el}, \tag{6.5}$$

where, unlike the expression given by (3.6) in CSAR mode, the elevation angle θ_{el} has to be taken into account due to the additional synthetic aperture (see Appendix A.3). Therefore, the trajectory of the platform can be redefined as $\vec{R}(\phi, \theta_{el}) = (R_x, R_y, R_z) = (|\vec{R}| \cos(\phi) \cdot \sin(\theta_{el}), |\vec{R}| \sin(\phi) \cdot \sin(\theta_{el}), |\vec{R}| \cos(\theta_{el}))$ with ϕ as the horizontal angular aperture.

In order to reduce the previous equation, it has to be assumed a target in the center, $\vec{p} = (0, 0, 0)$, and a distance to the track much greater than the height of the target and the height of the radar, i.e., $p_z \ll |\vec{R}(\phi)|$, $R_z \ll |\vec{R}(\phi)|$. In this way, (6.5) yields the following expression

$$s(\vec{r}_{xy}) = 2\pi \iint\limits_{\theta_{el} \; k} k^2 \cdot \sin(\theta_{el}) \cdot e^{jk_r \cdot \cot(\theta_{el} \cdot r_z)} \cdot J_0(2k \cdot \sin(\theta_{el}) \cdot |\vec{r}_{xy}|) \, dk \, d\theta_{el}. \tag{6.6}$$

In order to retrieve a closed form of (6.6) in the $\vec{r}_{xy} = (r_x, r_y, r_z = 0)$ plane, there should be a change of variables from (k, θ_{el}) to k_r provided $k_r = 2k \cdot \sin(\theta_{el})$, as follows

$$s(\vec{r}_{xy}) = 2\pi \int_{k_{r_1}}^{k_{r_2}} k_r \cdot J_0(k_r \cdot |\vec{r}_{xy}|)\, dk_r, \tag{6.7}$$

which can be reduced to a difference of two Bessel functions of the first kind

$$s(\vec{r}_{xy}) \approx \frac{2\pi}{|\vec{r}_{xy}|} \left(k_{r_2} \cdot J_1(k_{r_2} \cdot |\vec{r}_{xy}|) - k_{r_1} \cdot J_1(k_{r_1} \cdot |\vec{r}_{xy}|) \right). \tag{6.8}$$

Interestingly, k_r does not only depend on the system bandwidth, $BW = k_{\max} - k_{\min}$, and the wavelength, λ_c, as the IRF of CSAR does, but also on θ_{el} that is defined by the synthetic aperture in height. Hence, the new wavenumbers in the radial direction are defined as $k_{r_1} = 2k_{\min} \cdot \sin(\theta_{el_2}(R_{z,2}))$ and $k_{r_2} = 2k_{\max} \cdot \sin(\theta_{el_1}(R_{z,1}))$ with θ_{el} as a function of the minimum and maximum altitudes of the circular flights, $R_{z,1}$ and $R_{z,2}$, respectively.

Furthermore, if the IRF is analyzed in the z direction, then (6.6) becomes

$$s(\vec{r}_z) = \int_{\theta_{el}} \int_k k^2 \cdot \sin(\theta_{el}) \cdot e^{-jk_z \cdot r_z}\, dk\, d\theta_{el}, \tag{6.9}$$

where it can be seen that the synthetic aperture in elevation has to be taken into account. Also, if there is a transformation from (k, θ_{el}) to (k_r, k_z), then (6.9) can be expressed as

$$s(\vec{r}_z) = \int_{k_{z_1}}^{k_{z_2}} \int_{k_{r_1}}^{k_{r_2}} k_r \cdot e^{-jk_z \cdot r_z}\, dk_r\, dk_z, \tag{6.10}$$

in this way yielding

$$s(\vec{r}_z) \approx \gamma \cdot \mathrm{sinc}((k_{z_2} - k_{z_1}) \cdot r_z), \tag{6.11}$$

where γ is a constant factor, and the wavenumbers in the vertical directions are $k_{z_1} = 2k_{\min} \cdot \cos(\theta_{el_1}(R_{z,1}))$ and $k_{z_2} = 2k_{\max} \cdot \cos(\theta_{el_2}(R_{z,2}))$. Note that both k_z terms also depend on the system bandwidth, the wavelength and the synthetic aperture in elevation, i.e., the resolution of the sinc function depends on these parameters. In order to better understand (6.8) and (6.11), in Section 6.1.4, the effects of BW, λ_c and θ_{el} are deeply analyzed.

On the other hand, the integral given by (6.5) for a target that is off the center should be solved assuming $\vec{p} \neq (0, 0, 0)$, similar to (3.15) in Section 3.1.2. Thereby, the solution of the expression after some approximations can be expressed as

$$s(\vec{r}_{grid}) = \int_{\theta_{el}} \int_k \int_\phi k^2 \cdot \sin(\theta_{el}) \cdot e^{jk \cdot h} \cdot e^{jk \cdot g \cdot \cos(\phi)}\, d\phi\, dk\, d\theta_{el}, \tag{6.12}$$

where the integral with respect to θ_{el} indicates the synthetic aperture in elevation. Subsequently, the equation can be reduced to an integral of a Hankel transform, similar to (6.6), as follows

$$s(\vec{r}_{grid}) = 2\pi \int_{\theta_{el}} \int_k k^2 \cdot \sin(\theta_{el}) \cdot e^{jk \cdot h} \cdot J_0(k \cdot g)\, dk\, d\theta_{el}, \tag{6.13}$$

where the variables g and h are described in Section 3.1.2 [Moor 10]. One can see that (6.13) does not have a closed solution, therefore it has to be studied either numerically or in the frequency domain, as shown in Section 6.1.5.

6.1.4 Sidelobe analysis and geometric resolutions

Eq. (6.8) shows that subwavelength resolution can be achieved by the coherent integration over $360°$ and independent from the system bandwidth, BW. Nevertheless, narrow system bandwidths result in an increment of the 2-D sidelobe level of the Bessel function. As already discussed in Chapter 3, a typical PSLR with 50 MHz or 100 MHz system bandwidth and $\lambda_c = 0.23$ m is -8 dB. The first solution to suppress these sidelobes would be to increase the bandwidth of the system [Ponc 14a], however this is not always feasible. A second alternative would be to exploit the spectrum coverage of the synthetic aperture in elevation. To that end, the basic idea of InSAR for linear SAR modes is considered (see Section 2.3.1).

In [Guil 06], interferometric techniques were used in stripmap SAR mode to increase the signal bandwidth in the slant-range direction by coherently merging the information of two passes with a certain baseline, thus improving the resolution in ground range δ_{gr}. Similarly, HoloSAR results in an increment of the effective bandwidth in k_r and k_z directions, as shown in Figure 6.3, and consequently in a reduction of the PSLR in the (x, y) plane and in an improvement of the resolution in the vertical direction z. This improvement is analytically described by (6.8) and (6.11), since the wave numbers k_r and k_z are function of the elevation angle θ_{el} and the bandwidth of the system BW.
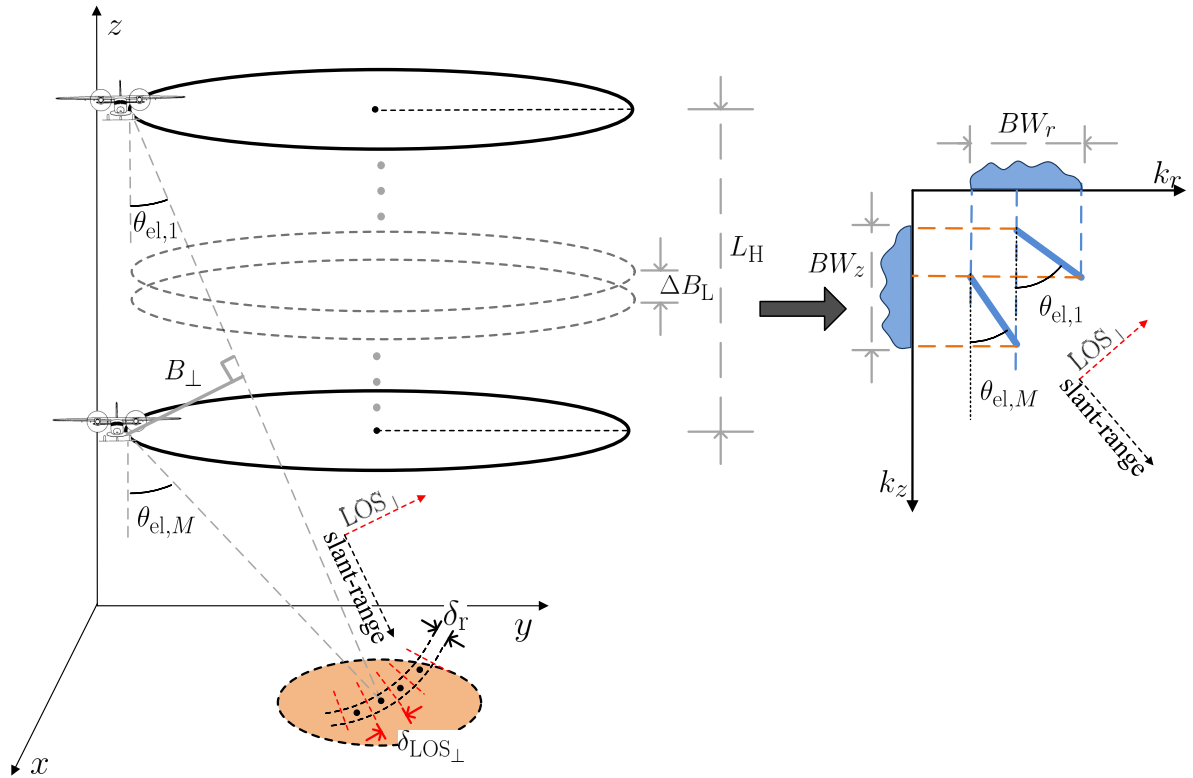
Figure 6.3: Acquisition geometry of HoloSAR for the interferometric analysis to estimate resolutions and sidelobe suppression. Note the improvement of the effective bandwidth, BW_r and BW_z when the spectrum is projected to k_r and k_z directions, respectively. In this case the maximum baseline $L_{\text{H},\perp}$ matches the critical baseline $B_{\perp,\text{crit}}$.

In order to better understand this theory, let us consider two tracks in elevation with a certain normal baseline $\Delta B_{\text{L},\perp}$. If the information of both acquisitions is coherently combined, then

the improvement in bandwidth can be estimated by the spectral shifts in the horizontal and vertical directions. As previously described in Section 2.3, (2.36) indicates the spectral shift in the (k_x, k_y) plane. Thereby, the effective bandwidth in the radial direction, k_r, is given by

$$BW_r = BW \cdot \sin(\theta_{el}) + \Delta f_r, \tag{6.14}$$

with $r = |\, \vec{p} - \vec{R}(\phi, \theta_{el})\, |$ and $\alpha_{in} = 0$. On the other hand, the effective bandwidth in the k_z direction is given by

$$BW_z = BW \cdot \cos(\theta_{el}) + \Delta f_z, \tag{6.15}$$

where the spectral shift in the vertical direction is

$$\Delta f_z = \frac{c}{4\pi} \cdot \frac{\partial \varphi_h}{\partial \delta r} = -\frac{c \cdot B_\perp}{\lambda_c \cdot r \cdot \sin(\theta_{el} - \alpha_{in})}, \tag{6.16}$$

with the phase φ_h defined by (2.33). It follows from (6.11) and (6.16) that the improved resolution along the vertical direction from (6.11) can be described as

$$\delta_z = \frac{1}{\sqrt{2\pi}} \cdot \frac{c}{BW_z \cdot \cos(\theta_{el})}. \tag{6.17}$$

In addition, if several passes in elevation are used, the maximum baseline $B_\perp = L_{H,\perp}$ should be considered. For a better improvement, the maximum baseline between two contiguous passes should be close to the critical baseline, $B_{\perp,crit}$, but not beyond. The critical baseline in the theory of SAR interferometry is defined as the minimum distance where the spectra do not overlap in the k_r direction, i.e., $\Delta f_r = BW$. In HoloSAR, the spectral shift in the vertical direction Δf_z, has to be taken into account. That is to say that the critical baseline is defined by the following expression

$$B_{\perp,crit} = \min\left(\frac{\lambda_c}{c} \cdot BW \cdot r \cdot \tan(\theta_{el} - \alpha_{in}), \frac{\lambda_c}{c} \cdot BW \cdot r \cdot \sin(\theta_{el} - \alpha_{in}) \right), \tag{6.18}$$

where the minimum is determined by the second term with the sine function.

Figure 6.4 illustrates the PSLR and δ_z as a function of BW and the number of tracks in elevation for a wavelength of $\lambda_c = 0.23$ m. Clearly, the PSLR and the resolution in the z direction have a non-linear improvement as the number of tracks increases.

Additionally, the separation between tracks should also consider resolution and ambiguities in the $\text{LOS}_\perp$ direction, i.e., $\delta_{\text{LOS}_\perp}$ and $\delta_{\text{LOS}_{\perp,amb}}$, which were previously described in Section 2.5.2 [Ponc 13b]. In this case, the range of closest approach is defined as $|\, \vec{p} - \vec{R}_{l_m}\, |$, which is the distance from the master circular track (e.g., usually the middle track) to the desired scatterer. Certainly, to achieve the best 3-D image quality $\delta_{\text{LOS}_\perp}$ and δ_z should be of the same order. Also, it can be understood from (6.17) that the vertical resolution will be limited by the system bandwidth even for wide apertures in elevation. However, this case is valid only for highly directive targets or when sensing is performed only from one side of the scene, i.e., narrow synthetic aperture in the azimuth direction such as TomoSAR [Minh 15]. Alternatively, if the scene of interest is observed for a wider azimuthal aperture (e.g., multiple azimuthal measurements such as circular), then the vertical resolution can be improved as described in section 6.2 and [Ponc 14b]. The theory developed in this section will be further analyzed with the IRF in the frequency domain in the following section.

(a)

(b)
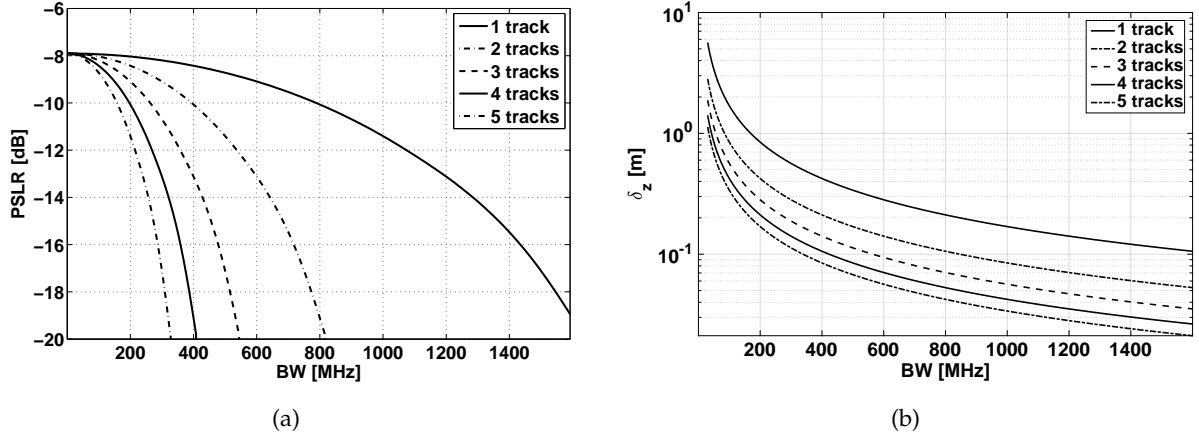
Figure 6.4: (a) Peak sidelobe ratio (PSLR) as function of the system bandwidth, BW, and the number of tracks in elevation. (b) Resolution in z direction as a function of BW and the number of tracks in elevation. Both curves assume that $\Delta B_{\mathrm{L}} \approx B_{\perp,\mathrm{crit}}$ and $\lambda_{\mathrm{c}} = 0.23$ m.

6.1.5 Frequency domain analysis of the IRF

An alternative to study the IRF of HoloSAR for point targets in and out the center is the analysis of their spectrum. The spectral support can be defined by the derivative of the phase function of the first exponential of (6.5), as follows

$$
\begin{aligned}
k_x &= \frac{\partial(-2k \cdot |\vec{p} - \vec{R}(\phi, \theta_{\mathrm{el}})|)}{\partial p_x} = \frac{2k \cdot (p_x - R_x)}{|\vec{p} - \vec{R}(\phi, \theta_{\mathrm{el}})|}, \\
k_y &= \frac{\partial(-2k \cdot |\vec{p} - \vec{R}(\phi, \theta_{\mathrm{el}})|)}{\partial p_y} = \frac{2k \cdot (p_y - R_y)}{|\vec{p} - \vec{R}(\phi, \theta_{\mathrm{el}})|}, \\
k_z &= \frac{\partial(-2k \cdot |\vec{p} - \vec{R}(\phi, \theta_{\mathrm{el}})|)}{\partial p_z} = -\sqrt{4k^2 - k_x^2 - k_y^2}.
\end{aligned}
\tag{6.19}
$$

In order to assess these expressions in a more representative way, a geometry similar to the experimental HoloSAR airborne campaigns, used in this thesis, was defined: $R_z = 2500$ m, $R_{xy} = 3700$ m, and $BW = 50$ MHz (see Section 6.4.1 and Section 6.5.1). Firstly, the IRF is analyzed for several central frequencies to better understand its behaviour as the wavelength changes. Figure 6.5 shows this simulation considering a fixed elevation angle θ_{el} and the following bands: P-(350 MHz), L-(1.29 GHz), S-(3.25 GHz), C-(5.3 GHz), and X-band (9.6 GHz). The images on the upper row illustrate the 3-D IRF spectrum in two different views, whereas the right image depicts the IRF in the time domain. Note that higher frequencies result in bigger gaps inside the ring-shaped spectrum, i.e., more missing frequencies, and thus, resulting in finer resolutions in the (x, y) plane. Conversely, lower bands offer coarser resolutions. In addition, it can be seen that the PSLR remains around -8 dB since a bandwidth of 50 MHz is used for the five cases (see Figure 6.5(c)). Interestingly, lower bands will show a greater PSLR for an increased system bandwidth, since spectrum gaps of the (k_x, k_y) spectrum are filled faster. This case is depicted in Figure 6.5(d), where the bandwidth is increased to 500 MHz, and in L-band and P-band the PSLR improves to -8.6 dB and -15.8 dB, respectively. Note than in general high-frequency systems have larger bandwidths than low-frequency ones, hence showing a better PSLR.
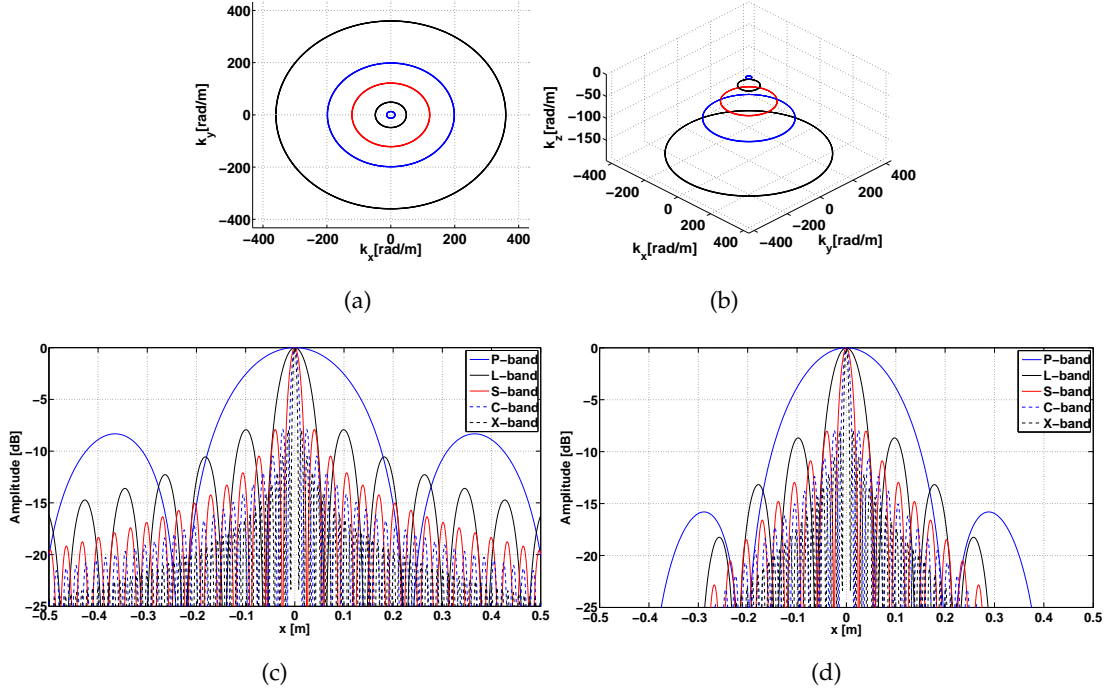
Figure 6.5: (a-b) Simulated multi-frequency spectrum for a target in the center with a chirp bandwidth of 50 MHz at different central frequencies: P-band (350 MHz, small blue), L-band (1.29 GHz, small black), S-band (3.25 GHz, red), C-band (5.3 GHz, blue), and X-band (9.6 GHz, black). (a) 2-D view. (b) 3-D view. (c-d) Amplitude in dB of the IRF in the x direction for the same wavelengths and two bandwidths, namely, (a) 50 MHz and (b) 500 MHz.

Moreover, the spectrum of HoloSAR is analyzed for a wavelength of $\lambda_c = 0.23$ m, and three targets at different positions, namely $\vec{p}_1 = (0, 0, 0)$, $\vec{p}_2 = (500, 500, 0)$, and $\vec{p}_3 = (1500, 1500, 0)$. Figure 6.6 illustrates the simulated spectrum for a constellation of three equally-spaced passes separated by a vertical distance of $\Delta B_{\mathrm{L}} = 400$ m (averaged $\Delta B_{\mathrm{L},\perp} = 331.44$ m), which is larger than the critical baseline $B_{\perp,\mathrm{crit}} = \min(256.16\,\mathrm{m}, 143.41\,\mathrm{m})$, in this way being more suitable for visualisation purposes. Notably, all images depict spectrum gaps, which occur due to the large separation between contiguous tracks, and as a result aliasing occurs every 1.58 m as shown in the time-domain IRF of Figure 6.8(b). Accordingly, the spectrum of every track is a part of a cone whose origin corresponds to the origin of the center of the circular trajectories, i.e., $(k_x, k_y, k_z) = (0, 0, 0)$. Therefore, off-the-center targets show slanted spectrums and IRFs.

Contrarily, Figure 6.7 shows the spectrum for a vertical baseline of twenty one passes separated by a distance of $\Delta B_{\mathrm{L}} = 40.0$ m. Since the averaged normal baseline $\Delta B_{\mathrm{L},\perp} = 33.1$ m has been reduced to a smaller magnitude than the critical baseline ($B_{\perp,\mathrm{crit}} = 143.41$ m), gaps do not occur (see also Figure 6.8(c)). Correspondingly, one can notice that the effective bandwidth is improved in this case by a factor of at least 3 and 5 in the horizontal and vertical planes, respectively. This results in geometric resolutions in the elevation direction of $\delta_{\mathrm{LOS}_\perp} = 0.8$ m and vertical direction of $\delta_z = 0.84$ m, and an interval of ambiguity in elevation $\delta_{\mathrm{LOS}_\perp,\mathrm{amb}}$ greater than 16 m.

Again, there is not a unique analytical solution for a target out of the center, and this can bee seen in the asymmetric shape of the spectrum of targets $\vec{p}_2$ and $\vec{p}_3$, which depends directly on
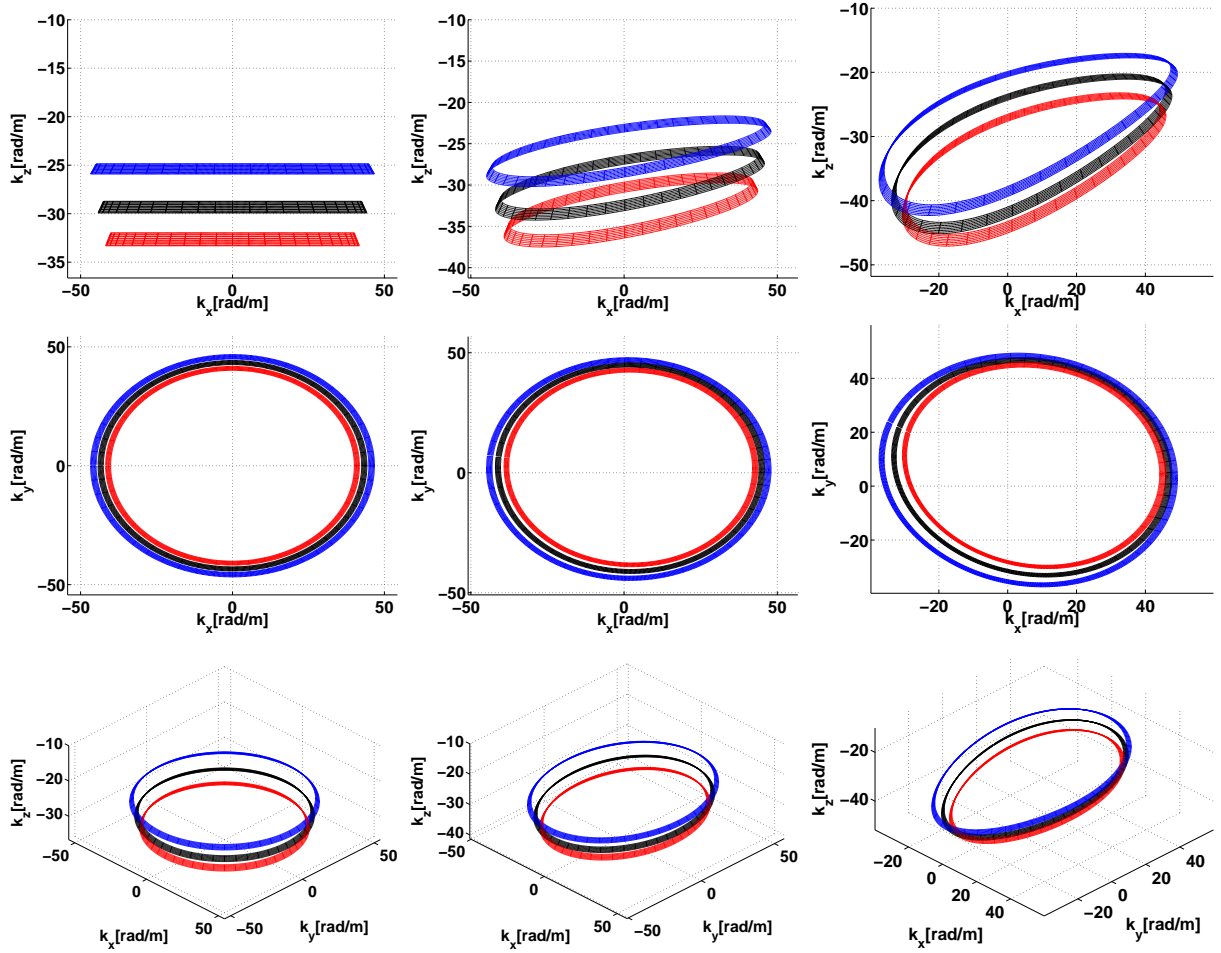
Figure 6.6: Simulated HoloSAR spectrum for a configuration of three circular passes with a vertical baseline of $\Delta B_{\mathrm{L}} = 400$ m, and for three targets ($\vec{p}_1$, $\vec{p}_2$, $\vec{p}_3$). Left column: $\vec{p}_1 = (0, 0, 0)$. Middle column: $\vec{p}_2 = (500, 500, 0)$. Right column: $\vec{p}_3 = (1500, 1500, 0)$.

the position of the target. In Section 6.5, this theory will be validated with the holographic tomogram of a Luneburg lens.

6.2 Focusing approaches of HoloSAR

In Section 5.3, coherent and incoherent imaging methods in the (x, y) plane in the CSAR mode for point-like and distributed scatterers were analyzed. It was shown that coherent imaging had better performance because targets were focused at their maximum resolution. In contrast, the incoherent approach depicted lower resolution because directivity and persistence are unknown for most of them. On the other hand, arcs or ring-shaped sidelobes in 2-D and cone-shaped artefacts in 3-D were also discussed. They occur due to the low resolution in the LOS$_\perp$ direction, and can be reduced by forming a synthetic aperture in elevation (see Section 3.4). Research with multicircular acquisitions and simulations have been carried out in recent years but only for highly-directive targets (e.g., man-made) and at higher frequencies (e.g., X-band).

In this respect, the goal of this Section is to investigate processing algorithms for the HoloSAR
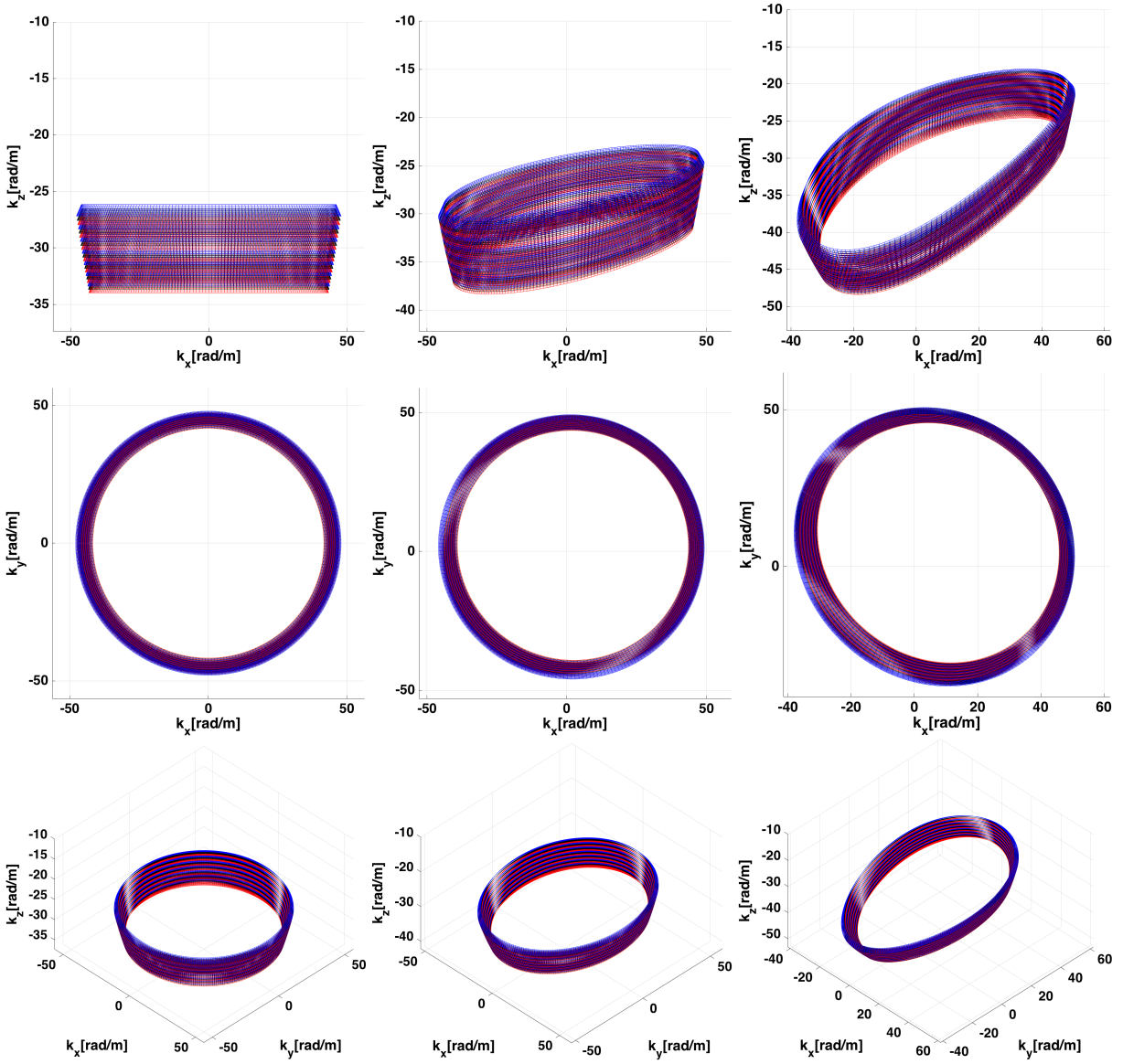
Figure 6.7: Simulated HoloSAR spectrum for a configuration of twenty one circular passes with a vertical baseline of $\Delta B_{\mathrm{L}} = 40.0$ m, and for three targets ($\vec{p}_1, \vec{p}_2, \vec{p}_3$). Left column: $\vec{p}_1 = (0, 0, 0)$. Middle column: $\vec{p}_2 = (500, 500, 0)$. Right column: $\vec{p}_3 = (1500, 1500, 0)$.

mode at lower bands, e.g., L- and P-band, and in the presence of mainly distributed targets, e.g., forested areas, semi-transparent media. This is done by understanding the backscattering in both the (x, y, z) and the $(\alpha, r, \mathrm{LOS}_\perp)$ spaces, thereby dividing the processing chain in three main approaches:

1. Coherent imaging.

2. Subaperture-based processing by incoherent imaging.

3. Subaperture-based processing using the GLRT method.

(a) $\Delta B_{\mathrm{L}} = 0$ m, 1 track　　(b) $\Delta B_{\mathrm{L}} = 400$ m, 3 tracks　　(c) $\Delta B_{\mathrm{L}} = 40$ m, 21 tracks
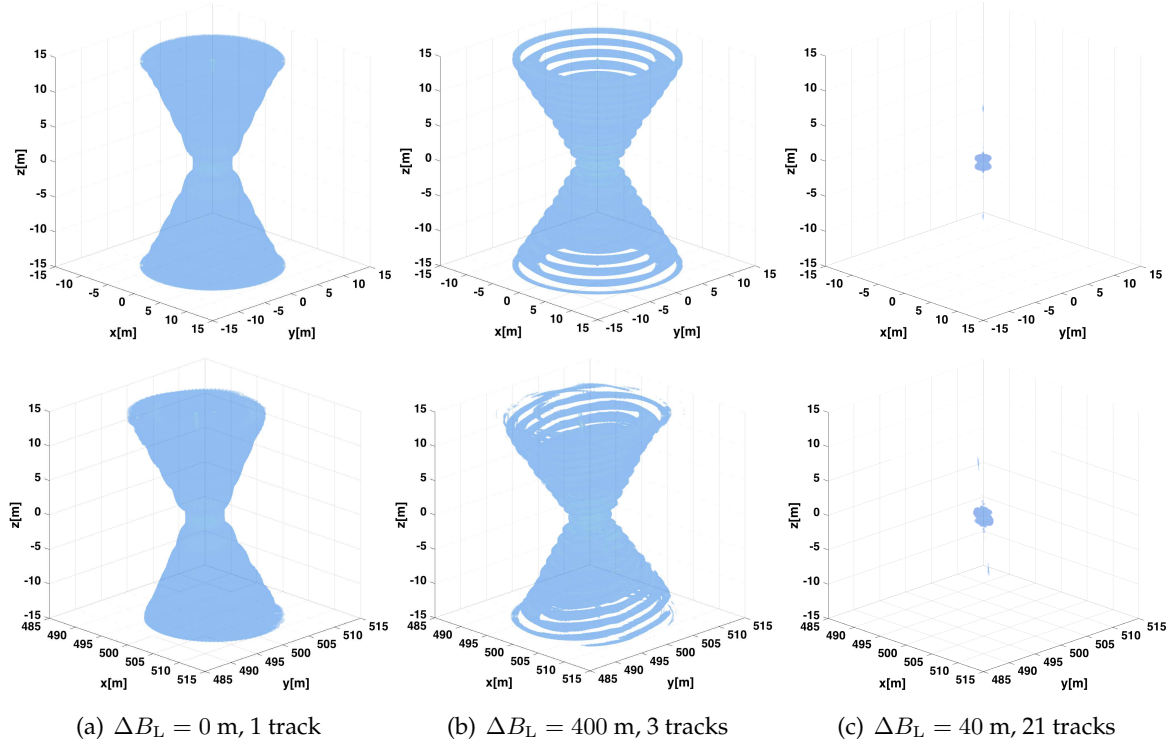
Figure 6.8: Simulated HoloSAR IRF for a configuration of three different vertical spatial baselines, and for two targets, $\vec{p}_1 = (0, 0, 0)$ (upper row) and $\vec{p}_2 = (500, 500, 0)$ (lower row). The corresponding spectra of all three-dimensional images can be seen in Figure 6.6 and Figure 6.7. The used threshold was set to see the voxels equal or greater than -13 dB.

6.2.1 Coherent imaging

The coherent processing of HoloSAR uses the FFBP for circular trajectories to compress the energy in both synthetic apertures, namely vertical and circular (see Section 4.2). That is to say that the FFBP is performed independently per circular flight, and afterward every 3-D image track is coherently combined in the (x, y, z) space to form the holographic tomogram. In addition, the expression given by (4.1) has to take into account L_{sub} as being partitioned by a factor of 2 in a recursive way, and the argument of the exponential as being defined by $\vec{r}_{\mathrm{grid},n}(\alpha, r)_{r_z}$ for different heights r_z and $\vec{R}(\phi, \theta_{\mathrm{el}})$ considering the synthetic aperture in elevation [Ponc 13b, Ponc 13a]. Another solution would be to do the FFBP directly in the $(\alpha, r, \theta_{\mathrm{el}})$ space, but for practical purposes the two-dimensional FFBP proposed in this thesis was used.

Due to the linearity of this approach, the acquisition geometry should fulfil the Nyquist criterion, thus being able to potentially achieve theoretical resolutions, as previously described in Section 6.1.4. Additionally, the computational load can be described as a modified version of (4.22) since now the number of circular passes and the number of images in the z direction have to be considered. Note that a factor that must be neglected is the computational load of the grids $O(\mathrm{grid})$, which can imply a significant change in the speedup factor, i.e., 2-D images are focused at a given height r_z and a DEM is not considered.

6.2.2 Subaperture-based processing

The second and third processing approaches are based on subapertures, i.e., the circular synthetic aperture is first divided in segments of $\Delta\phi$ degrees each. The subaperture number is indicated by $i = [1, .., N_{\text{sub}}]$, and the track number is denoted by $l = [1, .., l_{\text{m}}, .., M_{\text{t}}]$ with l_{m} being the master track used for processing.

In view of this fact, the 3-D processing is divided in four main stages:

1. The first stage is to focus N_{sub} stacks of 2-D images in the (r, α) plane using the FFBP (see Section 4.2). Every stack i of M_{t} images is denoted by the following expression

$$G_i = [s_{M_{\text{t}},\text{HH}}(\alpha, r)\, s_{M_{\text{t}},\text{VV}}(\alpha, r)\, s_{M_{\text{t}},\text{HV}}(\alpha, r)], \tag{6.20}$$

   (see Figure 6.9(a)). Unlike, the geometry used in the TomoSAR mode, this solution uses polar coordinates in the three dimensions, as depicted in Figure 6.9(b). It is important to remark that polarimetric decompositions (e.g., Pauli basis) should be done at this stage, since the solution of the third stage is not coherent.

2. The second stage is the phase calibration, and should be carried out per stack in order to improve the image quality in terms of resolution and PSLR along the third dimension. Unlike conventional phase calibration methods in the TomoSAR mode, the proposed approach performs an absolute calibration for all stacks, and it is based on the SVD of ground signatures (see Section 6.3).

3. The third step is the energy compression in the third dimension, namely the $\text{LOS}_\perp$ direction. To that end, BF (linear) and CS (non-linear) are used for every given position (α_0, r_0), i.e., a 1-D tomographic signals will be retrieved (see Section 2.5.2).

   Since it is expected to have non-deterministic targets, i.e., distributed, it is necessary the use of second order statistics, i.e., covariance matrices (see Section 2.5.2). However, at the cost of loosing resolution in both r and α dimensions. That is to say that the L neighbouring pixels of $G_i(\alpha_0, r_0)$ for the given position (α_0, r_0) should be considered as measurements (see Figure 6.9(a)). In this way, the complex measurements $Y = G_i'(\alpha_0, r_0)$ are of the form $Y \in \mathbb{C}^{3M_{\text{t}} \times L}$. On the other hand, the 3-D coordinate system is defined with respect to the master track l_{m} of every sub-aperture i and HH channel, where every voxel has the coordinates $x_p(\alpha, r, \theta_{\text{el}})$.

   Knowing the structure of Y and the 3-D geometry that defines the sensing matrix A, the system can be described as $YY^\dagger = A \operatorname{diag}(P)^\dagger A^\dagger$, where $A \in \mathbb{C}^{3M_{\text{t}} \times 3N_{\text{el}}}$ with $M_{\text{t}} \ll N_{\text{el}}$, and $P = \operatorname{diag}(XX^\dagger)$ as the desired reflectivity that contains the intensity of $X \in \mathbb{C}^{3N_{\text{el}}}$ (see Section 3.5.4).

   The solution with BF is dictated by $\widehat{x}_{\text{BF},i} = P$, whereas the problem with CS is addressed as follows

$$\widehat{x}_{\text{CS},i} = \arg\min_p \left\| YY^\dagger - A \operatorname{diag}(P) A^\dagger \right\|_F^2 + \lambda_1 \left\| \Psi \cdot P \right\|_1 \tag{6.21}$$

   where the signal P is assumed to be sparse in the Wavelet basis Ψ, $\|\cdot\|_F$ denotes the Frobenius norm, and λ_1 is a positive value that controls the trade-off between sparsity in

Ψ and the model mismatch. The total-variation (TV) norm was not used for this model, since the difference in image quality was not significant.

4. The last stage is the merging of all 3-D fully polarimetric images incoherently and statistically with the GLRT to form the holographic SAR tomogram. This will be discussed in detail in the following subsections.

(a) 2-D measurements G_i.

(b) 3-D geometry.
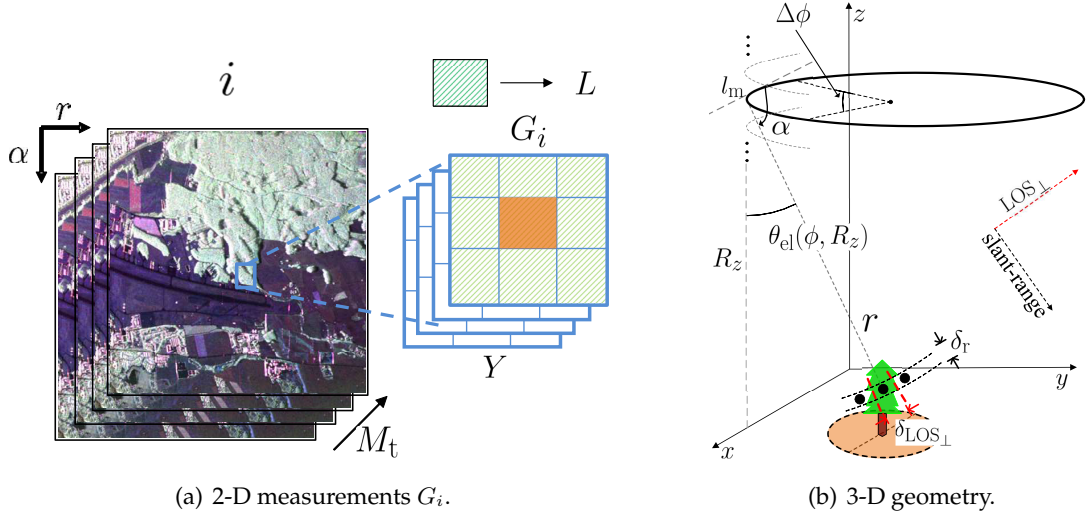
Figure 6.9: (a) G_i: stack of two-dimensional images in polar coordinates (α, r) corresponding to the subaperture i. The energy along $\text{LOS}_\perp$ for the (α, r) position (red) is retrieved by taking the measurements Y with the L neighbouring pixels (yellow) and using second-order statistics. (b) The system geometry is defined with respect to the master track l_m of the HH channel for every subaperture i in polar coordinates $x_p(\alpha, r, \theta_\text{el})$.

This solution is driven by the fact that cone-shaped sidelobes are function of the elevation and rotation angles, i.e., θ_el and ϕ, so they can be better suppressed in the $\text{LOS}_\perp$ direction with second-order statistics and non-linear methods, such as CS [Ponc 14b, Ponc 12]. In addition, the sampling criterion corresponding to a single subaperture in the $(\alpha, r, \theta_\text{el})$ space is much smaller than the criterion when focusing coherently the full circular aperture in the (x, y, z) space. This way of processing decreases the computational burden, but some scatterers might not be focused at their maximum resolution because angular persistence and directivity remains unknown for most of them.

Another advantage of this processing chain is the consideration of the wavefront curvature by using polar coordinates. Previous solutions with multicircular SAR acquisitions presume plane wavefronts and propose models based on 2-D and 3-D FFTs, i.e., the sensing matrix A defined by FFTs, however they are limited to very small regions [Aust 11, Ferr 09, Aust 09, Erti 10]. In contrast, the polar-based solution has the potential to use CS approaches based on FFTs for wide areas. Nevertheless, this is not discussed in detail, since it is out of the scope of this thesis.

(a) Horizontal plane (x, y).   (b) Vertical plane (x, z) or (y, z).
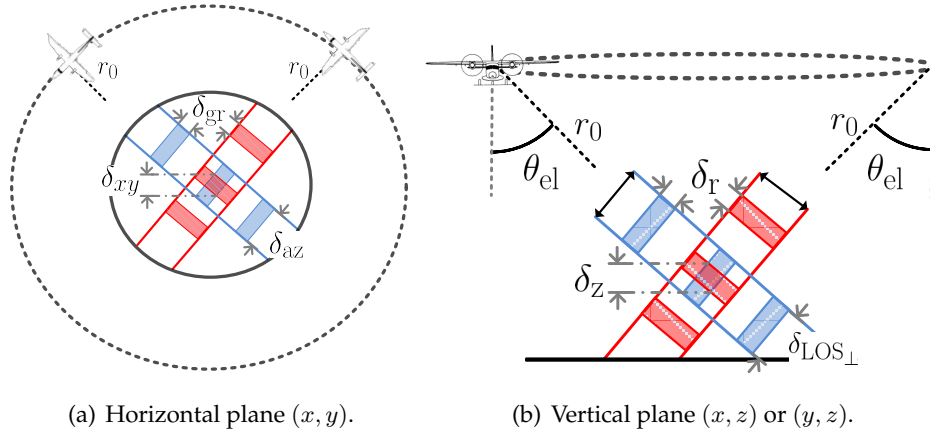
Figure 6.10: Three-dimensional resolution improvement corresponding to the incoherent imaging from two different look angles. Note that the geometric resolution values δ_{xy} and δ_z are improved for targets persisting longer than the subaperture size $\Delta\phi$. The elevation angle is indicated by θ_{el}, the closest approach is r_0, δ_{gr} is the ground range resolution, δ_{az} is the resolution in the along-track direction, $\delta_{LOS_\perp}$ is the resolution in the direction perpendicular to the line of sight, and δ_r is the range resolution.

Incoherent imaging

In order to add incoherently the energy of every 3-D image $\widehat{x}_{(.),i}(\alpha, r, \theta_{el})$, a global cartesian grid has to be defined, (x, y, z). This solution is performed under the assumption of natural targets, i.e., not man-made nor highly directive. Hence, the energy of scatterers with persistence longer than $\Delta\phi$ will be added up, and the best resolution in the (x, y) plane will be given by the geometric mean resolution between α and r directions, which are already degraded by multilooking during the tomographic processing in elevation (see stage 3). Similarly, the final resolution in the z direction will be given by the averaged geometric resolution between r and $LOS_\perp$ directions (see Figure 6.10). In fact, this plays an important role for vertical structure imaging, such as forests. Note that in the TomoSAR imaging mode with low-bandwidth systems, even with a very large synthetic aperture in elevation, the resolution in δ_z will not be enhanced, contrary to HoloSAR.

Moreover, scattering mechanisms are also separated by their polarimetric signature (HH-VV-HV), e.g., in forested areas and in the Pauli basis canopies are distinguished from tree trunks. This solution allows the recovering of different phase centres per subaperture, thus retrieving much more information than the linear SAR modes. In fact, this will be further discussed in the analysis of experimental results in Section 6.4.

Generalised likelihood ratio test (GLRT) imaging with coherent averaging

In order to use the GLRT for distributed targets a model based on second-order statistics was used. That is to say that in the statistical model the L neighbouring pixels are also taken into account, as it is the way of focusing along the $LOS_\perp$ direction. The GLRT algorithm is described

by the following analytical expression

$$I_G[\vec{r}_{\text{grid}}] = arg \max_{\phi_i, \Delta\phi, pol} \|I_i(\vec{r}_{\text{grid}}; \phi_i, \Delta\phi, pol)\|, \tag{6.22}$$

where $I_i(\cdot)$ is the intensity of the subaperture tomogram i of width $\Delta\phi$, e.g., $10°$, with $\left[-\frac{\Delta\phi}{2} + \phi_i, \frac{\Delta\phi}{2} + \phi_i\right]$ azimuthal support and polarisation *pol*. Eq. (6.22) pursues the best solution that maximises the intensity $I_G[\cdot]$ as a function of ϕ_i, $\Delta\phi$ and *pol*. Note that the main difference between the model described in [Vocc 09] and this model is the coherent averaging, which is given by the neighbouring pixels, since $I_i(\vec{r}_{\text{grid}}; \phi_i, \Delta\phi, pol)$ is estimated under the assumption of distributed scatterers.

Note that weighting is used in the range direction to suppress strong sidelobe contributions. This will be reflected as a slightly reduction in the system bandwidth coverage. Also, for all three methods, scattering mechanisms are also separated by their polarimetric signature (HH-VV-HV), e.g., canopies are well distinguished from the double-bounce reflection between ground and tree trunks in forested areas when the scattering matrix is decomposed in the Pauli basis. The HoloSAR imaging mode allows the recovery of multi-angular phase centres, thus retrieving much more information than the linear SAR modes. Figure 6.11 summarises through a flowchart the three processing approaches, namely coherent, incoherent and GLRT imaging.
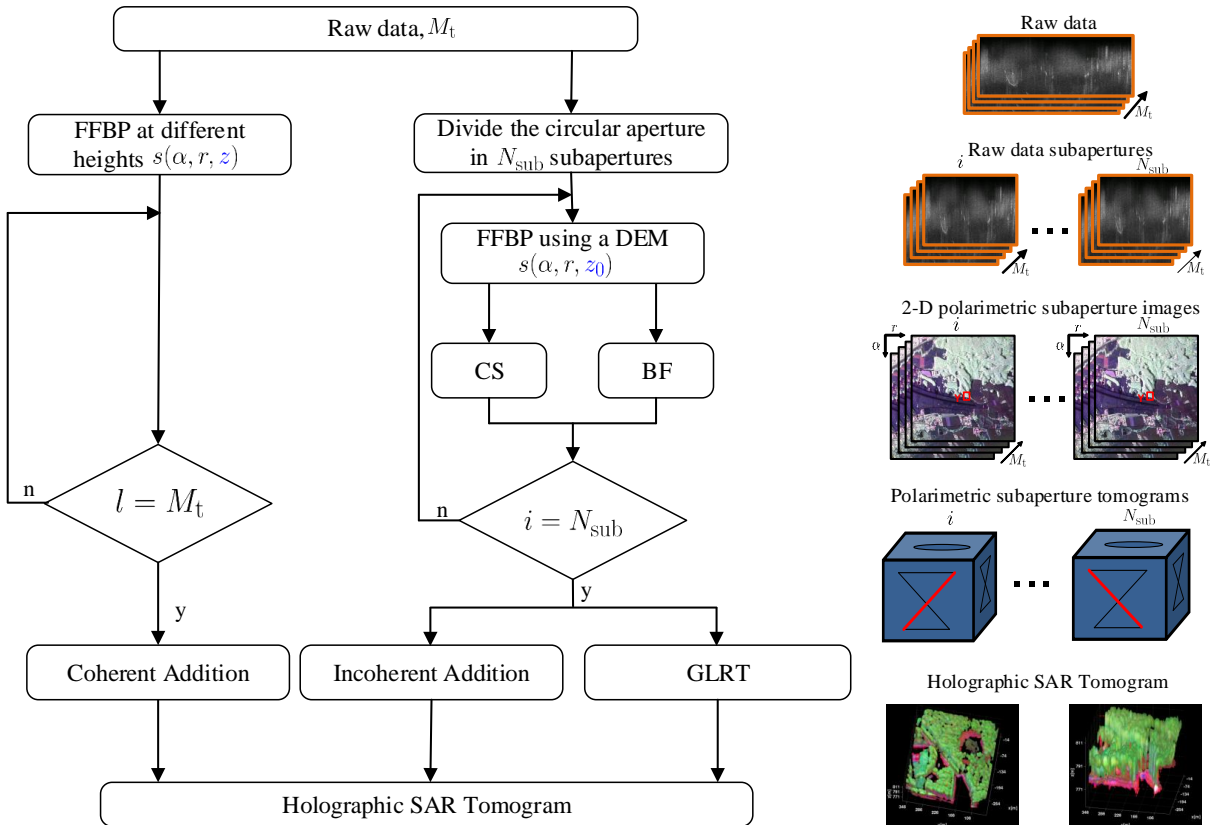
Figure 6.11: Flowchart of the processing chain of holographic SAR tomography mode. Right side: overview of the incoherent imaging with the CS and assuming sparsity in the wavelet basis.

6.3 SVD-based phase calibration

As described in Section 3.6, in order to achieve theoretical resolutions for wide-angular synthetic apertures the antenna phase center has to be estimated with high accuracy, depending on the required resolution. However, most of the conventional navigation systems do not fulfil the accuracy requirements. The methodology of this approach is based on the analysis of strong ground returns, and it is defined as follows.

Let us define the input of this algorithm as N_{sub} stacks of M_{t} fully polarimetric 2-D coregistered images, which are focused in the (α, r) plane (see Section 6.2.2). The input measurements, containing the information of the reference point, are described as $B_{i,HH-VV-HV} = [B_{i,HH} \; B_{i,VV} \; B_{i,HV}]$, and for simplicity the channel indicators are not used in the following description. In addition, a constant phase error per image l and per channel is estimated for a given stack i of M images for every channel HH, VV and HV.

The measurement vector is then described as $B_i = [b_l, ..., b_{M_{\text{t}}}]$ and the steering vector for the reference target is given by $B_{i,\text{ref}} = [b_{l,\text{ref}}, ..., b_{M_{\text{t}},\text{ref}}]$, so that the error vector can be estimated as $B_{\text{error},i} = B_i(-r_{\text{real},l} + \psi_{\text{rand}}) \cdot B_{i,\text{ref}}^*(r_{0,l})$ with

$$b_{\text{error},l} = \sigma \cdot \exp\left(j\frac{4\pi}{\lambda_{\text{c}}} \cdot (-r_{\text{real},l} + r_{0,l}) + \psi_{\text{rand}}\right), \tag{6.23}$$

where σ is the normalised amplitude, $r_{\text{real},l}$ is the real distance to the target, ψ_{rand} is the random phase due to speckle, $r_{0,l}$ is the distance computed from the platform to the reference point on ground, and $\psi_{err,l} = r_{0,l} - r_{\text{real},l}$ is the desired phase error.

However, the information contained in the images is degraded by multiplicative noise or speckle, which is described by ψ_{rand}, and makes the phase estimation unstable. In order to stabilise and denoise the signature, coherent averaging with the singular-value decomposition (SVD) is used. That is to say that instead of having a vector of B_i of M_{t} measurements, the input will be a matrix B_i of M_{t} by L measurements, where L is the number of neighbouring pixels in the range and the angular directions. Afterward the first singular vector of the SVD of B_i, i.e., $B_i = U\Sigma V^{\dagger}$ is taken under the assumption of a single phase center in the measured pixels. In this way, the matrix B_i can be reduced to a vector $\widehat{B}_i = B_i V'$, which contains the information of the strongest component, i.e., ground, significantly reducing the contribution of speckle. In fact, this solution is based on the theory previously described in Section 3.6.2. The new estimation is then given by the argument of $B_{\text{error},i} = \widehat{B}_i \cdot B_{i,\text{ref}}^*$ with

$$b_{\text{error},l} = \sigma \cdot \exp\left(j\frac{4\pi}{\lambda_{\text{c}}} \cdot (-r_{\text{real},l} + r_{0,l})\right). \tag{6.24}$$

An absolute calibration over the whole circular synthetic aperture can be performed by a given reference point from a DEM or a GPS measurement, in this way, achieving an accurate focusing. Contrarily, if the calibration is performed relative to every subaperture, then the resulting holographic tomogram could be out of focus.

The SVD-based phase calibration has the advantage of having a low computational cost because it converges with one iteration, and it is a suitable solution for experiments at low-frequency bands with narrow bandwidth for distributed scatterers, where very high resolution is not needed (see Section 6.4).

6.4   Holographic SAR tomography at P-band

(a)

(b)

(c)
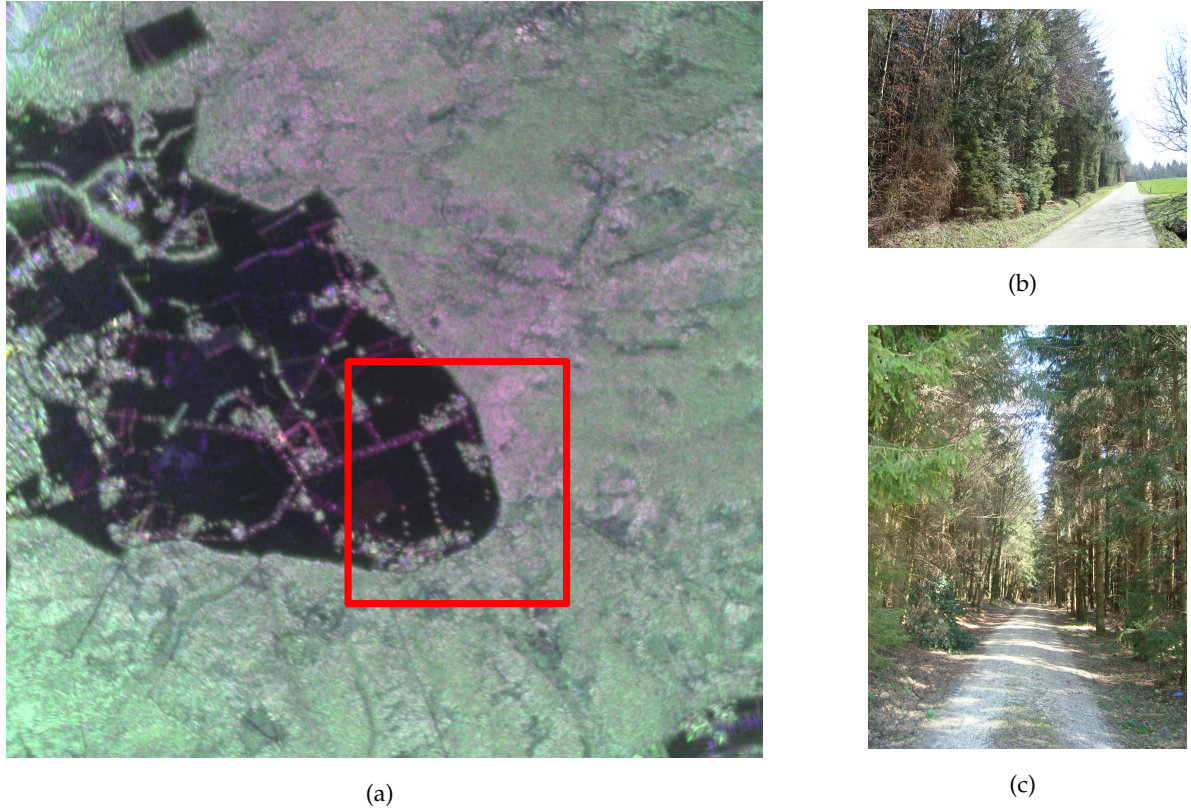
Figure 6.12: (a) Image in Pauli basis (blue: HH+VV, red: HH-VV, green: 2HV) focused with the FFBP, $360°$ integration processing using a DEM, region of Vordemwald, Switzerland, 2.6 km by 2.6 km, 0.25 m by 0.25 m sampling, red square: region of interest. (b)-(c) Optical images of the test site.

This section is devoted to demonstrate and validate the HoloSAR mode with multicircular data at P-band for the imaging of semi-transparent media [Ponc 14b]. Unlike L-band, P-band retrieves a stronger signature from ground than from the canopy, as shown in the remaining part of this chapter. Incoherent imaging with the FFBP for circular tracks, compressive sensing and beamforming (BF) are the approaches to focus holographic tomograms (see Section 6.2). A further purpose of this data collection is the validation of the SVD-phase calibration algorithm, which estimates constant phase errors from strong ground returns of multiple fully polarimetric 2-D images acquired at different positions in elevation, thus improving focusing in the LOS$_\perp$ direction (see Section 6.3).

6.4.1   Multicircular P-band campaign

The acquired multicircular data set consists of seven circular-like continuous passes obtained at different altitudes at P-band ($f_c = 351$ MHz) using the DLR's F-SAR system in 2012 (see Figure 6.13(a)). The test site is a forested region of 2.6 km by 2.6 km around the village of Vordemwald, Switzerland as seen in Figure 6.12. This area is limited by the capability of the aircraft to keep a certain roll angle, and by the projection of the 3 dB antenna pattern. As seen in Figure 6.13, the roll angle was around $-9°$, the pitch angle was in average $2.5°$, and the heading angle was

oscillating from $0\,^\circ$ to $360\,^\circ$ for every full circle. On the other hand, the antenna depression angle was $45\,^\circ$ with apertures of $20\,^\circ$ and $48\,^\circ$ in azimuth and elevation, respectively (see Figure 6.14). Certainly, the feasibility of imaging always the same spot during the whole acquisition with fixed antenna beams increases at lower bands (e.g., L- or P-band), than at higher bands (e.g., X-band). Furthermore, during this acquisition the aircraft was following predefined circular paths at different heights, thus performing more ideal-like synthetic apertures (e.g., circular and vertical apertures) and maximising the illuminated region. Therefore, the covered region of the P-band campaign increases by 1 km in diameter in comparison with the CSAR L-band survey.

(a)

(b)

(c)

(d)
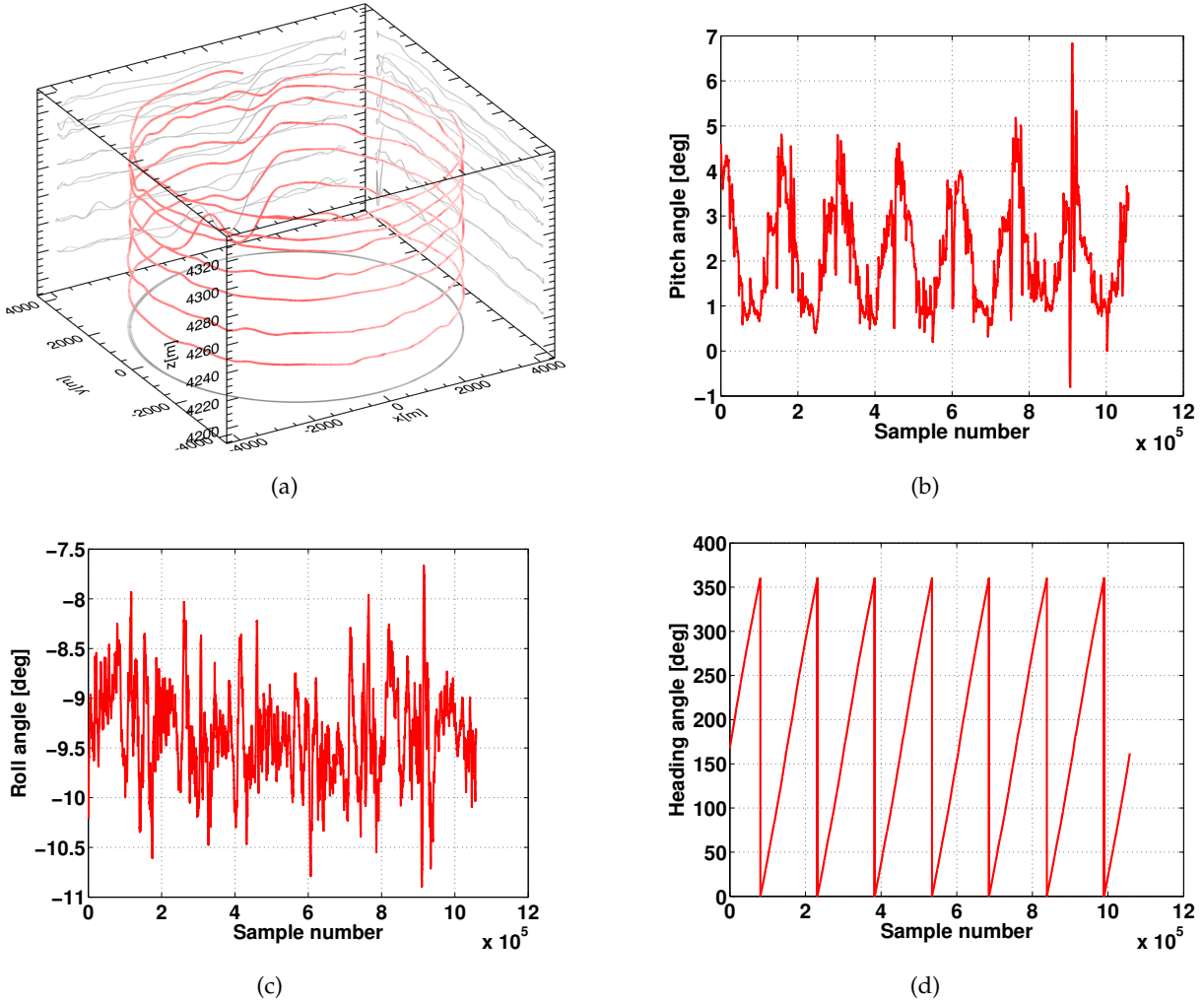
Figure 6.13: (a) 3-D track profile: experiment flown with the DLR's F-SAR sensor at P-band over the region of Vordemwald, Switzerland in 2012. Mean radius: 3850 m, mean altitude: 4270 m. (b)-(d) Aircraft attitude for the experimental acquisition with seven circular passes at P-band. (b) Pitch angle: mean of $2.5\,^\circ$. (c) Roll angle: mean of $-9\,^\circ$. (d) Heading angle: oscillates from $0\,^\circ$ to $360\,^\circ$ for every circular acquisition.

Due to Swiss RF regulations the allowed chirp bandwidth was limited to 20 MHz corresponding to a range resolution of $\delta_r = 7.5$ m. The aircraft operation was restricted to a certain flight level allowing a maximum and a minimum vertical baselines of $L_H = 120$ m and $\Delta B_L = 12$ m, respectively. The baseline distribution in the vertical direction was 12 m, 12 m, 18 m, 18 m, 24 m and 24 m. This particular configuration allows one to have a theoretical resolution in the

LOS$_\perp$ direction of $\delta_{\text{LOS}_\perp} \approx 27$ m and aliasing at $\delta_{\text{LOS}_\perp,\text{amb}} \approx 165$ m. In addition, the irregular distribution of the circular flights in the vertical direction was chosen to reduce mismatches during the compression in elevation, particularly with CS (see Section 3.5.4) [Axel 04]. The main parameters of this campaign are also summarised in Table A.2.
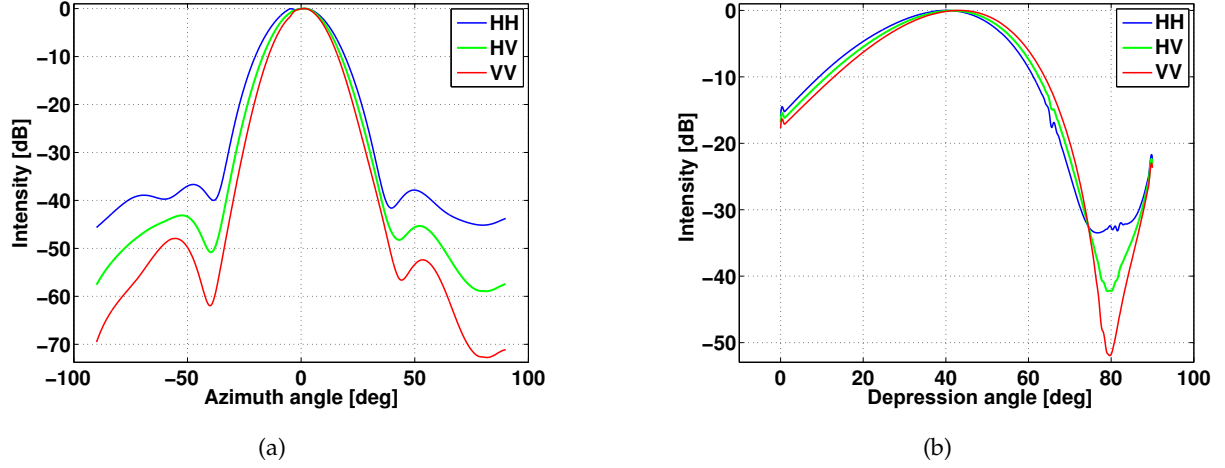
Figure 6.14: 1-D antenna patterns for the multicircular campaign at P-band. (a) Azimuth pattern with an angular resolution of $20\,^\circ$. (b) Depression pattern with an angular resolution of $48\,^\circ$. Note that the antenna pointing angle is about $45\,^\circ$.
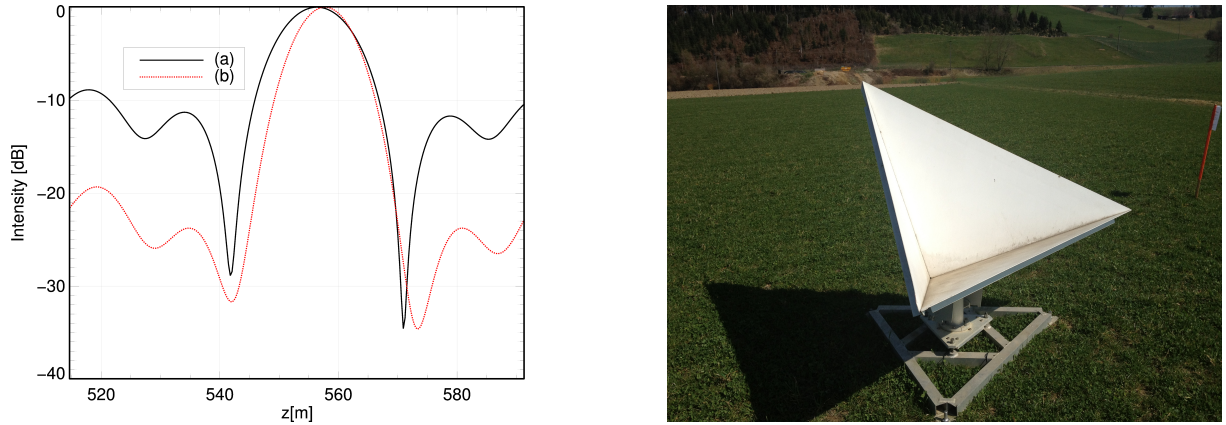
Figure 6.15: Left: Normalised intensity in dB as function of height z of a trihedral corner reflector of 1.5 m size pointing to the North. Before ((a) black line) and after ((b) red-dotted line) phase calibration using SVD. Right: Optical image of the corner reflector in the test site.

6.4.2 Experimental results

Due to limited access to the experimental area and the complex manoeuvres of placing enough reference targets as needed for the circular synthetic aperture, a trihedral corner reflector of 1.5 m size pointing to the North was set up. This reflector was used to validate the phase calibration algorithm with the following parameters for 3-D processing: angular integration of $\Delta\phi = 10\,^\circ$, $N_{\text{sub}} = 36$ subapertures, $M_{\text{t}} = 7$ circular passes or samples in elevation, and $L = 15$ neighbouring pixels. Figure 6.15 depicts the normalised intensity along height before and after phase calibration. Correspondingly, the phase-calibrated impulse response using BF

shows a better PSLR of about 10 dB difference, a more accurate position of the peak, as well as an improved resolution.
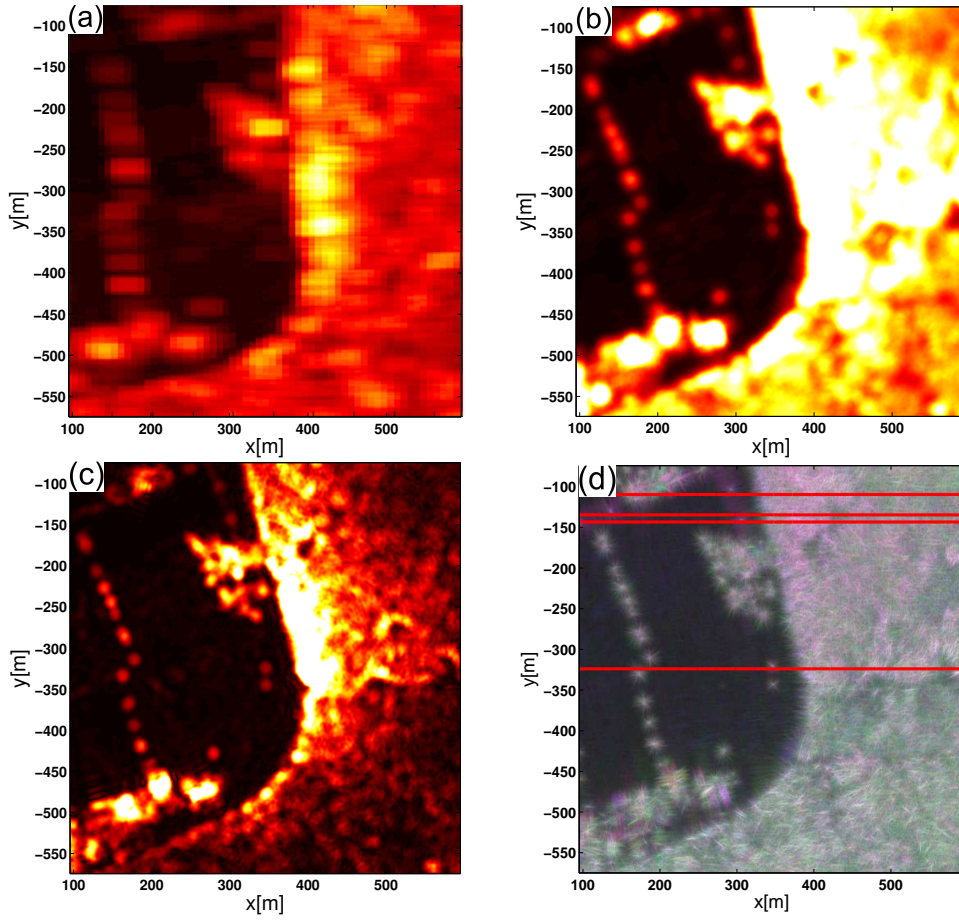
Figure 6.16: Region of 500 m by 500 m in Vordemwald, Switzerland. (a-c) Slices of the polarimetric SAR tomogram (total power) in the ($z = 554$ m) plane. (a) $\Delta\phi = 10\,°$, beamforming (BF), resolution similar to a TomoSAR tomogram. (b) $\Delta\phi = 360\,°$, incoherent imaging with BF. (c) $\Delta\phi = 360\,°$, incoherent imaging with compressive sensing (CS). Note the large improvement of resolution when going from (a) to (b) with BF, and from (b) to (c) with CS. (d) Image in the Pauli basis (blue: HH+VV, red: HH-VV, green: 2HV), $360\,°$ coherent processing with a single circular track and using a digital elevation model (DEM), 0.25 m x 0.25 m sampling. Red lines indicate the positions of the slices in the (x, z) plane shown in Figures 6.17-6.18.

After calibrating the phase of the 36 stacks for all polarisations, the energy in elevation should be retrieved to form the holographic tomograms. To that end, the next parameters per polarimetric channel were set: unknowns $\widehat{x}_{BF}$ and $\widehat{x}_{CS}$ of $N_{el} = 256$ pixels, Ψ containing the wavelet basis, and a penaliser of $\lambda_1 = 0.8$. The size of the processed area is 500 m by 500 m by 76 m in the (x, y, z) space (see region delineated with a red square in Figure 6.12). The results were focused with BF and CS, and are divided into two parts: analysis of the horizontal plane (x, y), and analysis of the vertical plane (x, z).

Figure 6.16(a-c) show the total power of the (x, y) slices at $z = 554$ m using three different processing approaches, as follows. Figure 6.16(a) is the image obtained with a single subaperture, which is analogous to the TomoSAR mode. Notably, resolutions in the (α, r) plane are degraded by coherent averaging, and consequently in the (x, y) plane. The transition from Figure 6.16(a)

(a) Lexicographic basis.
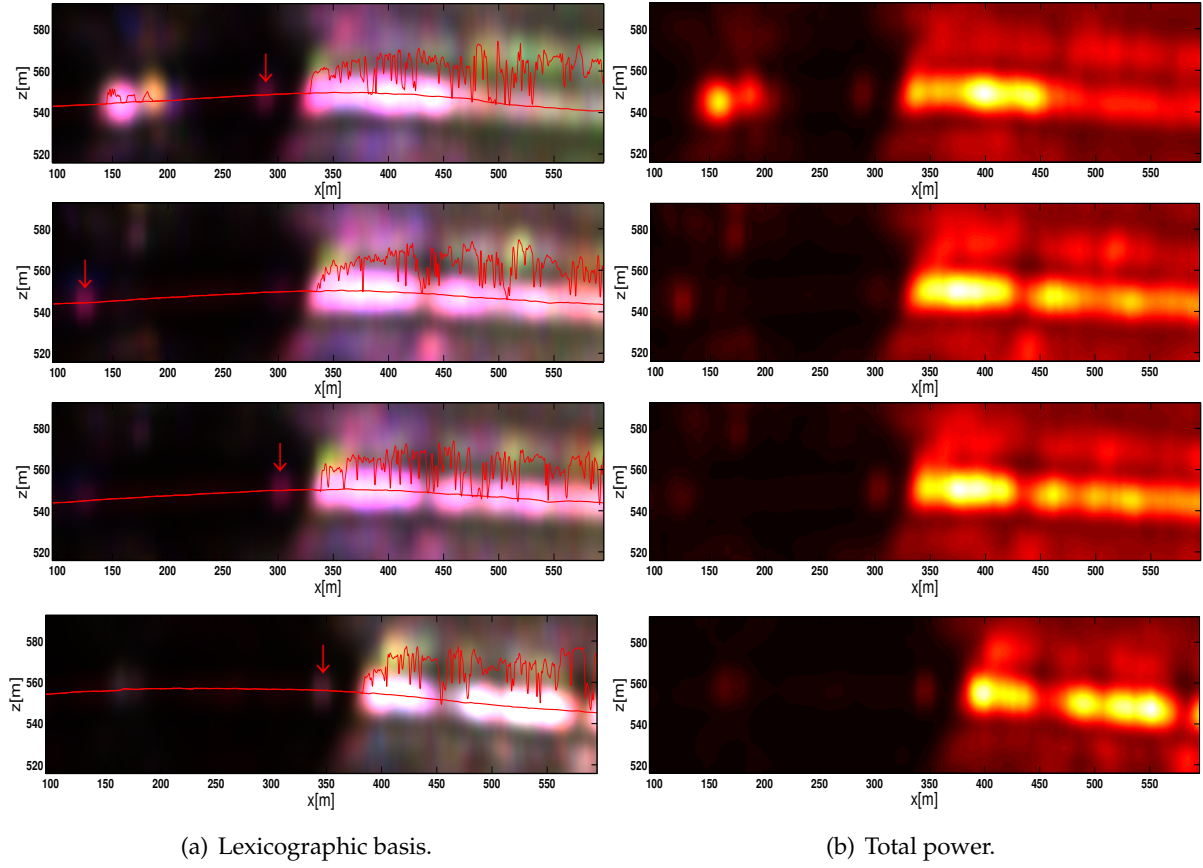
(b) Total power.

Figure 6.17: Slices in the (x, z) plane of the HoloSAR campaign at P-band in (a) the Lexicographic basis (blue: HH, red: VV, green: HV), and (b) Total power. The holographic tomograms were focused with beamforming (BF). The profile, shown with a red line, indicates the measurements of a LIDAR sensor (©SwissTopo). Point-like targets are indicated with red arrows: light-poles in the first three rows, and a corner reflector in the last row. Note that sidelobes in elevation degrade the image since only seven tracks were used.

to Figure 6.16(b) exemplifies the resolution improvement in the x and y directions by incoherent subaperture addition for targets that persist longer than $\Delta\phi$. This enhancement is given by the best resolution between r and α directions. Finally, as depicted in Figure 6.16(c), SCR and resolution for distributed and point-like scatterers are enhanced using CS. Targets, whose true height is $z = 554$ m are focused and show more energy than the targets that do not lie at this height. Ring- and arc-shaped sidelobes are not present, since the resolution in the $\text{LOS}_\perp$ direction is improved. Figure 6.16 (d) shows the region of interest in the Pauli basis. The image was focused coherently over $360°$ using in the CSAR imaging mode with the FFBP and a DEM (see Chapter 5). Due to the low system bandwidth, the spiky pattern shows low PSLR. The signal is then enhanced in the HoloSAR mode, where coherent averaging stabilises the signal due to the few measurements in elevation.

Regarding the vertical plane (x, z), Figure 6.17 depict slices focused with BF in the Lexicographic basis and the total power. These slices are indicated in Figure 6.16 (d) with red lines, and they correspond to the following positions: $y = -110$ m, $y = -135$ m, $y = -143$ m and $y = -324$ m from the upper row to the lower row, respectively. The LIDAR measurements (solid red line) show a good agreement with the obtained tomograms, hence demonstrating the

(a) CS in Lexicographic basis.

(b) CS total power.
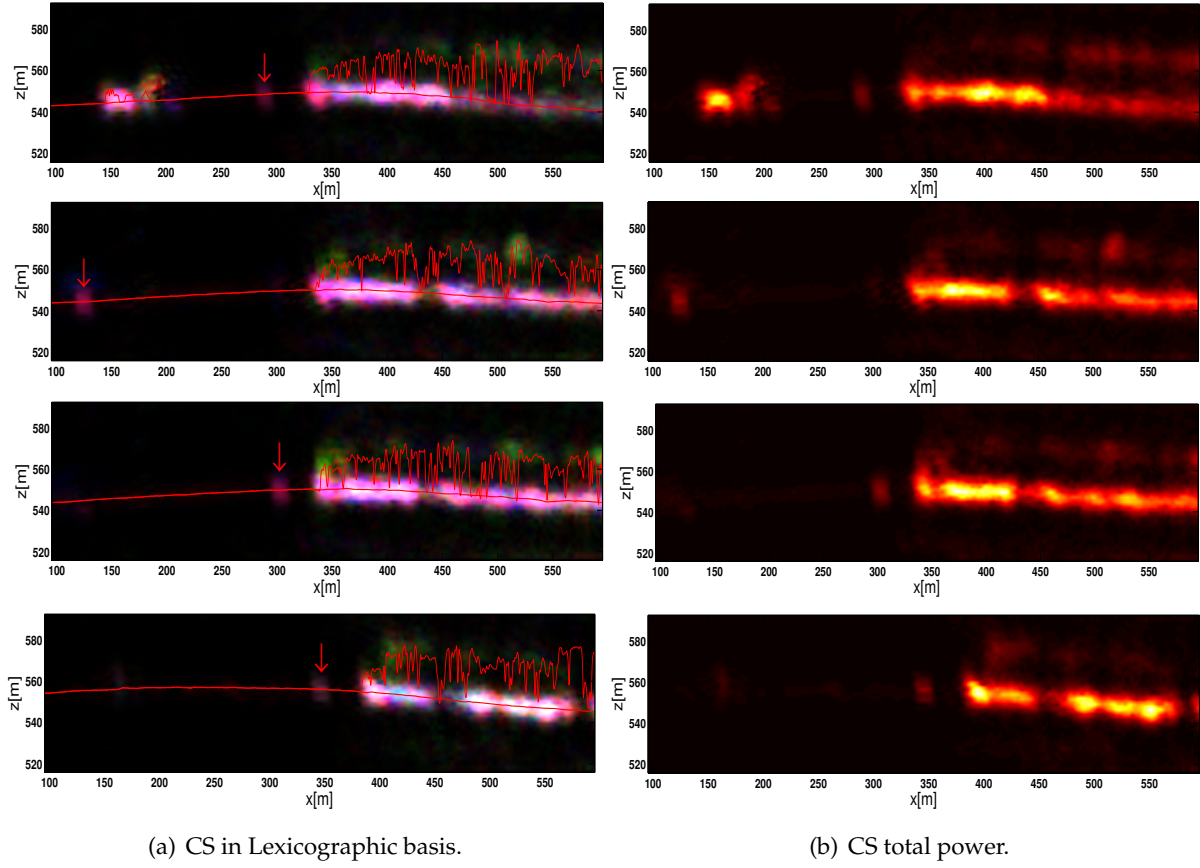
Figure 6.18: Slices in the (x, z) plane of the same positions in y direction as Figure 6.17, and focusing carried out with compressive sensing (CS) assuming sparsity in the wavelet basis. The holographic tomograms are in (a) the Lexicographic basis (blue: HH, red: VV, green: HV), and (b) total power. Also, LIDAR sensor (©SwissTopo) measurements are indicated with a red line. Point-like targets are indicated with red arrows: light-poles in the first three rows, and a corner reflector in the last row. In comparison to Figure 6.17 sidelobes in elevation (i.e., $\text{LOS}_\perp$) are highly reduced.
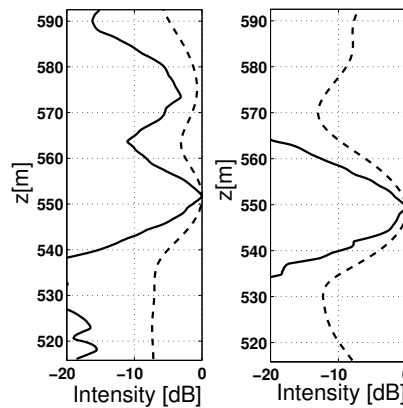
Figure 6.19: 1-D profiles BF (dotted) vs CS, z slices. Left image: tree structure, right image: light-pole. Note the improvement in resolution and the reduction of the cone-shaped sidelobes when using CS.

high precision of the proposed processing chain. Although the signal in elevation is stabilised by coherent averaging, cone-shaped sidelobes are not fully suppressed due to the limited num-
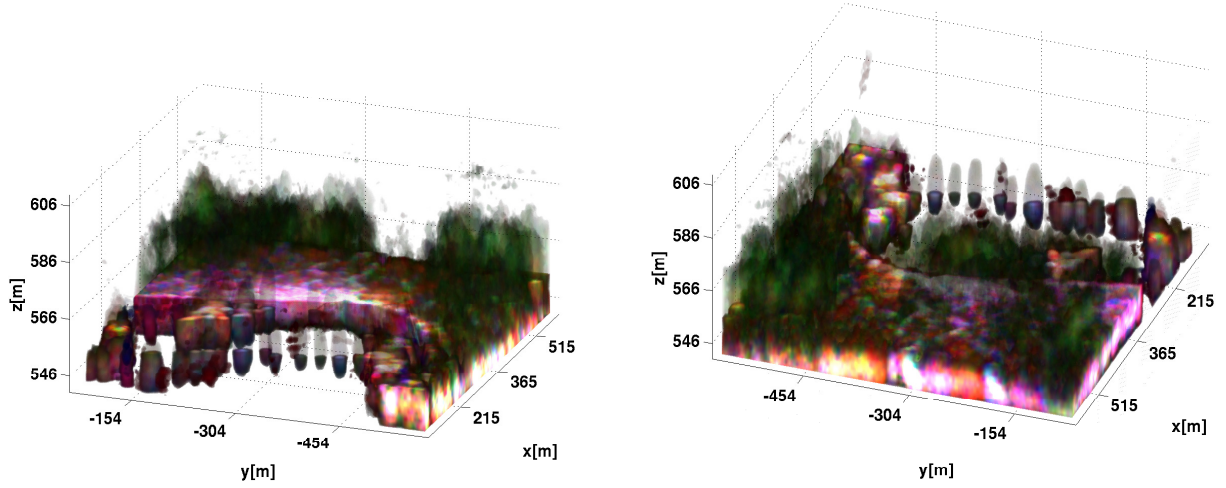
Figure 6.20: Fully polarimetric holographic SAR tomogram in the Lexicographic basis (blue: HH, red: VV, green: HV) using compressive sensing (CS). Both images show the same scene but rotated on the horizontal plane by $180°$. Voxels above ground have transparency to see through the forest. Note that trees structures in the forest are well reconstructed.

ber of measurements in elevation. Particularly, they occur in the right half of the holographic tomograms, where there are more than one phase centres. As a comparison, Figure 6.18 depicts the (x, z) slices at the same positions but focused with CS. Generally, sidelobes in elevation are highly reduced, thereby enhancing the signature of the tree trunks and canopies. In addition, point-like targets, indicated with red arrows, are also improved. These targets correspond to light poles in the first two rows of both Figures, whereas the last two rows indicate corner reflectors.

Furthermore, Figure 6.19 shows 1-D profiles of a tree (left image) at $(x = 470\,\text{m}, y = -287\,\text{m})$ and a light-pole (right image) at $(x = 290\,\text{m}, y = -109\,\text{m})$. As expected, the signature from the ground is stronger than the one from the canopy. In fact, some additional contribution can also appear due to ground penetration. Although resolution in the $\text{LOS}_\perp$ is improved with CS, the resolution of the ground in the vertical direction is limited by the range resolution, which is already degraded by coherent averaging. Again, images processed with CS for point-like and distributed targets show a high improvement in the resolution and a reduction of cone-shaped sidelobes of around 10 dB. Lastly, Figure 6.20 shows the 3-D rendering of the holographic tomogram using CS. These results indicate a better retrieval of tree canopy with respect to the conventional TomoSAR mode, since more . This holographic tomogram demonstrates the potential of this imaging mode for the monitoring of vegetated areas, a potential that is currently being investigated.

6.5 Holographic SAR tomography at L-band

The main goal of this section is to validate and analyse the HoloSAR concept at L-band over semi-transparent media. To that end, a fully polarimetric data collection over a forested area is analysed for three different focusing approaches, namely GLRT, coherent and incoherent imaging. The comparison of the three methods let us identify pros and cons when imaging
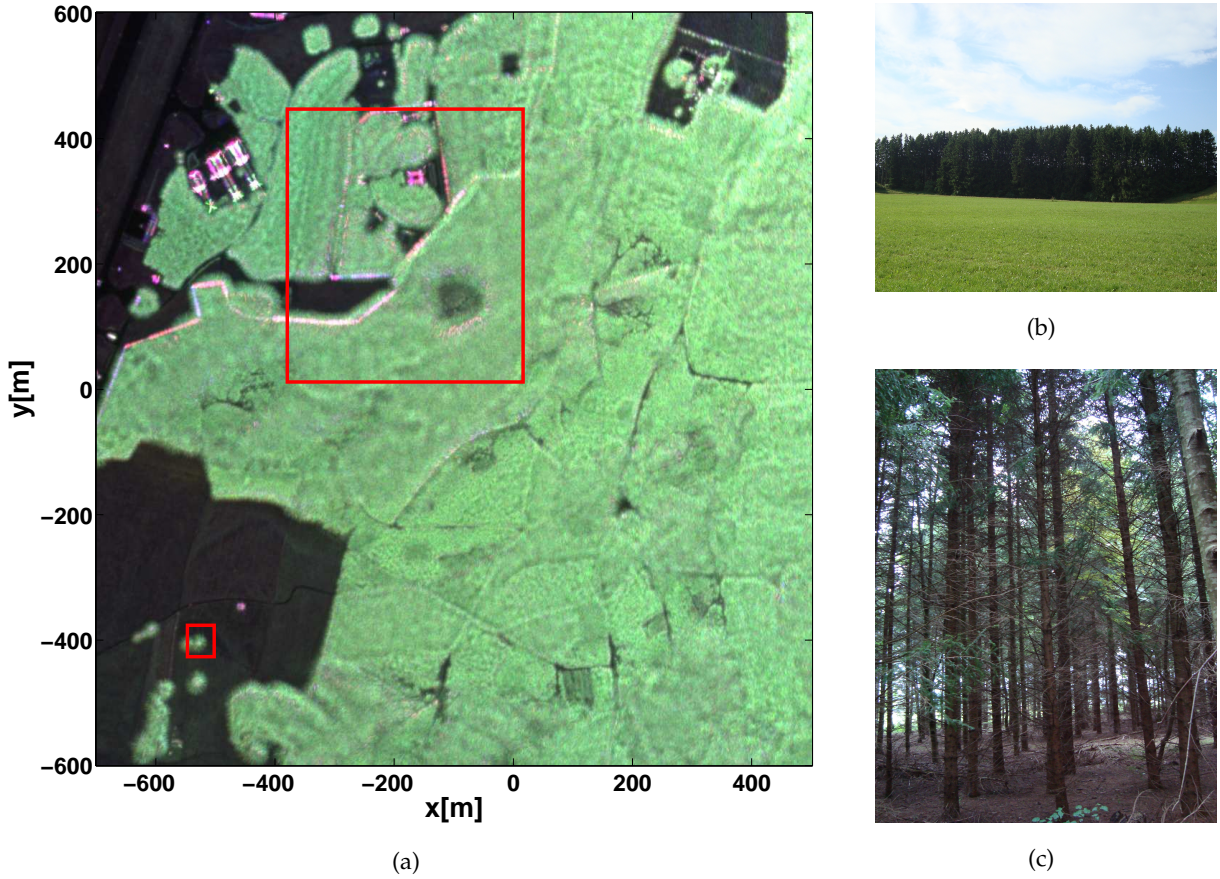
Figure 6.21: (a) Fully polarimetric high-resolution image in Pauli basis (blue: HH+VV, red: HH-VV, green: 2HV), $360°$ coherent addition using a DEM, 1.2 km by 1.2 km, 0.08 m by 0.08 m sampling. Red squares: regions of interest. (b)-(c) Optical images of the forested region in Kaufbeuren, Germany.

distributed targets. In order to get an accurate focusing, the PGA algorithm is implemented for HoloSAR. In this regard, an analysis of this algorithm in terms of sensitivity for the case of circular trajectories is given. In addition, the theory of the IRF with multiple circular passes is studied using a Luneburg lens. In this way, resolutions and sidelobes in 3-D are studied as a function of the system bandwidth and the number of tracks, thereby optimising the acquisition geometry for the best 3-D resolution and sidelobe suppression.

6.5.1 Multicircular L-band campaign

The L-band ($f_c = 1.29$ GHz) multicircular campaign was carried out with the DLR's F-SAR system in 2012 over the region of Kaufbeuren, Germany. The fully polarimetric data set consists of a cylindrical synthetic aperture formed by nineteen circular-like continuous passes, as shown in Figure 6.22(a) [Ponc 16b, Ponc 13b, Ponc 13a, Ponc 14c]. Similar to the P-band survey, the flight path was predefined to be as close as possible to an ideal circular synthetic aperture. As described in the previous campaigns, the aircraft attitude is defined by the pitch, roll and heading angles, as depicted in Figure 6.22. The average pitch angle was about $2°$, and was changing periodically to stabilise the airplane for every change in height. The roll angle was planned to be $10°$, however it was hard to keep due to weather conditions and the complicated
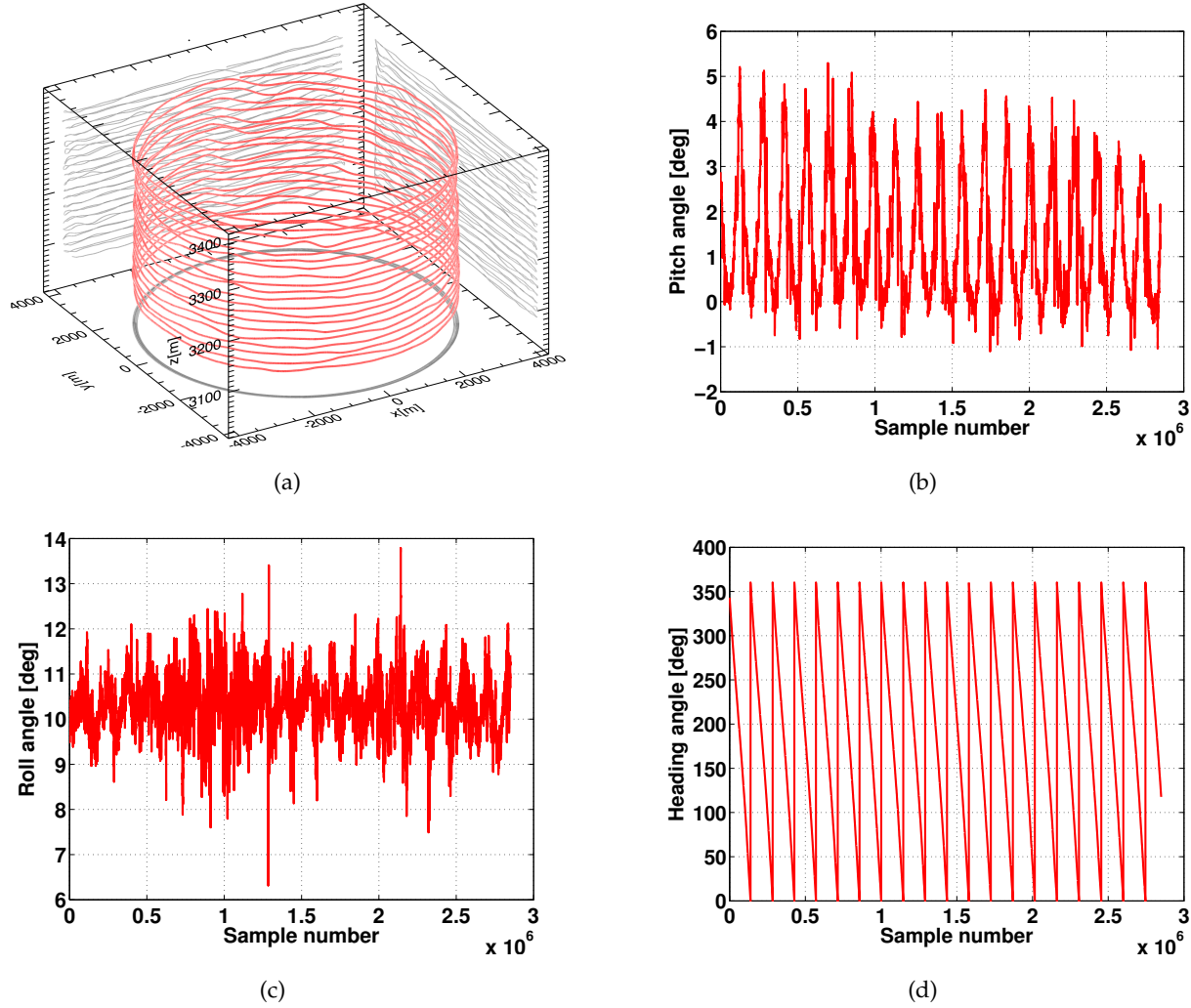
Figure 6.22: (a) 3-D track profile: acquisition carried out by the DLR's F-SAR sensor at L-band over the region of Kaufbeuren, Germany, in 2012. Mean radius: 3700 m, mean altitude: 3200 m. (b)-(d)Aircraft attitude for the experimental multicircular acquisition at L-band. (b) Pitch angle: mean of $2°$. (c) Roll angle: mean of $10°$. (d) Heading angle: oscillates from $0°$ to $360°$ for every circular acquisition.

manoeuvres that the pilot had to accomplish during the flight. The third angle was determined primarily by the rotation of the platform. On the other hand, the antenna pattern is defined by an angular aperture of $18°$ and $30°$ in azimuth and range directions, and by depression angle of $25°$ (see Figure 6.23). As explained before, the covered area is delimited by the geometric flight configuration and the 3 dB antenna pattern. In fact, this data collection covers an area of 2 km by 2 km, which has been improved in comparison to the first L-band flight (see Section 5.1). A zoom of 1.2 km by 1.2 km of this test site is depicted in Figure 6.21.

The setup of the cylindrical synthetic aperture consists of an average vertical baseline distribution of $\Delta B_{\mathrm{L}} = 15$ m, a maximum vertical baseline of $L_{\mathrm{H}} = 270$ m, (normal component consisting of $\Delta B_{\mathrm{L},\perp} = 223.72$ m), a mean radius of 3700 m, and a mean height of 3200 m. This constellation allows a customised processing of irregular and regular spacing in elevation. Consequently, the following parameters are derived: $\delta_{\mathrm{LOS}_\perp} = 2.32$ m and $\delta_{\mathrm{LOS}_{\perp,\mathrm{amb}}} = 41.7$ m, which correspond to the resolution and the interval of ambiguity in elevation, respectively. The
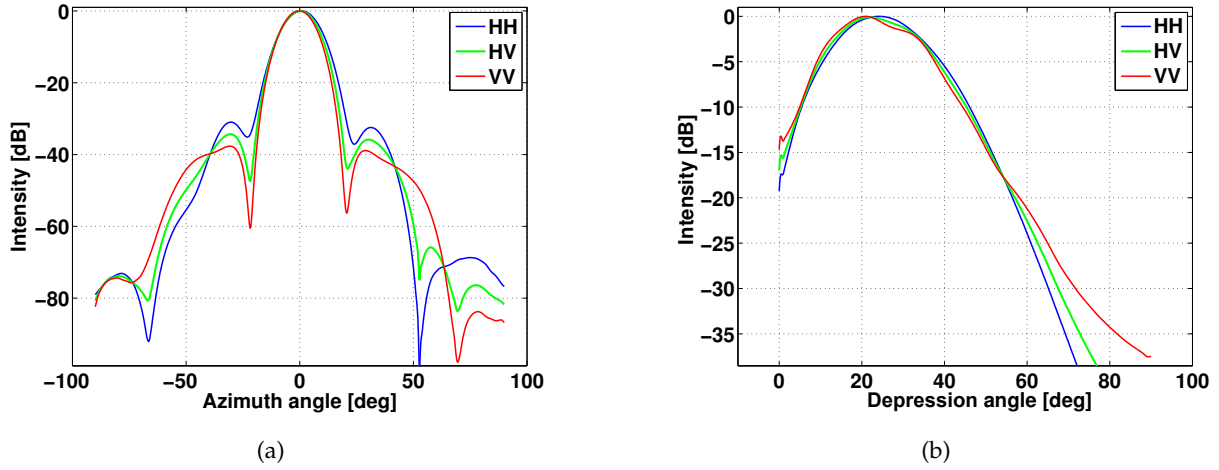
Figure 6.23: 1-D antenna patterns of the multicircular campaign at L-band. (a) Azimuth pattern with an angular resolution of $18\,^\circ$. (b) Depression pattern with an angular resolution of $30\,^\circ$. Note that the antenna pointing angle is about $25\,^\circ$.

transmitted chirp bandwidth is 50 MHz, which results in a slant range resolution of $\delta r = 3.0$ m, a vertical resolution of $\delta_z = 4.27$ m with a single pass, and the PRF is 500 Hz. The critical baseline is around $B_{\perp,\mathrm{crit}} = \min\left(256.15\,\mathrm{m}, 143.41\,\mathrm{m}\right)$, which is slightly reduced by weighting in the range direction. In this way, the effective bandwidth has an improvement of at least 1.8 times in the ground range and at least 2.5 times in the vertical direction, as aforementioned in Section 6.5.3. A summary of the flight configuration is also given in Table A.2.

6.5.2 PGA-based autofocusing

As aforementioned in Section 3.6, autofocus plays a fundamental role to focus wide-angle SAR accurately, and more importantly in the HoloSAR imaging mode since long synthetic apertures are formed, i.e., circular and vertical. This section describes the use of the phase gradient autofocusing (PGA) algorithm for the HoloSAR imaging mode (see Section 3.6).

Table 6.1: Parameters of the simulated reference targets of Figure 6.24 and setup of the experimental HoloSAR acquisition analysed in Figure 6.26. The group identification (ID) goes from the top to the bottom of the Figures.

ID	Reflectors	Pointing angle [deg]	Size [m]	Type
G1	4	$90, 270, 150, 330$	0.9	Trihedral
G2	4	$210, 30, 270, 90$	0.9	Trihedral
G3	1	0 to 360	0.6	Luneburg lens
G4	4	$30, 150, 330, 210$	0.9	Trihedral

Set up of reference targets

Theory of the PGA method establishes that there should be at least two reference targets for a given position in the slow time t in order to estimate the errors in the (x, y, z) space. In this
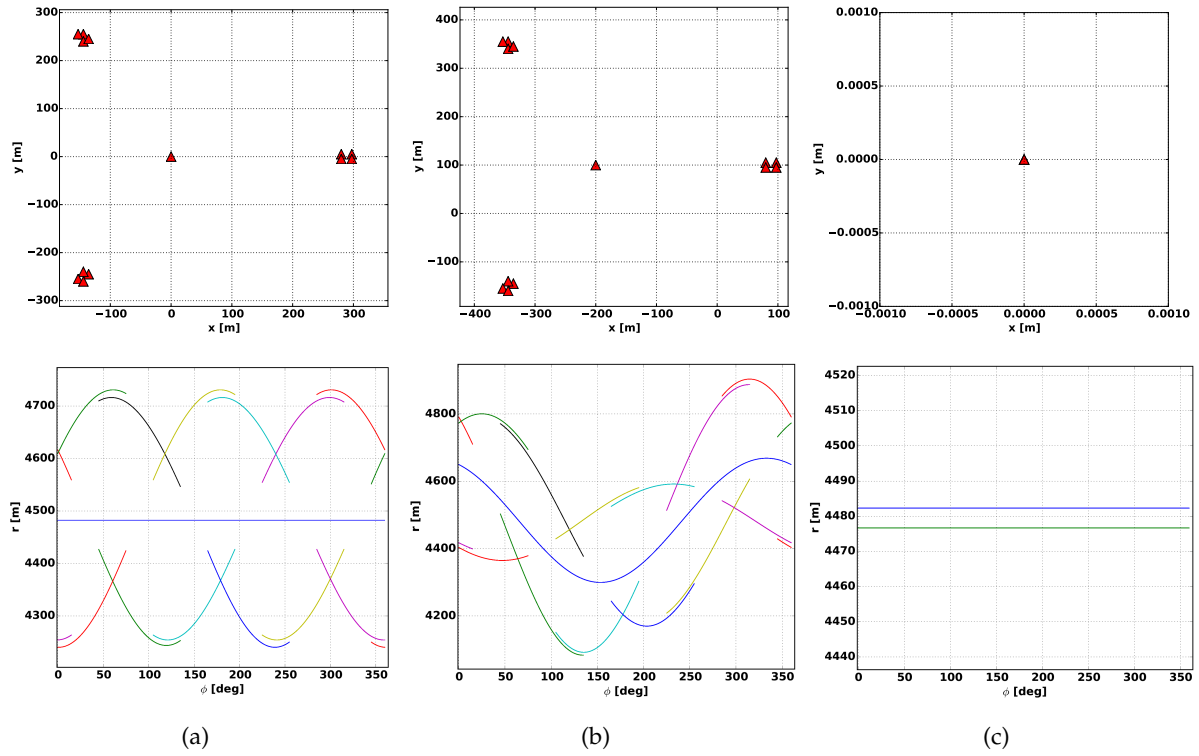
Figure 6.24: Setup and range histories of two possible configurations suitable for the PGA in case of circular trajectories. (a)-(b) Upper row: Trihedral corner reflectors (CR) and a Luneburg lens configuration in and off the center of the scene. Lower row: corresponding range histories for a single circular track. The setup of the CRs are described in Table 6.1. Note that the three range histories never cross, in this way being able to estimate errors in the (x, y, z) space even with redundant measurements. (c) Alternative solution with two Luneburg lenses displaced in the vertical direction by 5 m.

work two different configurations for reference targets are proposed. First, a setup of three groups of trihedral corner reflectors (CR) and a Luneburg lens are assumed (see Figure 6.24(a) and Figure 6.24(b)). To have a more accurate estimation and to cover the near and the far ranges at any angular instant ϕ, every group should be displaced from each other by a distance d_{xy} in the order of the scene radius, and the Luneburg lens should be in the center of the equidistant triangle formed by the group of corner reflectors.

The upper images of Figure 6.24(a)-6.24(b) illustrate a setup of a group of reference targets separated around $d_{xy} = 500$ m and assuming a constant height, while the bottom images show the corresponding range histories assuming a circular trajectory with a radius of $R_{xy} = 3700$ m at a height of $R_z = 2500$ m. The pointing direction of every group, numerated from the top to the bottom, and every corner reflector are listed in Table 6.1.

As can be seen, this configuration allows the retrieval of at least three reference measurements at different range distances per instant ϕ, which makes the system to become overdetermined and to obtain a better estimation of the vertical and horizontal components. Correspondingly, this particular geometry avoids interference between contiguous CR signatures so that a continuous error estimation can be obtained. It also allows the reflectors to be placed out of the scene center, as shown in Figure 6.24(b). In fact, this setup is a modified version of a previous

CSAR experimental realisation described in [Cant 07].

Alternatively, a setup of only two Luneburg lenses can be used. The lenses should be displaced in the vertical direction by a distance d_z, which is necessary to distinguish their signatures for any ϕ. However, this configuration might be not feasible in most situations since the distance in the vertical direction has to be in the order of the range resolution. Figure 6.24(c) depicts an example of two lenses placed in the scene center and separated by $d_z = 5$ m. This distance fulfils the requirement imposed by a system bandwidth of $BW = 50$ MHz, with which a vertical resolution of $\delta_z = 4.2$ m can be obtained.

The phase gradient is performed in subapertures of $\Delta\phi = 60°$ because it is assumed that every reflector persist at least for that angular range. After removing the factor due to the distance, the data of every subaperture i and every reference target n are low-pass filtered in the along-track direction. Depending on the size of the filtering window, clutter can be significantly suppressed but at the cost of losing high-frequency phase components, which can be used to estimate rapid platform movements due to turbulence. In [Buck 91], it has been shown that low-frequency errors, $r_{\text{err},n}(t) = r_{\text{const}} \cdot \cos(2\pi f_o t - \gamma_o)$ with r_{const} is a constant amplitude term, γ_o is a constant phase term and f_o as the frequency defined by the following interval $0 \le f_o \le 1/T_A$ where T_A is the aperture time in seconds, cause geometrical distortion and defocussing, whereas high-frequency components ($1/T_A \le f_o \le \infty$) tend to have less impact due to their lesser magnitude. Nevertheless, this topic is not deeply discussed in this thesis, because it is out of the scope.

(a)　　　　　　　　(b)　　　　　　　　(c)
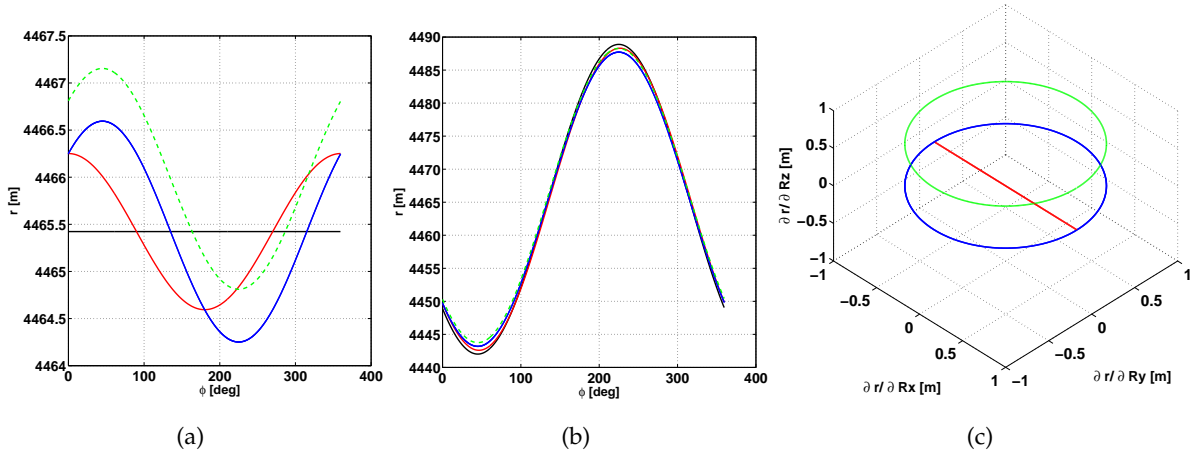
Figure 6.25: Track error projections in the range history. (a) Target in the center, $\vec{p}_1 = (0, 0, 0)$ m. (b) Target off the center, $\vec{p}_2 = (20, 20, 0)$ m. (c) Sensitivity or rate of change of the range history with respect to changes in the track. The black curve indicate the errorless range history, and the coloured curves show its modification after adding a constant error in the track $(\Delta R_x, \Delta R_y, \Delta R_z)$. Red curve: $(0.3, 0, 0)$ m. Blue curve: $(0.3, 0.3, 0)$ m . Green curve: $(0.3, 0.3, 0.3)$ m.

After the signal is filtered, the error in the LOS, $r_{\text{err},i,n}$, can be estimated with the derivative of the range-compressed data, as described by (3.56). Subsequently, the inversion of the system

can be obtained by means of the least squares, as follows

$$\Upsilon_{hv,i} = \begin{bmatrix} \frac{\partial \Upsilon_h}{\partial t} \\ \frac{\partial \Upsilon_v}{\partial t} \end{bmatrix} , \quad A_i = \begin{bmatrix} \pm \sin(\theta_{\mathrm{el},i,1}) & \cos(\theta_{\mathrm{el},i,1}) \\ \pm \sin(\theta_{\mathrm{el},i,2}) & \cos(\theta_{\mathrm{el},i,2}) \\ \pm \sin(\theta_{\mathrm{el},i,3}) & \cos(\theta_{\mathrm{el},i,3}) \end{bmatrix} , \quad R_{\mathrm{err},i} = \begin{bmatrix} r_{\mathrm{err},i,1} \\ r_{\mathrm{err},i,2} \\ r_{\mathrm{err},i,3} \end{bmatrix} . \tag{6.25}$$

In order to give a better insight on how the errors in the navigation system are projected in the LOS error estimation, the sensitivity of the system is analyzed. Eq. (6.26) describes the change of rate in the range history for a change in R_x, R_y and R_z directions. This formula is deduced by analysing the phase of the free-space Green's function (see Section 3.1).

$$
\begin{aligned}
\frac{r(R_x + \Delta R_x) - r(R_x)}{\Delta R_x} &= \frac{\sqrt{(R_x + \Delta R_x - x)^2 + (R_y - y)^2 + (R_z - z)^2}}{\Delta R_x} - \\
&\quad \frac{\sqrt{(R_x - x)^2 + (R_y - y)^2 + (R_z - z)^2}}{\Delta R_x} \\
\frac{r(R_y + \Delta R_y) - r(R_y)}{\Delta R_y} &= \frac{\sqrt{(R_x - x)^2 + (R_y + \Delta R_y - y)^2 + (R_z - z)^2}}{\Delta R_y} - \\
&\quad \frac{\sqrt{(R_x - x)^2 + (R_y - y)^2 + (R_z - z)^2}}{\Delta R_y} \\
\frac{r(R_z + \Delta R_z) - r(R_z)}{\Delta R_z} &= \frac{\sqrt{(R_x - x)^2 + (R_y - y)^2 + (R_z + \Delta R_z - z)^2}}{\Delta R_z} - \\
&\quad \frac{\sqrt{(R_x - x)^2 + (R_y - y)^2 + (R_z - z)^2}}{\Delta R_z}
\end{aligned}
\tag{6.26}
$$

Figure 6.25 depicts the projected error in the LOS for a point target in the center, $\vec{p}_2 = (0,0,0)$, and off the center, $\vec{p}_1 = (20,20,0)$, and a similar geometry as the HoloSAR campaign analyzed in this section. In addition, constant mismatches in the measured track of $(0.3,0,0)$ m (red curve), $(0.3,0.3,0)$ m (blue curve), and $(0.3,0.3,0.3)$ m (green curve) in the $(\Delta R_x, \Delta R_y, \Delta R_z)$ space are illustrated. Note that errors in the horizontal direction of the track in the order of 30 cm are reflected as a sinus with an amplitude of 1 m due to the circular geometry, whereas constant errors in the vertical direction are reflected as constant shifts in the range history. Moreover, for the target $\vec{p}_1$ changes in the range history for an error in the track are more prominent than those for $\vec{p}_2$, because the target is out of the center.

Error estimation

The PGA was employed with the configuration of several CR and a Luneburg lens, as listed in Table 6.1. Figure 6.26 shows an overview of the setup of reference targets around the runway of the Kaufbeuren airport. Figure 6.27 illustrates the estimated error in the LOS direction of the first seven tracks before (top row) and after integration (bottom row). The estimation reflects a sinus signal with an amplitude in the order of 1.5 m and a constant offset of around 0.5 m. As shown in Figure 6.25(b) and according to (6.26), these results can be understood as a two-component error: on the one hand, motion errors with high frequencies, and on the other hand, a constant bias (plus low-frequency variations) with low frequencies in the track due to a possible mismatch in the lever arm measurement, e.g., which are the ones giving the sinus-like shape to the estimated errors. Note that this curve form does not reflect the theoretical phase

(a)

(b)

(c)
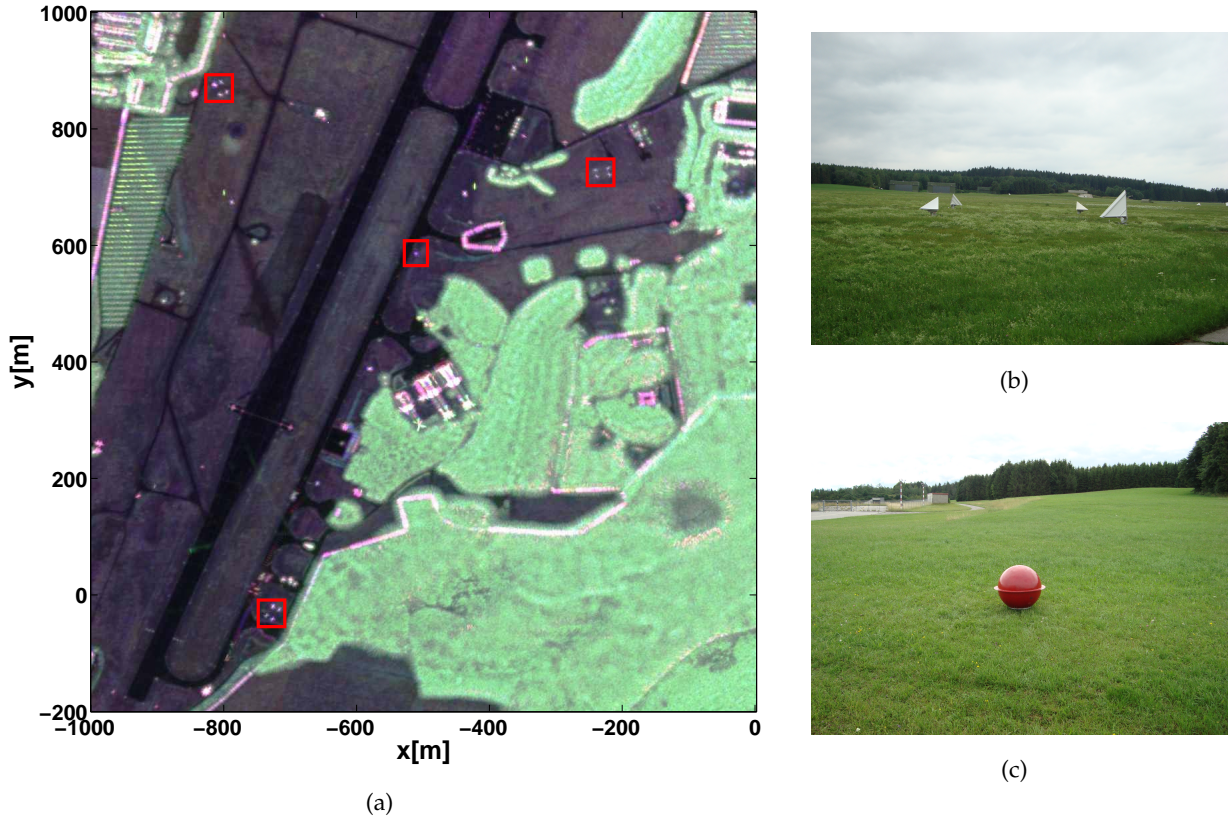
Figure 6.26: (a) Fully polarimetric high-resolution image of the test site with the setup of reference targets, i.e, trihedral corner reflectors and Luneberg lens. Red squares indicate the reflectors, which are identified as G1, G2, G3, and G4 from the top to the bottom of the image (refer also to Table 6.1). The image is in the Pauli basis (blue: HH+VV, red: HH-VV, green: 2HV), $360°$ coherent addition using a DEM, 1 km by 1.2 km in x and y directions, respectively, and 0.08 m by 0.08 m sampling. (b) Optical image of one of the groups of trihedral corner reflectors. (c) Optical image of the Luneburg lens.

center change of the Luneburg lens during the azimuthal illumination, since identical results were obtained by estimating the phase errors with only the corner reflectors.
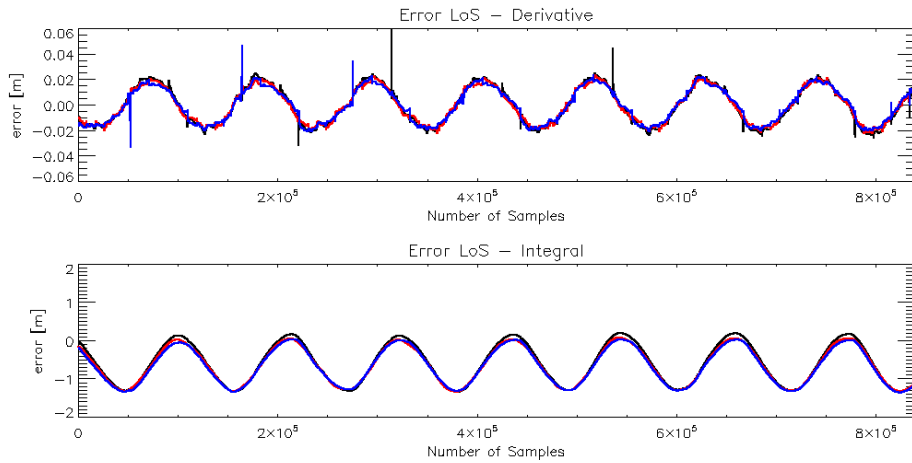
Figure 6.27: Estimated error in the line-of-sight (LOS) direction with the phase gradient autofocus (PGA) algorithm. (a) Derivative of the range history. (b) Estimated error after integration. The three colours indicate the three different range histories shown in Figure 6.24.

In order to show the projected errors in the image, the Luneberg lens was focused at the true height before and after PGA correction (see Figure 6.28). As mentioned before, the error in the line of sight is reflected as constant shifts and motion errors in the (x, y, z) space, and both were corrected with high accuracy.
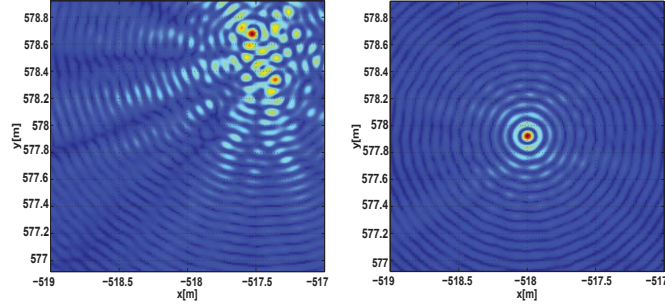
Figure 6.28: PGA Results for a Luneburg Lens, 2 m by 2 m, 7.5 mm by 7.5 mm pixel spacing, (x, y) plane. Left: before PGA correction. Right: after PGA correction. Note that uncompensated motion errors in the navigation data can be understood as constant displacements in the horizontal plane, as well as high-frequency motion components. The position of the lens is $\vec{p}_{\text{lun}} = (-518\,\text{m}, 577.96\,\text{m}, 757\,\text{m})$.

6.5.3 Impulse response function: Luneburg lens

Figure 6.29 depicts the total power in the time and frequency domains of the 3-D IRF of HoloSAR, which was measured with the backscattering of a Luneburg lens (positioned at $\vec{p}_{\text{lun}} = (-518\,\text{m}, 577.96\,\text{m}, 757\,\text{m})$) and different baseline distributions. The images were focused coherently over the full synthetic apertures with the FFBP [Ponc 14a], and the size of the processed region is 15 m by 15 m by 30 m in the (x, y, z) space.

Figure 6.29(a) shows the IRF with a single circular pass with a PSLR of -8 dB and a $\delta z \approx 4.2$ m for the given system bandwidth. As expected, due to the low resolution in the $\text{LOS}_\perp$, cone-shaped sidelobes distort the image. Figure 6.29(b) depicts the IRF after integrating three tracks in elevation (i.e., 1, 11, and 19) with a contiguous vertical distance of $\Delta B_\text{L} = 135$ m, which is close to the critical baseline, $B_{\perp,\text{crit}}$. Although the system bandwidth is improved by a factor of at least 1.8, aliasing can be seen as circles of different radius separated by 4 m along the $\text{LOS}_\perp$ direction. In addition, a similar effect can be seen in Figure 6.29(c) by adding coherently non-equidistant passes, i.e., 3, 6 and 19, with a vertical baseline distribution of $\Delta B_\text{L} = [45\,\text{m}, 195\,\text{m}]$. Furthermore, when ΔB_L is equal to the critical baseline, aliasing occurs. This is due to the fact that the Nyquist requirements in the $\text{LOS}_\perp$ direction are not fulfilled. In fact, this is better illustrated in the spectrum, where gaps in elevation can be seen. Therefore, the distance between tracks should be reduced. This case is shown in Figure 6.29(d) with the coherent integration of all circular passes. In this case, the PSLR is -8.6 dB, $\delta z \approx 2$ m, $\delta \text{LOS}_{\perp,\text{amb}} = 42$ m, and cone-shaped sidelobes in the $\text{LOS}_\perp$ direction were reduced from -13 dB to -25 dB with respect to the main lobe.

Until now, the impact of the vertical constellation has been discussed for 3-D imaging. However, it is also interesting to analyse it in the horizontal plane, as discussed next. Figure 6.30
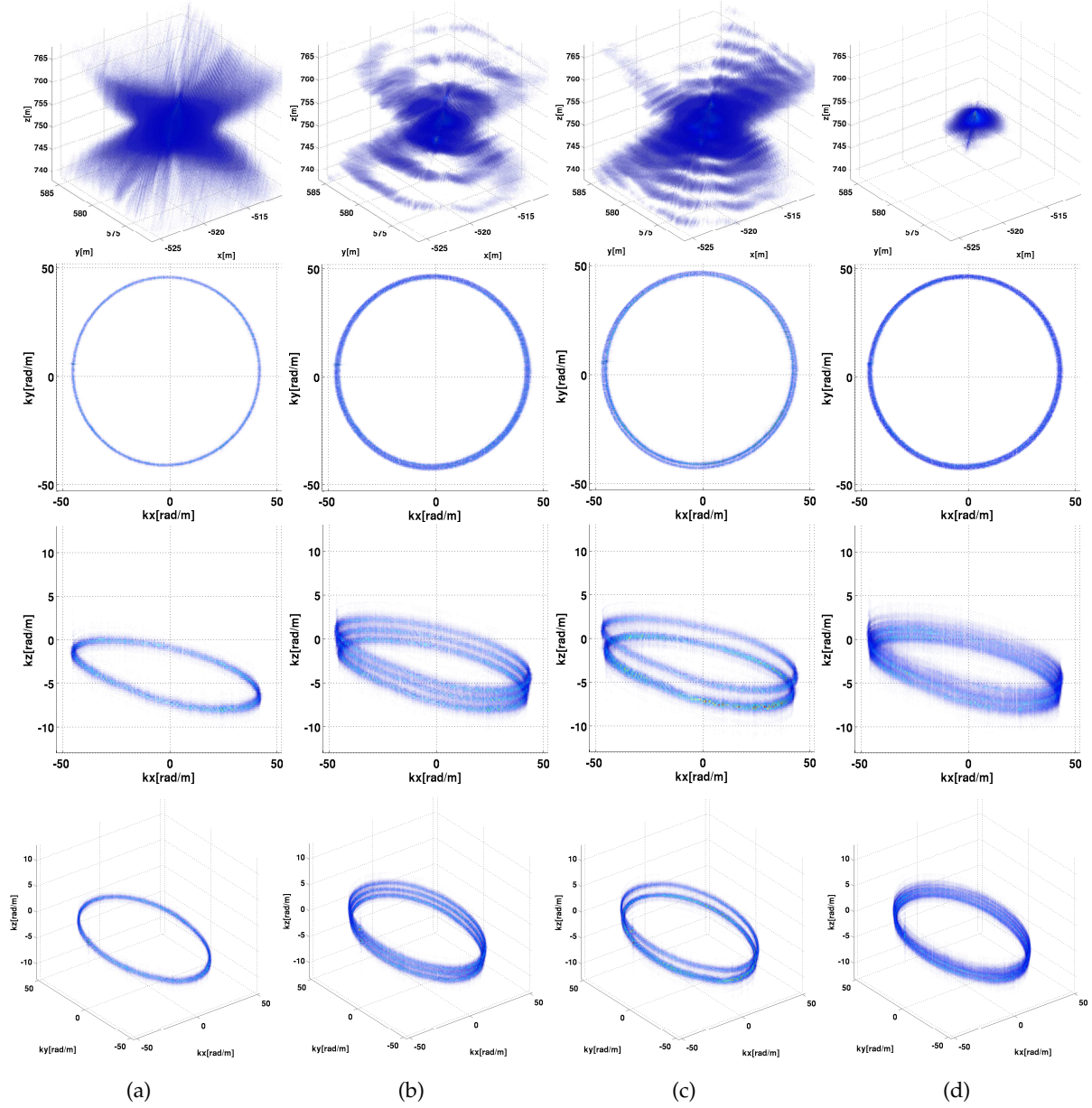
Figure 6.29: Total power of the 3-D impulse response function (IRF) of HoloSAR with the real data of a Luneburg lens. (a) 1 track. (b) 3 tracks separated by a distance of $\Delta B_\mathrm{L} = 135$ m, which is close to the critical baseline, $B_{\perp,\mathrm{crit}}$. (c) 3 tracks with random spacing, i.e., $\Delta B_\mathrm{L} = [45\,\mathrm{m}, 195\,\mathrm{m}]$. (d) 19 tracks with a mean distance of $\Delta B_\mathrm{L} = 15$ m.

illustrates (x, y) slices representing the total power of the 3-D IRF in dB at the height of the Luneburg lens, $z = 757$ m. Since the reference target was placed off the center of the scene, the IRF is not symmetric. Moreover, the main peak remains at its highest resolution for all slices and the peak of the first sidelobe remains unchanged for the given system bandwidth, 50 MHz (see Section 6.1.4). Also, it can be seen that secondary sidelobes are slowly mitigated by increasing the total vertical baseline L_H, e.g, from 0 m to 270 m. This can be seen in the transition from 1, 10 to 19 circular tracks, having (b) and (c) the same contiguous spacing $\Delta B_\mathrm{L} = 15$ m. Figure 6.30(d) shows the horizontal signature of the Luneburg lens by combining only 5 tracks but with a maximum vertical distance of $L_\mathrm{H} = 270$ m. Notably, a similar image quality as (c) can be obtained with far less number of tracks. To obtain this enhancement, it is necessary to consider

a track spacing ΔB_L in the order of the critical baseline, as described by (6.18). In fact, this solution is a good alternative for 2-D imaging improvement, particularly for low-bandwidth SAR systems.

(a) 1 track.

(b) 10 tracks.

(c) 19 tracks.

(d) 5 tracks.
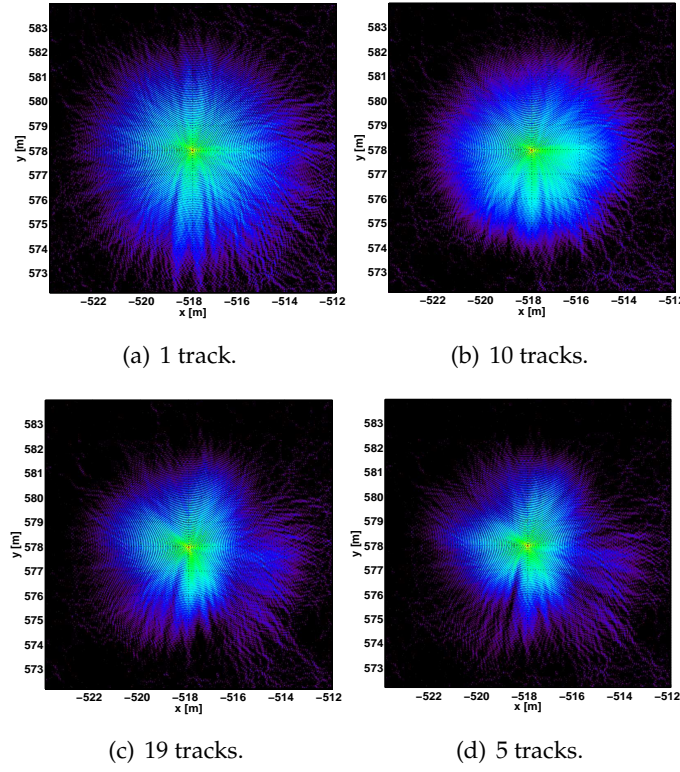
Figure 6.30: Total power in dB of horizontal slices of the 3-D IRF analyzed for different baseline configurations. The intensities correspond to the signature of a Luneburg lens. The size of the images is 12 m by 12 m, and the pixel spacing is 7.5 mm by 7.5 mm. The colour scale corresponds to 0 dB to -40 dB from red to black, respectively. Note the sidelobe improvement from (a) to (c) because the effective bandwidth is being increased by the elevation aperture. The signature given in (d) shows that it is possible to have a similar image quality in the (x, y) plane with far less tracks. This enhancement with only 5 tracks is of significant importance when it is desired to obtain 2-D high resolution images.

6.5.4   Single tree at 3-D high resolution

In order to understand the HoloSAR imaging mode for distributed backscattering, the signature of a single tree is studied for different baselines and focused by the coherent imaging. The target of interest was previously indicated as the first region of interest in Figure 6.21. Figure 6.31 depicts the holographic tomogram of a tree from two different views (upper and lower rows), and the coherent integration of different baseline constellations. Results show that although tree signatures are distributed, energy of cone-shaped sidelobes decrease as the number of tracks increases. If 3 tracks with a contiguous distance of $\Delta B_\mathrm{L} = 135$ m are coherently integrated, as illustrated in Figure 6.31 (b), then sidelobes are enhanced from -10 dB to -24 dB, however ambiguities occurs since the acquisition geometry fall short of the Nyquist criterion. Notably, results with the coherent addition of 19 tracks show enhancement in resolution, and

3-D sidelobe suppression, which result in a potential application of 3-D tree profile retrieval at high resolution and over $360°$.

(a) 1 track. (b) 3 tracks. (c) 19 tracks.
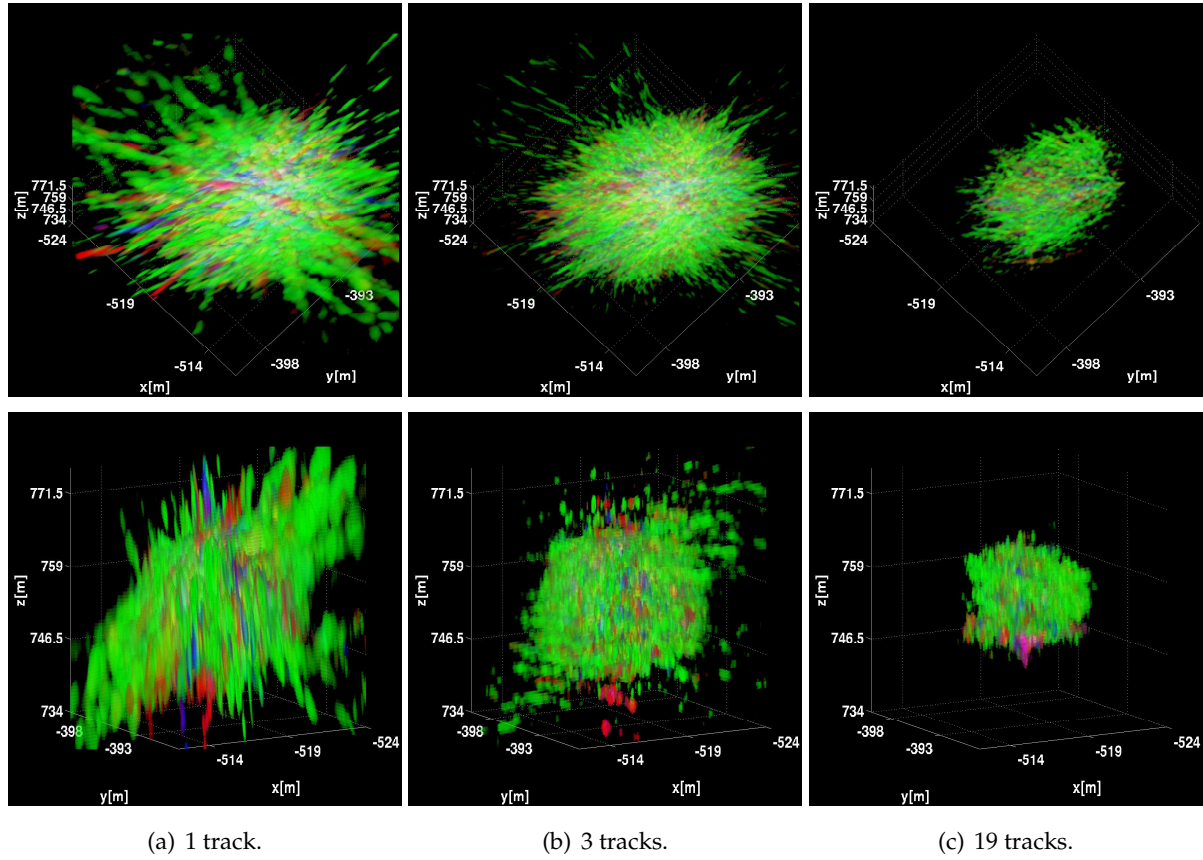
Figure 6.31: Holographic tomogram of a single tree, focused with the FFBP for circular trajectories and using different baseline distributions. (a) Single track. (b) Three tracks with a vertical baseline of $\Delta B_{\mathrm{L}} = 135$ m. (c) Nineteen tracks with a vertical baseline of $\Delta B_{\mathrm{L}} = 15$ m. Upper and lower rows show different perspective views.

6.5.5 Study of processing strategies

Besides the acquisition geometry of the HoloSAR acquisition, the anisotropic behaviour of the backscattering should be considered when processing. Particularly, this section is dedicated to study forest backscattering using the full synthetic apertures. To that end, the following methods were used: 1) incoherent imaging using the GLRT method, 2) incoherent imaging by the addition of the amplitude of all subapertures, and 3) coherent imaging of the full synthetic apertures (refer to Section 6.2.2). In the case of 1) and 2), the energy in elevation was retrieved with CS with coherent averaging, using Ψ as the wavelet basis, and a penaliser of $\lambda_1 = 0.7$.

Figure 6.32 illustrates a 3-D view of the holographic tomograms in the Pauli basis, and using the three approaches. The voxels show the highest intensities for better visualisation. The size of this region is 300 m by 300 m by 50 m in the x, y and z directions, respectively (see Figure 6.21). Correspondingly, results indicate a more stable signature with incoherent and coherent imaging solutions. This occurs due to the fact that the GLRT is assuming that targets persist only within the period of $\Delta\phi = 10°$, which means that targets that persist longer will not

(a) GLRT. (b) Incoherent. (c) Coherent.
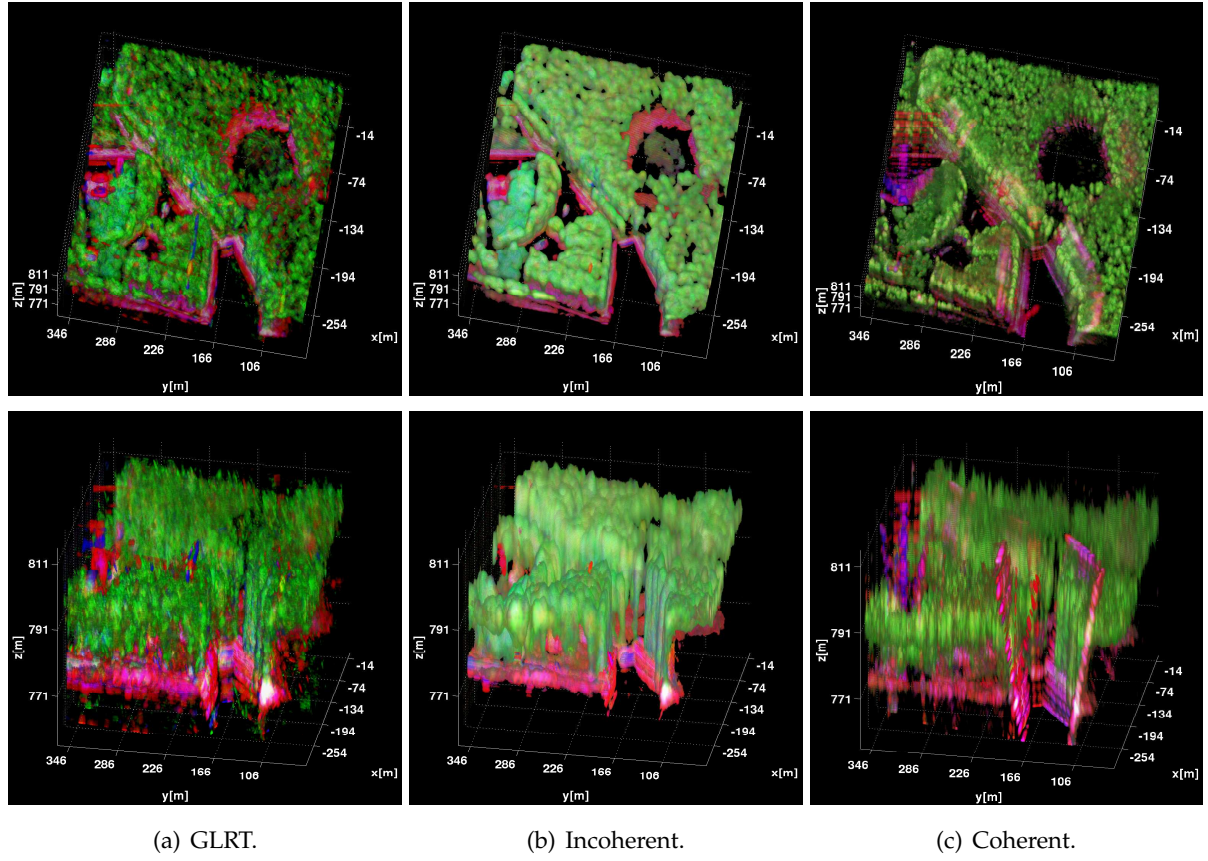
Figure 6.32: 3-D view of the area of study shown in Figure 6.21 with a dimension of 300 m by 300 m by 50 m in the (x, y, z) space. The first row shows the top view, while the second row depicts the rotated version. The holographic tomograms were focused at L-band in the Pauli basis (blue: HH+VV, red: HH-VV, green: 2HV). Every column corresponds to one of the three processing approaches, namely generalised likelihood ratio test (GLRT), incoherent and coherent imaging.

be enhanced, as it is in the other two cases (see also Section 6.4.1). In addition, cone-shaped sidelobes are better suppressed when the signature in the $\text{LOS}_\perp$ direction is solved with CS, however at the cost of resolution in the (x, y) plane. Regarding the coherent approach, strong contributions as double bounces of forest edges can be seen as high-power sidelobes in the elevation direction. This effect can be mitigated by means of weighting, however it was not used in this paper in order to obtain the maximum possible resolution. In fact, with the coherent approach more single trees and other features can be identified. To give better insight, slices in the horizontal and vertical planes are studied.

Figure 6.33 illustrates 2-D slices at two different positions in the y direction, namely $y = 105.5$ m and $y = 205.5$ m. Images in the first row were focused with the GLRT processing, whereas the second and the third were processed with the incoherent and the coherent methods, respectively. Interestingly, resolution in the horizontal plane is improved in the coherent approach, and even single trees inside the forest can be seen. That is to say that signatures of distributed backscattering will most likely be enhanced, if they are treated isotropic (refer also to Figure 6.31). Even so, holographic tomograms are degraded by sidelobes in the $\text{LOS}_\perp$ direction for strong signatures. This is the case of forest edges, which are identified as double-bounces in

(a) Slices in the $(x, y = 105.5\,\text{m}, z)$ plane.

(b) Slices in the $(x, y = 205.5\,\text{m}, z)$ plane.
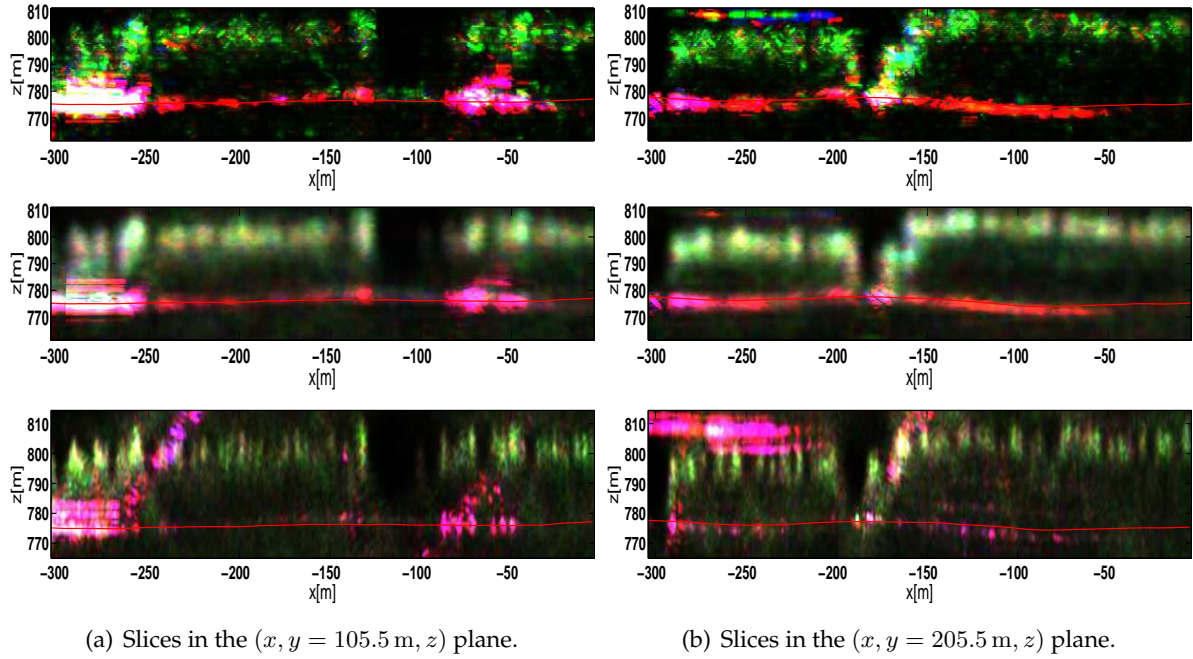
Figure 6.33: Slices in the (x, z) plane of the region shown in Figure 6.32. The holographic tomograms were focused in the Pauli basis (blue: HH+VV, red: HH-VV, green: 2HV). The profile, shown with a red line indicates the measurements of a LIDAR sensor (©SwissTopo). Every column corresponds to two different positions in the y direction. The rows indicate the focusing approaches, namely GLRT, incoherent and coherent imaging, from the upper to the lower row, respectively.

the Pauli basis, and can be seen in the third row as a diagonal crossing the forest and a thick line at the top of the canopies in (a) and (b), respectively. Contrarily, the GLRT and the incoherent algorithms indicate better sidelobe suppression since CS is used to retrieve the signature in elevation, however at the cost of resolution in the horizontal plane. Compared to other information source, HoloSAR measurements show a good match with the Lidar measurements, depicted with a red line.

Additionally, Figure 6.34 illustrates (x, y) slices at $z = 778$ m with tree trunk backscattering, and $z = 801$ m with signature from tree canopies. As aforementioned, the coherent approach shows an improved resolution in the (x, y) plane, which allows a more detailed information about tree distribution or forest density. However, linear methods are not always able to improve the PSLR of strong targets such as forest edges. As a result, distorting weaker targets such as the canopy backscattering.

As discussed in Section 6.4.1, the resolution in the horizontal and vertical planes can be enhanced with the incoherent approach for targets that persist longer than $\Delta\phi$. That is to say, the best resolution between r and α define the final resolution for (x, y), and similarly the best resolution between r and $\text{LOS}_\perp$ for (x, z) and (y, z). In the case of coherent imaging, the final resolution is given by the persistence of every target, in which case a significant improvement in the (x, y) plane occurs (refer to Section 6.1.4).

(a) GLRT. (b) Incoherent. (c) Coherent.
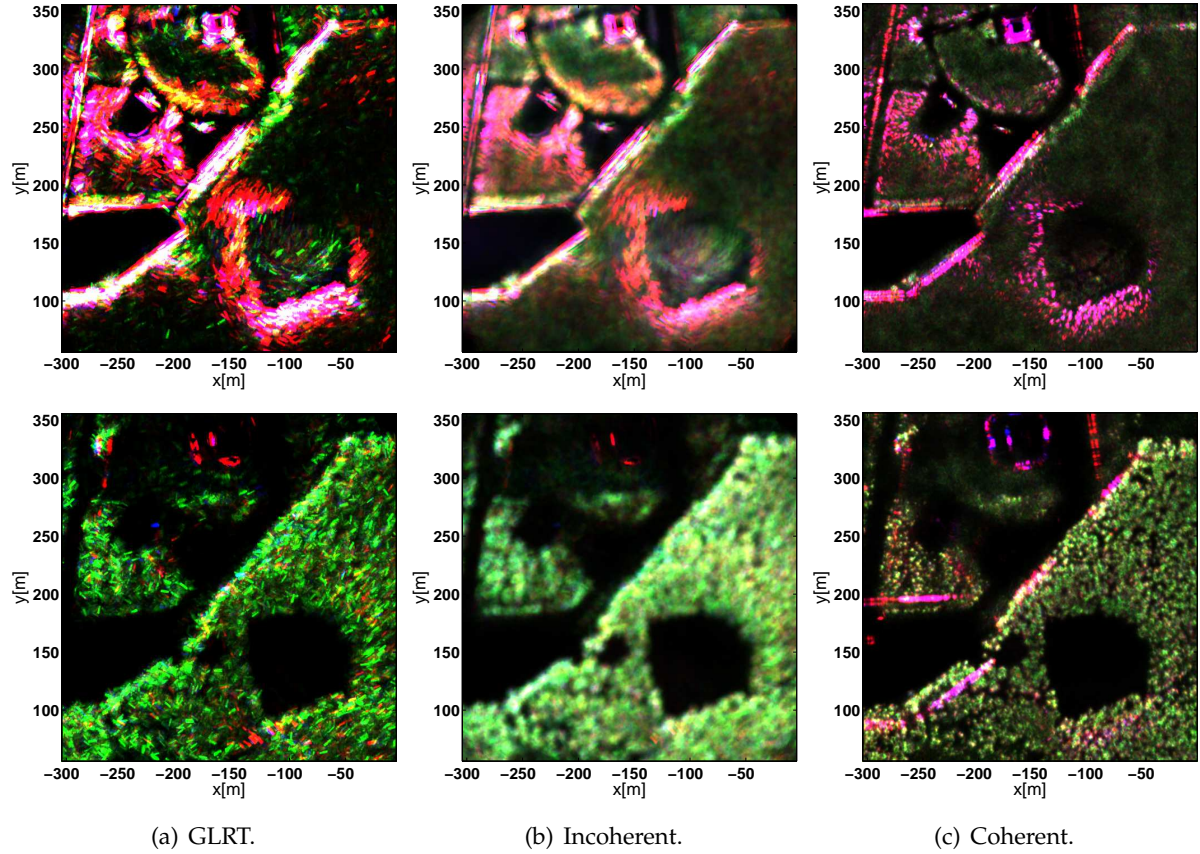
Figure 6.34: Slices in the (x, y) plane of the region shown in Figure 6.32. The holographic tomograms were focused in the Pauli basis (blue: HH+VV, red: HH-VV, green: 2HV). The upper row indicates a slice at $z = 778$ m with most of the targets as tree trunks, and the lower row at $z = 801$ m with tree canopies. On the other hand, every column corresponds to the three different processing methods, namely generalised likelihood ratio test (GLRT), incoherent and coherent imaging.

7 Conclusions and Outlook

This thesis has presented the first airborne demonstration of circular SAR (CSAR) and holographic SAR tomography (HoloSAR) imaging modes at low frequencies, i.e., L- and P-band, particularly for distributed scatterers. Focusing algorithms have been developed and the characteristics of the 3-D backscattering over $360°$ have been studied in this thesis. In Chapter 4, a fast factorised back-projection (FFBP) algorithm for circular trajectories was described and analysed. Unlike conventional CSAR processors, the FFBP algorithm for circular trajectories considers a non-ideal trajectory and the topography, while reducing the computational load. The FFBP algorithm was implemented in a CPU and a GPU, and its performance was measured with simulated and real data. Speedup factors in the order of 500 (CPU) and 1800 (GPU), when compared to the CPU-based direct back-projection (DBP) processing, were achieved. This algorithm was used to efficiently focus all the airborne data sets analysed in this thesis.

In Chapter 5, CSAR data recorded by the DLR's E-SAR airborne system at L-band was processed and analysed. It was shown that CSAR has a great potential to obtain very high-resolution images without the need of a high bandwidth system (94 MHz for the first campaign), as well as to perform tomographic imaging in forested areas. The first results indicated that coherent integration of the full circular aperture achieves the maximum possible resolution for each scatterer, in this way increasing the image quality. In addition, the efficiency of the FFBP for CSAR was demonstrated in terms of computational burden and accuracy, due to the precise consideration of the topography and the real flight track.

Furthermore, the coherent processing of the full aperture was also compared qualitatively to the incoherent addition of several subapertures. The former showed a better quality, hence allowing for a better identification of the observed scene. Several images have been analysed and compared with conventional stripmap SAR, where the detectability of targets and the image enhancement are more than evident. Man-made objects, such as buildings, hangers, shelters and fences show high directivity, whereas runway lights and light poles tend to behave as an isotropic scatterer. Regarding the signature of trees, tree-trunks (ground-trunk interaction) show an isotropic-like behaviour, similar to the signature of a light-pole. Despite being composed of anisotropic scatterers, tree-canopies focused at the erroneous height depict a signature similar to an isotropic-like target with circles-of-confusion, since they are physically concentrated around the same (x, y) coordinates, but are shifted into different directions when focused at the erroneous height. The results have shown that the 3-D signature of trees improves when data are added coherently. On the other hand, the ground has shown high resolution and an isotropic-like behaviour. Similarly, there is a strong mitigation of speckle for

these kind of extended targets due to the strong reduction of elemental scatterers within each resolution cell. In any case, further investigations are required to better evaluate their statistical behaviour.

Additionally, Chapter 5 has included the first demonstration with an airborne sensor of CSAR tomography of an isotropic target, i.e., the Luneburg lens, using a single circular pass. The first demonstration of a CSAR tomogram over a tree has been shown, obtaining as a result its polarimetric backscattering profile. Consequently, the 3-D imaging demonstration of semi-transparent media with one single circular pass has been proven, hence opening new possibilities for the monitoring of vegetated areas in the frame of biosphere research.

In Chapter 6, the concept of HoloSAR was redefined and introduced as an imaging mode to reconstruct fully polarimetric 3-D backscattering over $360°$. This technique is based on the strong similarities in acquisition and processing that holography, tomography and SAR have by forming a cylindrical aperture, i.e., a circular synthetic aperture in azimuth and a linear synthetic aperture in elevation. Subsequently, the 3-D IRF of HoloSAR has been deeply analysed, and it was validated with real airborne data of a Luneburg lens. In this study, it was shown that although HoloSAR allows resolution improvement when the separation between tracks is close to $B_{\perp,\text{crit}}$, the Nyquist requirements in the $\text{LOS}_\perp$ direction have to be met in order to achieve the optimum configuration. Besides the reduction of 3-D cone-shaped sidelobes, HoloSAR achieves sidelobe reduction in the (x, y) plane and improves the resolution along the z direction. Despite the unfeasibility of having a unique analytical solution of the IRF for a target off the center, its analysis in the frequency domain gives significant information to understand the full system in terms of acquisition geometry, PSLR, resolution, central frequency and target position.

Within Chapter 6, the first demonstration of fully polarimetric HoloSAR over forested areas at P- and L-band were presented. Both data collections were studied to retrieve the fully polarimetric 3-D backscattering with three different processing approaches, namely GLRT, coherent and incoherent imaging. The former was accomplished by using the FFBP for circular trajectories, whereas the last two, additionally used second-order statistics, beamforming (BF) and compressive sensing (CS) with wavelet dictionaries to retrieve the energy distribution in elevation. For the coherent imaging the FFBP was commonly applied to all circles.

The experimental data set at P-band of seven circular passes was analysed for the incoherent approach with BF and CS. The results indicated a suitable processing chain for point-like and distributed scatterers, where the resulting images using CS showed a significant improvement over BF. Based on the theory of CS, the baseline distribution in elevation was designed irregular, as a result achieving a good reconstruction with seven tracks. In both approaches, the resulting resolutions in the (x, y) plane for scatterers with persistence greater than a certain azimuth angular sector $\Delta\phi$ were enhanced by the incoherent combination of subapertures over $360°$. Current investigations of 3-D imaging over forested areas in the TomoSAR mode have shown that the tree trunk signature at P-band is much stronger than the signature from the canopy. In contrast, HoloSAR was shown to retrieve the full tree profile due to the multi-angular 3-D measurements and at higher resolution. A further issue addressed in this chapter was the phase calibration of the subapertures. An singular value decomposition (SVD) approach based

on strong ground backscattering signatures has been suggested and validated with P-band data. In fact, this approach can be used for a wider area if a DEM is given as reference.

The second data collection was performed at L-band with nineteen circular passes in elevation. In this respect, the analysis of the results has shown the first study of forested areas over the azimuth angular and elevation directions with the same three aforementioned focusing methodologies. Correspondingly, the analysed holographic tomograms have presented high directivity in the front edges of the forest since there is a strong ground-canopy contribution. On the other hand, canopies presented a random-like behaviour that results in coherent contributions even for narrow synthetic apertures (e.g, TomoSAR with stripmap or $10°$ with Holo-SAR). As expected, the analysed holographic SAR tomograms had better resolution in the x, y, z directions when using the coherent approach, whereas cone-shaped sidelobes were better suppressed with the incoherent method because super-resolution was achieved with CS. Notably, the best results were obtained when distributed backscattering was treated as isotropic.

An important aspect in the processing chain of HoloSAR is the accurate estimation of the antenna phase center. For this purpose, the phase gradient autofocusing (PGA) algorithm was also studied in Chapter 6. On the one hand, the methodology of a setup of three groups of corner reflectors and a Luneburg lens was presented. This particular configuration reduces interference of contiguous reference targets, and allows a precise phase error estimation, since three measurements at different range bins over the full synthetic apertures are given. The PGA algorithm was analysed in terms of its sensitivity for the specific case of circular synthetic apertures. Unlike linear SAR modes, constant offsets can be estimated due to the non-linear trajectory. Correspondingly, the analysis has shown that constant errors in the order of centimetres in the (x, y) space are reflected in the LOS direction as sine-like curves with amplitude in the order of meters and with a phase depending on the position of the reference targets. Contrarily, offsets in z are reflected as constant displacements in the LOS direction, and consequently in arc- and ring-shaped sidelobes in the (x, y) plane.

Overall, the HoloSAR imaging mode was shown to be a promising imaging mode because it has the potential to assess and help to understand natural environments due to its very high resolution and imaging capabilities over $360°$. It is anticipated to become of high interest for the geoscience community to better estimate biophysical parameters. Due to the acquired multi-angular measurements, HoloSAR can potentially reduce uncertainties in the estimation of the forest parameters like forest height, vertical profile, density and biomass, and particularly in the assumption of axisymmetry of tree structures. Compared to TomoSAR, HoloSAR offers low temporal decorrelation because continuous circular flights can be flown in a relatively short time. This imaging mode also tackles the problem of shadowing and layover effects due to the sensing over multiple aspect angles, however at the cost of imaging a smaller swath on ground.

7.1 Future work

Future work will need to be focused on applications regarding the 3-D signature over $360°$ of forested areas, the estimation of extinction factor and subsequently biomass retrieval. Ex-

perimental data acquisition of the same test site can be carried out and analysed under different weather conditions and using different 3-D SAR techniques (e.g., HoloSAR, TomoSAR and PolInSAR). Additionally, CSAR and HoloSAR can be used in the cryosphere to retrieve 3-D ice profiles, in the geosphere for 3-D high resolution mapping of volcanoes and cities, remote archeological survey of ruins through foliage, characterisation of crop fields and eventually even voids search in collapsed structures and in the underground [Ponc 15, Ponc 16a, Ponc 16d, Teba 16, Band 16]. Moreover, an open topic for HoloSAR research still exists to understand CSAR and HoloSAR imaging statistics, such as the mitigation of speckle in subwavelength resolution images. Also, classification algorithms can be developed either by analysing the complex reflectivity in subapertures or as a result of the coherent addition of the full synthetic apertures.
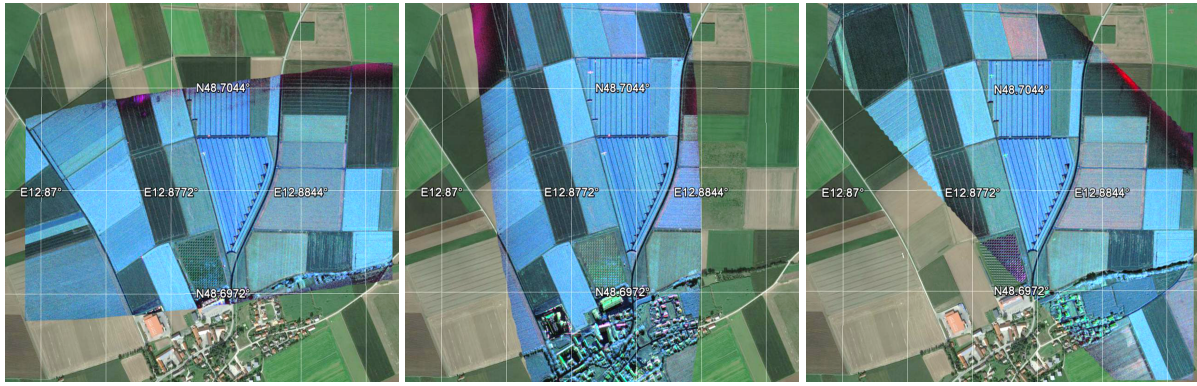
Figure 7.1: Fully polarimetric high-resolution images at X-band (bottom) in the Pauli basis (blue: HH+VV, red: HH-VV, green: 2HV) obtained by the coherent addition of $\Delta\phi = 10°$ [Ponc 16a]. Scene size: 1.5 km by 1.5 km. Aspect angles from left to right: $15°$, $85°$ and $330°$. Note that .

Top view. Perspective. Profile.
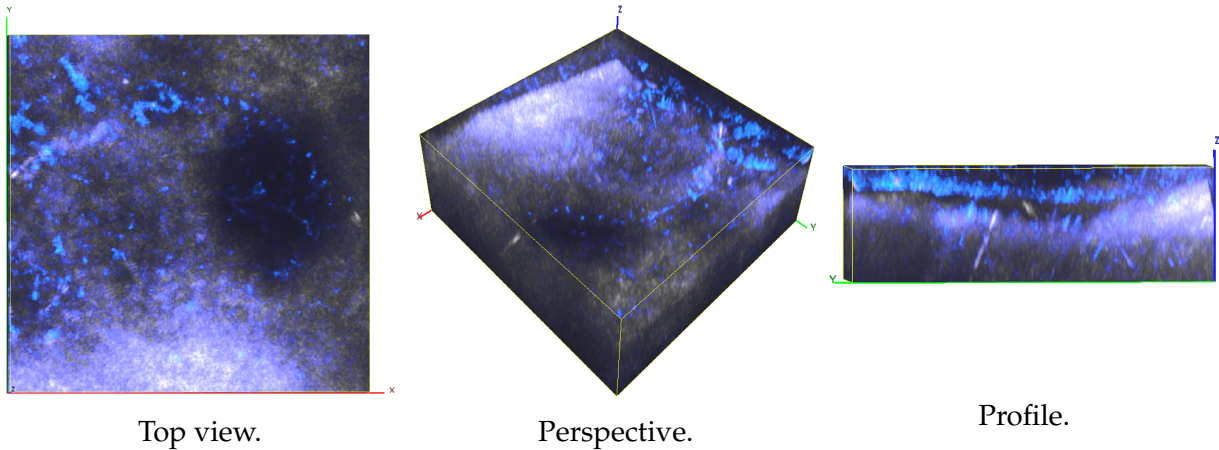
Figure 7.2: Rendering of a HoloSAR volume from different point of views over a glacier in K-Transect, Greenland [Ponc 16d]. The colour code corresponds to blue and white for HH and HV polarisations, respectively. Scene size: 500 m by 500 m by 100 m in the x, y and z directions, respectively.

Another potential field of future investigation is SAR interferometry with circular synthetic apertures in the presence of distributed scattering. Until now, interferometric approaches have been developed with a single circular flight to estimate terrain elevation from different looking angles using radargrammetry [Palm 12]. Likewise, the interferometric phase was exploited for

two simulated circular flights with a certain baseline in [Lin 11]. In [Lee 11], interferograms of several pairs of coregistered images were a subject of study. The circular synthetic apertures were first divided in subapertures, to be afterwards used to estimate the height of a scene with highly directive targets, i.e. vehicles, and assuming a single scatterer per resolution cell. Similarly, in [Aust 06], interferometric approaches were investigated for 3-D image reconstruction, provided that multiple scattering centres are within a radar resolution cell.

To continue the aforementioned investigations, suitable CSAR and HoloSAR data sets have already been recorded by the F-SAR system at X-/C-band over agricultural fields, and at L-/P-band over glaciers. In order to give an overview of the first results, 2-D and 3-D images are depicted in Figures 7.1 and 7.2. Figure 7.1 shows 2-D CSAR images acquired at X-band over agricultural fields in Wallerfing, Germany [Ponc 16a]. The images were obtained by an angular integration of $\Delta\phi = 10°$, and they correspond to the following viewing angles: $15°$, $85°$ and $330°$ from left to right. Note that the polarimetric signature of isotropic targets remains constant for different aspect angles. In addition, Figure 7.2 illustrates 3-D images from different view of a glacier in K-Transect, Greenland from a HoloSAR campaign at P-band [Ponc 16d]. The colour map indicates the HH and HV polarisations with blue and white, respectively. It can be seen that backscattering of crevasses is mainly obtained from the HH polarisation, whereas volume is more sensitive to the HV polarisation.
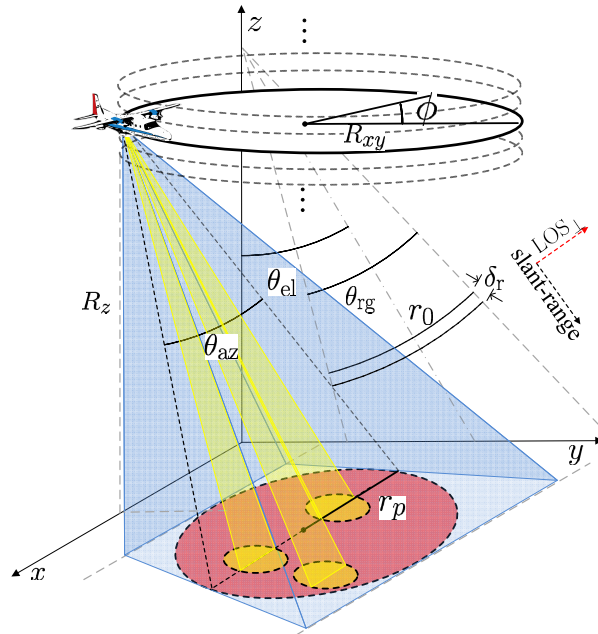
Figure 7.3: Beamforming and MIMO techniques for circular SAR and holographic SAR tomography, transmitter antenna beam in blue and multiple simultaneous receiver antenna beams in yellow [Ponc 14d, Ponc 16c]. The equivalent antenna beam, i.e., two-way illumination, after applying beamforming and MIMO techniques is depicted in red color.

A further research opportunity is to investigate solutions to overcome the limited size of the imaged scene in CSAR and HoloSAR. It is basically defined by the minimum half-power beamwidth (HPBW) in both the range and azimuth directions, and for high altitude platforms also by range ambiguities and the PRF. In [Ponc 14d, Ponc 16c], a solution has been proposed by means of multiple-input multiple-output (MIMO) techniques, thereby being able to extend future applications of CSAR and HoloSAR to much wider areas. The basic idea is to

exploit three different methods, namely scan-on-receive (SCORE), multi-channel reconstruction in azimuth (MCRA) and the use of orthogonal waveforms for quad-polarised systems [Gebe 09, Romm 13, Kim 11, Krie 14, More 15]. Indeed, this innovative concept has to be further studied to understand its main limitations and its possible application to spaceborne platforms. Figure 7.3 exemplifies the geometric configuration of a MIMO CSAR system, where the footprint is maximised by high-gain beams being beam-steered in elevation and in azimuth directions.

(a) 3-D view.

(b) Ground track.

(c) 3-D view.
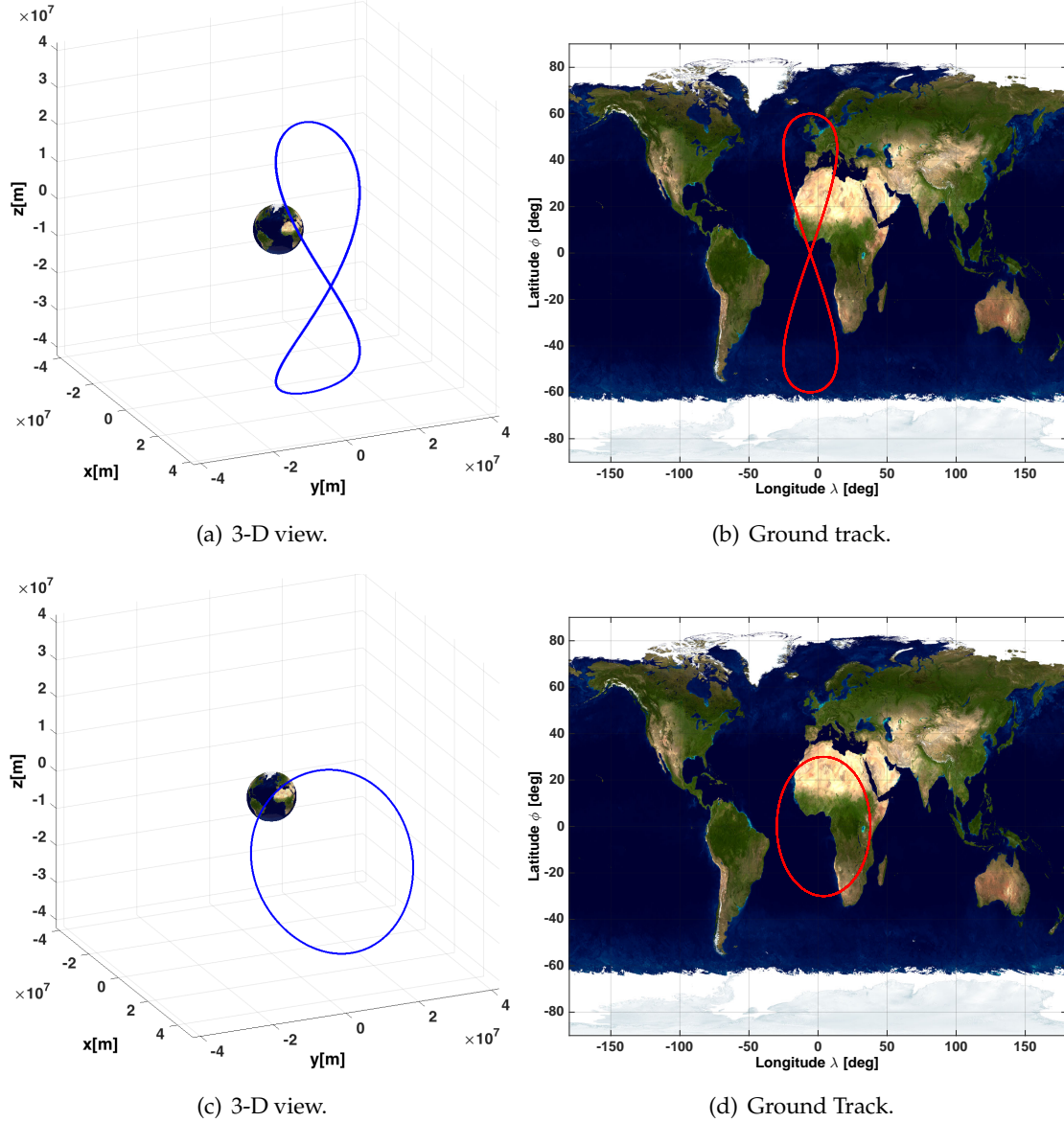
(d) Ground Track.

Figure 7.4: Future investigations on HoloSAR. (a-b) Tundra satellite movement (blue) with its corresponding Analemma ground track (red) [More 13]. (c-d) Circular satellite movement (blue) projected on Earth as a closed ground track (red).

Moreover, airborne CSAR and HoloSAR research with experimental realisations give a significant insight in the design of future space missions in the space range of low Earth orbits (LEO) at 700 km, medium Earth orbit (MEO) at $4,000$ km and geosynchronous Earth orbit SAR (GEOSAR) at $36,000$ km, as it has been done in recent years with stripmap and spotlight SAR for LEO space missions [Hoyo 16]. Particularly, in the MEO and the GEOSAR range the footprint size is no more a limitation, since regions in the order of hundreds or thousands of square

kilometres over the Earth can be covered. In this regard, efforts have been made to understand the limitations and advantages of such orbit concepts [Alme 12, Krie ay]. Specifically, in [Krie ay], a multistatic SAR constellation has been proposed. It consists of an illuminator in GEOSAR mode and multiple receivers in the LEO range. Similarly, in [Alme 12], the performance analysis for MEO and GEOSAR through Tundra orbits (Analemma ground tracks) and circular-like orbits (closed ground tracks), respectively, is studied (see Figure 7.4(a)-7.4(d)). It is shown that the ground coverage is significantly increased, while providing continuous monitoring of the observed region. Despite of the carried out research, there are still many research opportunities on this topic to better understand their potential and limitations.

A Appendix

A.1 DLR's SAR systems: E-SAR and F-SAR

In this thesis data acquired by both airborne SAR systems of DLR E-SAR and F-SAR are used. Both systems have been operated by the Microwaves and Radar Institute in cooperation with the DLR Flight Experiment Department. The E-SAR (Experimental Synthetic Aperture Radar System), operational until 2009, was designed and manufactured at DLR's Microwaves and Radar Institute and was installed onboard a DLR DO228 aircraft, a small STOL (short take-off and landing) aircraft (see Fig. A.1) [Horn 96, Reig 13b]. This aircraft has a maximum operating altitude of about 6000 m above see level and the nominal ground speed for SAR operation is about 90 m/s. The E-SAR was used primarily for research purposes since the beginning of 1989. The E-SAR was a high-resolution SAR system, which worked at L-, C-, X- and P- bands transmitting and receiving both vertical and horizontal polarisations (HH-HV-VV-VH). The E-SAR system operational flexibility could perform: single channel operation (one polarisation and one center frequency); along and across-track interferometric single-pass operation at X-band; polarimetric SAR mode (calibrated for L- and P- band); and repeat pass SAR interferometric-polarimetric mode at L- and P-bands and experimentally at C-band. The radar sensor was a modularly designed system containing four different RF segments for L-, C-, P- and X-band. Pulse generation and I/Q detection were located in the intermediate frequency section. The SAR raw data were stored in HDDC (high density digital cartridges, SONY SD-1) tapes using a single digital conversion and recording system. After transcription to hard disk drive, the standard E-SAR processor converted the raw data to calibrated image data products. The E-SAR technical specifications are summarised in Table A.1.

Figure A.1: The DO228 aircraft carrying the F-SAR sensor. The radar is able to acquire data simultaneously in X-, C-, S-, L- and P-band.

Table A.1: Technical specifications E-SAR and F-SAR systems.

	E-SAR				F-SAR				
Band	X	C	L	P	X	C	S	L	P
CF [GHz]	9.6	5.3	1.3	0.35	9.6	5.3	3.25	1.3	0.35 / 0.435
PRF [Hz]	up to 1200 (selectable)				5 k	5 k	5 k	10 k	12 k
Bandwidth [MHz]	max. 94 (selectable)				800	400	300	150	100
Sampling [bits]	6/6 or 8/8 (I/Q)				8 (real sampling)				
Data rates [MB/s]	8 or 16 (selectable)				247				
Polarisation	Fully L & P, dual C				Fully polarimetric				

Concurrently, a new airborne SAR system, the F-SAR, has been built and it is now fully operational at the Microwaves and Radar Institute. The F-SAR is the successor of the E-SAR system, and its development was motivated by the increasing demand for data being simultaneously acquired at different wavelengths and polarisations, and the demand for images with very high resolution [Reig 12b, Reig 12a, Reig 13a]. The F-SAR system is a fully modular system in X-, C-, S-, L- and P- bands with full polarimetric capability in all frequencies; single pass polarimetric interferometry capability in X- and S- bands; four recording channels with data rates of up to 1 Gbit/s per unit and fully reconfigurable operational modes. The radar is designed to cover a range of incidence angle from 20 ° to 55 ° degrees at an altitude of 6000 m above sea level. In order to simultaneously acquire data at different bands, the antenna mount holds seven right-looking dual polarised antennas: 3 for X-band, 1 for C-band, 2 for S-band and 1 for L- band. The P-band is mounted under the nose of the aircraft. The technical specifications for the F-SAR system are summarised in Table A.1.

A.2   Experimental realisation with E-SAR and F-SAR

As described in Chapter 5 and Chapter 6, three campaigns were run with the DLR's E-SAR and F-SAR systems. The first campaign was carried out at L-band in the CSAR mode in Kaufbeuren (Germany), whereas the second and the third were performed in the HoloSAR mode at P-band and L-band in Vordemwald (Switzerland) and Kaufbeuren (Germany), respectively. The three campaigns were analysed throughout this thesis to validate both imaging modes at low bands with fully polarimetric data. Table A.2 summarises the main parameters of the simulation and experimental realisations.

A.3   Special functions

This section is devoted to explain special functions, e.g., Gamma, Bessel and Hankel integrals, used throughout this thesis to derivate and understand the impulse response function (IRF) of circular SAR (CSAR) and holographic SAR tomography (HoloSAR) [Poul 10, Lebe 65].

Table A.2: Parameters of the circular and multicircular surveys.

	Simulated	L-band	P-band	L-band
Platform	n/a	E-SAR	F-SAR	F-SAR
Pulse repetition frequency [Hz]	400	400	504	500
Wavelength [m]	0.24	0.24	0.85	0.24
Bandwidth [MHz]	94	94	20	50
Number of passes in height	1	1	7	19
Flight radius [m]	~ 4400	~ 4400	~ 3850	~ 3700
Platform mean height [m]	~ 4200	~ 4200	~ 4270	~ 3200
Roll angle [°]	n/a	-9	-9	10
Antenna depression angle [°]	n/a	30	40	25
Antenna looking direction	n/a	left	left	right
Terrain [m]	700	DEM*	DEM*	DEM*
Aircraft speed [m/s]	90	~ 90	~ 90	~ 90
Date of acquisition	n/a	06.2008	09.07.2012	26.03.2012

*Digital elevation model

A.3.1 Gamma function

Commonly, the gamma function is used to understand the cylinder and hypergeometric functions, such as the Bessel or Hankel functions [Lebe 65]. A particular version of this integral is the upper incomplete gamma function, and it can be described by the next analytical expression

$$\Gamma(\varrho_1, \varrho_2) = \int\limits_{\varrho_2}^{\infty} e^{-t} t^{\varrho_1 - 1} \, \mathrm{d}t = \int\limits_{0}^{\infty} e^{-t} t^{\varrho_1 - 1} - \int\limits_{0}^{\varrho_2} e^{-t} t^{\varrho_1 - 1} \, \mathrm{d}t, \ \operatorname{Re} \varrho_1 > 0, \tag{A.1}$$

where the real part of ϱ_1 should be positive. Correspondingly, this expression can be used to describe a wide sort of integrals, such as

$$\Gamma(\varrho_1, \varrho_3) = \int\limits_{0}^{\infty} e^{-\varrho_3 \cdot t} t^{\varrho_1 - 1} \, \mathrm{d}t = \frac{\Gamma(\varrho_1, 0)}{\varrho_3^{\varrho_1}} \tag{A.2}$$

where ϱ_3 is a positive real number. In the following subsections, the Gamma function will be used to describe specific solutions to cylinder equations.

A.3.2 Bessel function

A cylinder function defines the solution of the following second-order linear differential equation

$$t'' + \frac{1}{\varrho_4} \cdot t' + \left(1 - \frac{\varrho_5^2}{\varrho_4^2}\right) \cdot t = 0, \tag{A.3}$$

where ϱ_4 is a complex variable and ϱ_5 is either a complex or a real value, which is also known as the Bessel's equation of order ϱ_5 [Lebe 65]. Particularly, one of the solutions to this equation

for a nonnegative integer $\varrho_5 = n$ is also known as the Bessel function of the first kind and order n. This function can be expressed as

$$J_n(\varrho_4) = \sum_{k=0}^{\infty} \frac{(-1)^k \cdot (\varrho_4/2)^{n+2k}}{k! \cdot (n+k)!}, \quad |\varrho_4| < \infty. \tag{A.4}$$

Moreover, two expressions from (A.4) can be obtained as a function of its derivative

$$J_n'(\varrho_4) + \frac{n}{\varrho_4} \cdot J_n(\varrho_4) = J_n - 1(\varrho_4), \quad J_n'(\varrho_4) - \frac{n}{\varrho_4} \cdot J_n(\varrho_4) = -J_n + 1(\varrho_4). \tag{A.5}$$

It follows from (A.4) that the Bessel function of the first kind and order n can be defined by integrals as

$$J_n(\varrho_4) = \frac{1}{2\pi} \cdot \int_0^{2\pi} e^{j(n\theta + \varrho_4 \cdot \cos(\theta))} \, d\theta, \tag{A.6}$$

and as a general closed approximation

$$J_{\varrho_5}(\varrho_4) \approx \frac{\varrho_4^{\varrho_5}}{2^{\varrho_5} \cdot \Gamma(1 + \varrho_5)}, \qquad \varrho_4 \to 0$$

$$J_{\varrho_5}(\varrho_4) \approx \sqrt{\frac{2}{\pi \varrho_4}} \cos(\varrho_4 - \frac{1}{2}\varrho_5 \pi - \frac{1}{4}\pi), \qquad \varrho_4 \to \infty, \tag{A.7}$$

for $\varrho_4 \geq 0$ and $\varrho_5 \geq 0$.

A.3.3   Hankel function

Furthermore, another class of cylinder functions are the Hankel functions or the Bessel functions of the third kind, which are expressed by linear combinations of Bessel functions of both, the first and second kind

$$H_{\varrho_5}^{(1)}(\varrho_4) = J_{\varrho_5}(\varrho_4) + jY_{\varrho_5}(\varrho_4), \quad H_{\varrho_5}^{(2)}(\varrho_4) = J_{\varrho_5}(\varrho_4) - jY_{\varrho_5}(\varrho_4), \tag{A.8}$$

where $Y_{\varrho_5}(\varrho_4)$ indicate the Bessel functions of the second kind, ϱ_5 can be arbitrary, and ϱ_4 is any point along from $-\infty$ and 0. In fact, the Hankel functions do not always have an analytical closed solution, thus expressing the result as an integral.

In this regard, the Hankel function can be expressed in terms of a sum of infinite Bessel functions of the first kind and $n = 0$ order

$$H_{\varrho_5}^{(1)}(\varrho_4) = \int_0^t \varrho_4 \cdot J_0(\varrho_4) \, d\varrho_4 = t \cdot J_1(t), \tag{A.9}$$

for $\varrho_4 \geq 0$ and where $H_{\varrho_5}^{(1)}(\varrho_4)$ is also referred as the Hankel transform.

A.3.4   Analysis of the 3-D back-projection equation

The derivation of (3.15) was accomplished by making the following approximations [Moor 10]. Let us take as a reference the formula given by (3.6)

$$s(\vec{r}_{\text{grid}}) = \int_{\theta_{\text{el}}} \int_k \int_\phi k^2 \cdot \sin(\theta_{\text{el}}) \cdot e^{-j2k \cdot |\vec{p} - \vec{R}(\phi)|} \cdot e^{j2k \cdot |\vec{r}_{\text{grid}} - \vec{R}(\phi)|} \, d\phi \, dk \, d\theta_{\text{el}}, \tag{A.10}$$

which describes the desired complex reflectivity as a function of three integrals in spherical coordinates, namely, elevation, radar bandwidth, and azimuth. The distance between the radar position $\vec{R}$ and the imaging grid $\vec{r}_{grid}$ can be expressed as

$$|\vec{r}_{grid} - \vec{R}| = \sqrt{|\vec{r}_{grid}|^2 + |\vec{R}|^2 - 2 \cdot \vec{r}_{grid} \cdot \vec{R}}, \tag{A.11}$$

with

$$\begin{bmatrix} \vec{R} \\ \vec{r}_{grid} \end{bmatrix} = \begin{bmatrix} R \cdot \sin(\theta_{el}) \cdot \cos(\phi) & R \cdot \sin(\theta_{el}) \cdot \sin(\phi) & R \cdot \cos(\theta_{el}) \\ r_x & r_y & r_z \end{bmatrix} \begin{bmatrix} \hat{x} \\ \hat{y} \\ \hat{z} \end{bmatrix}. \tag{A.12}$$

Subsequently, the argument of the right exponential can be redefined as follows

$$\begin{aligned} &= j2k \cdot \sqrt{|\vec{r}_{grid}|^2 + |\vec{R}|^2 - 2R \cdot (r_x \cdot \sin(\theta_{el}) \cdot \cos(\phi) + r_y \cdot \sin(\theta_{el}) \cdot \sin(\phi) + r_z \cdot \cos(\theta_{el}))} \\ &= j2k \cdot \sqrt{|\vec{r}_{grid}|^2 + |\vec{R}|^2 - 2R \cdot r_z \cdot \cos(\theta_{el}) - 2R \cdot \sin(\theta_{el}) \cdot (r_x \cdot \cos(\phi) + r_y \cdot \sin(\phi))} \\ &= j2k \cdot \sqrt{a - 2R \cdot \sin(\theta_{el}) \cdot (r_x \cdot \cos(\phi) + r_y \cdot \sin(\phi))} \\ &= j2k \cdot \sqrt{a - 2R \cdot r_{xy} \cdot \sin(\theta_{el}) \cdot (\cos(\alpha_r) \cdot \cos(\phi) + \sin(\alpha_r) \cdot \sin(\phi))} \\ &= j2k \cdot \sqrt{a + b \cdot \cos(\alpha_r - \phi)}, \end{aligned} \tag{A.13}$$

with $a = |\vec{r}_{grid}|^2 + |\vec{R}|^2 - 2R \cdot r_z \cdot \cos(\theta_{el})$, and $b = -2R \cdot r_{xy} \cdot \sin(\theta_{el})$. Similarly, the argument of the left integral can be reduced as

$$= -j2k \cdot \sqrt{c + d \cdot \cos(\alpha_p - \phi)}, \tag{A.14}$$

with $c = |\vec{p}|^2 + |\vec{R}|^2 - 2R \cdot p_z \cdot \cos(\theta_{el})$, and $d = -2R \cdot p_{xy} \cdot \sin(\theta_{el})$.

Equations (A.13) and (A.14) can be further simplified by removing the square roots from the rotation angle, ϕ, through Taylor series approximations, yielding

$$\begin{aligned} &= j2k \cdot \sqrt{a} \cdot \sqrt{1 + (b/a) \cdot \cos(\alpha_r - \phi)} \\ &= j2k \cdot \sqrt{a} \cdot (1 + (b/2a) \cdot \cos(\alpha_r - \phi)), \end{aligned} \tag{A.15}$$

and

$$\begin{aligned} &= -j2k \cdot \sqrt{c} \cdot \sqrt{1 + (d/c) \cdot \cos(\alpha_p - \phi)}, \\ &= -j2k \cdot \sqrt{c} \cdot (1 + (d/2c) \cdot \cos(\alpha_p - \phi)), \end{aligned} \tag{A.16}$$

where $\sqrt{1 + \varrho} \approx (1 + \varrho/2)$ for $|\varrho| < 1$. In this way, (A.10) can be rearranged as

$$s(\vec{r}_{grid}) = \int_{\theta_{el}} \sin(\theta_{el}) \cdot \int_k k^2 \cdot e^{j2k \cdot (\sqrt{a} - \sqrt{c})} \cdot \int_\phi e^{jk \cdot \left(\frac{b}{\sqrt{a}} \cdot \cos(\alpha_r - \phi) - \frac{d}{\sqrt{c}} \cdot \cos(\alpha_p - \phi)\right)} \, d\phi \, dk \, d\theta_{el}. \tag{A.17}$$

Then, the trigonometric function $\cos(\varrho_1 - \varrho_2) = \cos(\varrho_1)\cos(\varrho_2) + \sin(\varrho_1)\sin(\varrho_2)$ is used to reduce the argument of the second exponential, yielding

$$= jk \cdot \left(\cos(\phi) \left[\frac{b}{\sqrt{a}} \cdot \cos(\alpha_r) - \frac{d}{\sqrt{c}} \cos(\alpha_p) \right] - \sin(\phi) \left[\frac{b}{\sqrt{a}} \cdot \sin(\alpha_r) - \frac{d}{\sqrt{c}} \sin(\alpha_p) \right] \right), \tag{A.18}$$

and consequently, yielding

$$
\begin{aligned}
&= \mathrm{j}k \cdot \sqrt{m^2 + n^2} \cdot \sin(\phi + \varsigma), \\
&= \mathrm{j}k \cdot \sqrt{m^2 + n^2} \cdot \cos(\phi + \varsigma - \pi/2),
\end{aligned}
\tag{A.19}
$$

with

$$
\begin{aligned}
m &= \frac{b}{\sqrt{a}} \cdot \cos(\alpha_r) - \frac{d}{\sqrt{c}} \cos(\alpha_p) \\
n &= \frac{b}{\sqrt{a}} \cdot \sin(\alpha_r) - \frac{d}{\sqrt{c}} \sin(\alpha_p) \\
\varsigma &= \tan^{-1}\left(\frac{m}{n}\right) + \begin{cases} 0 & \text{if } n > 0 \\ \pi & \text{if } n < 0 \end{cases}.
\end{aligned}
\tag{A.20}
$$

Correspondingly, the closed solution of the first integral given by (A.17) can be found as follows

$$
\begin{aligned}
s(\vec{r}_{\mathrm{grid}}) &= \int_{\theta_{\mathrm{el}}} \sin(\theta_{\mathrm{el}}) \cdot \int_k k^2 \cdot e^{\mathrm{j}2k \cdot h} \cdot \int_\phi e^{\mathrm{j}k \cdot g \cos(\varsigma')} \, \mathrm{d}\phi \, \mathrm{d}k \, \mathrm{d}\theta_{\mathrm{el}} \\
&= 2\pi \int_{\theta_{\mathrm{el}}} \sin(\theta_{\mathrm{el}}) \cdot \int_k k^2 \cdot e^{\mathrm{j}2k \cdot h} \cdot J_0(k \cdot g) \, \mathrm{d}k \, \mathrm{d}\theta_{\mathrm{el}},
\end{aligned}
\tag{A.21}
$$

where $h = \sqrt{a} - \sqrt{c}$, $g = \sqrt{m^2 + n^2}$, and $\varsigma' = \phi + \varsigma - \pi/2$.

Bibliography

[Agui 13] E. Aguilera, M. Nannini, and A. Reigber. "Wavelet-Based Compressed Sensing for SAR Tomography of Forested Areas". *IEEE Trans. Geosci. Remote Sensing*, Vol. 51, No. 12, pp. 5283–5295, 2013.

[Alek 75] C. C. Aleksoff and C. R. Christensen. "Holographic Doppler imaging of rotating objects". *Applied optics*, Vol. 14, No. 1, pp. 134–141, 1975.

[Alme 12] V. Queiroz de Almeida. *Performance Analysis of Medium Earth Orbit and Geosynchronous Synthetic Aperture Radar*. German Aerospace Center (DLR), Microwaves and Radar Institute (HR), 2012. Diploma Thesis.

[Ash 12] J. Ash. "An Autofocus Method for Backprojection Imagery in Synthetic Aperture Radar". *IEEE Geosc. Remote Sens. Lett.*, Vol. 9, No. 1, pp. 104 –108, Jan. 2012.

[Aust 06] C. D. Austin and R. L. Moses. "Interferometric synthetic aperture radar detection and estimation based 3-D image reconstruction". In: *Algor. for Synt. Ape. Radar Ima. XIII*, pp. 43–54, SPIE Def. and Sec. Symp., 2006.

[Aust 08] C. D. Austin and R. L. Moses. "Wide-Angle Sparse 3D Synthetic Aperture Radar Imaging for Nonlinear Flight Paths". In: *IEEE Nat. Aeros. and Elec. Conf., 2008. NAECON 2008.*, pp. 330–336, IEEE, 2008.

[Aust 09] C. D. Austin, E. Ertin, and R. L. Moses. "Sparse multipass 3D SAR imaging: Applications to the GOTCHA data set". 2009.

[Aust 11] C. D. Austin, E. Ertin, and R. L. Moses. "Sparse signal methods for 3-D radar imaging". *Selec. Top. in Sig. Proc., IEEE Jou. of*, Vol. 5, No. 3, pp. 408–423, 2011.

[Axel 04] S. R. J. Axelsson. "Beam characteristics of three-dimensional SAR in curved or random paths". *IEEE Tran. Geosc. Remote Sen.*, Vol. 42, No. 10, pp. 2324–2334, Oct. 2004.

[Baml 99] R. Bamler and P. Hartl. "Synthetic aperture radar interferometry". *Inverse problems*, Vol. 14, No. 4, p. R1, 1999.

[Band 16] F. Banda, J. Dall, and S. Tebaldini. "Single and Multipolarimetric P-Band SAR Tomography of Subsurface Ice Structure". *IEEE Trans. on Geosc. and Rem. Sens.*, Vol. 54, No. 5, pp. 2832–2845, May 2016.

[Brow 67] W. M. Brown. "Synthetic Aperture Radar". *IEEE Tran. Aeros. Elec. Sys.*, Vol. 3, pp. 217 – 229, Mar. 1967.

[Brow 69] W. M. Brown and L. J. Porcello. "An introduction to synthetic-aperture radar". *Spectrum, IEEE*, Vol. 6, No. 9, pp. 52–62, 1969.

[Brow 99] L. Brown. *A radar history of World War II*. Institute of Physics Pub., 1999.

[Brya 03] M. L. Bryant, L. L. Gostin, and M. Soumekh. "3-D E-CSAR imaging of a T-72 tank and synthesis of its SAR reconstructions". *IEEE Tran. Aeros. Elec. Sys.*, Vol. 39, No. 1, pp. 211–227, 2003.

[Buck 91] S. Buckreuss. "Motion errors in an airborne synthetic aperture radar system". *Eur. Trans. on Telecom.*, Vol. 2, No. 6, pp. 655–664, 1991.

[Cand 06] E. J. Candès, J. K. Romberg, and T. Tao. "Stable signal recovery from incomplete and inaccurate measurements". *Commu. on pure and appl. mathe.*, Vol. 59, No. 8, pp. 1207–1223, 2006.

[Cand 08a] E. J. Candès. "The restricted isometry property and its implications for compressed sensing". *Comptes Rendus Math.*, Vol. 346, No. 9, pp. 589–592, 2008.

[Cand 08b] E. J. Candès and T. Tao. "Reflections on compressed sensing". *IEEE Inf. Theo. Soc. Newslet.*, Vol. 58, No. 4, pp. 20–23, 2008.

[Cand 11] E. J. Candès and Y. Plan. "A probabilistic and RIPless theory of compressed sensing". *Inf. Theo., IEEE Trans. on*, Vol. 57, No. 11, pp. 7235–7254, 2011.

[Cant 07] H. Cantalloube, E. Collin, and H. Oriot. "High Resolution SAR Imaging Along Circular Trajectories". In: *Synthetic Aperture Radar (EUSAR), Eur. Conf. on*, Barcelona, Spain, 23-28 July 2007.

[Cant 11] H. Cantalloube and C. Nahum. "Multiscale Local Map-Drift-Driven Multilateration SAR Autofocus Using Fast Polar Format Image Synthesis". *IEEE Trans. Geosci. Remote Sensing*, Vol. 49, No. 10, pp. 3730–3736, Oct. 2011.

[Carr 95a] W. G. Carrara, R. S. Goodman, and R. M. Majewski. *Spotlight Synthetic Aperture Radar: Signal Processing Algorithms*. Artech House Inc., 1995.

[Carr 95b] W. G. Carrara, R. S. Goodman, and R. M. Majewski. "Spotlight synthetic aperture radar- Signal processing algorithms(Book)". *Norwood, MA: Artech House, 1995.*, 1995.

[Ceti 01] M. Çetin and W. C. Karl. "Feature-enhanced synthetic aperture radar image formation based on nonquadratic regularization". *Im. Proc., IEEE Trans. on*, Vol. 10, No. 4, pp. 623–631, 2001.

[Chen 93] D. K. Cheng. "Fundamentals of engineering electromagnetics". 1993.

[Clou 95] S. R. Cloude and E. Pottier. "Concept of polarization entropy in optical scattering". *Optical Engineering*, Vol. 34, No. 6, pp. 1599–1610, 1995.

[Clou 96] S. Cloude and E. Pottier. "A review of target decomposition theorems in radar polarimetry". *IEEE Trans. Geosci. Remote Sensing*, Vol. 34, No. 2, pp. 498–518, 1996.

[Coll 06] E. Collin and H. Cantalloube. "Airborne SAR Imaging Along a Circular Trajec-
           tory". In: *Synthetic Aperture Radar (EUSAR), Eur. Conf. on*, Dresden, G., 16-18 May
           2006.

[Coll 08a] E. Collin and H. Cantalloube. "Assessment of physical limitations of high resolu-
           tion on targets at X-band from circular SAR experiments". In: *Synthetic Aperture
           Radar (EUSAR), Eur. Conf. on*, Friedrichshafen, Germany, 2-5 June 2008.

[Coll 08b] E. Collin and H. Cantalloube. "Circular SAR imagery for urban remote sensing".
           In: *Synthetic Aperture Radar (EUSAR), Eur. Conf. on*, Jun. 2008.

[Cumm 05] I. G. Cumming and F. H. C. Wong. *Digital Signal Processing of Synthetic Aperture
           Radar Data: Algorithms and Implementation*. *Artech House signal processing library*,
           Artech House, Incorporated, 2005.

[Curl 91] J. C. Curlander and R. N. McDonough. "Synthetic Aperture Radar: Systems and
           Signal processing". *New York: John Wiley & Sons, Inc, 1991.*, 1991.

[Cutr 66] L. J. Cutrona, E. N. Leith, L. J. Porcello, and W. Vivian. "On the application of
           coherent optical processing techniques to synthetic-aperture radar". *Proc. of the
           IEEE*, Vol. 54, No. 8, pp. 1026–1032, 1966.

[Dale 88] S. Dale and P. Edholm. "Inherent limitations in ectomography". *IEEE Trans. on
           Med. Imag.*, Vol. 7, No. 3, pp. 165–172, 1988.

[DeGr 05] S. DeGraaf. "3-D fully polarimetric wide-angle superresolution-based SAR imag-
           ing for ATR". In: *In Proc. of the Adap. Sen. Array Proc. Workshop*, Jun. 2005.

[DErr 12] M. D'Errico. *Distributed Space Missions for Earth System Monitoring*. Vol. 31,
           Springer, 2012.

[Desa 92] M. Desai and W. Jenkins. "Convolution backprojection image reconstruction for
           spotlight mode synthetic aperture radar". *IEEE Trans. on Image Proc.,,* Vol. 1, No. 4,
           pp. 505 –517, oct 1992.

[Dono 06] D. L. Donoho. "Compressed sensing". *Inf. The., IEEE Trans. on*, Vol. 52, No. 4,
           pp. 1289–1306, 2006.

[Dung 11] K. E. Dungan and L. C. Potter. "3-D Imaging of Vehicles using Wide Aperture
           Radar". *IEEE Tran. on Aeros. and Elec. Sys.*, Vol. 47, No. 1, pp. 187 –200, Jan. 2011.

[Ende 12] J. H. G. Ender. "Autofocusing ISAR Images via Sparse Representation". In: *Euro-
           pean Conf. Synthetic Aperture Radar (EUSAR)*, Apr. 2012.

[Erti 07] E. Ertin, C. Austin, S. Sharma, R. Moses, and L. C. Potter. "GOTCHA experience
           report: three-dimensional SAR imaging with complete circular apertures". In:
           Algorithms for SAR Imagery XIV, SPIE Def. and Sec. Symp., 2007.

[Erti 10] E. Ertin, R. L. Moses, and L. C. Potter. "Interferometric methods for three-
           dimensional target reconstruction with multipass circular SAR". *IET Radar, Sonar
           & Navigation*, Vol. 4, No. 3, pp. 464–473, 2010.

[Esch 10] T. Esch, A. Schenk, M. Thiel, T. Ullmann, M. Schmidt, and S. W. Dech. "Land cover classification based on single-polarized VHR SAR images using texture information derived via speckle analysis". In: *IEEE Inter. Geosc. and Remote Sen. Symp., 2010. IGARSS 2010.*, pp. 1875–1878, Jul. 2010.

[Fabe 09] R. Faber. "CUDA, Supercomputing for the Masses: Part 13, Using Textures memory in CUDA". `http://drdobbs.com/article/print?articleId=218100902&siteSectionName=`, Jun. 2009.

[Farh 75] N. Farhat. "High Resolution Microwave Holography and the Imaging of Remote Moving Objects". *Optical Engineering*, Vol. 14, No. 5, pp. 145499–145499, 1975.

[Ferr 01] A. Ferretti, C. Prati, and F. Rocca. "Permanent scatterers in SAR interferometry". *IEEE Tran. on Geosc. and Remote Sens.*, Vol. 39, No. 1, pp. 8–20, 2001.

[Ferr 03] L. Ferro-Famil, A. Reigber, E. Pottier, and W.-M. Boerner. "Scene Characterization Using Subaperture Polarimetric SAR Data". *IEEE Tran. on Geosc. and Remote Sens.*, Vol. 41, pp. 2264 – 2276, Oct. 2003.

[Ferr 09] M. Ferrara, J. Jackson, and C. Austin. "Enhancement of Multi-pass 3D Circular SAR Images Using Sparse Reconstruction Techniques". In: *Algor. for Synt. Ape. Radar Ima. XVI*, SPIE Def. and Sec. Symp., Apr. 2009.

[Ferr 11] P. Ferraro, A. Wax, and Z. Zalevsky. *Coherent Light Microscopy: Imaging and Quantitative Phase Analysis*. Vol. 46, Springer-Verlag Berlin Heidelberg, 1st Ed., 2011.

[Ferr 14] L. Ferro-Famil, S. Tebaldini, M. Davy, C. Leconte, and F. Boutet. "Very high-resolution three-dimensional imaging of natural environments using a tomographic ground-based SAR system". In: *The 8th Europ. Conf. on Ant. and Prop. (EuCAP 2014)*, pp. 3221–3224, April 2014.

[Forn 03] G. Fornaro, F. Serafino, and F. Soldovieri. "Three-dimensional focusing with multipass SAR data". *IEEE Tran. on Geosc. and Remote Sens.*, Vol. 41, No. 3, pp. 507–517, 2003.

[Forn 05] G. Fornaro, F. Lombardini, and F. Serafino. "Three-dimensional multipass SAR focusing: Experiments with long-term spaceborne data". *IEEE Tran. on Geosc. and Remote Sens.*, Vol. 43, No. 4, pp. 702–714, 2005.

[Forn 06] G. Fornaro, F. Lombardini, and F. Serafino. "Multidimensional imaging with ERS data". In: *Fringe 2005 Workshop*, p. 7, 2006.

[Forn 09] G. Fornaro, D. Reale, and F. Serafino. "Four-dimensional SAR imaging for height estimation and monitoring of single and double scatterers". *IEEE Tran. on Geosc. and Remote Sens.*, Vol. 47, No. 1, pp. 224–237, 2009.

[Forn 95] G. Fornaro and G. Franceschetti. "Image registration in interferometric SAR processing". *Rad., Son. and Nav., IEE Proc. -*, Vol. 142, No. 6, pp. 313–320, 1995.

[Frey 11a] O. Frey and E. Meier. "3-D Time-Domain SAR Imaging of a Forest Using Airborne Multibaseline Data at L- and P-Bands". *IEEE Trans. Geosci. Remote Sensing*, Vol. 49, pp. 3660 – 3664, Oct. 2011.

[Frey 11b] O. Frey and E. Meier. "Analyzing tomographic SAR data of a forest with respect to frequency, polarization, and focusing technique". *Geosc. and Rem. Sens., IEEE Trans. on*, Vol. 49, No. 10, pp. 3648–3659, 2011.

[Froe 08] P.-O. Froelind, L. Ulander, and A. Gustavsson. "First results on VHF-band SAR imaging using circular tracks". In: *Synthetic Aperture Radar (EUSAR), Eur. Conf. on*, Friedrichshafen, Germany, 2-5 June 2008.

[Froe 12] P.-O. Froelind, A. Gustavsson, M. Lundberg, and L. M. H. Ulander. "Circular-Aperture VHF-Band Synthetic Aperture Radar for Detection of Vehicles in Forest Concealment". *IEEE Tran. Geosc. Remote Sen.*, Vol. 50, No. 4, pp. 1329–1339, 2012.

[Frol 06] P.-O. Frolind and L. Ulander. "Evaluation of angular interpolation kernels in fast back-projection SAR processing". *Rad., Son. and Nav., IEE Proc. -*, Vol. 153, No. 3, pp. 243 – 249, Jun. 2006.

[Gabr 88] A. Gabriel and R. Goldenstein. "Crossed orbit interferometry: theory and experimental results from SIR-B". *International Journal of Remote Sensing*, Vol. 9, No. 5, pp. 857–872, 1988.

[Gall 10] M. Galloy. "GPULib with IDL 8.0 slide presentation. VI-Sualize 2010.". http://www.txcorp.com/pdf/GPULib/documentation/gpulib-with-idl80.pdf, 2010.

[Gebe 09] N. Gebert, G. Krieger, and A. Moreira. "Digital Beamforming on Receive: Techniques and Optimization Strategies for High-Resolution Wide-Swath SAR Imaging". *IEEE Tran. Aerosp. and Elect. Sys.*, Vol. 45, No. 2, pp. 564–592, April 2009.

[Glaz 93] J. K. Glazner and D. A. DiRosa. "A Comparison between Holographic SAR (HSAR) and Conventional Narrow Angle SAR". *EARSeL Adv. in Rem. Sens*, Vol. 2, No. 1, pp. 205–218, 1993.

[Grah 74] L. C. Graham. "Synthetic interferometer radar for topographic mapping". *Proceedings of the IEEE*, Vol. 62, No. 6, pp. 763–768, 1974.

[Gran 72] D. G. Grant. "Tomosynthesis: a three-dimensional radiographic imaging technique". *IEEE Trans. on Biomed. Engi.*, No. 1, pp. 20–28, 1972.

[Groh 71] G. Groh. "Holographic tomography using a circular synthetic aperture". *Applied optics*, Vol. 10, No. 11, pp. 2549–2550, 1971.

[Guil 06] S. Guillaso, A. Reigber, L. Ferro-Famil, and E. Pottier. "Range Resolution Improvement of Airborne SAR Images". *IEEE Geosc. Remote Sens. Lett.*, Vol. 3, No. 2, pp. 135–139, Jan. 2006.

[Hajn 09] I. Hajnsek, F. Kugler, L. Seung-Kuk, and K. Papathanassiou. "Tropical-Forest-Parameter Estimation by Means of Pol-InSAR: The INDREX-II Campaign ". *IEEE Tran. on Geosc. and Remote Sens.*, Vol. 47, pp. 481 – 493, Feb. 2009.

[Hall 05] B. Hallberg, G. Smith-Jonforsen, and L. M. Ulander. "Measurements on individual trees using multiple VHF SAR images". *IEEE Trans. Geosci. Remote Sensing*, Vol. 43, No. 10, pp. 2261–2269, 2005.

[Hans 01] R. F. Hanssen. *Radar interferometry: data interpretation and error analysis*. Vol. 2, Springer, 2001.

[Herm 02] G. T. Herman. *Computerized tomography*. Macmillan Press Ltd., 2002.

[Home 96] J. Homer, I. Longstaff, and G. Callaghan. "High resolution 3-D SAR via multi-baseline interferometry". In: *IEEE Inter. Geosc. and Remote Sen. Symp., 1996. IGARSS 1996.*, pp. 796–798, IEEE, 1996.

[Horn 96] R. Horn. "The DLR airborne SAR project E-SAR". In: *IEEE Inter. Geosc. and Remote Sen. Symp., 1996. IGARSS 1996.*, pp. 1624–1628 vol.3, 1996.

[Hoyo 16] T. Martinez del Hoyo and O. Ponce. "Understanding Spaceborne Missions for TomoSAR Imaging with Multi-Angular Acquisitions". In: *European Conf. Synthetic Aperture Radar (EUSAR)*, June 2016.

[Huan 12] Y. Huang, L. Ferro-Famil, and A. Reigber. "Under-Foliage Object Imaging Using SAR Tomography and Polarimetric Spectral Estimators". *IEEE Trans. on Geosc. and Rem. Sens.*, Vol. 50, No. 6, pp. 2213–2225, June 2012.

[Ishi 98] A. T.-K. C. Ishimaru and Y. Kuga. "An imaging technique using confocal circular synthetic aperture radar". *IEEE Tran. Geosc. Remote Sen.*, Vol. 36, pp. 1524–1530, Sep. 1998.

[Jako 06] C. V. Jakowatz and N. Doren. "Comparison of polar formatting and back-projection algorithms for spotlight-mode SAR image formation". In: *Proceedings of SPIE*, pp. 137–143, 2006.

[Jako 93] C. V. Jakowatz and D. E. Wahl. "Eigenvector method for maximum-likelihood estimation of phase errors in synthetic-aperture radar imagery". *J. Opt. Soc. Am. A*, Vol. 10, 1993.

[Kim 11] J.-H. Kim. *Multiple-Input Multiple-Output Synthetic Aperture Radar for Multimodal Operation*. Karlsruhe Institute of Technology (KIT), 2011. Ph.D. dissertation.

[Knab 79] J. Knab. "Interpolation of Band-Limited Functions Using the Approximate Prolate Series". *IEEE Trans. Inf. Theory*, Vol. IT-25, pp. 717–720, November 1979.

[Knae 95] K. K. Knaell and G. P. Cardillo. "Radar tomography for the generation of three-dimensional images". *IEEE Proc.-Rad., Son. and Navi.*, Vol. 142, No. 2, pp. 54–60, 1995.

[Knut 80] H. E. Knutsson, P. Edholm, G. H. Granlund, and C. U. Petersson. "Ectomography - a new radiographic reconstruction method - I. theory and error estimates". *IEEE Trans. on Biomed. Engi.*, No. 11, pp. 640–648, 1980.

[Krag 09] T. J. Kragh. "Minimum-entropy autofocus for three-dimensional SAR imaging". In: *Algor. for Synt. Ape. Radar Ima. XVI*, SPIE Def. and Sec. Symp., Apr. 2009.

[Krie 14] G. Krieger. "MIMO-SAR: Opportunities and Pitfalls". *IEEE Trans. Geosci. Remote Sensing*, Vol. 52, No. 5, pp. 2628–2645, May 2014.

[Krie ay] G. Krieger, I. Hajnsek, K. P. Papathanassiou, M. Younis, and A. Moreira. "Interferometric Synthetic Aperture Radar (SAR) Missions Employing Formation Flying". *Proceedings of the IEEE*, Vol. 98, No. 5, pp. 816–843, May.

[Lebe 65] N. N. Lebedev, R. A. Silverman, and D. Livhtenberg. *Special functions and their applications*. Prentice-Hall, 1965.

[Lebe 76] F. Leberl. "Mapping of lunar surface from side-looking orbital radar images". *The moon*, Vol. 15, No. 3-4, pp. 329–342, 1976.

[Lebe 91] F. W. Leberl, K. Maurice, J. Thomas, and W. Kober. "Radargrammetric measurements from the initial Magellan coverage of planet Venus". *Photogram. eng. and remo. sens.*, Vol. 57, pp. 1561–1570, 1991.

[Lee 08] F. Lee-Elkin. "Autofocus for 3D imaging". In: *Algor. for Synt. Ape. Radar Ima. XV*, SPIE Def. and Sec. Symp., Apr. 2008.

[Lee 11] F. Lee-Elkin and L. Potter. "An algorithm for wide aperture 3D SAR imaging with measured data". In: *Algorithms for SAR Imagery XVIII*, pp. 80510A–80510A, SPIE Def. and Sec. Symp., 2011.

[Lee 09] J.-S. Lee and E. Pottier. *Polarimetric radar imaging: from basics to applications. Optical science and engineering*, CRC Press, Taylor and Francis, 2009.

[Leit 71] E. N. Leith. "Quasi-holographic techniques in the microwave region". *Proc. of the IEEE*, Vol. 59, No. 9, pp. 1305–1318, 1971.

[Lin 11] Y. Lin, W. Hong, W. Tan, Y. Wang, and Y. Wu. "Interferometric circular SAR method for three-dimensional imaging". *IEEE Geosc. Remote Sens. Lett.*, Vol. 8, No. 6, pp. 1026–1030, 2011.

[Lomb 03] F. Lombardini and A. Reigber. "Adaptive spectral estimation for multibaseline SAR tomography with airborne L-band data". In: *IEEE Inter. Geosc. and Remote Sen. Symp., 2003. IGARSS 2003.*, pp. 2014–2016, Jul. 2003.

[Lomb 05a] F. Lombardini. "Analysis of non-gaussian speckle statistics in high-resolution SAR images". In: *IEEE Inter. Geosc. and Remote Sen. Symp., 2005. IGARSS 2005.*, pp. 1337–1340, 25-29 July 2005.

[Lomb 05b] F. Lombardini. "Differential tomography: A new framework for SAR interferometry". *IEEE Tran. on Geosc. and Remote Sens.*, Vol. 43, No. 1, pp. 37–44, 2005.

[Mace 08] K. A. Câmara de Macedo, R. Scheiber, and A. Moreira. "An Autofocus Approach for Residual Motion Errors With Application to Airborne Repeat-Pass SAR Interferometry". *IEEE Tran. on Geosc. and Remote Sens.*, Vol. 46, No. 10, pp. 3151–3162, Oct. 2008.

[Maju 07] U. K. Majumder, M. A. Temple, M. J. Minardi, and E. G. Zelnio. "Point spread function characterization of a radially Displaced Scatterer using Circular Synthetic Aperture Radar". In: *2007 IEEE Radar Conf.*, pp. 729–733, IEEE, 2007.

[Manc 81]   C. E. Mancill and J. M. Swiger. "A map drift autofocus technique for correcting higher order SAR phase errors". In: *Proc. 27th Annual Tri-Service Radar Sym. Rec.*, pp. 391 –400, 1981.

[Mass 98]   D. Massonnet and K. L. Feigl. "Radar interferometry and its application to changes in the Earth's surface". *Reviews of geophysics*, Vol. 36, No. 4, pp. 441–500, 1998.

[Mens 80]   D. Mensa, G. Heidbreder, and G. Wade. "Aperture synthesis by object rotation in coherent imaging". *IEEE Tran. Nucl. Sci.*, Vol. 27, No. 2, pp. 989–998, 1980.

[Mens 82]   D. Mensa and G. Heidbreder. "Bistatic synthetic-aperture radar imaging of rotating objects". *IEEE Tran. Aeros. Elec. Sys.*, No. 4, pp. 423–431, 1982.

[Mens 91]   D. L. Mensa. *High resolution radar cross-section imaging.* Vol. 1, Boston, MA, Artech House, 1991, 280 p., 1991.

[Minh 15]   D. H. T. Minh, S. Tebaldini, F. Rocca, T. Le Toan, L. Villard, and P. C. Dubois-Fernandez. "Capabilities of BIOMASS tomography for investigating tropical forests". *Geosc. and Rem. Sens., IEEE Trans. on*, Vol. 53, No. 2, pp. 965–975, 2015.

[Moor 07]   L. J. Moore and L. C. Potter. "Three-dimensional resolution for circular synthetic aperture radar". In: *Algorithms for Synthetic Aperture Radar Imagery XIV*, SPIE Def. and Sec. Symp., Apr. 2007.

[Moor 10]   L. J. Moore and U. K. Majumder. "An analytical expression for the three-dimensional response of a point scatterer for circular synthetic aperture radar". In: *Algorithms for Synthetic Aperture Radar Imagery XIV*, SPIE Def. and Sec. Symp., 2010.

[More 13]   J. A. Moreno Gonzalez. *Orbital Mechanics, Tutorial.* Technical University of Munich, 2013.

[More 15]   A. Moreira, G. Krieger, I. Hajnsek, K. Papathanassiou, M. Younis, P. Lopez-Dekker, S. Huber, M. Villano, M. Pardini, M. Eineder, F. D. Zan, and A. Parizzi. "Tandem-L: A Highly Innovative Bistatic SAR Mission for Global Observation of Dynamic Processes on the Earth's Surface". *IEEE Geosc. and Rem. Sens. Magazine*, Vol. 3, No. 2, pp. 8–23, June 2015.

[Mose 04]   R. L. Moses, E. Ertin, and C. Austin. "Synthetic aperture radar visualization". In: *Sign., Sys. and Comp., 2004. Conf. Rec. of the Thirty-Eighth Asilo. Conf. on*, pp. 13–17 Vol.1, 2004.

[Mose 05]   R. L. Moses and L. C. Potter. "Noncoherent 2D and 3D SAR reconstruction from wide-angle measurements". In: *13th Ann. Adap. Sens. Arr. Proc. Works., MIT Lincoln Laboratory*, 2005.

[Mott 92]   H. Mott. *Antennas for Radar and Communications: a Polarimetric Approach.* Wiley-Interscience, 1992.

[Muns 83]   D. C. Munson Jr., J. D. O'Brien, and W. K. Jenkins. "A tomographic formulation of spotlight-mode synthetic aperture radar". *Proceedings of the IEEE*, Vol. 71, No. 8, pp. 917–925, 1983.

[Nann 09a] M. Nannini. *Advanced Synthetic Aperture Radar Tomography: Processing Algorithms and Constellation Design*. Karlsruhe Institute of Technology (KIT), PhD Thesis, 2009.

[Nann 09b] M. Nannini, R. Scheiber, and A. Moreira. "Estimation of the minimum number of tracks for SAR tomography". *IEEE Tran. on Geosc. and Remote Sens.*, Vol. 47, No. 2, pp. 531–543, 2009.

[Nann 12] M. Nannini, R. Scheiber, R. Horn, and A. Moreira. "First 3-D reconstructions of targets hidden beneath foliage by means of polarimetric SAR tomography". *IEEE Tran. on Geosc. and Remote Sens.*, Vol. 9, No. 1, pp. 60–64, 2012.

[Neum 10] M. Neumann, L. Ferro-Famil, and A. Reigber. "Estimation of forest structure, ground, and canopy layer characteristics from multibaseline polarimetric interferometric SAR data". *IEEE Trans. Geosci. Remote Sensing*, Vol. 48, No. 3, pp. 1086–1104, 2010.

[Onho 12] N. O. Onhon and M. Çetin. "A sparsity-driven approach for joint SAR imaging and phase error correction". *Im. Proc., IEEE Trans. on*, Vol. 21, No. 4, pp. 2075–2088, 2012.

[Palm 12] S. Palm, H. M. Oriot, and M. H. Cantalloube. "Radargrammetric DEM Extraction Over Urban Area Using Circular SAR Imagery". *IEEE Tran. Geosc. Remote Sen.*, Vol. 50, No. 11, pp. 4720–4725, Nov. 2012.

[Pasm 05a] A. Pasmurov and J. Zinoviev. *Radar imaging and holography*. Stevenage, Herts, UK, The Institution of Electrical Engineers, Michael Faraday House, 2005.

[Pasm 05b] A. Pasmurov and J. Zinoviev. *Radar Imaging and Holography*. Stevenage, Herts, UK, The Institution of Electrical Engineers, Michael Faraday House, 2005.

[Pinh 09] M. Pinheiro, P. Prats, R. Scheiber, M. Nannini, and A. Reigber. "Tomographic 3D reconstruction from airborne circular SAR". In: *IEEE Inter. Geosc. and Remote Sen. Symp., 2009. IGARSS 2009.*, pp. III–21 – III–24, Jul. 2009.

[Ponc 12] O. Ponce, P. Prats, R. Scheiber, A. Reigber, and A. Moreira. "Multibaseline 3-D Circular SAR Imaging at L-band". In: *Synthetic Aperture Radar (EUSAR), Eur. Conf. on*, Apr. 2012.

[Ponc 13a] O. Ponce, P. Prats, R. Scheiber, A. Reigber, and A. Moreira. "Analysis and optimization of multi-circular SAR for fully polarimetric holographic tomography over forested areas". In: *Geosc. and Rem. Sens. Symp. (IGARSS), 2013 IEEE Int.*, July 2013.

[Ponc 13b] O. Ponce, P. Prats, R. Scheiber, A. Reigber, and A. Moreira. "First demonstration of 3-D holographic tomography with fully polarimetric Multi-Circular SAR at L-band". In: *Geosc. and Rem. Sens. Symp. (IGARSS), 2013 IEEE Int.*, July 2013.

[Ponc 14a] O. Ponce, P. Prats, M. Pinheiro, M. Rodriguez-Cassola, R. Scheiber, A. Reigber, and A. Moreira. "Fully-Polarimetric High-Resolution 3-D Imaging with Circular SAR at L-Band". *IEEE Trans. Geosci. Remote Sensing*, Vol. 52, pp. 3074 – 3090, 2014.

[Ponc 14b] O. Ponce, P. Prats, R. Scheiber, A. Reigber, and A. Moreira. "Polarimetric 3-D Reconstruction from Multicircular SAR at P-Band". *IEEE Geosc. Remote Sens. Lett.*, Vol. 11, pp. 803–807, 2014.

[Ponc 14c] O. Ponce, P. Prats, R. Scheiber, A. Reigber, and A. Moreira. "Study of the 3-D Impulse Response Function of Holographic SAR Tomography with Multicircular Acquisitions". In: *Synthetic Aperture Radar (EUSAR), Eur. Conf. on*, Jun. 2014.

[Ponc 14d] O. Ponce, T. Rommel, M. Younis, P. Prats, and A. Moreira. "Multiple-input multiple-output circular SAR". In: *Radar Symp. (IRS), 2014 15th Int.*, pp. 1–5, June 2014.

[Ponc 15] O. Ponce, P. Prats, R. Scheiber, A. Reigber, and A. Moreira. "Polarimetric 3-D imaging with airborne holographic SAR tomography over glaciers". In: *Geosc. and Rem. Sens. Symp. (IGARSS), 2015 IEEE Int.*, July 2015.

[Ponc 16a] O. Ponce, H. Joerg, R. Scheiber, P. Prats, I. Hajnsek, and A. Reigber. "First study on holographic SAR tomography over agricultural crops at C-/X-band". In: *Geosc. and Rem. Sens. Symp. (IGARSS), 2016 IEEE Int.*, July 2016.

[Ponc 16b] O. Ponce, P. Prats, R. Scheiber, A. Reigber, and A. Moreira. "First Airborne Demonstration of Holographic SAR Tomography with Fully Polarimetric Multi-circular Acquisitions at L-band". *IEEE Trans. Geosci. Remote Sensing*, Vol. 54, pp. 6170 – 6196, 2016.

[Ponc 16c] O. Ponce, F. Queiroz de Almeida, and T. Rommel. "Multiple-Input Multiple-Output Circular SAR for High Altitude Pseudo-Satellites". In: *Space Gener. Cong. (SGC) / Int. Astron. Cong. (IAC), 2016*, pp. 1–5, September 2016.

[Ponc 16d] O. Ponce, R. Scheiber, P. Prats, I. Hajnsek, and A. Reigber. "Multi-dimensional airborne holographic SAR tomography reconstruction for glaciers at L-/P-band". In: *Geosc. and Rem. Sens. Symp. (IGARSS), 2016 IEEE Int.*, July 2016.

[Pott 10] L. C. Potter, E. Ertin, J. T. Parker, and M. Cetin. "Sparsity and compressed sensing in radar imaging". *Procee. of the IEEE*, Vol. 98, No. 6, pp. 1006–1020, 2010.

[Poul 10] A. D. Poularikas. *Transforms and Applications Handbook; 3rd ed*. Electrical Engineering Handbook, CRC Press, Hoboken, 2010.

[Prat 04] P. Prats, A. Reigber, and J. J. Mallorqui. "Interpolation-free coregistration and phase-correction of airborne SAR interferograms". *IEEE Geosc. Remote Sens. Lett.*, Vol. 1, No. 3, pp. 188–191, 2004.

[Redd 03] N. Redding and T. Payne. "Inverting the spherical Radon transform for 3D SAR image formation". In: *Radar Conf., 2003. Proc. of the Int.*, pp. 466–471, Sept 2003.

[Reig 00] A. Reigber and A. Moreira. "First Demonstration of Airborne SAR Tomography Using Multibaseline L-Band Data". *IEEE Tran. Geosc. Remote Sen.*, Vol. 38, pp. 2142–2152, Sep. 2000.

[Reig 06] A. Reigber, P. Prats, and J. Mallorqui. "Refined Estimation of Time-Varying Baseline Errors in Airborne SAR Interferometry". *IEEE Geosc. Remote Sens. Lett.*, Vol. 3, Jan. 2006.

[Reig 12a] A. Reigber, M. Jager, J. Fischer, R. Horn, R. Scheiber, P. Prats, and A. Nottensteiner. "Performance of the L- and P-band subsystems of the F-SAR airborne SAR instrument". In: *European Conf. Synthetic Aperture Radar (EUSAR)*, pp. 286–289, 2012.

[Reig 12b] A. Reigber, M. Jager, M. Pinheiro, R. Scheiber, P. Prats, J. Fischer, R. Horn, and A. Nottensteiner. "Performance of the P-band subsystem and the X-band interferometer of the F-SAR airborne SAR instrument". In: *Geoscience and Remote Sensing Symposium (IGARSS), 2012 IEEE International*, pp. 5037–5040, 2012.

[Reig 13a] A. Reigber, M. Jager, R. Scheiber, P. Prats, R. Horn, and A. Nottensteiner. "Multispectral, polarimetric and interferometric SAR imaging with the F-SAR airborne SAR instrument". In: *Rad. Symp. (IRS), 2013 14th Int.*, pp. 27–32, 2013.

[Reig 13b] A. Reigber, R. Scheiber, M. Jager, P. Prats-Iraola, I. Hajnsek, T. Jagdhuber, K. P. Papathanassiou, M. Nannini, E. Aguilera, S. Baumgartner, R. Horn, A. Nottensteiner, and A. Moreira. "Very-high-resolution airborne synthetic aperture radar imaging: Signal processing and applications". *Proceedings of the IEEE*, Vol. 101, No. 3, pp. 759–783, 2013.

[Reig 97] A. Reigber and J. Moreira. "Phase unwrapping by fusion of local and global methods". In: *IEEE Inter. Geosc. and Remote Sen. Symp., 1997. IGARSS'97.*, pp. 869–871, IEEE, 1997.

[Rodr 11] M. Rodriguez-Cassola, P. Prats, G. Krieger, and A. Moreira. "Efficient Time-Domain Image Formation with Precise Topography Accommodation for General Bistatic SAR Configurations". *IEEE Tran. on Aeros. and Elec. Sys.*, Vol. 47, No. 4, pp. 2949 – 2966, Oct. 2011.

[Romm 13] T. Rommel, A. Patyuchenko, P. Laskowski, M. Younis, and G. Krieger. "An Orthogonal Waveform Scheme for Imaging MIMO radar Applications". In: *Rad. Symp. (IRS), 2013 14th Int.*, pp. 917–922, June 2013.

[Rose 00] P. A. Rosen, S. Hensley, I. R. Joughin, F. K. Li, S. N. Madsen, E. Rodriguez, and R. M. Goldstein. "Synthetic aperture radar interferometry". *Proceedings of the IEEE*, Vol. 88, No. 3, pp. 333–382, 2000.

[Rudi 92] L. I. Rudin, S. Osher, and E. Fatemi. "Nonlinear total variation based noise removal algorithms". *Physica D: Nonlinear Phenomena*, Vol. 60, No. 1, pp. 259–268, 1992.

[Sama 11] S. Samadi, M. Cetin, and M. Masnadi-Shirazi. "Sparse representation-based synthetic aperture radar imaging". *Rad. Sys., 2012 IET Int., Conf. on*, Vol. 5, pp. 182 – 193, Feb. 2011.

[Samc 06] P. Samczynski and K. Kulpa. "Concept of the Coherent Autofocus Map-Drift Technique". In: *Int. Radar Symp., IRS 2006*, pp. 1 – 4, 2006.

[Sand 10] R. Sandau, H.-P. Roeser, and A. Valenzuela. *Small Satellite Missions for Earth Observation: New Developments and Trends*. Springer, 2010.

[Sche 00] R. Scheiber and A. Moreira. "Coregistration of interferometric SAR images using spectral diversity". *IEEE Trans. Geosci. Remote Sensing*, Vol. 38, No. 5, pp. 2179–2191, Sep 2000.

[Schi 93] R. F. Schindel. "Three-Dimensional Aspects of Microwave Holography". *EARSeL Adv. in Rem. Sens*, Vol. 2, No. 1, pp. 129–144, 1993.

[Scud 78] H. J. Scudder. "Introduction to computer aided tomography". *Proc. of the IEEE*, Vol. 66, No. 6, pp. 628–637, 1978.

[Sego 10] D. J. Sego, H. Griffiths, and M. C. Wicks. "Waveform design for low frequency tomography". In: *2010 Int. Wavef. Diver. and Des. Conf. (WDD)*, pp. 230–237, IEEE, 2010.

[Sera 05] F. Serafino, F. Soldovieri, F. Lombardini, and G. Fornaro. "Singular value decomposition applied to 4D SAR imaging". In: *IEEE Inter. Geosc. and Remote Sen. Symp., 2005. IGARSS 2005.*, pp. 2701–2704, IEEE, 2005.

[Shan 09] S. K. Shan and J. R. S. Colin. "Image formation in holographic tomography: high-aperture imaging conditions". *Applied Optics*, Vol. 48, 2009.

[She 02] D. A. She, Z.and Gray, R. Bogner, J. Homer, and I. Longstaff. "Three-dimensional space-borne synthetic aperture radar (SAR) imaging with multiple pass processing". *International Journal of Remote Sensing*, Vol. 23, No. 20, pp. 4357–4382, 2002.

[Skol 00] M. I. Skolnik. "Radar in the twentieth century". *IEEE Aeros. Elec. Sys. Mag.*, Vol. 15, No. 10, pp. 27–43, Oct 2000.

[Skol 01] M. I. Skolnik. *Introduction to Radar Systems*. McGraw-Hill, New York, 2001.

[Soum 96] M. Soumekh. "Reconnaissance with slant plane circular SAR imaging". *Image Proc., IEEE Tran. on*, Vol. 5, No. 8, pp. 1252–1265, 1996.

[Soum 99] M. Soumekh. *Synthetic Aperture Radar Signal Processing: with MATLAB Algorithms*. John Wiley & Sons, 1999.

[Spag 95] U. Spagnolini. "2-D phase unwrapping and instantaneous frequency estimation". *IEEE Trans. Geosci. Remote Sensing*, Vol. 33, No. 3, pp. 579–589, 1995.

[Teba 16] S. Tebaldini, T. Nagler, H. Rott, and A. Heilig. "Imaging the Internal Structure of an Alpine Glacier via L-Band Airborne SAR Tomography". *IEEE Trans. on Geosc. and Rem. Sens.*, Vol. 54, No. 12, pp. 7197–7209, Dec 2016.

[Tell 10] M. Tello Alonso, P. Lopez-Dekker, and J. Mallorqui. "A Novel Strategy for Radar Imaging Based on Compressive Sensing". *IEEE Trans. Geosci. Remote Sensing*, Vol. 48, No. 12, pp. 4285–4295, Dec 2010.

[Torg 14] J. Torgrimsson, P. Dammert, H. Hellsten, and L. M. Ulander. "Factorized geometrical autofocus for synthetic aperture radar processing". *IEEE Trans. Geosci. Remote Sensing*, Vol. 52, No. 10, pp. 6674–6687, 2014.

[Torg 16] J. Torgrimsson, P. Dammert, H. Hellsten, and L. M. Ulander. "An efficient solution to the factorized geometrical autofocus problem". *IEEE Trans. Geosci. Remote Sensing*, Vol. 54, No. 8, pp. 4732–4748, 2016.

[Ulan 03] L. M. H. Ulander, H. Hellsten, and G. Stenstrom. "Synthetic-Aperture Radar Processing Using Fast Factorized Back-Projection". *IEEE Tran. on Aeros. and Elec. Sys.*, Vol. 39, No. 3, pp. 760–776, July 2003.

[Vert 09] S. Vertu, J.-J. Delaunay, I. Yamada, and O. Haeberlé. "Diffraction microtomography with sample rotation: influence of a missing apple core in the recorded frequency space". *Central European Journal of Physics*, Vol. 7, No. 1, pp. 22–31, 2009.

[Vocc 09] K. Voccola, B. Yazıcı, M. Ferrara, and M. Cheney. "On the relationship between the generalized likelihood ratio test and backprojection for synthetic aperture radar imaging". In: *Algorithms for SAR Imagery XVI*, pp. 73350I–1, SPIE Def. and Sec. Symp., 2009.

[Vu 12] V. T. Vu, T. K. Sjogren, M. I. Pettersson, and M. J. Minardi. "Studying CSAR systems using IRF-CSAR". In: *Rad. Sys., 2012 IET Int., Conf. on*, 22-25 Oct. 2012.

[Wile 65] C. Wiley. "Pulsed doppler radar methods and apparatus". Jul 1965. US Patent 3,196,436.

[Will 99] E. G. Williams. *Fourier acoustics: sound radiation and nearfield acoustical holography*. Access Online via Elsevier, 1999.

[Wu 87] R.-S. Wu and M. N. Toksöz. "Diffraction tomography and multisource holography applied to seismic imaging". *Geophysics*, Vol. 52, No. 1, pp. 11–25, 1987.

[Xu 99] W. Xu and I. Cumming. "A region-growing algorithm for InSAR phase unwrapping". *IEEE Trans. Geosci. Remote Sensing*, Vol. 37, No. 1, pp. 124–134, 1999.

[Yegu 99] A. F. Yegulalp. "Fast Backprojection Algorithm for Synthetic Aperture Radar". In: *The Record of the 1999 IEEE Radar Conf.*, pp. 60–65, 1999.

[Zebk 86] H. A. Zebker and R. M. Goldstein. "Topographic mapping from interferometric synthetic aperture radar observations". *Journal of Geophysical Research*, Vol. 91, No. B5, pp. 4993–4999, 1986.

[Zebk 92] H. Zebker and J. Villasenor. "Decorrelation in interferometric radar echoes". *IEEE Tran. on Geosc. and Remote Sens.*, Vol. 30, No. 5, pp. 950–959, 1992.

[Zeng 94] G. Zeng and G. Gullberg. "Can the backprojection filtering algorithm be as accurate as the filtered backprojection algorithm?". In: *Nuclear Sci. Symp. and Medi. Imag. Conf., 1994., 1994 IEEE Conf. Rec.*, pp. 1232–1236, Oct 1994.

[Zhan 08] X. Zhang, Y. Zhang, and J. Jiang. "Analysis and Computer Simulation of Circular Synthetic Aperture Radar with single frequency". In: *Synthetic Aperture Radar (EUSAR), Eur. Conf. on*, Jun. 2008.

[Zhu 12] X. X. Zhu and R. Bamler. "Demonstration of Super-Resolution for Tomographic SAR Imaging in Urban Environment". *IEEE Trans. Geosci. Remote Sensing*, Vol. 50, No. 8, pp. 3150–3157, 2012.